# Interaction of amyloid peptides with biomembranes and its implications in Alzheimers disease and type II diabetes

Inaugural-Dissertation

zur Erlangung des Doktorgrades
der Mathematisch-Naturwissenschaftlichen Fakultät
der Heinrich-Heine-Universität Düsseldorf

vorgelegt von

**Chetan Poojari**
aus Bangalore, India

Jülich, 24. Mai 2013

aus dem Institute of Complex Systems (ICS-6): Strukturbiochemie
des Forschungszentrum Jülich

Gedruckt mit der Genehmigung der
Mathematisch-Naturwissenschaftlichen Fakultät der
Heinrich-Heine-Universität Düsseldorf

Referent: Jun.-Prof. Dr. Birgit Strodel
Korreferent: Prof. Dr. Dieter Willbold

Tag der mündlichen Prüfung: 9. Juli 2013

# Statement of Authorship

I, Chetan Poojari, hereby certify that the work presented here is, to the best of my knowledge and belief, original and the result of my own investigations. I have fully acknowledged and referenced the ideas and work of others, whether published or unpublished, in my thesis. My thesis contains no material published elsewhere or extracted in whole or in part from a thesis submitted for a degree at this or any other university. Where the results are produced in collaboration with others, I have clearly mentioned my contributions.

# Abstract

Alzheimers disease (AD) and type II diabetes are associated with the aggregation of amyloid polypeptides into fibrillar $\beta$-sheet structures. One of the amyloid hypothesis is the toxicity resulting from amyloid-membrane interactions. The effects of amyloid peptides on lipid membrane behavior have been characterized experimentally, but structural and causal details are lacking. We use atomistic molecular dynamics simulations to investigate the behavior of the A$\beta$ peptide in AD and of the human islet amyloid polypeptide (hIAPP) in type II diabetes on lipid bilayers. We find that the membrane surface charge and the lipid tail type are determinants for transmembrane stability of A$\beta$ in lipid bilayers, while A$\beta$ oligomerization was observed to increase the translocation of water molecules across the bilayer. Furthermore, familial A$\beta$ mutations, which are known to speed up the peptide aggregation and increase brain toxicity, are studied. These simulations reveal that those A$\beta$ mutations, which are known to be more toxic than wild type A$\beta$, show a larger membrane disruptive effect in our simulations, which can be attributed to stable $\beta$-sheets inside the membrane. These results suggest that the altered neurotoxicity arising from mutations in A$\beta$ is not only a result of the altered aggregation propensity, but also originates from modified A$\beta$ interactions with neuronal membranes. The mechanism of membrane A$\beta$ insertion and permeation into the membrane hydrophobic core is still unclear, though very important in the development of AD. Therefore, we investigate the pathways and kinetics for A$\beta$ insertion and permeation into a POPC lipid bilayer using atomistic umbrella sampling simulations. The findings emphasize the importance of electrostatic interactions and hydrophobicity of the peptides during membrane insertion and membrane related toxicity. The studies on hIAPP reveal the formation of a barrel-like structure that induces water permeability and $Na^+$ ions penetration into the membrane, which is consistent with experimental evidence suggesting that type II diabetes pathology is linked to the destabilization of cellular ionic homeostasis mediated by toxic pores made of hIAPP peptides. Formation of barrel-like structures can also be expected for other amyloidogenic proteins and resolving such structures experimentally would assist in future modeling the molecular mechanism leading to AD and type II diabetes.

# Zusammenfassung

Die Alzheimersche Demenz (AD) und Typ 2 Diabetes stehen im Zusammenhang mit der Aggregation von amyloiden Polypeptiden in Fibrillen bestehend aus $\beta$-Faltblättern. Die Hypothese ist, dass die Toxizität dieser Peptide aus deren Wechselwirkung mit Zellembranen resultiert, die zur Zerstörung der Intaktheit der Membranen führt. Dieser Effekt von amyloiden Peptiden auf Lipidmembranen wurde experimentell nachgewiesen, jedoch sind die entsprechenden Peptidstrukturen und ein Verständnis dieses Prozesses auf atomarer Ebene nicht bekannt. In dieser Arbeit wurden atomare Molekulardynamik (MD)-Simulationen durchgeführt mit dem Ziel, das Verhalten des Amyloid-$\beta$-Peptids (A$\beta$) im Fall von AD und des menschlichen Insel-Amyloid-Polypeptids (hIAPP) bei Typ 2 Diabetes auf Lipidmembranen aufzuklären. Die Simulationen haben gezeigt, dass die Membranoberflächenladung und die Lipidschwanztypen einen wesentlichen Einfluss auf die Stabilität von A$\beta$ in Lipiddoppelschichten haben, während durch A$\beta$-Oligomerisierung die Membranen für die Translokation von Wassermoleklen durchlässiger werden. Weiterhin wurden familiäre A$\beta$-Mutationen studiert, die dafür bekannt sind, die Amyloidaggregation zu beschleunigen und die Gehirntoxizität zu steigern. Zudem bewirken diese A$\beta$-Mutationen eine stärkere Zerstörung der Membranen im Vergleich zum A$\beta$-Wildtyp, wie die MD-Simulationen dieser Arbeit aufdeckten und was durch stabilere $\beta$-Faltblätter innerhalb der Membran resultierend aus den Mutationen erklärt werden kann. Diese Ergebnisse lassen vermuten, dass die veränderte Neurotoxiztät der A$\beta$-Mutanten nicht nur ein Ergebnis der verstärkten Aggregationsneigung ist, sondern auch aus den modifizierten Wechselwirkungen von A$\beta$ mit neuronalen Membranen resultiert. Der Mechanismus des Eindringens von A$\beta$ in Zellmembranen ist noch nicht bekannt, seine Aufklärung aber sehr wichtig für das molekulare Verständnis der Entwicklung von AD. Mittels umbrellasampling MD wurden in dieser Arbeit die Thermodynamik und Kinetik des Eindringens von A$\beta$ in eine Lipiddoppelschicht untersucht. Die Ergebnisse dieser Simulationen zeigen, dass dieser Prozess ein Wechselspiel von elektrostatischen Wechselwirkungen für die Membranadsorption und der Hydrophobizität des Peptids während des Eindringens in die Membran ist. Die Simulationen mit hIAPP führten zur Ausbildung von $\beta$-zylinderartigen ($\beta$-barrel) Strukturen, die das Eindringen von Wasser and Natriumionen in die Membran induzieren, was konsistent ist mit experimentellen Befunden, dass die Pathologie von Typ 2 Diabetes verbunden ist mit der Destabilisierung der zellularen ion-

ischen Homeostase vermittelt durch toxische hIAPP-Poren. Man kann davon ausgehen, dass andere Amyloid-Proteine ebenfalls solche $\beta$-barrel-Strukturen ausbilden können. Die experimentelle Auflösung solcher Strukturen würde die zukünftige Modellierung von A$\beta$ und hIAPP begünstigen und bei Aufklärung der molekularen Mechanismen, die zu AD und Typ 2 Diabetes führen, helfen.

# Acknowledgements

I wish to express my deepest thanks to my supervisor, Jun.-Prof. Dr. Birgit Strodel, for her warm encouragement and valuable guidance. It was a pleasure to work and learn new things constantly under her guidance. My sincere thanks to Prof. Victor Batista and Dequan Xiao from Yale University for their continued collaboration with the hIAPP project.

I thank my co-researchers Jide, Ioan, Ken, Falk, Qinqhua, Bogdan, Philipp, Michael, Nam for sharing their invaluable knowledge and for inspiring me, which made working at the lab a rewarding and enjoyable time.

This project was funded by grants from the Forschungszentrum, Jülich for which I am most thankful. I gratefully acknowledge the Jülich Supercomputing Centre for providing and maintaining the computing resources used in this project.

I express my deepest gratitude to all my friends in Jülich for their invaluable motivation, support and understanding.

This acknowledgement would be always incomplete without thanking my parents and my brother for their love and support throughout my research. Love you amma and poppa.

# Contents

# List of abbreviations

| | |
|---|---|
| Å | Angstrom |
| AD | Alzheimers disease |
| AFM | Atomic force microscopy |
| APP | amyloid precursor protein |
| CG | coarse grained |
| Chol | cholesterol |
| CPE | carboxypeptidase E |
| DOPC | 1,2-dioleoyl-sn-glycero-3-phosphocholine |
| DPPC | 1,2-dipalmitoyl-sn-glycero-3-phosphocholine |
| DPPG | dipalmitoylphosphoglycerol |
| DSPC | 1,2-distearoyl-sn-glycero-3-phosphocholine |
| ER | endoplasmic reticulum |
| gA | gramicidin |
| GM1 | ganglioside |
| hIAPP | human islet amyloid polypeptide |
| $L_\alpha$ or $L_d$ | liquid-crystalline or liquid-disordered phase |
| $L_\beta$ or $S_o$ | solid-gel or solid-ordered phase |
| $L_\beta'$ | ordered-gel phase with tilted chains |
| $L_o$ | liquid-ordered phase |
| LPS | lipopolysaccharide |
| LUVs | unilamellar vesicles |

| | |
|---|---|
| MD | Molecular dynamics |
| MscL | mechanosensitive channels |
| MSD | mean square displacement |
| $P_{\beta}'$ | rippled bilayer |
| PBC | periodic boundary conditions |
| PC | phosphatidylcholine |
| PC1/3 | prohormone convertase 1/3 |
| PC2 | prohormone convertase 2 |
| PE | phosphatidylethanolamine |
| PG | phosphatidylglycerol |
| PI | phosphatidylinositol |
| PME | Particle Mesh Ewald |
| PMF | potential of mean force |
| POPC | 1-palmitoyl-2-oleoyl-sn-glycero-3-phosphocholine |
| PPPM | particle-particle particle-mesh |
| PS | phosphatidylserine |
| PS-1 | presenilin-1 |
| PS-2 | presenilin-2 |
| RMSD | Root mean square deviation |
| RMSF | Root mean square fluctuation |
| SFG | sum frequency generation |
| SM | sphingomyelin |
| $T_M$ | phase transition temperature |

# List of Figures

# 1 Introduction

## 1.1 Cell - Unit of Life

All living organisms consist of cells. Cells vary in their size, shape and composition depending on their function. Cellular organisms can be classified into prokaryotes and eukaryotes. Prokaryotes are unicellular or single cell organisms which include bacteria and archaea, while eukaryotes are multicellular organisms containing billions of cells, for example plants and animals. Cells are enclosed by membranes, serving as permeability barriers. The fluid mosaic model proposed by Singer and Nicholson in 1972 [1] was the first step towards understanding the complex structure of biological membranes. This model proposed membranes to be composed of lipids and proteins distributed randomly lacking any organization. However, later studies showed the existence of ordered domains in the membrane surrounded by lipids in a disordered state [2–5]. A well known example of ordered domains in membranes are lipid rafts [6–8]. Lipid rafts are small ordered domains enriched with cholesterol (Chol), sphingolipids and proteins [9]. Lipid rafts are important in many cellular processes. The distribution of lipids between the two leaflets of the lipid membrane is asymmetric [10,11]. In mammalian membranes, the outer leaflet of the membrane is usually composed of phosphatidylcholine (PC) [12] and sphingomyelin (SM) [13] lipids , whereas the inner leaflet of the membrane facing the cytoplasm consists of phosphatidylserine (PS) [14] and phosphatidylethanolamine (PE) [15] lipids. Loss in asymmetry is known to trigger coagulation cascades and cell scavenging processes [16–18], especially when PS is present in the outer leaflet of the membrane. Studies have reported the presence of PS in the outer leaflet of cancerous and other pathological cells [19]. Bacterial species vary substantially with regard to the composition of their membranes, and are divided into gram-positive and gram-negative bacteria. Gram-positive bacteria have a single membrane bilayer composed mainly of phosphatidylglycerol (PG) lipids, whereas gram-negative bacteria are more complex exhibiting a double membrane [20]. The outer membrane is composed of zwitterionic PE lipids with anionic PG lipids in the inner leaflet and lipopolysaccharide (LPS) protruding out in the outer leaflet [21,22], while the inner or the cytoplasmic membrane consists mainly of PE and PG lipids [23].

### 1.1.1 Membrane lipids

Lipids in biological membranes are grouped into three main classes: a) glycerophospholipids, b) sphingolipids, and c) sterols. Glycerophospholipids, also known as phospholipids, consist of a sn-glycerol-3-phosphate backbone with carbon atoms at positions C1 and C2 esterified to fatty acyl chains (sn-1 and sn-2). The Glycerol group along with the phosphate moiety form the lipid headgroup. The coupling of he phosphate moiety with additional groups creates phospholipids with different headgroups, such as zwitterionic PC and PE, which carry neutral charge at physiological pH, and anionic PS, PG and phosphatidylinositol (PI) carrying negative charge. In Fig. 1.1 the structures of lipids are shown.

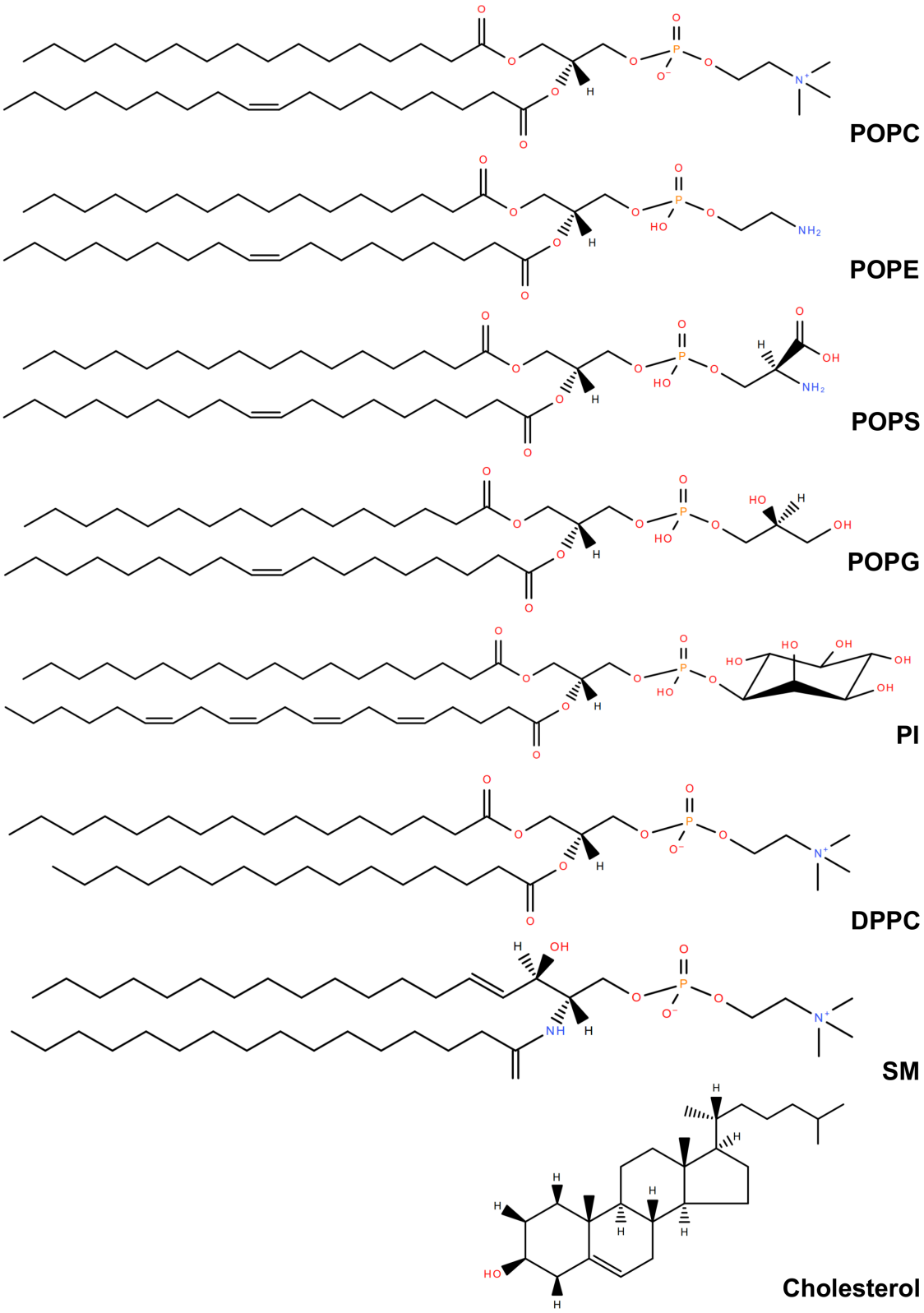


Figure 1.1: The structures of common lipids in biological membranes drawn using LIPID MAPS online tools [24].

Lipid headgroups and acyl chains make up the hydrophilic and hydrophobic region of the membrane, respectively. Fig. 1.2 shows the lipid bilayer patch with regions marked from $z = 0-1$ nm as hydrophobic acyl chain region, $z = 1-2$ nm as hydrophilic headgroup region and above $z > 2$ nm as the aqueous region.

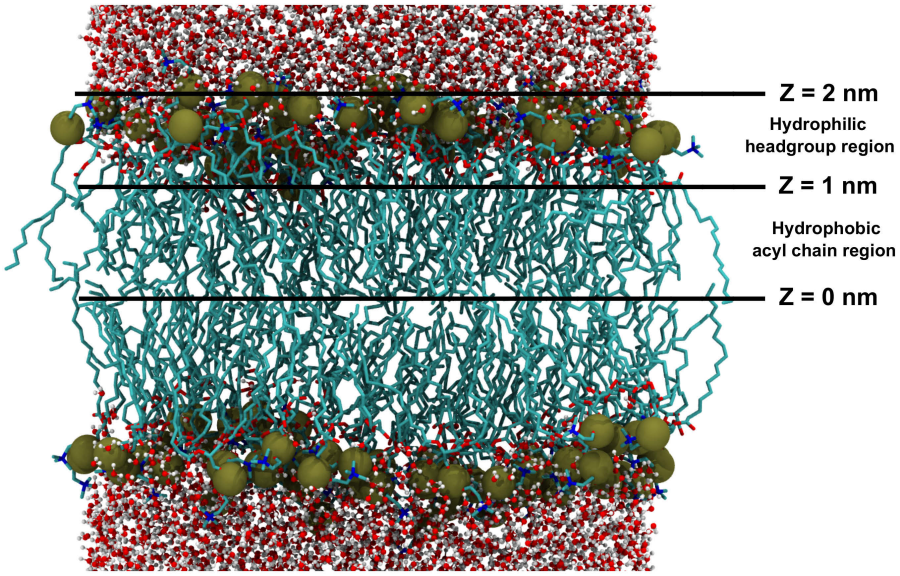


Figure 1.2: Snapshot of a lipid membrane showing hydrophilic and hydrophobic regions. The lipid phosphorous atoms are rendered as spheres, lipid tails as licorice and water molecules as CPK.

The two acyl chains vary in their hydrocarbon length and in the number of double bonds present in each chain. For example, 1-palmitoyl-2-oleoyl-sn-glycero-3-phosphocholine (POPC) has a saturated sn-1 acyl chain with 16 carbon atoms, whereas the unsaturated sn-2 acyl chain has 18 carbon atoms with one double bond. In case of 1,2-dipalmitoyl-sn-glycero-3-phosphocholine (DPPC), both sn-1 and sn-2 acyl chains are saturated with 16 carbon atoms in each chain. Unlike glycerophospholipids, sphingolipids are derived from sphingosine, an unsaturated 18-carbon amino alcohol chain, which is attached to a fatty acyl chain through amide linkage to form ceramide. Addition of phosphocholine or phosphoethanolamine to the 1-hydroxy group of a ceramide yields SM, an important and most common sphingophospholipid (Fig. 1.1). SM are known for its insulation of nerve fibres and in signal transduction. Linking ceramide with monosaccharides and oligosaccharides forms glycosphingolipids cerebrosides and gangliosides respectively which are essential in cell recognition and differentiation. The third major class of lipids are sterols. In mammalian cell membranes, cholesterol is the most abundant sterol with four non-planar rings and a C3 hydroxyl group.

### 1.1.2 Lipid polymorphism and phase transition

The amphiphatic nature of lipid molecules allows them to spontaneously self-assemble into bilayers in solution. The lipids undergo polymorphism leading to the formation of lamellar and non-lamellar phases, which depends on lipid composition and conditions [25]. The lamellar phase refers to a state resembling lipid bilayers in membranes (Fig. 1.3) [26]. The lipids have a phase transition temperature ($T_M$), above which they exist in a liquid-crystalline or liquid-disordered phase ($L_\alpha$ or $L_d$), and below $T_M$ lipids are in a solid-gel or solid-ordered phase ($L_\beta$ or $S_o$). Lipids in the $L_d$ phase have flexible acyl chains and are loosely packed with rapid rotational and lateral diffusion of the lipids, whereas lipids in the $S_o$ phase, which is mostly composed of saturated lipids, are highly ordered with a reduced lateral diffusion compared to $L_d$. When sterols are added to bilayer forming lipids, a liquid-ordered phase ($L_o$) is observed [27]. In the $L_o$ phase the acyl chains are highly ordered as in the $S_o$ phase, but have a greater lateral diffusion as in the $L_d$ phase. Additionally, intermediate phases are observed between the $L_\beta$ and $L_\alpha$ phases. On cooling $L_\alpha$ phase bilayers below the main $T_M$, a rippled bilayer $P_\beta'$ is formed, and on further cooling an ordered-gel phase with tilted chains (denoted as $L_\beta'$) is observed [28].

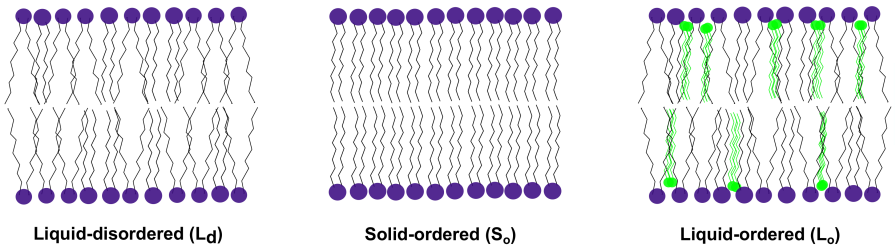


Figure 1.3: The structures of the lamellar phase.

Non-lamellar phases, also known as non-bilayer phases, are intermediate events important for membrane fusion, fission and pore formation. Non-lamellar phases include the hexagonal (I), hexagonal (II), and three-dimensional cubic phases (Fig. 1.4). The hexagonal (I) phase are cylinders with positive or convex curvature, having the nonpolar tails in the center and the polar headgroup outside interacting with water (e.g., micellar aggregates)[29,30]. Hexagonal (II) phases are cylinders with negative or concave curvature, having the polar headgroups and water inside, and the nonpolar tails sticking outside [29,30]. The hexagonal (II) phase is also known as inverted hexagonal phase (e.g., reverse micellar aggregates). Cubic phases form discontinuous three dimensional cubes composed of several curved bilayers, with bilayers being solvated on both sides [31–33].

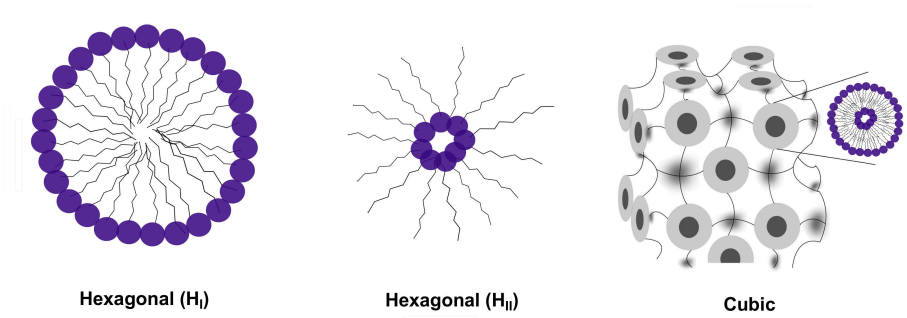


Figure 1.4: The structures of the non-lamellar phase.

### 1.1.3 Lipid geometry and thermodynamics

The geometry of the amphiphilic lipids determine whether the lipids will aggregate into lamellar or non-lamellar (hexagonal) phases [29,30,34]. Lipids with headgroups and acyl chains occupying similar cross-sectional areas are usually cylindrical in shape, and they favour bilayer structures (e.g., PC and SM). Lipids with a larger hydrophilic cross sectional area (phosphoinositides) have an inverted conical shape introducing a positive curvature to the structure, such as in micelles. Lipids with a smaller hydrophilic cross sectional area (PE) have a conical shape introducing a negative curvature to the structure, such as in reverse micelles [29–31,33,34] (Fig. 1.5).

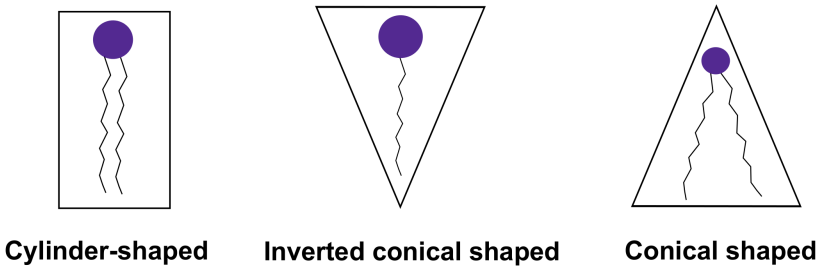


Figure 1.5: The lipid shape.

However, lipid acyl chains above or below their $L_\beta$ to $L_\alpha$ phase transition temperature are highly dynamic and are not confined to the shapes described above. Thermodynamics provides more insight into the shape concept by determination of the free energy per lipid molecule on occupying different volumes in different phases. The four shape-dependent components contributing to the free energy per lipid molecule are elastic bending of the lipid monolayer, hydrocarbon-packing energies, hydration and electrostatic potentials [35]. Lipid monolayers in a bilayer or the lamellar phase are generally flat with zero curvature, whereas in the non-lamellar hexagonal phase they are tightly curled into cylinders with

either positive or negative curvature (Fig. 1.6) [36]. The elastic free energy, $\mu_E$ [35], is given as:

$$\mu_E = k(1/R - 1/R_0)^2 \tag{1.1}$$

where $k$ is the elastic constant. The elastic bending of the lipid monolayer is expressed in terms of $R$, which is the radius of curvature of the lipid/water interface, with positive $R$ for the hexagonal (II) Phase and negative $R$ for the hexagonal (I) phase (Fig. 1.6). $R_0$ describes the radius of curvature for the monolayer at equilibrium, which minimizes the elastic free energy (Fig. 1.6) [34–36].

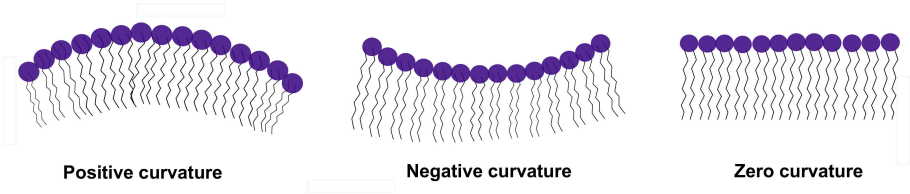


Figure 1.6: The curvature of lipid monolayers in lamellar and non-lamellar phases.

Factors, such as temperature and unsaturation decrease $R_0$ by increasing the splay of the acyl tails, while factors such as an increased size and charge of the headgroup area, increase $R_0$ [35]. Therefore, PC lipids with larger $R_0$ are in a lamellar phase at higher temperatures, where as unsaturated PE lipids with smaller $R_0$ go into the hexagonal (II) phase at the same temperature. When $R = R_0$, the lipid monolayer is elastically relaxed and curls to lower the elastic energy [35].

Hydrocarbon-packing energies depend on the water/lipid ratio. In the hexagonal (II) phase, the increase in water/lipid ratio increases the hydrocarbon-packing free energy. At a given condition (such as temperature and geometry) for a particular lipid, the tails are expected to be of same relaxed length. When there is a difference in relaxed length of the tails, the free energy for hydrocarbon-packing increases, which is due to the absence of parallel water/lipid interfaces in both monolayers composing the bilayer. When the hydration level is decreased, lipid cylinders cannot express a large $R_0$ value. On the other hand, if the hydration level is increased excessively, headgroup surfaces are split due to hydration repulsion [35]. Similarly, electrostatic repulsion due to the presence of charges at the lipid surface decreases the free energy required for the separation of the headgroup surface, while the electrostatic contribution is small for lipids with neutral surface charge (e.g., PC lipids) [35].

In lipid bilayers, attractive van der Waals interactions between neighbouring lipids also contributes to the phase behaviour [37]. The interaction strength depends on the length of the acyl chains and their hydrocarbon packing property. Lipids with longer acyl chains have an increased interaction strength due to the larger volume occupied by the tails,

decreasing the lateral diffusion of the lipids, whereas lipids with shorter acyl chain length are more fluid due to a reduced interaction strength and an increased lateral diffusion. Acyl chain length along with its degree of unsaturation influences the $T_M$ of the lipid species. $T_M$ increases by 5 – 10 °C with an increase in acyl chain length by 2 carbon atoms, which is due to the larger area occupied by the longer tails and increased van der Waals interaction strength requiring more heat to disrupt the ordered structure. $T_M$ decreases by 55 – 70 °C on addition of a single double bond due to the kink produced by the double bond, which increases the flexibility of the acyl chains and disrupts the ordered packing of hydrocarbon chains [37]. For example, DPPC lipids with no double bonds in their acyl chains (saturated lipids) adopt $S_o$ phase at room temperature and have $T_M$ at 325 K, whereas POPC lipids with an unsaturated acyl chain form the $L_d$ phase with $T_M$ at 298 K.

### 1.1.4 Phase separation and lipid rafts

The above discussed phase transition occurs at a defined $T_M$ in a single component lipid bilayer system. Co-existence of both $L_d$ and $L_o$ phases in binary and ternary bilayer systems occurs with lipids having high and low-melting temperatures and in the presence of cholesterol [38,39]. When excess cholesterol is added to binary or ternary mixtures, cholesterol rich phases are also seen [40]. The co-existence of different lipid phases can be represented by phase diagrams for bilayer mixtures (Fig. 1.7) [40]. Mixed bilayer systems exhibit a rich phase behaviour due to (un)favourable interactions between the lipids. For example, in a binary system containing 1,2-dioleoyl-sn-glycero-3-phosphocholine (DOPC) and high-melting lipids leads to a sharp phase separation into $L_d$ and $L_o$ [41]. On addition of cholesterol to binary mixtures (1,2-distearoyl-sn-glycero-3-phosphocholine (DSPC) + DOPC, SM + DOPC, DPPC + DOPC or SM + POPC), regions with multiple phases are observed [41]. Cholesterol is an important molecule driving domain formation in membranes, increasing the bilayer thickness and stiffening the membrane. Cholesterol and saturated SM co-exist as a single phase, with the headgroup of SM protecting cholesterol from being exposed to solvent. In the ternary mixture of Cholesterol + SM + DOPC, cholesterol localizes at the interface of SM and DOPC and reduces the line tension at the interface [42,43]. The mixed bilayer systems display phase separation and studying their properties is important in understanding the biological function of lipid rafts in cellular membranes as lipid rafts also exhibit similar properties.

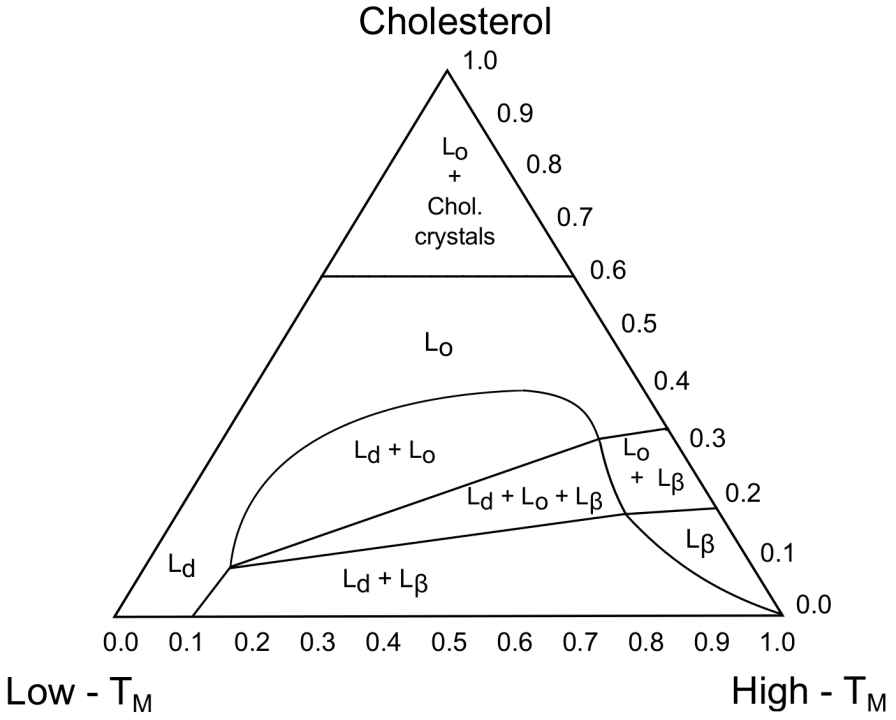


Figure 1.7: The phase diagram for a ternary lipid mixture, containing lipids with high and low-melting temperatures and cholesterol. The phase diagram shows regions of two-phase ($L_d + L_\beta$, $L_o + L_\beta$, $L_d + L_o$, $L_o$ + chol. crystals) and three-phase ($L_d + L_o + L_\beta$) coexistence.

Rafts are nanodomains in membranes with various biological functions. Membrane rafts are defined as nanoscale (10 – 200 nm), dynamic, ordered, enriched with sphingolipid, sterol and saturated lipid domains surrounded by lipids which are in $L_d$ phase [9]. Lipids rafts are known to facilitate protein-protein interactions through selective lipid based sorting of protein intake and exclusion. Proteins which are able to partition into $L_o$ regions are mostly sequestered into raft domains. The presence of proteins in membrane rafts are known to stabilize the raft nanodomains through protein-lipid and protein-protein interactions and also help in the growth of raft domains [44]. However, it is unclear if rafts pre-exist in plasma membranes and promote raft-assisted protein insertion into membrane, or whether protein aggregation at the membrane surface trigger lipid domain formation. One of the model raft studies proposes spontaneous unstable $L_o$ raft domains in plasma membranes, which are stable on short timescales ($< 0.1$ ms) but can be stabilized by proteins having transmembrane domains or by lipid-anchored proteins [45]. Stability of the rafts is further increased by reducing the line tension at the boundary between the $L_d$ and $L_o$ phases. Reduction in line tension is possible if the protein interacts at the interface of two phases thereby acting as surfactant. Another possibility to reduce the

line tension is the presence of a cholesterol molecule at the raft interface [43,46]. Both lipid anchored and transmembrane proteins modify the lipid environment in its vicinity affecting the stability of the domain and the bilayer thickness [46]. Raft domains in $L_o$ or $S_d$ generally have longer tails and are thicker than the surrounding $L_d$ membrane. Therefore with increasing bilayer thickness, the stability of a $L_o$ domain increases as line tension is reduced with the surrounding $L_d$ phase of the membrane [47–49].

### 1.1.5 Intramembrane protein-lipid interactions

Proteins and lipids have the ability to segregate into specific domains, which is important for both functioning and maintaining the stability of the systems. Intramembrane protein-lipid interactions can be classified into different types based on the residence time of a lipid at the protein-lipid interface [50]. Lipids with high lateral and rotational diffusion coefficients have reduced interaction with the transmembrane domain of the protein and therefore spends less time at the protein-lipid interface. Such lipids are called as bulk lipids. Lipids having reduced diffusion rate form a lipid shell around the protein. These lipids are termed as annular lipids. The reduced diffusion rate is due to favourable interactions with the protein surfaces both at the hydrophilic interface and in the hydrophobic part of the membrane. Residence time of individual lipids in the lipid shell can vary based on the lipid type and its interaction strength [51]. Here the exchange rates between the bulk lipids and lipid shell is reduced as well. The third type of lipids interacting with the protein in cell membranes is referred to as non-annular type of lipids and have much lower diffusion rates than the annular lipids. Non-annular lipids have specific interactions with the protein complexes and are usually found located within the membrane-protein complexes.

Interactions at the protein-lipid interface have impact on properties such as the area per lipid, hydrophobic thickness of the bilayer, lateral diffusion of lipids, order parameter of lipid tails, lateral membrane pressure, charge distribution at the protein-lipid interface and localization of amino acid side chains [52].

The area per lipid is a widely studied parameter as it is related to other membrane properties. The area per lipid varies for each lipid species and depends on the composition of the lipid headgroup. Lipids with PC headgroups are larger and occupy a larger volume than the lipids with PE headgroups. The lipid headgroup arrangement can be altered on interaction with proteins and the extent of disruption depends on the charges present at the protein-lipid interface.

Hydrophobic thickness of the bilayer is the end-to-end lipid headgroup distance. The bilayer thickness of a membrane ranges from 3.5 to 5.5 nm. The thickness mainly depends on the length of the lipid acyl chains in pure membranes without proteins. The bilayer thickness can be altered in the presence of proteins due to hydrophobic mismatch between

the hydrophobic region of the bilayer and the transmembrane domain of the protein. Cholesterol is also known to increase the membrane thickness by increasing the ordering of lipid tails, which in turn stiffens the membrane [41,45]. The lateral diffusion of lipids depends on many properties, such as the interactions between the lipid headgroups and protein, hydrophobic matching or mismatch, degree of saturation of the lipid acyl chains, length of lipid tails and the lipid phase. Lipids in the $L_d$ phase are more dynamic with increased diffusion rate than the lipids in the gel phase. Lipids with double bonds in their acyl chains (unsaturated lipids) are more flexible and diffuse more rapidly than lipids without double bond (saturated lipids). Lipids with longer acyl chain length have a larger area for interaction with adjacent lipids, which reduces the diffusion of lipids. Lipids within close vicinity of a protein have different diffusion rates than the bulk lipids.

The order parameter of lipid acyl chains depends on the carbon atom number along the chain and on the degree of saturation. For example, in a POPC lipid, which has both a saturated palmitic acid chain and an unsaturated oleic acid chain, will show a different order parameter profile for both chains. Saturated chains will exhibit higher ordering than unsaturated tails due to the kink produced at the double bond making this tail more disordered. The presence of protein alters the order parameter, with the acyl chains close to the protein experiencing maximum effect due to tilted chains.

Lateral membrane pressure largely affects the structure and dynamics of the protein in the membrane. The conformation of the protein depends on the balance of free energy between the hydrophilic and hydrophobic parts of the membrane and the protein [29]. A fine balance of attractive and repulsive forces between the hydrophobic and hydrophilic parts of the membrane is necessary to drive spontaneous assembly of a lipid bilayer. The hydrophobic-hydrophilic interface of the membrane is tightly packed through strong attractive forces to avoid exposure of hydrophobic tails to the solvent, which is energetically costly [34]. The pressure profile (along $z$-axis) is strong and negative in the interface region. The tight packing is compensated by steric and electrostatic repulsions at the headgroup region and by repulsive entropic forces at the acyl chain region [53,54]. Lateral pressure is negative at the hydrophobic-hydrophilic interface, which is balanced by the positive pressure in the interior of the membrane. These forces are sufficient to affect the conformation of the protein in the membrane. In a relaxed or equilibrium state where there are no external forces applied to the bilayer, the lateral force balances to zero.

Charge distribution at the protein-lipid interface is important for regulation of many channel proteins including mechanosensitive channels (MscL), which requires an anionic lipid environment for binding to its positively charged residues [55,56]. Another example is the antibiotic peptide gramicidin (gA), which forms channels only in the case of hydrophobic match between the lipid acyl chain and its potassium conducting conformation [57–59].

The localization of amino acid side chains plays an important role in the stability of protein-lipid interactions. Polar interactions occur between the lipid headgroups and positively charged polar amino acids, such as lysine and arginine at the membrane-water interface [52]. The aromatic residues tyrosine and tryptophan also localize near the membrane-water interface, interacting via hydrogen bonds with the lipid headgroups [60]. The indole group in tryptophan is also known to stabilize lipid acyl chains by adopting a lamellar orientation, supporting its role in anchoring proteins to lipids [61]. Protein-lipid interactions are further stabilized by nonpolar interactions between the transmembrane domain of the protein and hydrophobic lipid tails [62,63].

## 1.2 Aggregation of amyloids in Alzheimer's disease and type 2 diabetes

The aggregation of proteins into fibrillar structures or plaques are a characteristic feature of many neurodegenerative diseases (e.g., Alzheimer's and Parkinson's disease) and nonneuropathic localized diseases (e.g., type 2 diabetes and atrial amyloidosis) [64]. Experiments reveal fibril structures to be composed of several twisted protofilaments, which form long rope like fibrils of 7–13 nm in diameter [64]. The protofilaments in fibrils are arranged to form cross $\beta$-sheet structures, which run perpendicular to the fibril axis. Several studies have reported fibrils to be less toxic than the prefibrillar aggregates or oligomers [65–68]. The latter are thought to be cytotoxic by altering cell membrane properties [69–74]. The suggested mechanism of amyloid-membrane interactions and subsequent membrane disruption is shown in Fig. 1.8 [75,76].

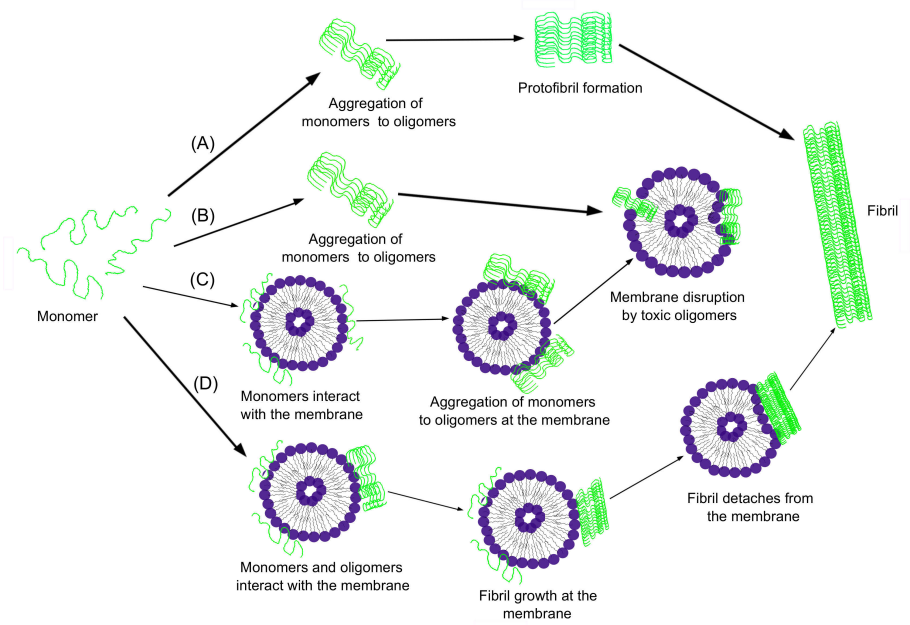


Figure 1.8: Schematic representation of different mechanisms of interaction between amyloid (hIAPP and A$\beta$) and membranes, causing membrane damage and cytotoxicity. Mechanism (A) shows aggregation of monomers in extracellular space. It includes formation of toxic oligomers, protofibrils and the matured fibril. Mechanism (B) shows interaction of oligomers at the membrane surface followed by membrane damage. Mechanism (C) shows interaction of monomers at the membranes surface leading to oligomer formation and membrane damage. Mechanism (D) shows interaction of monomers and oligomers at the membrane surface, followed by fibril growth and detachment from the membrane, and later accumulates in the extracelluar space.

### 1.2.1 Interaction of Abeta peptide with membranes in Alzheimer's disease

Alzheimer's disease (AD) is a neurodegenerative disorder associated with synaptic loss, abnormalities in functioning of neurons, neuronal cell death and extracellular accumulation of senile plaques composed of the neurotoxic amyloid-$\beta$ peptide (A$\beta$) [77,78]. A$\beta$ is derived from the amyloid precursor protein (APP), a type-1 membrane integral glycoprotein through sequential cleavage by $\beta$- and $\gamma$-secretases [79] (Fig. 1.9). The major alloforms of A$\beta$ are A$\beta_{40}$ and A$\beta_{42}$, which differ by the presence of two amino acids, I41 and A42 at the C-terminus of the latter. The more hydrophobic A$\beta_{42}$ is the prevalent alloform seen in amyloid plaques, and has a greater tendency to aggregate into fibrils and plaques [80,81]. The 'amyloid cascade hypothesis' proposes that assemblies of A$\beta$ initiate

a process leading to neuronal dysfunction and cell death [82]. The most potent neurotoxic assemblies appear to be oligomeric, rather than fibrillar, in nature [66,83]. There is acceptable evidence suggesting that A$\beta$ exerts its cytotoxic effect by interacting with membranes of neurons and other cerebral cells, such as astrocytes, microglial and cerebral endothelial cells [84,85]. A potential pathway for A$\beta$ toxicity lies in its ability to alter biophysical membrane properties [86–89]. A$\beta$ aggregates cause membrane disruption and increased permeability, allowing excessive leakage of ions, particularly calcium ions [90]. This imbalance in calcium homeostasis promotes neuronal excitotoxicity [90,91]. A$\beta_{42}$ oligomers interact with lipid raft related ganglioside GM1, further accelerating the amyloidogenic processing of APP [92]. Atomic force microscopy (AFM) experiments with A$\beta$ isoforms; A$\beta_{40}$ [93] and A$\beta_{42}$ [94] revealed ion-channel-like structures in membranes, which are able to cause cellular ionic imbalance [93,95–98].

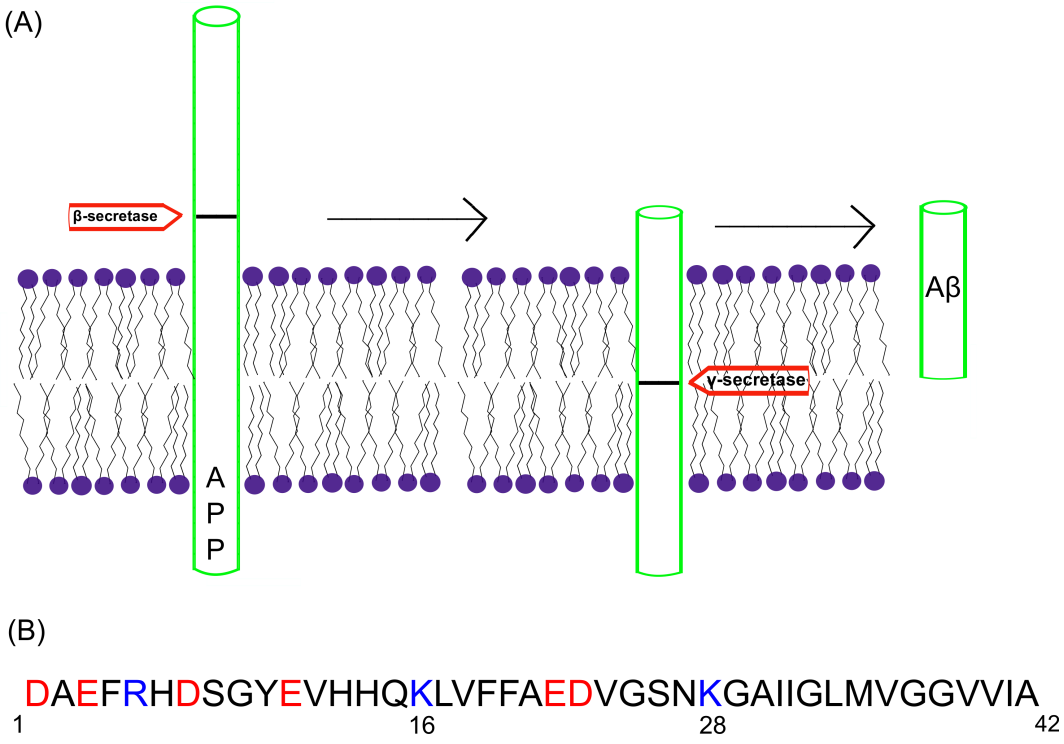


Figure 1.9: In (A) the sequential cleavage of the amyloid precursor protein (APP) by $\beta$- and $\gamma$-secretases to produce A$\beta$ is depicted. (B) shows the sequence of A$\beta_{42}$, colored according to physicochemical properties of the residues: blue, basic and red, acidic.

A study on soluble and aggregated forms of A$\beta_{40}$ on rat cortical synaptic plasma membrane using small angle X-ray diffraction and fluorescence spectroscopy showed that the monomer penetrates into the hydrophobic core of the bilayer, whereas the aggregated form was found interacting with the phospholipid headgroups [99]. Similarly, soluble A$\beta_{42}$ was

found to intercalate the membrane of giant unilamellar vesicles composed of POPC or POPC/SM/Chol, altering permeability properties of the bilayer [100]. However, permeabilization of lipid bilayers can also be caused by soluble amyloid oligomers [101]. Further experimental work carried out on A$\beta_{40}$ inserted into a zwitterionic phosphatidylcholine bilayer revealed that the perturbation of the bilayer integrity is caused by short $\beta$-sheet assemblies embedded in the lipid bilayer [102].

NMR spectroscopy studies on A$\beta_{40}$ in a membrane-mimicking environment concluded that the peptide is unstructured in the N-terminal region from residues 1–14 and that the C-terminal hydrophobic residues from 15–36 adopt an $\alpha$-helical conformation with a kink at residues 25-27 [103]. This kink may be significant in membrane insertion and conformational rearrangements [103]. Coles et al. proposed three possible models corresponding to different A$\beta$ insertion depths in the membrane based on structural findings for A$\beta_{40}$ [103]. The two experimentally determined insertion depths have K28 and V24, respectively, at the membrane-water interface [103,104]. A third proposed model is with K16 at the membrane-water interface, where the entire $\alpha$-helical conformation adopted by A$\beta_{40}$ (residues 15–36) spans the plasma membrane [103].

Various computational studies of A$\beta$ interacting with lipids have been performed to gain structural information at an atomistic level [105–125]. An atomistic model of A$\beta$ channel structures developed by Nussinov and co-workers provided information about the A$\beta$ conformation in membranes and ion-channel activity [105,106]. In another study they found that the channels break into mobile $\beta$-sheet subunits, which enable toxic ionic flux [107]. Strodel and coworkers also proposed A$\beta$ pore models composed of tetrameric to hexameric A$\beta$ subunits, which are similar to the models suggested by Nussinov and coworkers [112].

Familial forms of AD increase A$\beta$ production or the propensity of A$\beta$ to aggregate [82]. Until now four genes affecting APP, presenilin-1 (PS-1), presenilin-2 (PS-2) and apolipoprotein E have been identified to be linked to AD. Mutations in three of these genes (APP, PS-1 and PS-2) are known to increase the production of the A$\beta$ alloforms A$\beta_{40}$ and A$\beta_{42}$. So far 19 pathogenic missense mutations have been discovered in APP, of which seven are located in the region encoding A$\beta$. English (H6R) [126] and Tottori (D7N) [127] mutants show increased fibril elongation compared to wild-type (WT) A$\beta$ [128]. The Dutch mutant (E22Q) [129,130] favors A$\beta_{40}$ production and leads to a $\beta$-sheet structure [131–134]. The Flemish mutant (A21G) [135] forms stable oligomers with decreased fibril formation [136], while the Arctic mutation (E22G) [137] increases neurotoxic protofibril production [138,139]. The Italian mutant (E22K) promotes faster aggregation of A$\beta_{40}$ and A$\beta_{42}$ [134] and the Iowa mutant (D23N) [140] forms fibrils faster than WT A$\beta$.

Lazo et al. [141] through limited proteolysis experiments, identified the 10-residue fragment A$\beta_{21-30}$ to be protease-resistance in both A$\beta$ alloforms A$\beta_{40}$ and A$\beta_{42}$. The

decapeptide A$\beta_{21-30}$ itself exhibits similar protease resistance to full length A$\beta$, suggesting its role in folding and aggregation of A$\beta$ into toxic oligomers. Lazo et al. [141] also postulated that partial unfolding of A$\beta_{21-30}$ segment would be necessary for fibrillization of A$\beta$. Several experimental and computational studies have accounted for the structure of the A$\beta_{21-30}$ fragment and discussed the importance of its hydrophobic and electrostatic interactions in the folding process [142–148].

### 1.2.2 Interaction of human islet amyloid polypeptide with membranes in type 2 diabetes

The human islet amyloid polypeptide (hIAPP), also called amylin, is a neuroendocrine hormone coexpressed and cosecreted along with insulin by $\beta$-cells of the pancreatic islets of Langerhans [149,150]. Aggregation of hIAPP into islet amyloid deposits destroys $\beta$-cells, which is linked to the development of type 2 diabetes [151–153]. While the pathological role of hIAPP in type 2 diabetes is unquestioned, the physiological function of hIAPP has not been fully resolved yet. At physiological concentrations hIAPP is known to reduce food intake [154], suppress gastric emptying [155], and inhibit glucagon release from pancreatic $\alpha$-cells [156,157]. At higher concentrations, hIAPP acts as an insulin antagonist by inhibiting insulin secretion [158–160].

IAPP is stored in secretory granules along with insulin [161–164]. Similar to insulin, IAPP is initially expressed as preproprotein. IAPP is an 89 amino acid residue pre-proIAPP, with 22 amino acid signal sequence [165–167]. Initial cleavage of signal sequence takes place at endoplasmic reticulum (ER) [76], which produces 67 amino acid residue proIAPP. Proteolytic cleavage of proIAPP to 37 amino acid IAPP takes place at secretory vesicles by two endoproteases [76], prohormone convertase 2 (PC2) and prohormone convertase 1/3 (PC1/3) [168–171]. PC2 cleaves proIAPP at the $NH_2$ terminus (between R11 and K12), whereas PC1/3 cleaves proIAPP at the COOH terminus (between R51 and N52) [76]. The proIAPP is further processed by carboxypeptidase E (CPE) at COOH terminus [172], which removes K50 and R51 [76]. CPE processing exposes glycine residue (G49) which is used for COOH-terminal amidation. Residues C2 and C7 of IAPP are involved in intramolecular disulfide bridge [172] (Fig. 1.10).

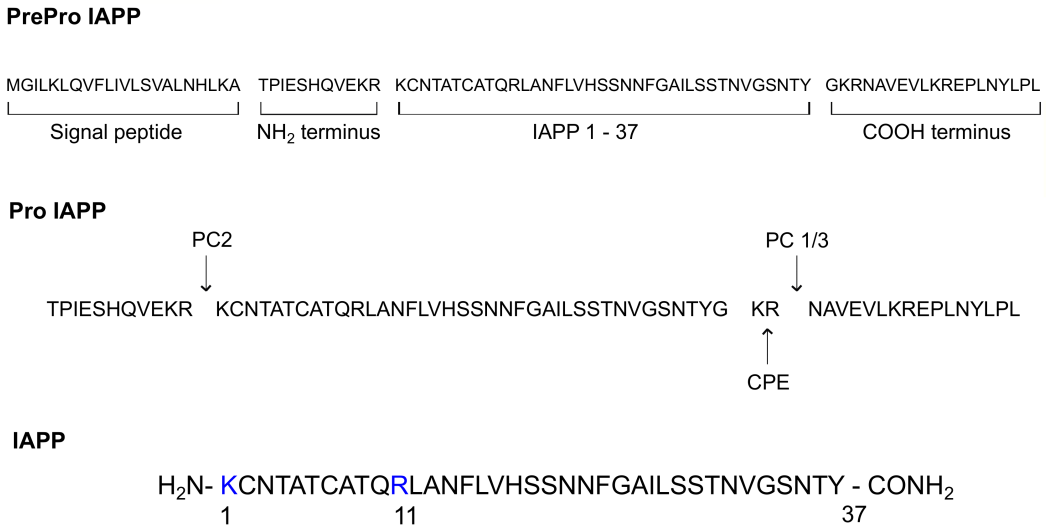


Figure 1.10: Processing of human preproIAPP in beta cells resulting in the formation of IAPP. PreproIAPP is an 89 amino acid residue peptide, including a 22 amino acid signal peptide. Initial cleavage of the signal peptide produces the 67 residue peptide proIAPP. Proteolytic cleavage of proIAPP to 37 amino acid IAPP by two endoproteases, prohormone convertase 2 (PC2) and prohormone convertase 1/3 (PC1/3) is indicated in arrows. PC2 cleaves proIAPP at the $NH_2$ terminus (between R11 and K12), whereas PC1/3 cleaves proIAPP at the COOH terminus (between R51 and N52). proIAPP is further processed by carboxypeptidase E (CPE) at the COOH terminus, which removes K50 and R51. The CPE processing exposes glycine residue at position 49 (G49), which is used for COOH-terminal amidation. Sequence of IAPP is colored according to physicochemical properties of the residues: blue, basic.

In its normal state the 37-residue hIAPP peptide adopts an unstructured conformation, while in the disease state hIAPP misfolds into $\beta$-sheet-rich amyloids. Luca *et al.* have examined the structure of the hIAPP aggregates using solid-state NMR and showed that hIAPP aggregates consist of parallel $\beta$-sheets [173]. This conclusion is supported by electron paramagnetic resonance spectroscopy and infrared reflection absorption spectroscopy studies [174,175]. It was shown that the mid-region from residues S20 to S29, in particular residues G24–S28 are crucial for fibril formation and toxicity [176]. In contrast, rodent IAPP (rIAPP) does not form fibrils and differs to hIAPP by six residues [177]. Three proline amino acid substitutions in the amyloidogenic region at positions 25, 28 and 29 are likely to prevent rIAPP from fibril formation. A single missense mutation in hIAPP at position 20 (S20G) is associated with early onset of type 2 diabetes and was shown to be more fibrillogenic and cytotoxic than wild type (WT) hIAPP [178]. Apart

from amino acid substitutions inducing or inhibiting hIAPP fibrillization, it is known that membranes catalyse fibril formation by enhancing nucleation [179–182]. Knowledge of the conformation adopted by membrane-bound hIAPP is essential for the understanding of the mechanism of hIAPP induced membrane disruption and for the development of potential aggregation inhibitors for hIAPP. Studies on hIAPP in the presence of large unilamellar vesicles (LUVs) have reported the peptide to adopt an $\alpha$-helical structure [182]. An $\alpha$-helical conformation was also seen in the membrane-mimicking solvent trifluoroethanol [183]. However, after longer incubation with LUVs hIAPP adopts a $\beta$-sheet conformation [182]. AFM revealed pore like structures in membranes, indicating channel formation by hIAPP [184]. However, the orientation of the hIAPP $\beta$-sheets relative to the lipid membrane surface at the early stage of amyloid formation has yet to be established.

Over the last decade several mechanisms of amyloidogenic cytotoxicity have been reported [85,185,186]. The two most popular mechanisms of hIAPP cytotoxicity are ion channel formation by oligomers [184,187] and alteration in membrane morphology by fibril growth at the membrane surface [69,188–191]. It was demonstrated that hIAPP monomers are also capable of inserting into lipid monolayers, which is followed by hIAPP aggregation inside the membrane and also with hIAPP species on the membrane surface [175,192]. The latter lead to fibril growth at the membrane surface, changing the overall membrane fluidity and morphology. Another reported mechanism for cytotoxicity is extraction of lipid molecules by hIAPP aggregates causing ion permeation [180,193]. The initial interaction between hIAPP and negatively charged membranes is mediated by the N-terminal residues K1, R11 and H18 [181]. The N-terminal residues 1–19 of hIAPP differ from rIAPP by just one amino acid: H18 in hIAPP and R18 in rIAPP. A fluorescence microscopy study showed rapid increase in the intracellular calcium level after addition of $\text{hIAPP}_{1-19}$ to large unilamellar vesicles, while $\text{rIAPP}_{1-19}$ was ineffective [194]. The membrane disruption ability of $\text{hIAPP}_{1-19}$ is pH dependent. At pH 6.0, where H18 is protonated, $\text{hIAPP}_{1-19}$ behaved like $\text{rIAPP}_{1-19}$ and disrupted the membrane only mildly, while the membrane disruption ability of $\text{hIAPP}_{1-19}$ was regained after deprotonation of H18 at pH 7.3 [194]. NMR experiments of $\text{IAPP}_{1-19}$ at pH 7.3 showed the toxic hIAPP peptide adopting a transmembrane orientation, while the nontoxic rat peptide was bound to the surface of the membrane [195]. At pH 6.0, $\text{hIAPP}_{1-19}$ was oriented at the micelle surface similar to $\text{rIAPP}_{1-19}$ at pH 7.3 [195]. This change in orientation is in agreement with the significantly reduced ability of $\text{hIAPP}_{1-19}$ to cause membrane disruption at pH 6.0.

For the support and explanation of the above experimental findings, molecular simulations were performed to probe the interactions between hIAPP and membranes [196–198]. In one of these studies it was demonstrated that, when the N-terminal segment of hIAPP monomers and dimers are preinserted into an anionic lipid bilayer, hIAPP aggregation

takes place via the C-terminal peptide segment, while the N-terminal residues are attracted to the membrane surface as a result of electrostatic interactions with the lipid headgroups [196]. Another study, where WT and S20G hIAPP$_{1-25}$ were placed as helix on the membrane surface, found that the helical structure is stable for WT hIAPP$_{1-25}$ while in case of the S20G mutant an L-shaped structure resembling fibril was seen [197]. When annular-like hIAPP structures were inserted into a zwitterionic lipid bilayer, the channels were seen to break into small oligomeric subunits resembling pore-like structures obsereved in AFM experiments [198]. By combining experimental chiral sum frequency generation (SFG) spectroscopy and ab initio SFG simulation, hIAPP was found to orient with a tilting angle of 48° when interacting with a dipalmitoylphosphoglycerol (DPPG) monolayer. Such a tilting orientation might have a strong damage to the lipid membrane [199].

# 2 Aims

The importance of numerical methods to study membrane properties, domain formations, protein-lipid interactions has considerably increased in the past 10 years. Molecular dynamics (MD) simulations in combination with all-atom or coarse grained (CG) methods of the biomolecules are commonly used in membrane-protein research. The CG approach involves combining neighbouring atoms into a single bead, allowing us to reach time scales which are not accessible with atomistic MD simulations. However, with CG methods atomistic details are lost. Molecular dynamics simulations can be efficiently used to analyse the molecular mechanisms of protein-lipid interactions as the interactions between atoms can be studied with high resolution, which cannot be obtained by experimental techniques. With the availability of supercomputers and optimized simulation packages, biological systems containing several thousands of atoms can nowadays be treated successfully. Chapter 3 discusses in detail the physical basics of MD simulations. In Chapter 4, the results of our MD simulations studying the interactions between the amyloid peptides A$\beta$ and hIAPP and lipid bilayers are presented and discussed. A$\beta$ and hIAPP share a similar mechanism of membrane disruption. The motivation for studying amyloid peptide-membrane interactions using MD simulations is that experimental techniques have so far not been able to resolve the mechanism by which the amyloid peptides disrupt the membrane. Also the conformations adopted by these peptides on or inside the membrane are largely unknown yet. Understanding the membrane damage mechanism and the membrane-bound conformations of these peptides would have significant impact in this field of research as it would facilitate the design of potentially effective drugs against these amyloid diseases.

# 3 Methods

## 3.1 Classical Mechanics:Newton's second law

Molecular dynamics (MD) simulation is based on Newtons's law of motion, $F = ma$. Once the force applied on each particle is known, it becomes easy to track the acceleration of each particle in the system. Integrating the equations of motion yields a trajectory describing the positions, velocities and accelerations of the particles at varying time. Several properties can be determined from the generated trajectories. Improvement in computational algorithms and the availability of supercomputers has facilitated researchers in studying biological systems at microsecond time scale.

Newton's second law or the equation of motion for particle $i$ is given by [200,201]:

$$F_i = m_i a_i \tag{3.1}$$

where $F_i$ is the force exerted on the particle, $m_i$ is its mass and $a_i$ is the acceleration of particle $i$. The acceleration is the second derivative of the position with respect to time:

$$a_i = \frac{d^2 r_i}{dt^2} = \frac{dv_i}{dt} \tag{3.2}$$

where $v_i$ is the velocity of particle $i$. Each particle in the system of $N$ particles experiences a force exerted from all other particles, so that the forces are functions of the $3N$ particle coordinates. Hence, Newton's second law of motion is given as a set of $3N$ coupled second order differential equations:

$$F_i = m_i \frac{d^2 r_i}{dt^2} \tag{3.3}$$

The force $F_i$ acting on a particle can be expressed as the gradient of the potential energy, $U$:

$$F_i = -\nabla_i U \tag{3.4}$$

On combining equations (3.3) and (3.4), we get:

$$-\frac{dU}{dr_i} = m_i \frac{d^2 r_i}{dt^2} \tag{3.5}$$

Here, the derivative of the potential energy can be related to the changes in position of

the particle as a function of time. Therefore, to calculate the changes of the system (i.e., the trajectory) we only need to know the potential energy function, an initial distribution of velocities and accelerations, and the initial positions of the atoms. The equations of motion are deterministic, i.e. we can predict the state of the system at any time in future or past. The initial velocities $v_i$ are often chosen randomly from a Maxwell-Boltzmann or Gaussian distribution [201], which gives the probability of atom $i$ having the velocity $v_{i,x}$ in the direction of $x$ at temperature $T$:

$$P(v_{i,x}) = \left(\frac{m_i}{2\pi k_B T}\right)^{1/2} \exp\left(-\frac{1}{2}\frac{m_i v_{i,x}^2}{k_B T}\right) \tag{3.6}$$

where $k_B$ is the Boltzmann constant.

## 3.2 Integration algorithms

In the above mentioned equations of motion, the velocities and accelerations are considered to be constant, which is a sufficient assumption for short times. For longer times equation (3.5) has to be solved by integration, which is, however, analytically not possible for biomolecular systems where $N$ is large. Instead numerical integrators can be used to overcome this problem. Thus algorithms were developed to propagate positions, velocities and accelerations of the system in time using a time step in the range of $\delta t = 1$ fs [200]. With such small time step many molecular processes can be studied. All integration algorithms discussed below assume the positions, velocities and accelerations to be approximated by a Taylor series expansion.

### 3.2.1 Verlet algorithm

The Taylor expansions are given as [200–202]:

$$r(t+\delta t) = r(t) + v(t)\delta t + \frac{1}{2}a(t)\delta t^2 + ... \tag{3.7}$$

$$v(t+\delta t) = v(t) + a(t)\delta t + \frac{1}{2}b(t)\delta t^2 + ... \tag{3.8}$$

$$a(t+\delta t) = a(t) + b(t)\delta t + \frac{1}{2}c(t)\delta t^2 + ... \tag{3.9}$$

where $r$ is the position, $v$ is the velocity (the first derivative of $r$ with respect to time) and $a$ is the acceleration (the second derivative of $r$ with respect to time), while the higher derivatives of $r$ (i.e., $b$ and $c$) are typically neglected. The most commonly used algorithm

for integrating the equations of motion is the Verlet algorithm, which is derived from:

$$r(t+\delta t) = r(t) + v(t)\delta t + \frac{1}{2}a(t)\delta t^2 + ... \tag{3.10}$$

$$r(t-\delta t) = r(t) - v(t)\delta t + \frac{1}{2}a(t)\delta t^2 - ... \tag{3.11}$$

Summing these two Taylor expressions, we get:

$$r(t+\delta t) = 2r(t) - r(t-\delta t) + a(t)\delta t^2 \tag{3.12}$$

Thus the Verlet algorithm uses position $r(t)$ and acceleration $a(t)$ at time $t$ and the position from the previous time $t - \delta t$ to calculate the new position at time $t + \delta t$. The algorithm uses no explicit calculated velocities. The advantages of this algorithm is that it is straightforward to implement and has modest storage requirements. The disadvantage is its moderate precision.

### 3.2.2 Leap-Frog algorithm

The Leap-Frog algorithm was developed in an effort to avoid the disadvantages of the Verlet algorithm. It is of the form [200,201,203]:

$$r(t+\delta t) = r(t) + v(t+\frac{1}{2}\delta t)\delta t \tag{3.13}$$

$$v(t+\frac{1}{2}\delta t) = v(t-\frac{1}{2}\delta t) + a(t)\delta t \tag{3.14}$$

Here, the velocities are first calculated at time $t + \frac{1}{2}\delta t$. Next, these are used to calculate the new positions at $t + \delta t$. In this way, the velocities 'leap-frog'over the positions, then the positions leap over the velocities. The advantage of the Leap-Frog algorithm over the Verlet algorithm is that the velocities are included explicitly here. The disadvantage is that the velocities and positions are not calculated at the same time, which means that the contributions of the potential energy from the positions and the kinetic energy from the velocities to the total energy cannot be calculated at the same time.

### 3.2.3 Velocity Verlet algorithm

The Velocity Verlet algorithm yields positions, velocities and accelerations at time $t$ and does not compromise precision [200,201,204]:

$$r(t+\delta t) = r(t) + v(t)\delta t + \frac{1}{2}a(t)\delta t^2 \tag{3.15}$$

$$v(t+\delta t) = v(t) + \frac{1}{2}[a(t) + a(t+\delta t)]\delta t \tag{3.16}$$

Here, more than two calculations have to be done for a single time step, since calculation of the velocities $v(t+\delta t)$ requires acceleration values at $(t)$ and $(t+\delta t)$. So, first the positions are determined at $(t+\delta t)$ and then the velocities at time $(t+\delta t)$ are computed.

## 3.3 Statistical Mechanics

The microscopic state of a system is interpreted by the momentum and position of its atoms, which together define coordinates in a multi-dimensional space called phase space [201]. Each system consisting of $N$ particles has $6N$ dimensions in this space. The current state of the system is described by a single point in phase space. Thus an ensemble can be defined as a collection of single points in phase space, which satisfy the conditions of a chosen thermodynamic state. An MD simulation generates many such single points in phase space as a function of time belonging to the same ensemble but having varying conformations of the system. Several different ensembles with different characteristics are described below.

### 3.3.1 Microcanonical ensemble (NVE)

The microcanonical ensemble [205,206], also called NVE ensemble is a thermodynamic state of the system where distinct microstates have a constant number of particles ($N$), a constant volume ($V$) and a fixed energy ($E$). This corresponds to an thermally isolated system. If the number of accessible microstates is given as $\Omega$, then the probability of finding the system to be in a particular microstate is $1/\Omega$:

$$P(m) = \frac{1}{\Omega(E)} \tag{3.17}$$

where $\Omega$ is the number of microstates with energy $E$ and $P(m)$ is the probability of microstate $m$.

### 3.3.2 Canonical ensemble (NVT)

In the canonical ensemble [205,206] the system is allowed to exchange energy with the heat bath. The thermodynamic state of this system is characterized by having a constant number of particles ($N$), a constant volume ($V$) and a well defined temperature ($T$). The probability $P(m)$ of finding the system to be in a particular microscopic state $m$ with

energy level $E(m)$ is given as:

$$P(m) = \frac{e^{-E_m/k_BT}}{\sum_m e^{-E_m/k_BT}} \tag{3.18}$$

### 3.3.3 Isobaric-Isothermal Ensemble (NPT)

The isobaric-isothermal ensemble [205] maintains a constant number of particles ($N$), a constant pressure ($p$) and a well defined temperature ($T$), but the energy ($E$) and volume ($V$) fluctuate at thermal equilibrium. Here the system is in contact with a barostat at pressure $p$ where it exchanges volume (and work) and with a thermostat at temperature $T$ where it exchanges energy. The NPT ensemble is important for the simulation of lipid bilayer systems [207] and chemical reactions which are usually carried out at constant pressure. The probability $P(m)$ is:

$$P(m) = \frac{e^{-(E_m+pV_m)/k_BT}}{\sum_m e^{-(E_m+pV_m)/k_BT}} \tag{3.19}$$

At constant pressure the state with low $(E + pV)$ is more likely than a state with high $(E + pV)$.

### 3.3.4 Grand canonical Ensemble ($\mu$VT)

The grand canonical ensemble is a system where the thermodynamic state is characterized by a constant chemical potential ($\mu$), constant volume ($V$) and a well defined temperature ($T$). In this ensemble, the system is in thermal contact with a reservoir and heat bath, allowing the exchange of energy with the bath at temperature $T$ and the exchange of particles with the reservoir at chemical potential $\mu$. The probability $P(m)$ of the system being in microstate $m$, having particle number $N_m$ and energy $E_m$ is:

$$P(m) = \frac{e^{-(N_m\mu-E_m)/k_BT}}{\sum_m e^{-(N_m\mu-E_m)/k_BT}} \tag{3.20}$$

## 3.4 Thermostats

Simulations at constant temperature are necessary to understand the changes in behaviour of a molecular system with temperature, such as folding and unfolding of proteins, or phase transitions in lipids. They are also important for comparison with experiments as experiments are usually carried out at constant temperature. It is also necessary

to control the temperature during molecular dynamic simulations to avoid drift during equilibration, which might be due to integration errors or excess heating due to frictional forces. Following thermostats can be used to simulate molecular systems at constant temperature:

### 3.4.1 Berendsen thermostat

The Berendsen thermostat is a weak coupling algorithm [200,208], where the system is coupled to an external heat bath with a fixed temperature ($T_{bath}$). This heat bath supplies and removes energy from the system as necessary by scaling the velocities at every time step. The difference between the temperatures of the system and the bath determines the rate of change in temperature:

$$\frac{dT(t)}{dt} = \frac{1}{\tau_T}\left[T_{bath} - T(t)\right] \tag{3.21}$$

Here, $\tau_T$ is a coupling parameter, which determines how tightly the bath and the system are coupled to each other. Larger $\tau_T$ means weak coupling and vice versa. If $\tau_T$ equals the time step ($\tau = \delta t$), the algorithm is equal to the velocity scaling method. A coupling constant $\tau_T$ value of 0.4 ps is usually used for $\delta t = 1$ fs. The temperature is altered by scaling the velocities, using the scaling factor:

$$\lambda^2 = 1 + \frac{\delta t}{\tau_T}\left(\frac{T_{bath}}{T(t)} - 1\right) \tag{3.22}$$

In MD simulations, the temperature is computed from the system's kinetic energy using the equipartition theorem:

$$\frac{1}{2}k_B T = \frac{1}{2}m_i v_{i,x}^2 \tag{3.23}$$

### 3.4.2 Velocity-rescaling thermostat

The Berendsen thermostat discussed above generates incorrect sampling and suppresses the fluctuations of the kinetic energy. The velocity rescaling thermostat [209], which is similar to the Berendsen thermostat, produces a correct ensemble by adding a stochastic term to ensure that it produces the correct kinetic energy distribution:

$$dK = (K_{bath} - K)\frac{dt}{\tau_T} + 2\sqrt{\frac{K K_{bath}}{3N}}\frac{dW}{\sqrt{\tau_T}} \tag{3.24}$$

Here, $K$ denotes the kinetic energy and $dW$ is the Wiener process (a continuous-time stochastic process).

### 3.4.3 Nose-Hoover thermostat

The Berendsen algorithm is extremely efficient in reaching the desired target temperature, after which a switch has to be made to a different thermostat which can produce the canonical ensemble. The Nose-Hoover thermostat [200], which is an extended ensemble first proposed by Nose [210] and later modified by Hoover [211], can be used for canonical ensemble simulations. The equations of motion are modified by adding a thermal reservoir and a friction term. The friction force is proportional to the particle velocity and friction parameter $\xi$, which is a dynamic quantity having its own momentum ($p_\xi$):

$$\frac{d^2 r_i}{dt^2} = \frac{F_i}{m_i} - \frac{p_\xi}{Q}\frac{dr_i}{dt} \tag{3.25}$$

where $Q$ determines the strength of the coupling. The friction parameter $\xi$ is determined by:

$$\frac{dp_\xi}{dt} = (T - T_{bath}) \tag{3.26}$$

with $T_{bath}$ being the reference temperature and $T$ the temperature of the system.

## 3.5 Barostats

Similar to thermostats, the systems can also be coupled to barostats to control the pressure of the system. The common barostats used in molecular simulations are explained below.

### 3.5.1 Berendsen barostat

The Berendsen barostat is similar to the Berendsen thermostat [200,208]. Here the system is coupled to a pressure bath and maintains constant pressure ($p_{bath}$) by altering its volume. The rate in pressure change is given by:

$$\frac{dp(t)}{dt} = \frac{1}{\tau_p}\left[p_{bath} - p(t)\right] \tag{3.27}$$

where $\tau_p$ is the coupling constant and determines how tightly the bath and the system are coupled to each other, while $p(t)$ is the pressure at time $t$. To adjust the volume of the system, the atomic coordinates are scaled by the factor $\lambda^{1/3}$

$$\lambda = 1 - k\frac{\delta t}{\tau_p}(p - p_{bath}) \tag{3.28}$$

Here, $k$ is the experimental isothermal compressibility.

### 3.5.2 Parrinello-Rahman barostat

In simulations of, e.g. lipid bilayer systems where fluctuations in pressure and volume are important, the weak-coupling Berendsen algorithm does not simulate the true NPT ensemble. In such cases, the Parrinello-Rahman [212,213] approach which is similar to Nose-Hoover temperature coupling, can be used:

$$\frac{db^2}{dt^2} = VW^{-1}b'^{-1}(p - p_{bath}) \tag{3.29}$$

Here, $b$ represents the box vectors, $V$ is the volume of the box, $W^{-1}$ determines the coupling strength and $p$ and $p_{bath}$ denote the current and reference pressures, respectively. The Parrinello-Rahman barostat is usually employed along with the Nose-Hoover thermostat.

## 3.6 Potential energy functions

The total potential energy ($U$) of a molecular system can be interpreted as a sum of the bonded and non-bonded potential terms [200,201,214]:

$$U_{total} = U_{bonded} + U_{non-bonded} \tag{3.30}$$

The bonded interactions originate from the covalent bonds holding the atoms together and they include terms for bonds, angles and dihedral angles. Biomolecular force fields also use improper dihedral interactions to define the planarity of aromatic groups and to enforce chirality:

$$U_{bonded} = U_{bond} + U_{angle} + U_{dihedral} + U_{improper} \tag{3.31}$$

The non-bonded interactions account for atoms which are not bonded to each other and separated by three or more covalent bonds. Non-bonded interactions include van der Waals and electrostatic interactions:

$$U_{non-bonded} = U_{vdW} + U_{elec} \tag{3.32}$$

Furthermore, any additional terms known to affect the energy of a molecular system can be added to the above expressions. The simplest energy function used in force fields to

model biosystems is as follows:

$$\begin{aligned} U(r_N) = & \sum_{bonds} \frac{1}{2} k_{ij} (l_{ij} - l_{ij,0})^2 \\ & + \sum_{angles} \frac{1}{2} k_{ijk} (\theta_{ijk} - \theta_{ijk,0})^2 \\ & + \sum_{improper} \frac{1}{2} k_{ijkl} (\xi_{ijkl} - \xi_{ijkl,0})^2 \\ & + \sum_{dihedrals} V_{ijkl} [1 + \cos(n\phi_{ijkl} - \phi_{ijkl,0})] \\ & + \sum_{i=1}^{N} \sum_{j=i+1}^{N} 4\varepsilon_{ij} \left[ \left( \frac{\sigma_{ij}}{r_{ij}} \right)^{12} - \left( \frac{\sigma_{ij}}{r_{ij}} \right)^{6} \right] \\ & + \sum_{i=1}^{N} \sum_{j=i+1}^{N} \frac{q_i q_j}{4\pi\varepsilon_0 r_{ij}} \end{aligned} \tag{3.33}$$

where $U(r_N)$ denotes the potential energy expressed as a function of the positions of $N$ atoms. The first four terms in equation (2.34) model the covalently bonded interactions in the structure of the molecular system, whereas the last two terms model the interactions between different molecules and between atoms within a molecule separated by at least 3 bonds.

### 3.6.1 Bond stretching

The bond stretching term models the interaction between two atoms $i$ and $j$ which are covalently bonded (e.g., C-C, C-H, C-O etc.). Molecules undergo vibrational motions and the energy required to compress or stretch their bond lengths $l_{ij}$ from their equilibrium values $l_{ij,0}$ are modelled as harmonic potentials by applying Hookes law:

$$U_b = \sum_{bonds} \frac{1}{2} k_{ij} (l_{ij} - l_{ij,0})^2 \tag{3.34}$$

The bond energy $U_b$ is calculated as a sum over all covalent bonds in the molecule. Each covalent bond in the molecule is treated as a harmonic spring with a unique force constant $k_{ij}$. Due to vibrational motions, the bond length $l_{ij}$ deviates from its equilibrium value $l_{ij,0}$. The harmonic potential is a good assumption when the deviation from $l_{ij,0}$ is around 0.1 Å or less. At larger deviation, where the atoms dissociate with no further interaction, the Morse potential can be used and is more accurate. It is of the form:

$$U_b(ij) = D_e \{1 - \exp[-a(l_{ij} - l_{ij,0})]\}^2 \tag{3.35}$$

Here, $D_e$ denotes the depth of the potential energy minimum and $a = \omega\sqrt{\frac{\mu}{2D_e}}$ where $\mu$ is the reduced mass and $\omega$ is the frequency of the bond vibration. However, the Morse potential is usually not used in simulations involving molecular mechanics force fields since it needs three additional parameters to be specified for each bond, lacking the computational efficiency, and also because bond breaking is conceptually different.

### 3.6.2 Angle bending

The angle bending term describes the deviation of a bond angle geometry. Interaction between three atoms (e.g. C-C-C, C-C-H, C-O-C etc.) are modelled, in which the first and third atoms are covalently bonded to the second atom. Deviation of the actual angle $\theta_{ijk}$ from its equilibrium value $\theta_{ijk,0}$ is modelled using Hookes law:

$$U_a = \sum_{angles} \frac{1}{2} k_{ijk}(\theta_{ijk} - \theta_{ijk,0})^2 \tag{3.36}$$

$U_a$ is the sum over all valence angle energies in the molecule, and the energy increases harmonically with deviation of the angle from its equilibrium value $\theta_{ijk,0}$. The force constants $k_{ijk}$ for angle bending are generally smaller than $k_{ij}$ for bond vibration, as a smaller amount of energy is needed to distort an angle from its equilibrium $\theta_{ijk,0}$ value than to compress or stretch a bond. The force constants for bond stretching and angle bending tries to preserve the correct chemical structure of the molecule and at the same time does not allow bond breakage.

### 3.6.3 Torsion angle potential

In a four atom $i - j - k - l$ system, where $i - j, j - k, k - l$ are covalently bonded, the torsional potential describes the energy change associated with rotation around the $j - k$ bond. The torsional angle potential is expressed as a sum over cosine functions and assumed to be periodic. The angle potential for proper dihedrals is of the form:

$$U_d = \sum_{dihedrals} V_{ijkl} \left[1 + \cos(n\phi_{ijkl} - \phi_{ijkl,0})\right] \tag{3.37}$$

where $\phi_{ijkl}$ is the torsional angle defined as the angle formed between the $ijk$ and the $jkl$ planes. The torsional angle may vary in the range from $[0°, 360°]$ or $[-180°, 180°]$, with $0°$ corresponding to the cis configuration i.e. $i$ and $l$ lie on the same side, and $180°$ being the trans configuration. $V_{ijkl}$ represents the energy barrier and $n$ the periodicity of the torsion, i.e. the energy associated with rotation of a bond should return to the same value if it is rotated by $360°$ for periodicity $n = 1$. The torsional angle potential terms also include the rotational between atoms separated by 3 covalent bonds. Thus,

this steric barrier has contributions from non-bonded interactions. The energy required for distorting a molecule by bond rotation is less compared to bond stretching or angle bending, hence larger structural deviations can be expected resulting from torsion.

### 3.6.4 Improper torsion

Out-of-plane terms can be incorporated into force fields to achieve a specific configuration. The out-of-plane motion is referred to as improper torsion. The improper torsional potential is a harmonic potential of the form:

$$U_{id} = \sum_{improper} \frac{1}{2} k_{ijkl}(\xi_{ijkl} - \xi_{ijkl,0})^2 \tag{3.38}$$

The improper dihedral angles are generally used in united atom force fields to preserve the stereochemistry at chiral centres, to maintain a planar configurations of the ester and amide groups, and also for aromatic ring structures.

### 3.6.5 van der Waals interactions

$U_{vdW}$ is the van der Waals energy describing repulsive and attractive interatomic forces between atoms $i$ and $j$ that are not directly bonded. $U_{vdW}$ can be interpreted as the interactions between the non-polar parts of the system, for example the interaction between the hydrophobic tails of the lipid bilayer or between methane molecules. Van der Waals interactions between two atoms is usually described as a 12-6 Lennard-Jones (LJ) potential of the form:

$$U_{vdW} = \sum_{i=1}^{N} \sum_{j=i+1}^{N} 4\varepsilon_{ij} \left[ \left( \frac{\sigma_{ij}}{r_{ij}} \right)^{12} - \left( \frac{\sigma_{ij}}{r_{ij}} \right)^{6} \right] \tag{3.39}$$

The attractive $r_{ij}^{-6}$ energies in the LJ potential is due to London interactions (e.g., dipole-dipole interaction), whereas the repulsive $r_{ij}^{-12}$ energies model the inter-nuclear repulsion and Pauli-exclusion principle. At short distances $U_{vdW}$ is repulsive due to overlap of the two electron clouds of the atoms, while it is zero at large distances. The atoms experience attraction at intermediate distance due to induced dipole-dipole interactions from the two electon clouds.

### 3.6.6 Electrostatic interactions

$U_{elec}$ accounts for the interactions between partial point charges $q_i$ and $q_j$ of atoms $i$ and $j$, respectively. They are modelled using the Coulombic potential:

$$U_{elec} = \sum_{i=1}^{N} \sum_{j=i+1}^{N} \frac{q_i q_j}{4\pi\varepsilon_0 r_{ij}} \tag{3.40}$$

Here, $r_{ij}$ is the distance between two atoms having charges $q_i$ and $q_j$ and $\varepsilon_0$ represents permittivity of the vacuum. Coulombic interactions are considered as long range interactions due to their slow decay with distance. Like for the LJ potential, the Coulombic potential is only evaluated when atoms $i$ and $j$ are separated by at least three covalent bonds. Usually, the calculation of the non-bonded interactions in a molecular system is the time consuming part. Using the predefined cutoff distances speeds up the computations. In such a scheme, the interactions beyond the cutoff distance are ignored.

## 3.7 Periodic boundary conditions

The classical way of minimizing or eliminating surface effects for systems of infinite size is to use periodic boundary conditions (PBC) [214]. In PBC, the cubic box containing the system is replicated in all directions to form an infinite lattice. During simulation, when a molecule leaves the central cell, its periodic image enters through the opposite face with the same orientation, thereby removing any effect of boundaries on the system. Thus when a molecule passes across a boundary, all its images move as well. These image cells have the same size and shape, and contain the same molecules as the central cell. The molecules can easily pass across the cells due to open boundaries. Saving the coordinates of the molecule in the central cell is sufficient, thus it is not required to save the coordinates from all the cells. The replication of cells depends on the range of intermolecular forces. For short-range non-bonded interactions such as the truncated Lennard-Jones model, only cells adjoining the central cell are needed. For cubes in three dimensions, the central cell has 26 identical adjacent image cells, whereas squares in two dimensions have 8 identical adjacent image cells. For long-range electrostatic interactions, which will extend beyond the boundary of a box, truncating the interaction at a certain distance leads to non-physical distributions of the molecules with discontinuous forces and energies. Therefore, lattice sum methods such as Ewald Sum [215], Particle Mesh Ewald (PME) [216,217] and particle-particle particle-mesh (PPPM) [216,218,219] are required for the calculation of electrostatic interactions under PBC.

## 3.8 Membrane-protein simulation setup

The use of MD simulations to study membrane protein interactions has rapidly grown since the first membrane-embedded protein simulation in 1994 [220]. To date, MD simulations have been successfully used to study protein insertion, channel proteins, ion pumps, G-protein coupled receptors, transmembrane peptides [221,222] etc. Here, we discuss the four major steps in setting up a membrane-protein simulation [223]:

### 3.8.1 Orienting protein and membrane

When trying to insert a protein into a pre-existing bilayer, the most common approach is to orient the protein and membrane in the same coordinate frame. Insertion of the protein can be based on the chemical composition aligning the hydrophobic part of the protein with the hydrophobic tails of the lipid bilayer, and the charged residues of the protein at the membrane-water interface. If available, the membrane position of the protein as determined from experimental studies are used. Some of the tools used to insert a protein into a membrane are VMD [224], the editconf tool available the MD package GROMACS [225], or self-written scripts.

### 3.8.2 Preparation and packing of lipids

The most crucial step insetting up a membrane-protein simulation is the assembly of lipids and proteins into a single system. Several approaches can be found in the literature for insertion of a protein into a bilayer. But often these techniques either delete excess lipids within a cut-off range causing the the bilayer to shrink and also creating a hole within the bilayer, which subsequently require, long time to equilibrate the protein-bilayer system, or they assume the protein shape to be cylindrical, which can only be used in case of highly symmetrical helix bundles. However, most membrane proteins are irregularly shaped. The most efficient approach for protein insertion is to use a pre-equilibrated bilayer and scale the lipid positions [223]. In this method the protein is first superimposed onto the bilayer patch at a desired orientation and depth. The second step is to expand the bilayer by translating the lipid molecules in $x$ and $y$ direction, while the protein position is unchanged. The third step involves a series of compression steps, so that the lipid molecules are brought back to their natural positions based on area per lipid for that particular lipid type. Any lipid molecules overlapping with the protein are deleted. This approach avoids that a large number of lipids being deleted and serves as a good starting point for subsequent solvation.

### 3.8.3 Solvation

During the preparatory steps described above, in most cases water molecules are removed as the system can be easily solvated later. While solvating a membrane-protein system, care must be taken that water molecules are not added into the hydrophobic interior of the bilayer. In case the water molecules have penetrated into the hydrophobic interior, they can be removed based on distance cut-off or based on their $z$ position. Alternatively, water molecules entering the hydrophobic interior of the bilayer can be avoided by first increasing the van der Waals radii of the carbon atoms from the default value of 0.15 nm to a value of 0.40 nm. In this case, the vdW parameters have to be modified while solvating. After solvation, the system can be viewed in VMD [224] to check for the presence of any water molecules inside the hydrophobic membrane interior. The presence of 3 – 5 water molecules can be manually deleted. Before moving on to equilibration, it is important to reset the van der Waals radii of carbon to its default value.

### 3.8.4 Equilibration

The equilibration time depends on the initial preparation of the system and the system size. In our studies, a pure lipid bilayer patch with 128 lipids equilibrated for 40 ns was used [226]. In our peptide-bilayer simulations, an initial equilibration under isothermal-isochoric conditions was performed for 100 ps during which the protein heavy atoms and phosphorous atoms of the lipid headgroups were restrained with a force constant of 1000 $\mathrm{kJ\,mol^{-1}\,nm^{-2}}$. Here, the v-rescale thermostat with a coupling constant of 0.1 ps was used to regulate the temperature of the peptide, lipids, and solvent/ions separately. The systems were then equilibrated under isothermal-isobaric (NPT) conditions for 30 ns. For the NPT ensemble the Nose-Hoover thermostat was used to regulate the temperature along with semiisotropic Parrinello-Rahman pressure coupling. The bilayer normal $z$-direction and $xy$-plane were coupled separately with a time constant of 5.0 ps maintaining a constant pressure of 1 bar independently in all directions. An isothermal compressibility of $4.5 \times 10^5$ $\mathrm{bar^{-1}}$ was applied in all box dimensions. Long-range electrostatics were calculated using the Particle Mesh-Ewald method in connection with periodic boundary conditions. Van der Waals and Coulombic interaction cutoffs were set to 1.2 nm and the LINCS algorithm [227] was used to constrain all bond lengths. Following equilibration, production MD runs were performed for 500 ns for each system. Here the parameter settings were similar to the NPT equilibration step, except that all restraints were removed and the time constant for pressure coupling was set to 2.0 ps for maintaining a constant pressure of 1 bar. The time step $\delta t$ for integration was 2 fs with coordinates and velocities saved every 20 ps for analysis.

## 3.9 Analysis

Following analysis methods are particularly useful for membrane protein systems:

### 3.9.1 Root mean square deviation

The root mean square deviation (RMSD) is the measure of the differences between the coordinates of two structures, usually calculated for the backbone atoms of the two superimposed structures. The RMSD can be calculated with:

$$RMSD = \sqrt{\frac{1}{N}\sum_{i=1}^{N} \|r_i^{\alpha} - r_i^{\beta}\|^2} \tag{3.41}$$

where $r_i$ are the coordinates of atom $i$ and $\alpha$ and $\beta$ refer to the two different structures used in the calculation. An RMSD value is commonly expressed in Angstrom (Å) unit.

### 3.9.2 Root mean square fluctuation

The root mean square fluctuation (RMSF) is the measure of the deviation between the position of the atom and some reference position, which is typically the time-averaged position obtained from a trajectory. The RMSF can be calculated with:

$$RMSF = \sqrt{\frac{1}{T}\sum_{t_j=1}^{T} (r_i(t_j) - \widetilde{r}_i)^2} \tag{3.42}$$

where $T$ is the time of the simulation, $r_i$ are the coordinates of atom $i$ at time $t_j$ and $\widetilde{r}_i$ is the reference position of atom $i$.

### 3.9.3 Area per lipid and bilayer thickness

The area per lipid can be calculated by taking the lateral $x$ and $y$ dimensions of the simulation box divided by number of lipid molecules in each leaflet. The bilayer thickness is measured by considering the phosphate-to-phosphate (P–P) distance between both leaflets of the bilayer. We used the grid-based membrane analysis tool GRIDMAT-MD [228] to calculate the area per lipid and the bilayer thickness.

### 3.9.4 Deuterium order parameter

To characterize the effects of the peptide on the orient ational mobility of the lipid molecules, we studied the lipid tail order parameter $S_{\mathrm{CD}}$ defined as

$$S_{\mathrm{CD}} = \left\langle \frac{3\cos^2\theta - 1}{2} \right\rangle , \tag{3.43}$$

where $\theta$ is the angle between the C–H bond vector (in the simulation) or the C–D bond vector (in the experiment) and the bilayer normal. The angular brackets indicate averaging over lipids and over time.

### 3.9.5 Lateral diffusion coefficient

The lateral diffusive motion for lipid molecules in a membrane can be characterized by its mean square displacement (MSD) [229]:

$$MSD = \langle (r(t) - r_0)^2 \rangle = 4Dt \tag{3.44}$$

where $r(t)$ is the time-dependent position of the molecule, $r_0$ is the initial position of the molecule and $D$ is the diffusion coefficients of the lipid molecule.

# 4 Results

The main aim of this thesis work is the study of the interactions between lipid membranes and the amyloidogenic peptides A$\beta$ and hIAPP, to unravel key aspects of the membrane damage caused by amyloid. To this end, we performed all-atom MD simulations, which can be divided into four categories:

(1) **How the amyloid-$\beta$ peptide and membranes affect each other: an extensive simulation study**

In this study we carried out simulations totaling over 6 microseconds in simulation time to investigate the behavior of A$\beta_{42}$ in zwitterionic and anionic lipid bilayers. We simulated transmembrane $\beta$-sheets (monomer and tetramer) resulting from a global optimization study [112] and a helical structure obtained from an NMR study [103]. In all simulations A$\beta_{42}$ remained embedded in the bilayer. It was found that the surface charge and the lipid tail type are determinants for transmembrane stability of A$\beta_{42}$ with zwitterionic surfaces and unsaturated lipids promoting stability. From the considered structures, the $\beta$-sheet tetramer is most stable as a result of interpeptide interactions. We performed an in-depth analysis of the translocation of water in the A$\beta_{42}$-bilayer systems. We observed that this process is generally fast (within a few nanoseconds) yet generally slower than in the peptide-free bilayers. It is mainly governed by the lipid type, simulation temperature and A$\beta_{42}$ conformation. The rate limiting step is the permeation through the hydrophobic core, where interactions between A$\beta_{42}$ and permeating $H_2O$ molecules slow the translocation process. The $\beta$-sheet tetramer allows more water molecules to pass through the bilayer compared to monomeric A$\beta$, allowing us to conclude that the experimentally observed permeabilization of membranes must be due to membrane-bound A$\beta$ oligomers, and not monomers.

*BBA-Biomembranes*, 1828(2):327339, 2013 (impact factor (IF) 4.11). Complete execution of molecular dynamics simulations and 90% of the manuscript.

(2) **Stability of transmembrane amyloid $\beta$-peptide and membrane integrity tested by molecular modeling of site-specific A$\beta_{42}$ mutations**

Natural mutations in A$\beta_{42}$, such as the Arctic mutation (E22G) have been shown to increase A$\beta_{42}$ aggregation and neurotoxicity, leading to the early-onset of Alzheimer's disease. The mutant peptides also have a variable ability to disrupt bilayer integrity. To test the connection between A$\beta_{42}$ mutation and peptide–membrane interactions, we inserted A$\beta_{42}$ variants (wild-type and E22G, D23G, E22G/D23G, K16M/K28M and K16M/E22G/D23G/K28M mutants) as $\beta$- sheet monomers and tetramers into membranes. The effects of charged residues on transmembrane A$\beta_{42}$ stability and membrane integrity is analyzed at atomistic level. We observed an increased stability for the E22G A$\beta_{42}$ peptide and a decreased stability for D23G compared to wild-type A$\beta_{42}$, while D23G has the largest membrane-disruptive effect. These results suggest that the altered neurotoxicity arising from mutations in A$\beta$ is not only a result of the altered aggregation propensity, but also originates from modified A$\beta$ interactions with neuronal membranes.

*Manuscript submitted to PLoS One* (IF 4.09). Complete execution of molecular dynamics simulations and 90% of the manuscript.

(3) **Membrane permeation induced by aggregates of huma n islet amyloid polypep tides**

Here, we focus on aggregates of the human islet amyloid polypeptide (hIAPP) implicated in type II diabetes. We find that hIAPP trimers and tetramers preserve their $\beta$-sheet secondary structures when inserted into lipid bilayers and lead to water permeation and $Na^+$ intrusion, consistent with ion-toxicity in islet $\beta$-cells. In particular, hIAPP trimers insert into bilayers of dipalmitoyl-phosphatidylglycerol (DPPG) at 60° relative to the membrane/water interface and form barrel-like structures that induce water permeability comparable to channel-forming proteins, like aquaporins and gramicidin-A. The predicted disruptive orientation is consistent with the amphiphilic properties of the hIAPP aggregates and could be probed by chiral sum frequency generation (SFG) spectroscopy, as predicted by the simulated SFG spectra.

*Manuscript submitted to Biophys.J.* (IF 4.13). Complete execution of molecular dynamics simulations and 80% of the manuscript.

(4) **Trapping the events of amyloid-$\beta$ insertion into membranes**

A$\beta$ insertion and permeation into the membrane hydrophobic core is still unclear, though very important in the development of AD. Therefore, we investigate the pathways and kinetics for A$\beta$ insertion and permeation into a POPC lipid bilayer using atomistic umbrella sampling simulations. We calculate the potential of mean force (PMF) for the insertion of the A$\beta$ fragment, A$\beta_{21-32}$ into a POPC membrane along a single reaction coordinate. Here A$\beta_{21-32}$ (WT) and Arctic type A$\beta_{21-32}$ (E22G) is studied to investigate the effect of charges, as the E22G mutant is known to increase neurotoxic protofibril production and is more toxic than WT A$\beta$. The results emphasize the importance of electrostatic interactions for membrane binding and hydrophobicity of the peptides for membrane insertion. The PMF profiles reveal an overall smaller barrier for the membrane insertion of E22G A$\beta_{21-32}$ compared to WT, suggesting that the more favourable peptide-lipid interactions for Arctic type A$\beta$ may play a role in its increased neurotoxicity.

*Manuscript under preparation.* Complete execution of molecular dynamics simulations and 90% of the manuscript.

In the following the results of these four studies are presented as manuscripts, which are either published, submitted or in preparation. References given in the following sections refer to the individual manuscripts (and not the references given at the end of this thesis).

## 4.1 How the amyloid-$\beta$ peptide and membranes affect each other: an extensive simulation study

Biochimica et Biophysica Acta 1828 (2013) 327–339

Contents lists available at SciVerse ScienceDirect

Biochimica et Biophysica Acta

journal homepage: www.elsevier.com/locate/bbamem

# How the amyloid-β peptide and membranes affect each other: An extensive simulation study

Chetan Poojari [a], Andreas Kukol [b], Birgit Strodel [a,c,*]

[a] Research Centre Jülich, Institute of Complex Systems: Structural Biochemistry, 52425 Jülich, Germany
[b] University of Hertfordshire, School of Life Sciences, College Lane, Hatfield AL10 9AB, United Kingdom
[c] Institute of Theoretical and Computational Chemistry, Heinrich Heine University Düsseldorf, 40225 Düsseldorf, Germany

ARTICLE INFO

*Article history:*
Received 26 March 2012
Received in revised form 3 September 2012
Accepted 4 September 2012
Available online 10 September 2012

*Keywords:*
Amyloid-beta peptide
Phospholipid membranes
Molecular simulations
Water permeation
Alzheimer's disease

ABSTRACT

The etiology of Alzheimer's disease is thought to be linked to interactions between amyloid-β (Aβ) and neural cell membranes, causing membrane disruption and increased ion conductance. The effects of Aβ on lipid behavior have been characterized experimentally, but structural and causal details are lacking. We used atomistic molecular dynamics simulations totaling over 6 μs in simulation time to investigate the behavior of $A\beta_{42}$ in zwitterionic and anionic lipid bilayers. We simulated transmembrane β-sheets (monomer and tetramer) resulting from a global optimization study and a helical structure obtained from an NMR study. In all simulations $A\beta_{42}$ remained embedded in the bilayer. It was found that the surface charge and the lipid tail type are determinants for transmembrane stability of $A\beta_{42}$ with zwitterionic surfaces and unsaturated lipids promoting stability. From the considered structures, the β-sheet tetramer is most stable as a result of interpeptide interactions. We performed an in-depth analysis of the translocation of water in the $A\beta_{42}$-bilayer systems. We observed that this process is generally fast (within a few nanoseconds) yet generally slower than in the peptide-free bilayers. It is mainly governed by the lipid type, simulation temperature and $A\beta_{42}$ conformation. The rate limiting step is the permeation through the hydrophobic core, where interactions between $A\beta_{42}$ and permeating $H_2O$ molecules slow the translocation process. The β-sheet tetramer allows more water molecules to pass through the bilayer compared to monomeric Aβ, allowing us to conclude that the experimentally observed permeabilization of membranes must be due to membrane-bound Aβ oligomers, and not monomers.


## 1. Introduction

Alzheimer's disease (AD) is a neurodegenerative disorder associated with synaptic loss, abnormalities in functioning of neurons, neuronal cell death and extracellular accumulation of senile plaques composed of the neurotoxic amyloid-β peptide (Aβ) [1,2]. Aβ is derived from the amyloid precursor protein (APP), a type-1 membrane integral glycoprotein through sequential cleavage by β- and γ-secretases [3]. The major alloforms of Aβ are $A\beta_{40}$ and $A\beta_{42}$, which differ by the presence of two amino acids, I41 and A42 at the C-terminus of the latter. The more hydrophobic $A\beta_{42}$ is the prevalent alloform seen in amyloid plaques, and has a greater tendency to aggregate into fibrils and plaques [4,5]. There is appreciable evidence suggesting that Aβ exerts its cytotoxic effect by interacting with membranes of neurons and other cerebral cells, such as astrocytes, microglial and cerebral endothelial cells [6,7]. A potential pathway for Aβ toxicity lies in its ability to alter biophysical membrane properties [8–11]. Aβ aggregates cause membrane disruption and increased permeability, allowing excessive leakage of ions, particularly calcium ions [12]. This imbalance in calcium homeostasis promotes neuronal excitotoxicity [12,13]. $A\beta_{42}$ oligomers interact with lipid raft related ganglioside GM1, further accelerating the amyloidogenic processing of APP [14].

Various experimental studies investigating the interactions between Aβ and phospholipids have revealed that Aβ prefers to bind to negatively charged lipids compared to zwitterionic lipids [15–17]. It has been shown that the enhanced association of Aβ with anionic lipid membranes leads to the insertion of Aβ into the membrane [15–17] and induces the formation of β-sheets [15,17–19] and Aβ fibrils [19–21]. NMR spectroscopy studies on $A\beta_{40}$ in a membrane-mimicking environment concluded that the peptide is unstructured in the N-terminal region from residues 1–14 and that the C-terminal hydrophobic residues from 15 to 36 adopt an α-helical conformation with a kink at residues 25–27 [22]. This kink may be significant in membrane insertion and conformational rearrangements [22]. Coles et al. proposed three possible models corresponding to different Aβ insertion depths in the membrane based on structural findings for $A\beta_{40}$ [22]. The two experimentally determined insertion depths have K28 and V24, respectively, at the membrane–water interface [22,23]. A third proposed model is with K16 at the membrane–water interface, where the entire α-helical conformation adopted by $A\beta_{40}$ (residues 15–36) spans the plasma

* Corresponding author at: Research Centre Jülich, Institute of Complex Systems: Structural Biochemistry, 52425 Jülich, Germany. Tel.: +49 2461 613670.
*E-mail address:* b.strodel@fz-juelich.de (B. Strodel).

0005-2736/$ – see front matter © 2012 Elsevier B.V. All rights reserved.
http://dx.doi.org/10.1016/j.bbamem.2012.09.001

membrane [22]. A study on soluble and aggregated forms of $A\beta_{40}$ on rat cortical synaptic plasma membrane using small angle X-ray diffraction and fluorescence spectroscopy showed that the monomer penetrates into the hydrophobic core of the bilayer, whereas the aggregated form was found interacting with the phospholipid headgroups [24]. Similarly, soluble $A\beta_{42}$ was found to intercalate the membrane of giant unilamellar vesicles composed of 1-palmitoyl 2-oleoyl phosphatidylcholine (POPC) or POPC/sphingomyelin (SM)/cholesterol (Chol), altering permeability properties of the bilayer [25]. However, permeabilization of lipid bilayers can also be caused by soluble amyloid oligomers [26]. NMR, CD, fluorescence and monolayer studies on $A\beta_{42}$ inserted into a POPC/POPS (palmitoyl-oleoyl phosphatidylserine) bilayer showed reduction in membrane stability with an increase in membrane fluidity [27]. This study also indicated that $A\beta_{42}$ alone could destabilize the membrane integrity in absence of ions, and that the peptide adopts a $\beta$-sheet structure in the membrane with increase in $\beta$ content when $Cu^{2+}$ is added [27]. Further experimental work carried out on $A\beta_{40}$ inserted into a zwitterionic phosphatidylcholine bilayer revealed that the perturbation of the bilayer integrity is caused by short $\beta$-sheet assemblies embedded in the lipid bilayer [28]. Atomic force microscopy of $A\beta_{42}$ [29] and $A\beta_{40}$ [30] in reconstituted membranes revealed ion-channel-like structures, which are able to cause cellular ionic imbalance [30–34]. Lal and coworkers also demonstrated through biochemical analysis that A$\beta$ forms stable tetramers and hexamers in lipid membranes [29].

It was shown that theoretical approaches are needed as a complement to experimental studies probing the principles governing $A\beta_{42}$ aggregation and A$\beta$–membrane interactions [35,36]. Various computational studies of A$\beta$ interacting with lipids have been performed to gain structural information at an atomistic level [37–59]. An atomistic model of A$\beta$ channel structures developed by Nussinov and coworkers provided information about the A$\beta$ conformation in membranes and ion-channel activity [37,38]. In another study they found that the channels break into mobile $\beta$-sheet subunits, which enable toxic ionic flux [39]. Strodel and coworkers also proposed A$\beta$ pore models composed of tetrameric to hexameric A$\beta$ subunits, which are similar to the models suggested by Nussinov and coworkers [46]. In [47] the stability of transmembrane $\beta$-barrel structures, each composed of eight A$\beta$ fragments $A\beta_{25-35}$, was investigated. Molecular dynamics (MD) studies of $A\beta_{40}$ inserted in a dipalmitoyl phosphatidylcholine (DPPC) bilayer with the peptide positioned with either K28, V24 or K16 at the membrane–water interface showed that in either case the peptide remained partially embedded in the membrane [48]. Loss of $\alpha$-helicity in favor of $\beta$-strands was observed when the peptide was inserted at K28 and V24, whereas with K16 at the interface $\alpha$-helicity was retained. For the deeper insertion depths, water molecules were seen entering the hydrophobic core accumulating near the charged residues of the peptide within the bilayer. It has also been reported that $A\beta_{40}$ causes DPPC lipid headgroup disorder and reduces the membrane thickness around A$\beta$ [49]. In a recent study, Lemkul and Bevan explored the interactions between $A\beta_{40}$ and several pure and mixed model membranes, and lipid rafts, both with and without GM1 [50]. $A\beta_{40}$ remained inserted in the membranes without GM1, but in several instances exited the raft containing GM1 initiated through hydrogen bonding of $A\beta_{40}$ with GM1. Another study on $A\beta_{40}$ preinserted in a DPPC bilayer found the peptide exiting the membrane and adsorbing to its surface, with helix conformation being the major secondary structure observed in the membrane-adsorbed A$\beta$ structure [54]. In a recent MD simulation study, the self-assembly of A$\beta$ in a mixed DPPC/cholesterol bilayer was investigated, uncovering the formation of a short parallel $\beta$-sheet between two peptides [59].

In the present MD study, we report the behavior of $A\beta_{42}$ preinserted into zwitterionic POPC and DPPC bilayers, and anionic 1-palmitoyl 2-oleoyl phosphatidylglycerol (POPG) bilayers. Here, our focus is on membrane-spanning structures based on the observation that A$\beta$ can form pore-like structures in reconstituted membranes [30–34]. Due to conflicting experimental results as to whether A$\beta$ is in a helical or in a $\beta$-sheet conformation in a lipid bilayer, we considered both transmembrane conformations as starting structures for our MD simulations in order to investigate whether the secondary structure leads to different behavior of the membrane-inserted $A\beta_{42}$ peptide. We used a $\beta$-sheet structure (monomer and tetramer) obtained from a global optimization approach [46] and a helix structure from an NMR study in an apolar solvent [22]. During each of the 500 ns MD simulations, $A\beta_{42}$ remains embedded in the lipid bilayer. We discuss our results in terms of structural stability of $A\beta_{42}$ and its effects on membrane functionality.

## 2. Methods

### 2.1. Starting structures

The two initial membrane-spanning $A\beta_{42}$ structures are a $\beta$-sheet and a helical conformation. The transmembrane $\beta$-sheet was obtained from a study for the $A\beta_{42}$ monomer and small oligomers using a global optimization approach in an implicit membrane model [46]. In this structure, the more hydrophobic C-terminal region starting from residue 17 is fully inserted into the hydrophobic membrane core, forming an antiparallel $\beta$-sheet with two turn regions, the first ranging from residues 23 to 29 and the second one involving residues 37 and 38. The first turn is prominent in many A$\beta$ structures identified from experiment [60–63] and simulation [64–66]. However, each of these models predicts a distinct turn structure. Ma and Nussinov independently predicted that the A$\beta$ peptide amyloid adopts a U-turn $\beta$-strand–loop–$\beta$-strand motif [66], qualitatively agreeing with the Tycko et al. model [63]. Lührs et al. [62] presented a 3D structure of $A\beta_{17-42}$ fibrils with a U-turn bent $\beta$-sheet based on hydrogen/deuterium-exchange NMR data, which further validates the computational model of Ma and Nussinov [66] and is consistent with the experimental model of Petkova et al. [63]. All these models, including our $\beta$-hairpin structure [46] share the key structural features of the salt bridge between Asp23 and Lys28 and the intramolecular hydrophobic cluster between Leu17/Phe19 and Ile32/Leu34. We decided to use our $\beta$-hairpin model as starting structure as it also provides a structural model for the more hydrophilic residues 1–16, which form a $\beta$-hairpin outside the membrane [46]. We study this transmembrane $\beta$-sheet as monomer (denoted SHEET in the following) and tetramer as obtained in [46] (Fig. 1a and b). The $\alpha$-helical starting structure was obtained from an NMR study of $A\beta_{40}$ in an apolar solvent (PDB ID: 1BA4) [22]. We extended the 40 residue peptide to $A\beta_{42}$ by adding the two hydrophobic residues I41 and A42 in a coil conformation. Our motivation behind this extension was to study the role of the extra I41 and A42 residues in peptide–lipid interactions and the resulting structural changes in the peptide and membrane. Previous studies revealed an increased stability provided by I41 and A42 to the antiparallel $\beta$-sheet when compared to $A\beta_{40}$ [67]. Furthermore, by using the same peptide we wanted to be able to compare our findings for the helical and $\beta$-sheet transmembrane structures. The helical structure was studied for two insertion depths: (i) with K16 (denoted HEL-16) and (ii) with D23 (denoted HEL-23) at the membrane–water interface (Fig. 1c and d). Note that this nomenclature refers to the initial condition only as no restraints are imposed on the peptide. This implies that during the MD simulations the peptide can experience secondary structure changes and/or transpositions within the lipid bilayers so that the final state of an MD run does not necessarily correspond to the initial notation.

All our simulations were carried out at physiological pH giving rise to charge $-3$ for $A\beta_{42}$ with His residues modeled uncharged, Asp and Glu negatively charged, and Lys and Arg assumed being protonated. Our choice of the protonation state for the ionizable residues was based on their $pK_a$ values as a function of depth in the membrane [68]. At pH 7, Lys and Arg become deprotonated only when they are in close vicinity to the membrane center, while the $pK_a$ values of Asp and Glu rise above 7 inside the membrane core. In our simulations $A\beta_{42}$ is positioned such that K16, E22, D23 and K28 are at the membrane–water interface. Therefore, we assumed positive charges for

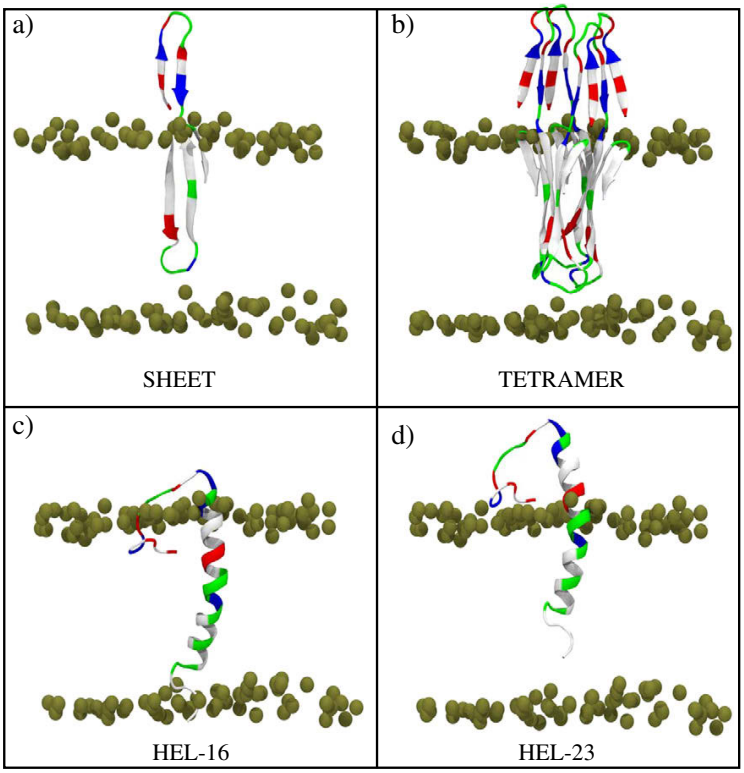


**Fig. 1.** Initial structures for the MD runs: (a) β-sheet monomer (SHEET), (b) β-sheet tetramer, (c) α-helix inserted with K16 at the membrane–water interface (HEL-16), (d) α-helix inserted with D23 at the membrane–water interface (HEL-23). The peptide is shown in cartoon and colored based on the physicochemical properties of the residues: blue, basic; red, acidic; white, hydrophobic; and green, polar. The bilayer phosphorus atoms are shown as Van der Waals spheres in tan color. Lipid tails and water molecules are not shown for clarity.

K16 and K28, and negative charges for E22 and D23. While this choice for Lys is undoubted, E22 and D23 are borderline cases as their protonation state could change during the MD simulation. Ideally, one would like to perform constant pH MD simulations. Such a method was recently implemented into GROMACS for explicit water simulations [69], which is, however, not available yet for simulations including lipid bilayers. The N- and C-terminals were capped to nullify the effect of terminal residues in peptide–lipid interactions.

### 2.2. Molecular dynamics simulations

All MD simulations were performed with the GROMACS 4.0 package [70]. The $A\beta_{42}$ peptide was described using the GROMOS96 53A6 force field [71], and the lipids were modeled with modified Berger force field parameters for use with the GROMOS96 53A6 force field [72]. Recently, we demonstrated that the GROMOS96 53A6 force field is able to correctly model the structural propensities of $A\beta_{40}$ and $A\beta_{42}$ [73]. Initial coordinates of 128 lipids for POPC, DPPC and POPG bilayers equilibrated with water for 40 ns were obtained from Kukol's work on lipid models [72]. We performed 100 ns MD simulations of the pure lipid bilayers for comparison with our simulations involving $A\beta_{42}$. For the latter, $A\beta_{42}$ was inserted into the pre-equilibrated lipid membrane using the INFLATEGRO script [74]. Once $A\beta_{42}$ was inserted into the lipid membrane, the structures were solvated with SPC water molecules, $Na^+$ counterions were added to balance the peptide and POPG charge, and 0.1 M NaCl salt was added to bring the system to a near physiological salt concentration. The simulations were carried out in a $65\times65\times95$ Å$^3$ box. An initial equilibration under isothermal–isochoric conditions was performed for 100 ps during which the protein heavy atoms and phosphorous atoms of the lipid headgroups were restrained with a force constant of 1000 kJ mol$^{-1}$ nm$^{-2}$. Here, the v-rescale thermostat with a coupling constant of 0.1 ps was used to regulate the temperature of the peptide, lipids, and solvent/ions separately at 298 K for the POPC and POPG simulations, and at 325 K for the DPPC simulations. The higher simulation temperature for DPPC is necessary for the membrane to remain fluid, which is already guaranteed for POPC and POPG at 298 K. The systems were then equilibrated under isothermal–isobaric (NPT) conditions for 30 ns. For the NPT ensemble the Nose–Hoover thermostat was used to regulate the temperature along with semiisotropic Parrinello–Rahman pressure coupling. The bilayer normal *z*-direction and *xy*-plane were coupled separately with a time constant of 5.0 ps maintaining a constant pressure of 1 bar in all directions. An isothermal compressibility of $4.5\times10^5$ bar$^{-1}$ was applied in all box dimensions. Long-range electrostatics were calculated using the Particle Mesh-Ewald method in connection with periodic boundary conditions. Van der Waals and Coulombic interaction cutoffs were set to 12 Å and the LINCS algorithm was used to constrain all bond lengths. Following equilibration, production MD runs were performed for 500 ns for each system. Here the parameter settings were similar to the NPT equilibration step, except that all restraints were removed and the time constant for pressure coupling was set to 2.0 ps for maintaining a constant pressure of 1 bar. The time step for integration was 2 fs, with coordinates and velocities saved every 20 ps for analysis.

### 2.3. Analysis

The structural stability of $A\beta_{42}$ was analyzed separately for the N-terminal residues outside the membrane and the C-terminal residues

inside the hydrophobic bilayer core. For A$\beta_{42}$ inserted at K16, the N-terminal residues thus range from 1 to 16 and the C-terminal residues from 17 to 42, whereas for A$\beta_{42}$ with D23 at the membrane–water interface residues 1–23 and residues 24–42 were considered as N- and C-terminal segments, respectively. The secondary structure of A$\beta_{42}$ was analyzed using the DSSP (dictionary of protein secondary structure) method [75]. The tilt angle of the peptide inside the bilayer core relative to the membrane normal and motion of the peptide along the membrane normal was calculated using GROMACS analysis tools. Water permeation across the membrane was quantified using VMD [76]. The probability of hydrogen bond (H-bond) formation, either between peptide and water or between peptide carbonyl and amide groups, was considered based on a cutoff distance of 3.6 Å between donor and acceptor atoms and a cutoff angle off linearity of 30°. We used the grid-based membrane analysis tool GRIDMAT-MD to calculate the area per lipid and the bilayer thickness [77]. For the bilayer thickness we report phosphate-to-phosphate (P–P) distances. To characterize the effects of the peptide on the orientational mobility of the lipid molecules we calculated the lipid tail order parameter $S_{CD}$ defined as

$$S_{CD} = \left\langle \frac{3\cos^2\theta - 1}{2} \right\rangle , \quad (1)$$

where $\theta$ is the angle between the C – H bond vector (in the simulation) or the C – D bond vector (in the experiment) and the bilayer normal. The angular brackets indicate averaging over lipids and over time.

## 3. Results and discussion

In all cases A$\beta_{42}$ remained inside the bilayer throughout the MD simulations on the sub-microsecond scale. This finding is independent of the secondary structure of the starting conformation and the lipid bilayer type. The final structures after 500 ns of MD simulations of the SHEET, HEL-16, HEL-23 starting structures in a POPC, DPPC and a POPG bilayer are presented in Fig. 2. These figures show that the N-terminal segment of the peptide is generally adsorbed to the bilayer surface of the upper leaflet as a result of electrostatic interactions and hydrogen bonding. These interactions rupture the lipid packing and lead to a tilt of the lipids around the peptide, allowing passage of water molecules into the hydrophobic core of the bilayer. The peptide residues, rendered as pink spheres in Fig. 2, are those involved in H-bond formation with the water molecules entering the bilayer. This is a measure of how deep water molecules can enter the hydrophobic core once they have passed the head group region and can form H-bonds with the transmembrane part of A$\beta_{42}$. It should be noted, however, that this does not indicate that the water molecules also translocate the membrane. Water translocation was considered only when a water molecule passed both headgroup regions, and not when it entered and exited at the same side of the bilayer. In the Supporting material the change of residual secondary structure during the MD simulations is presented (Figs. S1–S4). Our analysis of the MD trajectories showed that all A$\beta_{42}$ structures considered are relatively stable on the time scale of the simulations in terms of their overall position in the bilayer and with regard to their secondary structure. We, therefore, show the final MD states as representative structures in Fig. 2.

In order to establish what kind of variations are to be expected for a system when simulated multiple times, we repeated the simulation of the SHEET in POPC two more times. These MD simulations were initiated from the same starting structure (Fig. 1a) yet with different initial velocity distributions. The final structures of the three 500 ns MD simulations of SHEET in POPC are shown in Fig. S5a, while in Fig. S5b the corresponding secondary structure analysis is presented. It can be seen that in all three cases the transmembrane $\beta$-sheet is stable and does not move considerably along the membrane normal. Only the structures of the N-terminal residues outside the membrane are different resulting from the combined action of electrostatic interactions between charged N-terminal A$\beta_{42}$ residues and lipid headgroups, a high preference for random coil structures of the N-terminal residues in water, and stochastic conformational changes associated with thermal movements. However, in all three cases the N-terminus of A$\beta_{42}$ is attracted by the membrane surface. The analysis of the effects of the SHEET structure on the POPC bilayer revealed very similar results for these three MD simulations, too. These findings allow us to conclude that structural changes of SHEET inside the membrane core are mainly a result of statistical fluctuations around the stable $\beta$-sheet structure, which is likely to be stable on a much longer time scale, while the structure of the N-terminus would probably change further when simulated for longer. Depending on the lipid type and initial A$\beta_{42}$ structure, transmembrane A$\beta_{42}$ displays different stabilities, which will be discussed in the following, where effort was made to address whether observed instabilities are inherent and likely to be more pronounced on a longer timescale.

### 3.1. Effects of transmembrane A$\beta_{42}$ on lipid bilayers

From our MD simulations we found that the effects of transmembrane A$\beta_{42}$ monomer on the bilayers depend more on the lipid type than on the inserted A$\beta_{42}$ structure. The analysis of the bilayer properties is summarized in Table 1. This table lists the area per lipid and bilayer thickness, the average number of H-bonds between A$\beta_{42}$ and water molecules in the bilayer core, the number of intrapeptide H-bonds (including interpeptide H-bonds in case of the A$\beta_{42}$ tetramer) in the bilayer core, the number of water molecules passing the membrane in the vicinity of A$\beta_{42}$, and the average motion of A$\beta_{42}$ along the bilayer normal. In Figs. S6 and S7 images of the bilayer thickness calculated for the final states of the MD simulations are shown. In almost all cases we observed that the upper leaflet has a lower area per lipid headgroup than the lower leaflet. However, both the upper and lower leaflets have a decreased area per lipid headgroup when compared to the bilayers without peptide. This area contraction results from attractive electrostatic forces and H-bonds between A$\beta_{42}$ residues and lipid headgroups. For the bilayer thickness we find that the average thickness of POPC and POPG bilayers is hardly affected by embedded A$\beta_{42}$ with thickness changes less than 1 Å. However, Fig. S6 reveals that the POPC, POPG and DPPC thicknesses around A$\beta_{42}$ are decreased in order to improve the hydrophobic matching between bilayer and A$\beta_{42}$, whose hydrophobic width is smaller than those of the lipids (i.e., negative hydrophobic mismatch). The three bilayers studied exhibit a similar thickness of about 25–30 Å in the neighborhood of the peptide, which corresponds to the hydrophobic width of the latter for both $\beta$-sheet and helical structures. This implies that the thinner region close to A$\beta_{42}$ is compensated by an increase in thickness further away from the peptide [49,78] as evidenced by Figs. S6 and S7. This effect is most pronounced for DPPC, for which we observe P–P distances reaching up to 50 Å (Fig. S6), corresponding to an increase of average thickness by 3–4.5 Å, when compared to the peptide-free bilayer.

An increased bilayer thickness results from increased lipid chain order. We therefore calculated the order parameter $S_{CD}$ of acyl chain 1 (sn-1) separately for the POPC, DPPC and POPG lipids within 5 Å of A$\beta_{42}$, and for the lipids, which are more than 5 Å away from A$\beta_{42}$. We chose sn-1 because this acyl chain is identical for POPC, DPPC and POPG guaranteeing comparability. The results of this analysis are shown in Fig. 3. For comparison we also present $S_{CD}$ of sn-1 of the pure POPC, DPPC and POPG bilayers obtained from 100 ns MD runs of the peptide-free lipid bilayers. The lipid order is generally decreased around the peptide as the corresponding $S_{CD}$ value is smaller than the one for the peptide-free bilayer, while lipid order is increased for the lipids further away from the peptide. This effect is most pronounced for A$\beta_{42}$ in DPPC, which is in agreement with the marked increase of the DPPC bilayer thickness with increasing

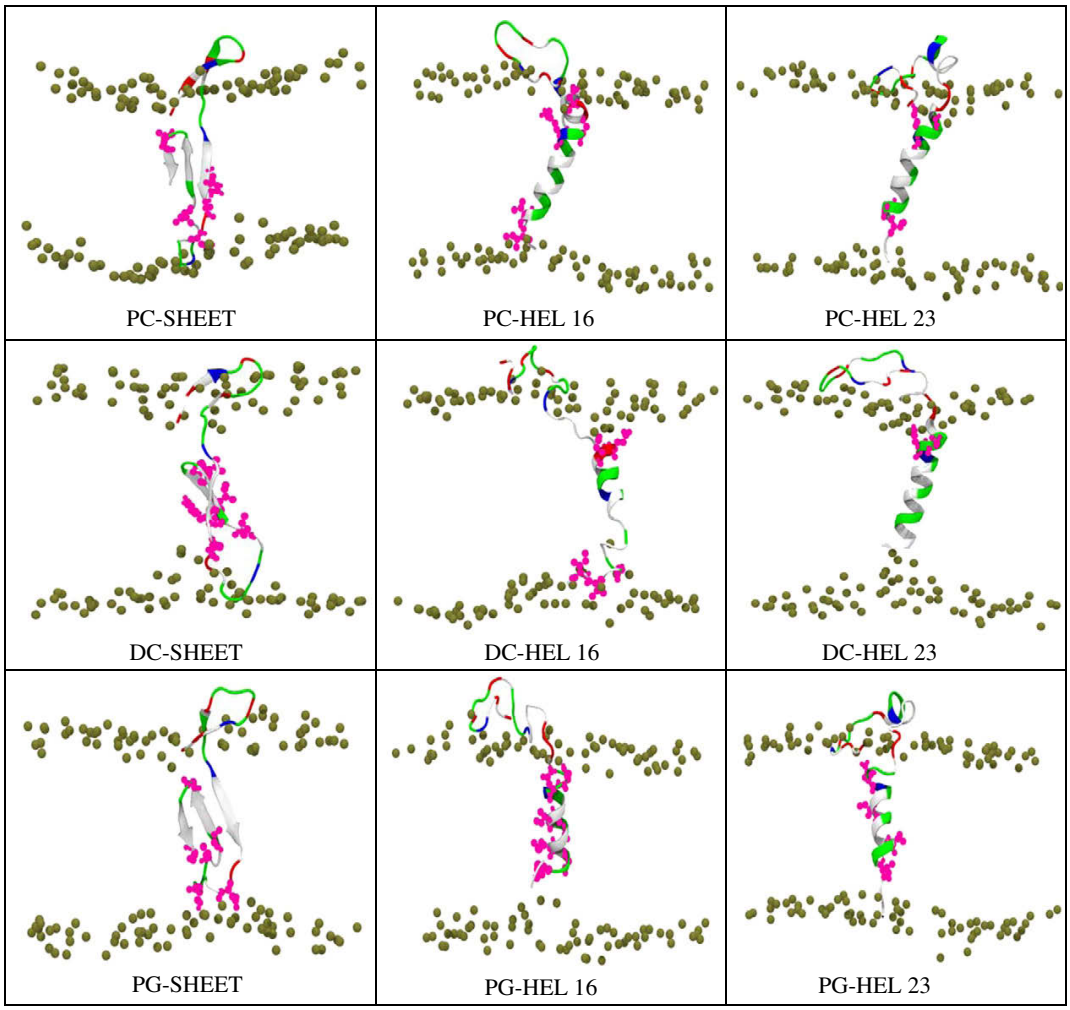


**Fig. 2.** Final states after 500 ns MD simulations of A$\beta_{42}$ in POPC (PC), DPPC (DC) and POPG (PG) bilayers. For coloring explanation see Fig. 1. Peptide residues marked with pink spheres are involved in H-bond formation with water molecules entering the bilayer.

distance to the peptide. This behavior can be explained by the saturated acyl chains, which are less able to adapt to the peptide than lipids with unsaturated chains [78]. SHEET and HEL-23 inflict the largest ordering effect on DPPC with HEL-23 already increasing the lipid order for the lipids within 5 Å of A$\beta_{42}$. The corresponding plot of the bilayer thickness (Fig. S6) shows that only the lipids very close to HEL-23 are markedly disordered. In POPC the (dis)ordering effect of A$\beta_{42}$ on the lipids is smallest. Only for the middle section of the sn-1 chain in POPC, which is close to the double bond of the unsaturated sn-2 acyl chain, the lipid tail order is increased for the lipids greater than 5 Å away from the peptide. In POPG the disordering effect for lipids within 5 Å of the peptide is more pronounced than in POPC, which is due to the repulsive interactions between the negatively charged head groups and the negative charges in the N-terminal part of A$\beta_{42}$. A similar impact on acyl chain order and bilayer thickness was observed for negatively mismatched transmembrane helices [79] and helical A$\beta_{40}$ in a DPPC bilayer [49]. Thus, our simulation results show that A$\beta_{42}$ inserted as monomeric or tetrameric $\beta$-sheet leads to a similar bilayer perturbation as membrane-embedded helical A$\beta_{40}$ [49].

### 3.2. The transmembrane SHEET structure

In the SHEET structure, the negatively charged residues E22 and D23 cause the lipid headgroups of the lower leaflet to be shifted upwards into the hydrophobic core resulting from interactions with the headgroups, thereby facilitating the entry of water molecules from the bottom of the bilayer. Most of these water molecules remain in the vicinity of the charged A$\beta_{42}$ residues within the membrane. However, the water molecules can also form H-bonds with peptide carbonyl and amide groups, which are not involved in intrapeptide H-bonds. The results in Table 1 show that, irrespective of the bilayer type, the SHEET structure forms more H-bonds with water molecules and fewer intrapeptide H-bonds compared to the helical structures under study. Therefore, hydrophobic residues can also interact with water inside the hydrophobic bilayer core via H-bond formation as indicated by the pink spheres in Fig. 2. However, the translocation of water molecules depends on the lipid type, not the number of water molecules crossing the headgroup region. For instance, while there are, on average, 18 and 19 H-bonds between A$\beta_{42}$ and $H_2O$ molecules for

**Table 1**
Effects of Aβ$_{42}$ on lipid bilayers in terms of area per lipid headgroup, bilayer thickness, number of translocated water molecules, number of H-bonds between Aβ$_{42}$ and water in the hydrophobic membrane core, number of H-bonds between peptide carbonyl and amide groups (i.e., intrapeptide H-bonds for for SHEET, HEL-16 and HEL-23; intra- and interpeptide H-bonds for the tetramer), and the motion of the center of mass of Aβ$_{42}$ along the membrane normal with respect to its initial value at the start of the MD run. For the simulations of the pure lipid bilayers, average values were obtained from 100 ns MD simulations starting from bilayers from previous 40 ns MD runs [72]. For the results with Aβ$_{42}$, average values were calculated for the last 400 ns of the 500 ns MD simulations. Only for the water translocation all occurrences during each of the 500 ns MD simulations are reported.

| Aβ$_{42}$ structure | Bilayer | Area per lipid [Å$^2$] | | Bilayer | Translocation | H-bonds | | Aβ$_{42}$ motion along $z$ [Å] |
|---|---|---|---|---|---|---|---|---|
| | | Top leaflet | Bottom leaflet | thickness [Å] | #$H_2O$ | Aβ$_{42}$/$H_2O$ | CO/NH | |
| Peptide-free | POPC | 69.3[a] | 69.3 | 35.1 | 1[b] | n/a | n/a | n/a |
| SHEET | | 62.6 | 63.4 | 35.5 | 1 | 18 | 10 | 2.6 |
| HEL-16 | | 63.4 | 67.5 | 35.4 | 1 | 6 | 12 | 8.9 |
| HEL-23 | | 65.2 | 68.5 | 35.0 | 3 | 3 | 13 | −5.3 |
| Tetramer | | 62.0 | 65.3 | 34.9 | 5 | 95 | 50 | 5.1 |
| Peptide-free | DPPC | 62.3[a] | 62.3 | 37.1 | 4[b] | n/a | n/a | n/a |
| SHEET | | 53.7 | 54.5 | 41.5 | 20 | 19 | 9 | −0.5 |
| HEL-16 | | 50.9 | 56.6 | 40.3 | 16 | 18 | 10 | 4.6 |
| HEL-23 | | 51.8 | 57.1 | 41.6 | 13 | 2 | 14 | 1.9 |
| Peptide-free | POPG | 70.0[a] | 70.0 | 34.8 | 1[b] | n/a | n/a | n/a |
| SHEET | | 69.3 | 69.3 | 34.5 | 2 | 13 | 8 | −3.7 |
| HEL-16 | | 64.0 | 69.7 | 34.3 | 1 | 9 | 10 | 9.0 |
| HEL-23 | | 64.0 | 68.7 | 34.5 | 1 | 9 | 10 | −6.4 |

[a] The experimental values for the area per lipids of the peptide-free bilayers are: POPC, 68.3 Å$^2$ [92]; DPPC, 64.0 Å$^2$ [93]; and POPG, 67.3 Å$^2$ [94].
[b] The number of $H_2O$ molecules passing the peptide-free bilayers was obtained from 100 ns MD simulations while those involving Aβ$_{42}$ from 500 ns MD simulations.

SHEET in POPC and DPPC, respectively, only one water molecule is able to cross the POPC bilayer. This is far less than the 20 water molecules translocating through the DPPC bilayer within the 500 ns simulation.

Depending on the lipid type, we observe almost none to minor loss of β-strands in the hydrophobic core of the bilayer (Figs. 2 and S1–S3). We find the SHEET structure to be most stable in POPC and least stable in DPPC. In the three simulations of SHEET in POPC, the largest change we observed was a slight upward motion of the whole peptide by 2 to 3 Å. In order to analyze how much the salt bridge between D23 and K28 helps stabilize the transmembrane SHEET, we calculated the distance between the anionic carboxylate of either E22 or D23 and the cationic ammonium from K28 (Fig. S8). In none of the bilayers a salt bridge between E22 and K28 exists. It can be seen that a salt bridge between D23 and K28 is formed only in POPC, while in DPPC and POPG this salt bridge is not present. This observation correlates well with the high SHEET stability observed in POPC. In the DPPC simulation the SHEET structure becomes unstable because of the missing salt bridge leading to a widening of the turn between residues 23 and 29. Instead, E22 and D23 interact with the headgroups of the lower leaflet, leading to further destabilization of the SHEET structure in DPPC: the peptide unfolds from β-sheet to coil and bend structures, except for residues L17–F20, L34–V36, V40 and I41. In DPPC the SHEET structure hardly moved along the membrane normal (see Table 1). In the simulation with POPG, we observe a transient loss of β-sheet to coil from residues L17 to A21, and from sheet-turn-sheet to sheet-bend-coil for residues G33 to I41 during the initial 170 ns of the MD run. However, for the remainder of the MD simulation the β-sheet has reformed and is considerably stable despite the missing D23–K28 salt bridge. Due to electrostatic repulsion between the negatively charged N-terminal Aβ$_{42}$ part and the negatively charged headgroup region, the peptide was pushed deeper into the membrane by about 3.7 Å.

### 3.3. Helical Aβ$_{42}$ with K16 at the membrane–water interface (HEL-16)

The simulations of HEL-16 were performed for comparison with the SHEET structure, which has K16 at the membrane–water interface. A key finding for HEL-16 in POPC and POPG is that the peptide moves considerably upwards, i.e., by 8.9 Å and 9.0 Å respectively. This vertical motion is driven by the considerable reduction in free energy when removing the charged residues E22 and D23 from the hydrophobic core [68], leading to the alignment of these two residues with the bilayer–water interface. It thus follows that HEL-16 becomes identical to the HEL-23 conformation in the course of the POPC and POPG simulations. The negative headgroup charge in POPG leads to a stronger influx of water into the membrane as shown by the higher number of H-bonds between Aβ$_{42}$ and $H_2O$ in POPG compared to

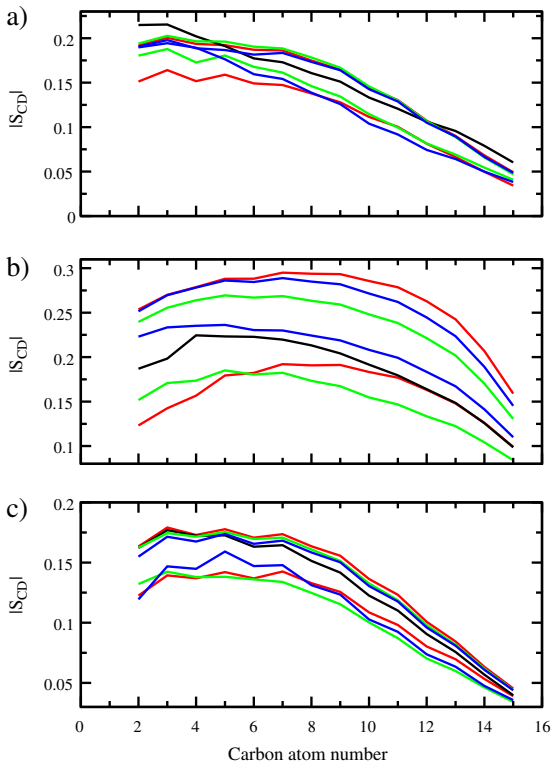


**Fig. 3.** Time-averaged (over the last 400 ns of the MD simulations) order parameter $S_{CD}$ of the sn-1 chain of (a) POPC, (b) DPPC, and (c) POPG lipids. Results are shown for SHEET (red), HEL-16 (green) and HEL-23 (blue) and are distinguished for the lipids within 5 Å of Aβ$_{42}$ (solid) and for the lipids >5 Å away from Aβ$_{42}$ (dashed). For comparison, $S_{CD}$ of the sn-1 chain obtained from 100 ns MD runs of peptide-free lipid bilayers is also presented (black).

POPC (Table 1). However, in both POPC and POPG we find only one $H_2O$ molecule translocating through the membranes in the vicinity of A$\beta_{42}$. In the POPC bilayer, water molecules entering the upper leaflet mainly interact with residues E22–S26 around the headgroup region, whereas water molecules entering the lower leaflet interact with the C-terminal residues G37–A42. Conversion of the $\alpha$-helix to turn structure is found for residues D23–S26, which are inside the membrane in the vicinity of the headgroup region interacting with water. A high stability of the transmembrane helical structure is seen for residues N27–V39, which are well placed within the hydrophobic core. The last three residues, V40–A42, retained their coil structure and caused the lower lipid headgroups to slightly shift upwards.

In POPG only residues K28–G37 of HEL-16 remain $\alpha$-helical, while the other residues adopt coil and turn conformations. We can thus conclude that the helix in POPG is less stable than in POPC, which is confirmed by the fewer intrapeptide H-bonds in POPG (Table 1). Another interesting observation is that HEL-16 in POPC is more strongly tilted with an average tilt angle of 20°, while in POPG the tilt angle is only 13°. This difference cannot be explained by the hydrophobic mismatch between A$\beta_{42}$ and the membranes as (i) the hydrophobic mismatch is the same for POPC and POPG; and (ii) an increased tilt angle is commonly found for positive hydrophobic mismatch between transmembrane helices and lipid bilayers to fully incorporate the hydrophobic peptide residues into bilayers [79]. We therefore conjecture that the different tilt angles observed for HEL-16 in POPC and POPG originate from the different head groups (see Section 3.5).

In case of HEL-16 in a DPPC bilayer, the $\alpha$-helical structure is only stable between residues A21 and A30, whereas the other residues inside the DPPC membrane (K16–F20 and I31–A42) unfold to turn and bend structures (Figs. 2 and S1) leading to fewer intrapeptide H-bonds compared to HEL-16 in POPC. A considerable amount of water molecules is able to enter the hydrophobic bilayer region as evidenced by the large number of H-bonds between A$\beta_{42}$ and $H_2O$ (Table 1). While many of the water molecules remain in the vicinity of the headgroup regions and mainly interact with residues V18–D23 and G37–A42, we observe an increased water flow through the DPPC membrane in the vicinity of HEL-16. During the 500 ns MD simulation, 16 $H_2O$ molecules traversed the bilayer, i.e., four molecules fewer than for SHEET in DPPC but markedly more than for HEL-16 in POPC and POPG. A further difference to the POPC and POPG simulations is that HEL-16 in DPPC does not move upwards leaving E22 and D23 inside the hydrophobic core, which induces helix-to-coil transitions in A$\beta_{42}$.

### 3.4. Helical A$\beta_{42}$ with D23 at the membrane–water interface (HEL-23)

HEL-23 in POPC and POPG bilayers moved downwards by 5.3 Å and 6.4 Å, respectively. This downward motion leaves the negatively charged residues E22 and D23 in the upper headgroup region, but allows a reduced negative mismatch between A$\beta_{42}$ and the bilayers. HEL-23 in DPPC, on the other hand, moves somewhat upwards by 4.6 Å. Here, the lipids around HEL-23 in the lower DPPC leaflet have moved upwards to compensate for the negative hydrophobic mismatch. Nonetheless, the final structures in Fig. 2 show that the vertical location of HEL-23 in POPC, DPPC and POPG is very similar.

The transmembrane $\alpha$-helix of HEL-23 is relatively stable in all three bilayers (albeit to different degrees), whereas the residues outside the membrane lose their helicity in favor of disordered coil and turn conformations. Residues E22 and D23 interact strongly with the headgroups of the upper leaflet, causing headgroup disorder and a reduction of the area per lipid. As for HEL-16, HEL-23 displayed a larger tilt of 23° in POPC and a reduced tilt of only 13° in POPG. In POPC, the helix is stable within the membrane between residues V24–V39, which is also reflected in the relatively high number of 13 intrapeptide H-bonds. Most of the water molecules entering the bilayer interact with the peptide around the headgroup regions and do not penetrate deeply into the hydrophobic core. On average, there are only three H-bonds between A$\beta_{42}$ and $H_2O$ molecules in the POPC bilayer, while three water molecules were observed to cross the POPC bilayer with HEL-23 inserted in it. The comparison between HEL-16 and HEL-23 in POPC shows that both systems behave very similarly after 250 ns, at which time HEL-16 has already moved upwards, positioning E22 and D23 at the membrane–water interface. In the simulation with DPPC, HEL-23 retains its transmembrane $\alpha$-helical structure, which is different from HEL-16 in DPPC, which was not stable. Even the terminal hydrophobic residues I41 and A42 fold from coil to $\alpha$-helix in HEL-23, adding further to the stability of this structure. The high $\alpha$-helical stability leads to 14 intrapeptide H-bonds and only two A$\beta_{42}$–$H_2O$ H-bonds in the DPPC bilayer. It should be noted that the helix in HEL-23 in DPPC was stable despite the elevated simulation temperature of 325 K necessary in the DPPC simulations, compared with 298 K in the POPC and POPG simulations.

As for SHEET and HEL-16 in DPPC we also observe considerable water flow across the membrane for HEL-23 in DPPC though the translocation is somewhat reduced compared with the other two cases (i.e., 13 $H_2O$ molecules versus 20 and 16, respectively). Our simulations of HEL-23 in POPG revealed a loss of the $\alpha$-helix from residues L17 to N27, which instead adopt coil and turn conformations leading to only 10 intrapeptide H-bonds. On the investigated timescale, the $\alpha$-helix is stable between residues K28 and G38. The last three residues extend to a coil structure reaching the bottom membrane surface, thereby disordering adjacent headgroups. Like in POPC, HEL-16 and HEL-23 behave very similarly in POPG after HEL-16 has moved upwards, bringing E22 and D23 in the headgroup area. This behavior includes stability, H-bond formation, water translocation and peptide tilt.

### 3.5. Mixed POPC/POPG bilayer simulations of HEL-23

To better understand the influence of the lipid type on the helical structures in POPC and POPG, we performed two more 100 ns MD simulations of HEL-23 in mixed POPC/POPG bilayers with asymmetric lipid distribution. The simulation of HEL-23 is also representative of HEL-16 as the latter becomes HEL-23 in POPC and POPG. The asymmetric lipid distribution was chosen such that in one simulation the upper leaflet was composed of only POPG lipids and the lower leaflet of only POPC lipids, while in the other simulation it was the other way round, i.e., POPC in the upper and POPG in the lower leaflet. The helical structure was preinserted with D23 at the membrane–water interface (HEL-23). The final structures after 100 ns of MD simulations are shown in Fig. 4a and b. The comparison of the POPC/POPG and POPG/POPC (here the order of the lipids refers to the upper and lower leaflets) results emphasizes the destabilizing effect of the anionic headgroups on the helix, when POPG is in the upper leaflet (Fig. 4b). In this region the helical structure is lost up to residue 26 in favor of coil structures, while the helix is stable between residues 15 and 38 in POPC/POPG. Residues 37 to 42 are in different coil conformations in the POPC/POPG and POPG/POPC simulations. These findings are in agreement with the results for POPC and POPG simulations, which also revealed a destabilizing effect of the lower headgroups on the vicinal helical A$\beta_{42}$ residues. In both POPC/POPG and POPG/POPC A$\beta_{42}$ is tilted by on average 23°, which is different to the smaller tilt in the POPG bilayer.

To better understand why HEL-23 (and HEL-16) stability and tilt angle differ in POPC and POPG, we looked more closely at the interactions of A$\beta_{42}$ with adjacent lipids. Fig. 4c and d shows the final state of HEL-23 with the lipid and water molecules within 5 Å of the peptide for the POPC and POPG simulations, respectively. It is immediately obvious that more lipid molecules are in the direct neighborhood of A$\beta_{42}$ in POPC than in POPG. The reduced lipid density in POPG, which is a result of electrostatic repulsion between the POPG headgroups, allows A$\beta_{42}$ more orientational freedom inside the membrane. It can be seen that the POPC lipids around A$\beta_{42}$ are more ordered than the POPG lipids, which is supported by our findings from the order parameter analysis

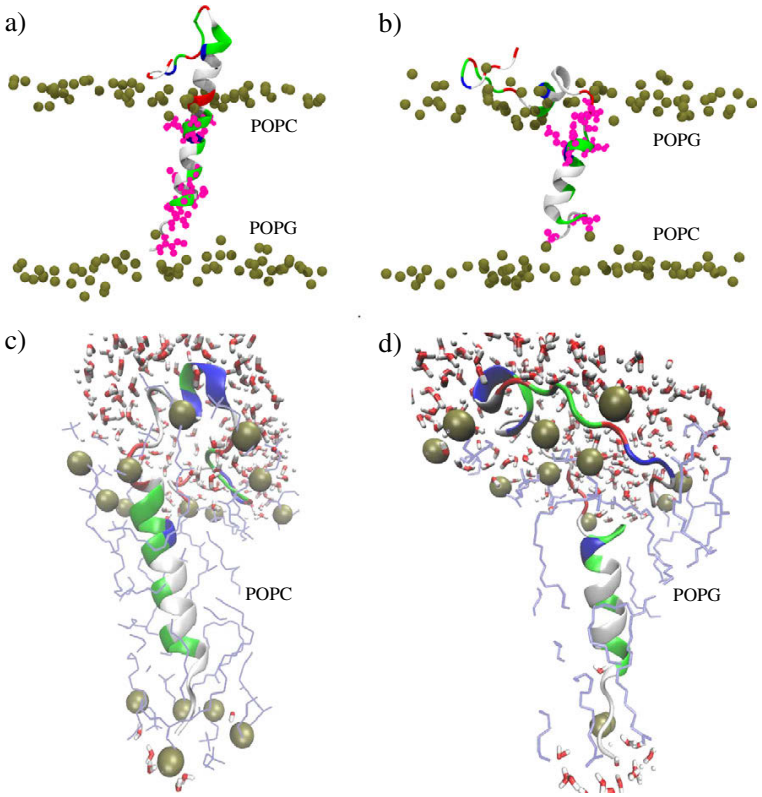


**Fig. 4.** Panels (a) and (b) show the final states after 100 ns MD simulations of HEL-23 in mixed POPC/POPG and POPG/POPC bilayers, respectively. Here, the order of the lipid type refers to the upper/lower leaflet. For coloring explanation see Fig. 1. Panels (c) and (d) show a close-up of the final states after 500 ns MD simulations of HEL-23 in POPC and POPG, respectively. The lipids (Van der Waals spheres in tan for phosphorus atoms, light-blue lines for lipid tails) and water molecules (licorice representation with red for oxygen atoms and white for hydrogen atoms) are shown within 5 Å of A$\beta_{42}$. For coloring explanation for A$\beta_{42}$ see Fig. 1.

in Fig. 3. The POPC lipid order seems to inflict a tilt on HEL-23 in POPC. The reduced lipid density around A$\beta_{42}$ in POPG allows more water molecules to enter the hydrophobic core, which induce helix-to-coil transitions in residues D23 to N27. The same happens in the lower POPG leaflet where one $H_2O$ molecule interacts with V39 (Fig. 4d), thereby destroying the helical structure for this residue, while the helix for V39 in HEL-23 in POPC remains intact (Fig. 4c). Therefore, we can conclude that the reduced lipid density and increased lipid disorder around helical A$\beta_{42}$ in POPG, inducing water influx into the hydrophobic core, are responsible for the smaller tilt angle and larger structural instability of HEL-23 in POPG. Aside, it should be noted that in both POPC and POPG simulations a $\pi$-helix is sampled in the N-terminal region between V13 and K16, i.e., this helix seems to be a stable structural element for A$\beta$ adsorbed to the membrane surface [51,55].

The asymmetric bilayer composition leads to increased water permeation: within the two 100 ns MD simulations we observed two and one $H_2O$ molecules traverse the POPC/POPG and POPG/POPC bilayers, respectively. On a 500 ns time scale this corresponds to on average 10 and 5 $H_2O$ molecules, respectively. The increased water permeation in comparison to the symmetric one-component POPC and POPG bilayers can be explained by a nonzero net dipole moment of the asymmetric bilayers [80,81]. This asymmetry also seems to induce directional water flow from POPG to POPC, as observed for three traversing events of water molecules through the bilayers. However, it should be noted that this effect needs to be tested on a longer time scale. In general, the electrostatic potential of cell membranes is crucial for numerous membrane-mediated biological phenomena, such as the activation of voltage-gated membrane proteins, conductance of ionic channels, binding of therapeutic solutes to membranes, and trafficking across cell membranes [82].

### 3.6. The transmembrane $\beta$-sheet tetramer

Our motivation for studying the transmembrane $\beta$-sheet tetramer was to test whether it is more stable than the single transmembrane $\beta$-sheet and could thus serve as building block for a pore composed of several A$\beta_{42}$ $\beta$-sheet oligomers [37–39,46]. Furthermore, we wanted to investigate whether the A$\beta_{42}$ tetramer is able to disturb the lipid bilayer sufficiently in order to allow increased water translocation and ion passage through the membrane as found experimentally [26]. We performed the simulation for the $\beta$-sheet tetramer only in a POPC bilayer as the monomeric SHEET structure was most stable in this bilayer type. The final structure of this 500 ns MD simulation is shown in Fig. 5.

We observe that, unlike in the monomeric SHEET, the N-terminal $\beta$-hairpins are stable in the tetramer (see DSSP plot in Fig. S4). They interact with each other rather than with the bilayer surface, causing the N-terminal regions to stick out into the water instead of being adsorbed to the bilayer surface, as we observed for all monomeric transmembrane A$\beta_{42}$ structures. Along with the overall negative charge of the N-terminal

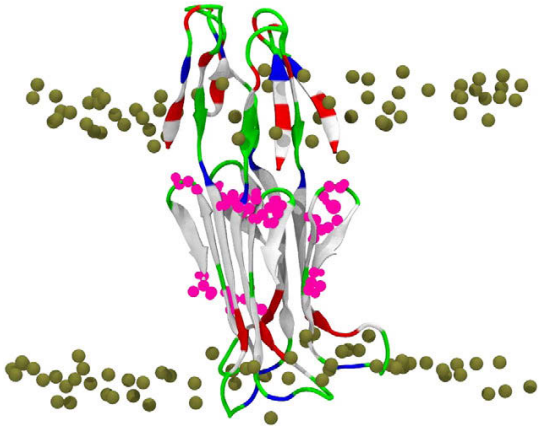

**Fig. 5.** Final state of the 500 ns MD simulation of the A$\beta_{42}$ $\beta$-sheet tetramer in a POPC bilayer. For coloring explanation see Fig. 1.

half of the peptide, this structure might thus act as a funnel for cations to be inserted into the membrane in larger A$\beta$ assemblies composed of our tetramer model [83]. The transmembrane $\beta$-strands were more stable throughout the simulations compared to the $\beta$-sheet monomer, which is also reflected in the increased number of intra- and interpeptide H-bonds per peptide, when compared to SHEET in POPC. The increased stability, resulting from favorable interpeptide interactions [46], leads to a decrease in peptide–lipid interactions as Fig. S9 supports. Water molecules enter the membrane in the upper and lower leaflets, and mainly interact with the negatively charged residues E22 and D23 around the lower lipid headgroup region and with polar residues near the upper headgroup region. Table 1 shows that, on average, there are 95 H-bonds between A$\beta_{42}$ and water within the membrane, i.e., around 24 H-bonds per peptide. The tetramer thus allows more water to enter the POPC bilayer than the monomeric SHEET. It also leads to an increased membrane translocation when compared to monomeric A$\beta_{42}$ in POPC, as five $H_2O$ molecules were found to cross the bilayer within the 500 ns simulation.

From the last observation we can conclude that increased permeabilization of lipid bilayers due to A$\beta$ can only result from transmembrane A$\beta$ oligomers and not monomers, which is in agreement with experimental findings [26]. In the study by Glabe and coworkers it is further reported that A$\beta_{42}$ oligomers increase the conductance of lipid bilayers, with the increase in conductivity being proportional to the concentration of oligomers [26]. They do not find any evidence for pore formation or ion selective conductance. Instead, soluble oligomers appear to enhance the ability of ions to move through the lipid bilayer on their own. While we have not observed the translocation of ions in our simulations, steady water permeation is a prerequisite for ions crossing the lipid bilayer through protein-facilitated diffusion. Hence, the $\beta$-sheet tetramer in our study is still too small or of the wrong conformation, as steady water flow could not be observed. The structure and size of the smallest A$\beta$ oligomer facilitating the conductance of lipid bilayers remain to be elucidated. However, to our knowledge, our simulation study is the first one to address the permeabilization of lipid bilayers resulting from A$\beta_{42}$, employing a rigorous bottom-up approach (see Section 3.8). Previous simulations of membrane-embedded A$\beta$ monomers report the entry of water molecules into the bilayer and interacting with charged residues in the C-terminal segment of the peptide, yet no water passage across the membrane was mentioned [48]. Nussinov and coworkers, on the other hand, used a top-down approach by constructing annular channels guided by NMR data for A$\beta$ fibrils [62,63] and studied the stability and conductivity of such channels using MD [37–45].

### 3.7. Comparison of transmembrane A$\beta_{42}$ in POPC, DPPC and POPG

A$\beta_{42}$ in POPC and POPG bilayers behaved more similarly when compared to A$\beta_{42}$ inserted in a DPPC bilayer. Possible explanations for this result are the larger length and the saturation of the hydrophobic tails in DPPC compared to POPC and POPG, and the higher temperature in the DPPC simulations. However, the anionic headgroup charges of POPG also influence the structural stability by inducing structural transformations to coil conformations in the membrane-inserted A$\beta_{42}$ residues close to the headgroup regions. These findings apply to A$\beta_{42}$ in the SHEET, HEL-16 and HEL-23 configuration. For the SHEET structure, we observed a broadening of the $\beta$-hairpin towards a U-shaped $\beta$-strand–loop–$\beta$-strand motif, which is in agreement with previous computational [37,38,66] and experimental [62,63] models. However, it should be noted that this structural model was found for the fibril. It remains to be demonstrated by means of experimental structure determination that the $\beta$-strand–loop–$\beta$-strand motif is also present in membranes [26]. A$\beta_{42}$ inserted into a POPC bilayer as a $\beta$-sheet or helix is relatively stable within the membrane core, which is supported by experimental results demonstrating that A$\beta_{42}$ remains well embedded in the lipid environment composed of POPC or POPC/SM/Chol [25]. The stable $\beta$ structure seen in our simulations is also in agreement with experimental work, finding that A$\beta_{40}$ is present as a $\beta$-sheet in a POPC bilayer [28]. Also, for A$\beta_{42}$, the $\beta$ state in the membrane hydrophobic core of a POPC/POPS mixed bilayer could be identified to be destabilizing the membrane by increasing its permeability [27]. The formation of $\beta$-sheet between two peptides was also reported in a recent simulation study probing the self-assembly of A$\beta$ in a mixed DPPC/cholesterol bilayer [59]. We observed the highest transmembrane stability for the $\beta$-sheet tetramer, which is supported by experimental work reporting that A$\beta_{42}$ forms stable tetramers within membranes [29].

The simulations with DPPC resulted in a more pronounced loss of secondary structure for both SHEET and HEL-16 conformations within the membrane core as compared to the corresponding POPC and POPG simulations. In addition to a larger hydrophobic mismatch, the higher simulation temperature in the MD simulations with DPPC may also add to more fluctuations in the peptide. The HEL-23 conformation, however, adopts a stable $\alpha$-helix inside the membrane. Our findings for the helical structures inserted in a DPPC bilayer are different than those obtained from MD simulations by Xu et al. [54]. They inserted the helical structure with K28 at the DPPC membrane–water interface and observed that A$\beta_{40}$ left the hydrophobic core in less than 100 ns associating with the bilayer surface, where it remained $\alpha$-helical. These discrepancies may be due to any or all of the following: (i) the missing two hydrophobic residues I41 and A42 in A$\beta_{40}$, (ii) the different initial insertion depths, (iii) usage of different force fields, and (iv) different protocols employed to insert the peptide into the membrane [48]. Other MD simulations with A$\beta_{40}$ in a DPPC bilayer reported that the peptide remained partially embedded in the bilayer when it was inserted with K28 at the membrane–water interface [48]. Moreover, a complete loss of helicity was observed within the first 10 ns of these simulations. When A$\beta_{40}$ was inserted with K16 at the interface, the peptide remained embedded in the bilayer and retained its $\alpha$-helicity in the central segment [48], which is in agreement with our results.

The variety of simulation results points to the possibility that none of the MD simulations performed so far [48,54] fully describes the equilibrium configurational distribution of the peptides and membranes. This conclusion also includes our simulations, even though our simulations were performed on a 500 ns time scale. On much longer timescales—probably beyond microsecond timescales—major configurational changes and membrane translocation of A$\beta$ could take place. Studying these processes is prohibitively expensive using

all-atom MD simulations, requiring coarse-grained and/or advanced sampling techniques instead.

### 3.8. Water permeation

Strong interactions between the A$\beta_{42}$ peptide and lipids give rise to both disordering of the lipid headgroup arrangement and tilt of the lipids around the peptide. This tilt allows entry of water molecules into the hydrophobic membrane core, where they can form H-bonds with polar and non-polar A$\beta_{42}$ residues. Some of these water molecules manage to cross to the other side of the lipid bilayers. Here, we observe the largest number of translocation events in the DPPC simulations (see Table 1). Among the POPC and POPG simulations we find the largest membrane permeability for the $\beta$-sheet tetramer in POPC, which is, however, not increased compared to the peptide-free bilayers. In the 100 ns MD runs of peptide-free lipid bilayers, we observed one permeating $H_2O$ molecule for both POPC and POPG, while four water molecules translocated through the DPPC bilayer. It thus follows that the investigated A$\beta_{42}$ structures do not increase the water translocation compared with the lipid-only bilayers; in some cases the presence of transmembrane A$\beta_{42}$ even diminishes this process. There was no penetration and translocation of ions in any of the simulated systems.

In order to understand the different water permeabilities in the different bilayers, we have to consider the diffusion of water across the membranes and the interactions between transmembrane $H_2O$ molecules and A$\beta_{42}$. In general, water molecules cross lipid membranes by two pathways, which one calls the lipid pathway and the water channel pathway. The lipid pathway refers to water crossing the lipid bilayer by diffusion while the water channel pathway results from membrane proteins, which provide an aqueous channel through which water can pass. In the latter case the water flux is very high and cannot be accounted for by water diffusion across lipid barriers. The water permeability for the lipid pathway can be approximated by a 3-slab model, where the inverse of the permeability $P$ is equal to the sum of the two headgroup resistances and the hydrocarbon resistance [84]:

$$\frac{1}{P} = \frac{2}{P_h} + \frac{1}{P_c} \ . \tag{2}$$

Here, $P_h$ is the permeability through the headgroup region and $P_c$ is the permeability through the hydrocarbon core. For simplicity, $P_c$ is assumed to have the form for a homogeneous hydrocarbon slab of thickness $\Delta_c$ [84]:

$$P_c = \frac{KD_c}{\Delta_c} \ , \tag{3}$$

where $K$ is the partition coefficient of water into the hydrocarbon slab and $D_c$ is the coefficient of diffusion of water within the hydrocarbon region. The 3-slab model assumes that the headgroups act as a partial barrier for entry of water into the hydrocarbon region. To account for the fractional area that is open to the entry of water molecules, a structural factor given by $(A-A_0)/A$ is used, where $A_0$ is the headgroup barrier area at which the permeability approximates to zero. Then, the theory states: [84]

$$P_h = \left(\frac{KD_h}{\Delta_h}\right)\left(\frac{A-A_0}{A}\right), \tag{4}$$

where $K$ is again the same partition coefficient, $D_h$ is the effective coefficient of diffusion in the headgroup region and $\Delta_h$ is its thickness. Eq. (4) shows that the permeability increases with increasing area per lipid, which corresponds to decreasing lipid chain order.

Since the headgroups are identical for POPC and DPPC, $\Delta_h$ and $A_0$ are the same for both lipids. However, the water diffusion depends on the actual temperature, thus $D_h$ will be different in the DPPC and POPC simulations. In order for the theory to predict a larger $P$ for DPPC at 325 K than for POPC at 298 K, Eqs. (2) to (4) require (i) a larger $K$ and/or (ii) larger $D_h$ and $D_c$ to compensate for the effects of the larger thickness $\Delta_c$ and smaller $A$ of DPPC. Measurements by Schatzberg showed that for *n*-hexadecane the water solubility increases 2.3-fold by increasing the temperature from 298 K to 318 K [85]. At 325 K we expect the increase of $K$ to be even more pronounced. Turning to the effect of water diffusion in the hydrocarbon chain region, measurements of the diffusion of water through hydrocarbon liquids showed that $D_c$ increases by a factor of 1.44 in *n*-hexadecane when the temperature is increased from 298 K to 318 K [85]. For the self-diffusion of water in water, denoted $D_w$, the following temperature dependence was found [86]:

$$D_w(T) = D_w(298) + 0.06 \times 10^{-9} \mathrm{m^2\ s^{-1}\ K^{-1}} (T-298) \ , \tag{5}$$

with the diffusion of water in water at 298 K being $D_w(298) = 4.3\times10^{-9}\mathrm{m^2\ s^{-1}}$ for the SPC water model [87]. It follows that $D_w(325)$ is $5.92\times10^{-9}\mathrm{m^2\ s^{-1}}$, which is about 1.38 times higher than $D_w(298)$. One can thus assume that the rate of water diffusion in the headgroup regions is also about a 1.4 times higher at 325 K compared to 298 K.

The increased water permeation seen in our DPPC simulations is therefore a composite effect of increased water diffusion resulting from the increased simulation temperature of 325 K, and the larger partition coefficient of water in DPPC compared to POPC near the headgroup regions resulting from the reduced lipid order in the vicinity of A$\beta_{42}$. To test this conclusion we performed a 100 ns simulation of SHEET in POPC at 325 K. In this short time 14 $H_2O$ molecules were able to pass the membrane. To a large degree this markedly increased water permeability is due to an increased water partition coefficient $K$ for POPC at 325 K, as this temperature is well above the transition from the gel to liquid phase for this lipid type. It has been shown that the permeability of (poly)unsaturated PC lipids rises exponentially with increase in reduced temperature $(T-T_m)/T_m$, where $T_m$ is the gel-to-liquid crystalline phase transition temperature [88].

The above reasoning allows explaining the increased membrane permeation of DPPC compared to POPC and POPG bilayers. However, the water translocation in our simulations is further complicated by interactions of the water molecules entering the lipid bilayers with the inserted A$\beta_{42}$ peptide. To illustrate this process, snapshots of a water molecule crossing the POPC bilayer at 298 K in the vicinity of the SHEET structure are shown in Fig. 6. The whole translocation process takes about 12 ns. Most of the time the water molecule spends in the hydrophobic core interacting, via H-bond formation, either with the polar residue G31 or with residue V40, which is close to the polar residues G37 and G38, and the negatively charged C-terminus. These interactions induce a decelerated translocation process compared to the peptide-free bilayers, where the membrane passage of water is generally faster; in some cases it is even by a factor of twenty faster. A more detailed analysis of the translocation times can be found in the Supporting material.

It should finally be noted that the above discussion of water permeation is based on the use of non-polarizable force fields, which leads to an increase of $\approx$1 kcal mol$^{-1}$ of the free-energy barrier for transfer of a water molecule from bulk to the interior of a 1,2-dimyristoyl-sn-glycero-3-phosphatidylcholine (DMPC) bilayer compared to when polarizable models for DMPC and water are employed [89]. The reduced free-energy barrier computed with the latter force field (4.5–5.5 kcal mol$^{-1}$) results from the decrease of the average water dipole moment from 2.6 D in bulk to 1.88 D in membrane interior, which is, compared to experiment, correctly predicted by the polarizable water model. However, since non-polarizable force fields were used in all our simulations, the findings of our water permeation analysis should not be affected.

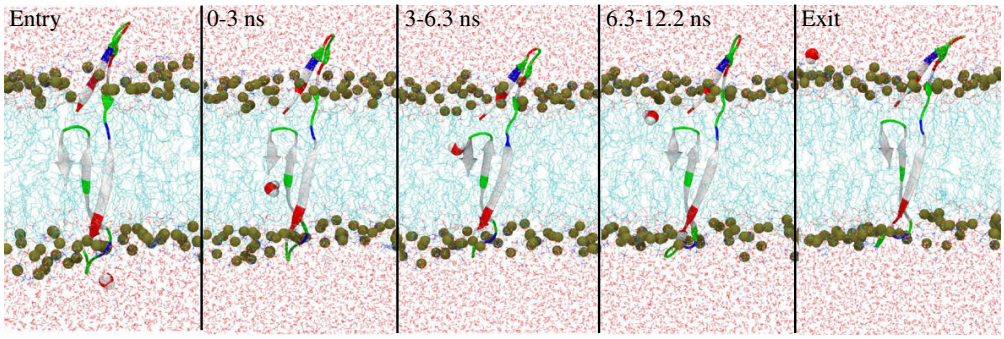


**Fig. 6.** Five snapshots depicting the process of water permeating through a POPC bilayer with an inserted $A\beta_{42}$ peptide in the SHEET structure.

## 4. Conclusions

Association of $A\beta$ with neuronal cell membranes and resulting neuronal toxicity is a well known AD hypothesis [90] with $A\beta$ exerting its cytotoxic effect by increasing membrane fluidity [24]. Previously, it was reported that permeabilization of membranes was caused by $A\beta$ oligomers [26], but later it was shown that the $A\beta_{42}$ monomer can also intercalate the membrane and alter its properties [25]. There is increasing evidence that $A\beta$ adopts a $\beta$ conformation in the membrane [27,28], yet an experimental atomistic model of membrane-bound $A\beta$ is still lacking. Molecular simulations offer the potential of predicting such structures [46,83,91], and, in addition, provide information about conformational transitions of $A\beta$ and it interactions with lipid bilayers. To this end, we performed molecular simulations of transmembrane $A\beta_{42}$ considering both helical and $\beta$-sheet conformations preinserted in POPC, DPPC and POPG bilayers. The MD simulations on the sub-microsecond timescale revealed the highest stability in POPC for both helical and $\beta$-sheet $A\beta_{42}$. Hydrophobic mismatch and lipid order of DPPC, and anionic surface charges of POPG bilayers are responsible for structural instabilities of $A\beta_{42}$ in these bilayers. However, $A\beta_{42}$ remained embedded in the bilayers in all of our MD simulations. The stability of the transmembrane $\beta$-sheet structure can be increased via oligomerization, where favorable interpeptide interactions, especially the formation of interpeptide H-bonds add to the stability of this structure [46].

We observed the translocation of one or more water molecules in the vicinity of the membrane-inserted $A\beta_{42}$. An in-depth analysis of this process revealed that $A\beta_{42}$-mediated water permeation is generally fast (within a few nanoseconds) yet generally slower than in the peptide-free bilayers. It is governed by a number of factors:

1. The lipid type, as it influences the water permeation via the area per lipid and partition coefficient of water.
2. The simulation temperature, as it influences the diffusion of water and solubility of water in the membranes.
3. The $A\beta_{42}$ structure, as the rate limiting step is the membrane permeation in the hydrophobic core due to interactions between $A\beta_{42}$ and the penetrating $H_2O$ molecules.

Compared to the monomeric $A\beta_{42}$ structures in POPC, the $\beta$-sheet tetramer increases the translocation of water through the POPC bilayers. This finding allows us to conclude that membrane permeabilization by membrane-bound $A\beta$ must be due to $A\beta$ oligomers, which is in agreement with experimental findings [26].

Our simulation studies were performed with model lipid bilayers composed of only one or two lipid types. Studying the behavior of $A\beta$ in a more complex, neuronal membrane mimicking model bilayer would certainly help the understanding of the pathogenicity underlying AD [50,58,59]. Furthermore, the length and time scales of the simulations need to be extended in order to study the $A\beta$ membrane association and its effect on membrane maintenance. Experimental work focused on resolving the structure of $A\beta$ in and on lipid membranes would assist in modeling the molecular events leading to AD.

## Acknowledgements

CP and BS gratefully acknowledge the Jülich Supercomputing Centre for providing and maintaining the computing resources used in this work (Computing time grant JISB32). Work at the University of Hertfordshire made use of the Science and Technology Research Institute high-performance computing facility. We thank Kenneth L. Osborne for proofreading the manuscript.

## Appendix A. Supplementary data

Supplementary data to this article can be found online at http://dx.doi.org/10.1016/j.bbamem.2012.09.001.

## References

[1] D.J. Selkoe, The origins of Alzheimer disease — a is for amyloid, J. Am. Med. Assoc. 283 (2000) 1615–1617.
[2] E.D. Roberson, L. Mucke, 100 years and counting: prospects for defeating Alzheimer's disease, Science 314 (2006) 781–784.
[3] G. Thinakaran, E.H. Koo, Amyloid precursor protein trafficking, processing, and function, J. Biol. Chem. 283 (2008) 29615–29619.
[4] J.T. Jarrett, E.P. Berger, P.T. Lansbury, The carboxy terminus of the beta-amyloid protein is critical for the seeding of amyloid formation - implications for the pathogenesis of Alzheimers-disease, Biochemistry 32 (1993) 4693–4697.
[5] S.G. Younkin, The role of A beta 42 in Alzheimer's disease, J. Physiol. Paris 92 (1998) 289–292.
[6] A. Mohamed, E.P. de Chaves, A internalization by neurons and glia, Int. J. Alzheimers Dis. 2011 (2011) 127984.
[7] T.L. Williams, L.C. Serpell, Membrane and surface interactions of Alzheimers $A\beta$ peptide — insights into the mechanism of cytotoxicity, FEBS J. 278 (2011) 17.
[8] S.M. Butterfield, H.A. Lashuel, Amyloidogenic protein-membrane interactions: mechanistic insight from model systems, Angew. Chem. Int. Ed. Engl. 49 (2010) 5628–5654.
[9] E. Terzi, G. Holzemann, J. Seelig, Interaction of Alzheimer beta-amyloid peptide(1–40) with lipid membranes, Biochemistry 36 (1997) 14845–14852.
[10] A. Buchsteiner, T. Hauss, S. Dante, N.A. Dencher, Alzheimer's disease amyloid-beta peptide analogue alters the ps-dynamics of phospholipid membranes, Biochim. Biophys. Acta 1798 (2010) 1969–1976.
[11] G.P. Eckert, W.G. Wood, W.E. Mueller, Lipid membranes and beta-amyloid: a harmful connection, Curr. Protein Pept. Sci. 11 (2010) 319–325.
[12] F.J. Sepulveda, J. Parodi, R.W. Peoples, C. Opazo, L.G. Aguayo, Synaptotoxicity of Alzheimer beta amyloid can be explained by its membrane perforating property, PLoS One 5 (2010).
[13] M.P. Mattson, B. Cheng, D. Davis, K. Bryant, I. Lieberburg, R.E. Rydel, Beta-amyloid peptides destabilize calicum homeostasis and render human cortical-neurons vulnerable to excitotoxicity, J. Neurosci. 12 (1992) 376–389.
[14] I. Peters, U. Igbavboa, T. Schuett, S. Haidari, U. Hartig, X. Rosello, S. Boettner, E. Copanaki, T. Deller, D. Koegel, W.G. Wood, W.E. Mueller, G.P. Eckert, The interaction of beta-amyloid protein with cellular membranes stimulates its own production, Biochim. Biophys. Acta 1788 (2009) 964–972.
[15] E. Terzi, G. Hölzemann, J. Seelig, Interaction of Alzheimer-amyloid peptide(1–40) with lipid membranes, Biochemistry 36 (1997) 14845–14852.
[16] C. Ege, K. Lee, Insertion of Alzheimer's abeta 40 peptide into lipid monolayers, Biophys. J. 87 (2004) 1732–1740.

[17] E. Terzi, G. Holzemann, J. Seelig, Alzheimer beta-amyloid peptide 25–35: electrostatic interactions with phospholipid membranes, Biochemistry 33 (1994) 7434–7441.
[18] J. McLaurin, A. Chakrabartty, Characterization of the interactions of Alzheimer β-amyloid peptides with phospholipid membranes, Eur. J. Biochem. 245 (1997) 355–363.
[19] C. Ege, J. Majewski, G. Wu, K. Kjaer, K. Lee, Templating effect of lipid membranes on Alzheimer's amyloid beta peptide, Chemphyschem 6 (2005) 226–229.
[20] A. Chauhan, I. Ray, V. Chauhan, Interaction of amyloid beta-protein with anionic phospholipids: possible involvement of lys28 and c-terminus aliphatic amino acids, Neurochem. Res. 25 (2000) 423–429.
[21] E.Y. Chi, C. Ege, A. Winans, J. Majewski, G. Wu, K. Kjaer, K.Y.C. Lee, Lipid membrane templates the ordering and induces the fibrillogenesis of Alzheimer's disease amyloid-peptide, Proteins 72 (2008) 1–24.
[22] M. Coles, W. Bicknell, A.A. Watson, D.P. Fairlie, D.J. Craik, Solution structure of amyloid beta-peptide(1–40) in a water-micelle environment. Is the membrane-spanning domain where we think it is? Biochemistry 37 (1998) 11064–11077.
[23] E. Tischer, B. Cordell, Beta-amyloid precursor protein — location of transmembrane domain and specificity of gamma-secretase cleavage, J. Biol. Chem. 271 (1996) 21914–21919.
[24] R.P. Mason, R.F. Jacob, M.F. Walter, P.E. Mason, N.A. Avdulov, S.V. Chochina, U. Igbavboa, W.G. Wood, Distribution and fluidizing action of soluble and aggregated amyloid beta-peptide in rat synaptic plasma membranes, J. Biol. Chem. 274 (1999) 18801–18807.
[25] E.E. Ambroggio, D.H. Kim, F. Separovic, C.J. Barrow, K.J. Barnham, L.A. Bagatolli, G.D. Fidelio, Surface behavior and lipid interaction of Alzheimer beta-amyloid peptide 1–42: a membrane-disrupting peptide, Biophys. J. 88 (2005) 2706–2713.
[26] R. Kayed, Y. Sokolov, B. Edmonds, T.M. McIntire, S.C. Milton, J.E. Hall, C.G. Glabe, Permeabilization of lipid bilayers is a common conformation-dependent activity of soluble amyloid oligomers in protein misfolding diseases, J. Biol. Chem. 279 (2004) 46363–46366.
[27] T.L. Lau, E.E. Ambroggio, D.J. Tew, R. Cappai, C.L. Masters, G.D. Fidelio, K.J. Barnham, F. Separovic, Amyloid-beta peptide disruption of lipid membranes and the effect of metal ions, J. Mol. Biol. 356 (2006) 759–770.
[28] M.R.R. de Planque, V. Raussens, S.A. Contera, D.T.S. Rijkers, R.M.J. Liskamp, J.M. Ruysschaert, J.F. Ryan, F. Separovic, A. Watts, β-sheet structured beta-amyloid(1–40) perturbs phosphatidylcholine model membranes, J. Mol. Biol. 368 (2007) 982–997.
[29] H. Lin, R. Bhatia, R. Lal, Amyloid β protein forms ion channels: implications for Alzheimer's disease pathophysiology, FASEB J. 15 (2001) 2433–2444.
[30] A. Quist, I. Doudevski, H. Lin, R. Azimova, D. Ng, B. Frangione, B. Kagan, J. Ghiso, R. Lal, Amyloid ion channels: a common structural link for protein misfolding disease, Proc. Natl. Acad. Sci. U. S. A. 102 (2005) 10427–10432.
[31] N. Arispe, H. Pollard, E. Rojas, β-amyloid $Ca^{2+}$-channel hypothesis for neuronal death in Alzheimer disease, Mol. Cell. Biochem. 140 (1994) 119–125.
[32] H. Lin, Y. Zhu, R. Lal, Amyloid β protein (1–40) forms calcium-permeable, $Zn^{2+}$-sensitive channel in reconstituted lipid vesicles, Biochemistry 38 (1999) 11189–11196.
[33] S.K. Rhee, A.P. Quist, R. Lal, Amyloid β protein-(1–42) forms calcium-permeable, $Zn^{2+}$-sensitive channel, J. Biol. Chem. 273 (1998) 13379–13382.
[34] Y. Hirakura, M.C. Lin, B.L. Kagan, Alzheimer amyloid $Aβ_{1-42}$ channels: effects of solvent, pH, and congo red, J. Neurosci. Res. 57 (1999) 458–466.
[35] R. Friedman, Aggregation of amyloids in a cellular context: modelling and experiment, Biochem. J. 438 (2011) 415–426.
[36] J.E. Straub, D. Thirumalai, Toward a molecular theory of early and late events in monomer to amyloid fibril formation, Annu. Rev. Phys. Chem. 62 (2011) 437–463.
[37] H. Jang, J. Zheng, R. Lal, R. Nussinov, New structures help the modeling of toxic amyloid beta ion channels, Trends Biochem. Sci. 33 (2008) 91–100.
[38] H. Jang, J. Zheng, R. Nussinov, Models of beta-amyloid ion channels in the membrane suggest that channel formation in the bilayer is a dynamic process, Biophys. J. 93 (2007) 1938–1949.
[39] H. Jang, F.T. Arce, R. Capone, S. Ramachandran, R. Lal, R. Nussinov, Misfolded amyloid ion channels present mobile beta-sheet subunits in contrast to conventional ion channels, Biophys. J. 97 (2009) 3029–3037.
[40] H. Jang, F. Arce, M. Mustata, S. Ramachandran, R. Capone, R. Nussinov, R. Lal, Antimicrobial protegrin-1 forms amyloid-like fibrils with rapid kinetics suggesting a functional link, Biophys. J. 100 (2011) 1775–1783.
[41] R. Capone, M. Mustata, H. Jang, F.T. Arce, R. Nussinov, R. Lal, Antimicrobial protegrin-1 forms ion channels: molecular dynamic simulation, atomic force microscopy, and electrical conductance studies, Biophys. J. 98 (2010) 2644–2652.
[42] R. Capone, H. Jang, S.A. Kotler, B.L. Kagan, R. Nussinov, R. Lal, Probing structural features of Alzheimer's amyloid-beta pores in bilayers using site-specific amino acid substitutions, Biochemistry 51 (2012) 776–785.
[43] F.T. Arce, H. Jang, S. Ramachandran, P.B. Landon, R. Nussinov, R. Lal, Polymorphism of amyloid beta peptide in different environments: implications for membrane insertion and pore formation, Soft Matter 7 (2011) 5267–5273.
[44] R. Capone, H. Jang, S.A. Kotler, L. Connelly, F.T. Arce, S. Ramachandran, B.L. Kagan, R. Nussinov, R. Lal, All-d-enantiomer of β-amyloid peptide forms ion channels in lipid bilayers, J. Chem. Theory Comput. 8 (2012) 1143–1152.
[45] L. Connelly, H. Jang, F.T. Arce, R. Capone, S.A. Kotler, S. Ramachandran, B.L. Kagan, R. Nussinov, R. Lal, Atomic force microscopy and MD simulations reveal pore-like structures of all-d-enantiomer of Alzheimer's β-amyloid peptide: relevance to the ion channel mechanism of ad pathology, J. Phys. Chem. B 116 (2012) 1728–1735.
[46] B. Strodel, J. Lee, C. Whittleston, D. Wales, Transmembrane structures for Alzheimer's $Aβ_{1-42}$ oligomers, J. Am. Chem. Soc. 132 (2010) 13300–13312.
[47] Z. Chang, Y. Luo, Y. Zhang, G. Wei, Interactions of $Aβ_{25-35}$ β-barrel-like oligomers with anionic lipid bilayers and resulting membrane leakage: an all-atom molecular dynamics study, J. Phys. Chem. B 115 (2011) 1165–1174.
[48] J.A. Lemkul, D.R. Bevan, A comparative molecular dynamics analysis of the amyloid beta-peptide in a lipid bilayer, Arch. Biochem. Biophys. 470 (2008) 54–63.
[49] J.A. Lemkul, D.R. Bevan, Perturbation of membranes by the amyloid beta-peptide — a molecular dynamics study, FEBS J. 276 (2009) 3060–3075.
[50] J.A. Lemkul, D.R. Bevan, Lipid composition influences the release of Alzheimer's amyloid beta-peptide from membranes, Protein Sci. 20 (2011) 1530–1545.
[51] C.H. Davis, M.L. Berkowitz, Interaction between amyloid-beta peptide and phospholipid bilayers: a molecular dynamics study, Biophys. J. 96 (2009) 785–797.
[52] C.H. Davis, M.L. Berkowitz, Structure of the amyloid-beta (1–42) monomer absorbed to model phospholipid bilayers: a molecular dynamics study, J. Phys. Chem. B 113 (2009) 14480–14486.
[53] C.H. Davis, M.L. Berkowitz, A molecular dynamics study of the early stages of amyloid-beta(1–42) oligomerization: the role of lipid membranes, Proteins 78 (2010) 2533–2545.
[54] Y.C. Xu, J.J. Shen, X.M. Luo, W.L. Zhu, K.X. Chen, J.P. Ma, H.L. Jiang, Conformational transition of amyloid beta-peptide, Proc. Natl. Acad. Sci. U. S. A. 102 (2005) 5403–5407.
[55] N. Miyashita, J.E. Straub, D. Thirumalai, Structures of β-amyloid peptide 1–40, 1–42, and 1–55—the 672–726 fragment of APP-in a membrane environment with implications for interactions with γ-secretase, J. Am. Chem. Soc. 131 (2009) 17843–17852.
[56] R. Friedman, R. Pellarin, A. Caflisch, Amyloid aggregation on lipid bilayers and its impact on membrane permeability, J. Mol. Biol. 387 (2009) 407–415.
[57] R. Friedman, R. Pellarin, A. Caflisch, Soluble protofibrils as metastable intermediates in simulations of amyloid fibril degradation induced by lipid vesicles, J. Phys. Chem. Lett. 1 (2010) 471–474.
[58] J. Zhao, Q. Wang, G. Liang, J. Zheng, Molecular dynamics simulations of low-ordered Alzheimer beta-amyloid oligomers from dimer to hexamer on self-assembled monolayers, Langmuir 27 (2011) 14876–14887.
[59] L.N. Zhao, S.W. Chiu, J. Benoit, L.Y. Chew, Y. Mu, Amyloid beta peptides aggregation in a mixed membrane bilayer: a molecular dynamics study, J. Phys. Chem. B 115 (2011) 12247–12256.
[60] C.J. Barrow, A. Yasuda, P.T. Kenny, M.G. Zagorski, Solution conformations and aggregational properties of synthetic amyloid β-peptides of Alzheimer's disease: Analysis of circular dichroism spectra, J. Mol. Biol. 225 (1992) 1075–1093.
[61] J.P. Lee, E.R. Stimson, J.R. Ghilardi, P.W. Mantyh, Y.A. Lu, A.M. Felix, W. Llanos, A. Behbin, M. Cummings, $^1$H NMR of Aβ amyloid peptide congeners in water solution. Conformational changes correlate with plaque competence, Biochemistry 34 (1995) 5191–5200.
[62] T. Lührs, C. Ritter, M. Adrian, D. Riek-Loher, B. Bohrmann, H. Döbeli, D. Schubert, R. Riek, 3d structure of Alzheimer's amyloid-β(142) fibrils, Proc. Natl. Acad. Sci. U. S. A. 102 (2005) 17342–17347.
[63] A.T. Petkova, W.M. Yau, R. Tycko, Experimental constraints on quaternary structure in Alzheimer's β-amyloid fibrils, Biochemistry 45 (2006) 498–512.
[64] F. Massi, J.W. Peng, J.P. Lee, J.E. Straub, Simulation study of the structure and dynamics of the Alzheimer's amyloid peptide congener in solution, Biophys. J. 80 (2001) 31–44.
[65] J.E. Straub, J. Guevara, S. Huo, J.P. Lee, Long time dynamic simulations: exploring the folding pathways of an Alzheimer's amyloid Aβ-peptide, Acc. Chem. Res. 35 (2002) 473481.
[66] B. Ma, R. Nussinov, Stabilities and conformations of Alzheimer's β-amyloid peptide oligomers (Aβ(16–22), Aβ(16–35) and Aβ(10–35)): sequence effects, Proc. Natl. Acad. Sci. U. S. A. 99 (2002) 14126–14131.
[67] D.L. Mobley, D.L. Cox, R.R.P. Singh, M.W. Maddox, M.L. Longo, Modeling amyloid beta-peptide insertion into lipid bilayers, Biophys. J. 86 (2004) 3585–3597.
[68] J.L. MacCallum, W.F.D. Bennetta, D.P. Tieleman, Distribution of amino acids in a lipid bilayer from computer simulations, Biophys. J. 94 (2008) 3393–3404.
[69] S. Donnini, F. Tegeler, G. Groenhof, H. Grubmüller, Constant pH molecular dynamics in explicit solvent with λ-dynamics, J. Chem. Theory Comput. 7 (2011) 1962–1978.
[70] B. Hess, C. Kutzner, D. van der Spoel, E. Lindahl, Gromacs 4: algorithms for highly efficient, load-balanced, and scalable molecular simulation, J. Chem. Theory Comput. 4 (2008) 435–447.
[71] C. Oostenbrink, A. Villa, A.E. Mark, W.F.V. Gunsteren, A biomolecular force field based on the free enthalpy of hydration and solvation: the GROMOS force-field parameter sets 53A5 and 53A6, J. Comput. Chem. 25 (2004) 1656–1676.
[72] A. Kukol, Lipid models for united-atom molecular dynamics simulations of proteins, J. Chem. Theory Comput. 5 (2009) 615–626.
[73] O.O. Olubiyi, B. Strodel, Structures of the amyloid β-peptides $Aβ_{1-40}$ and $Aβ_{1-42}$ as influenced by pH and a D-peptide, J. Phys. Chem. B 116 (2012) 3280–3291.
[74] C. Kandt, W.L. Ash, D.P. Tieleman, Setting up and running molecular dynamics simulations of membrane proteins, Methods 41 (2007) 475–488.
[75] W. Kabsch, C. Sander, Dictionary of protein secondary structure — pattern-recognition of hydrogen-bonded and geometrical features, Biopolymers 22 (1983) 2577–2637.
[76] W. Humphrey, A. Dalke, K. Schulten, VMD — visual molecular dynamics, J. Mol. Graphics 14 (1996) 33–38.
[77] W.J. Allen, J.A. Lemkul, D.R. Bevan, GridMAT-MD: a grid-based membrane analysis tool for use with molecular dynamics, J. Comput. Chem. 30 (2009) 1952–1958.
[78] A. Cordomí, J.J. Perez, Molecular dynamics simulations of rhodopsin in different one-component lipid bilayers, J. Phys. Chem. B 111 (2007) 7052–7063.
[79] H.J. Kaiser, A. Orłowski, T. Róg, T.K.M. Nyholm, W. Chai, T. Feizi, D. Lingwood, I. Vattulainen, K. Simons, Lateral sorting in model membranes by cholesterol-mediated hydrophobic matching, Proc. Natl. Acad. Sci. U. S. A. 108 (2011) 16628–16633.
[80] A.A. Gurtovenko, I. Vattulainen, Calculation of the electrostatic potential of lipid bilayers from molecular dynamics simulations: methodological issues, J. Chem. Phys. 130 (2009) 215107.
[81] A.A. Gurtovenko, I. Vattulainen, Intrinsic potential of cell membranes: opposite effects of lipid transmembrane asymmetry and asymmetric salt ion distribution, J. Phys. Chem. B 113 (2009) 7194–7198.

[82] S. McLaughlin, The electrostatic properties of membranes, Annu. Rev. Biophys. Biophys. Chem. 18 (1989) 113–136.
[83] Y. Shafrir, S. Durell, N. Arispe, H.R. Guy, Models of membrane-bound Alzheimer's Abeta peptide assemblies, Proteins 78 (2010) 3473–3487.
[84] S. Tristram-Nagle, D. Kim, N. Akhunzada, N. Kučerka, J.C. Mathai, J. Katsaras, M. Zeidel, J. Nagle, Structure and permeability of fully hydrated diphytanoylPC, Chem. Phys. Lipids 163 (2010) 630–637.
[85] P. Schatzberg, Diffusion of water through hydrocarbon liquids, J. Polym. Sci. Part C: Polym. Lett. 10 (1965) 87–92.
[86] R. Mills, Self-diffusion in normal and heavy water in the range 1–45 °C, J. Phys. Chem. 77 (1973) 685–688.
[87] P. Mark, L. Nilsson, Structure and dynamics of the TIP3P, SPC, and SPC/E water models at 298 K, J. Phys. Chem. A 105 (2001) 9954–9960.
[88] K. Olbrich, W. Rawicz, D. Needham, E. Evans, Water permeability and mechanical strength of polyunsaturated lipid bilayers, Biophys. J. 79 (2000) 321–327.
[89] B.A. Bauer, T.R. Lucas, D.J. Meninger, S. Patel, Water permeation through dmpc lipid bilayers using polarizable charge equilibration force fields, Chem. Phys. Lett. 508 (2011) 289–294.
[90] O. Wirths, G. Multhaup, T.A. Bayer, A modified beta-amyloid hypothesis: intraneuronal accumulation of the beta-amyloid peptide—the first step of a fatal cascade, J. Neurochem. 91 (2004) 513–520.
[91] S. Durell, H. Guy, N. Arsipe, E. Rojas, H. Pollard, Theoretical models of the ion channel structure of amyloid $\beta$-protein, Biophys. J. 67 (1994) 2137–2145.
[92] N. Kučerka, S.T. Nagle, J.F. Nagle, Structure of fully hydrated fluid phase lipid bilayers with monounsaturated chains, J. Membr. Biol. 208 (2005) 193–202.
[93] N. Kučerka, S.T. Nagle, J.F. Nagle, Closer look at structure of fully hydrated fluid phase DPPC bilayers, Biophys. J. 90 (2006) L83–L85.
[94] N. Kučerka, B.W. Holland, C.G. Gray, B. Tomberli, J. Katsaras, Scattering density profile model of POPG bilayers as determined by molecular dynamics simulations and small-angle neutron and X-ray scattering experiments, J. Phys. Chem. B 116 (2012) 232–239.

Poojari, Kukol and Strodel
How the amyloid-β peptide and membranes affect each other: an extensive simulation study

# Supporting Material

# How the amyloid-β peptide and membranes affect each other: an extensive simulation study

Chetan Poojari
Research Centre Jülich
Institute of Complex Systems: Structural Biochemistry
52425 Jülich
Germany

Andreas Kukol
University of Hertfordshire
School of Life Sciences
College Lane, Hatfield AL10 9AB
United Kingdom

Birgit Strodel*
Research Centre Jülich
Institute of Complex Systems: Structural Biochemistry
52425 Jülich
Germany

*Corresponding author.
Email: b.strodel@fz-juelich.de; Tel.: +49 (0)2461 613670, Fax: +49 (0)2461 618766

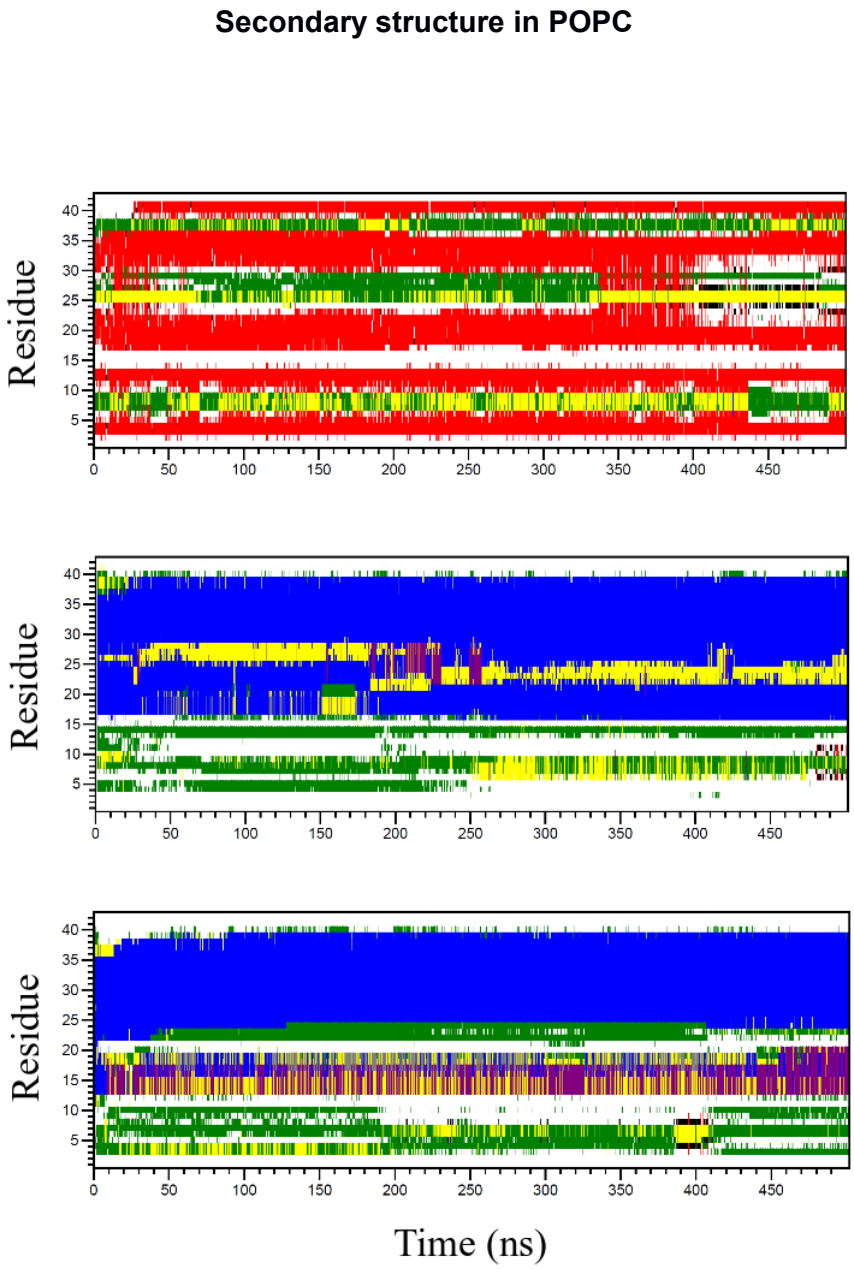


**FIGURE S1:** Secondary structure analysis using DSSP for 500 ns MD simulations of $A\beta_{42}$ monomer as (top) SHEET, (middle) HEL-16 and (bottom) HEL-23 in a POPC bilayer. Legend: white, coil; red, β-sheet; black, β-bridge; green, bend; yellow, turn; blue, α-helix; purple, π-helix; grey, $3_{10}$-helix.

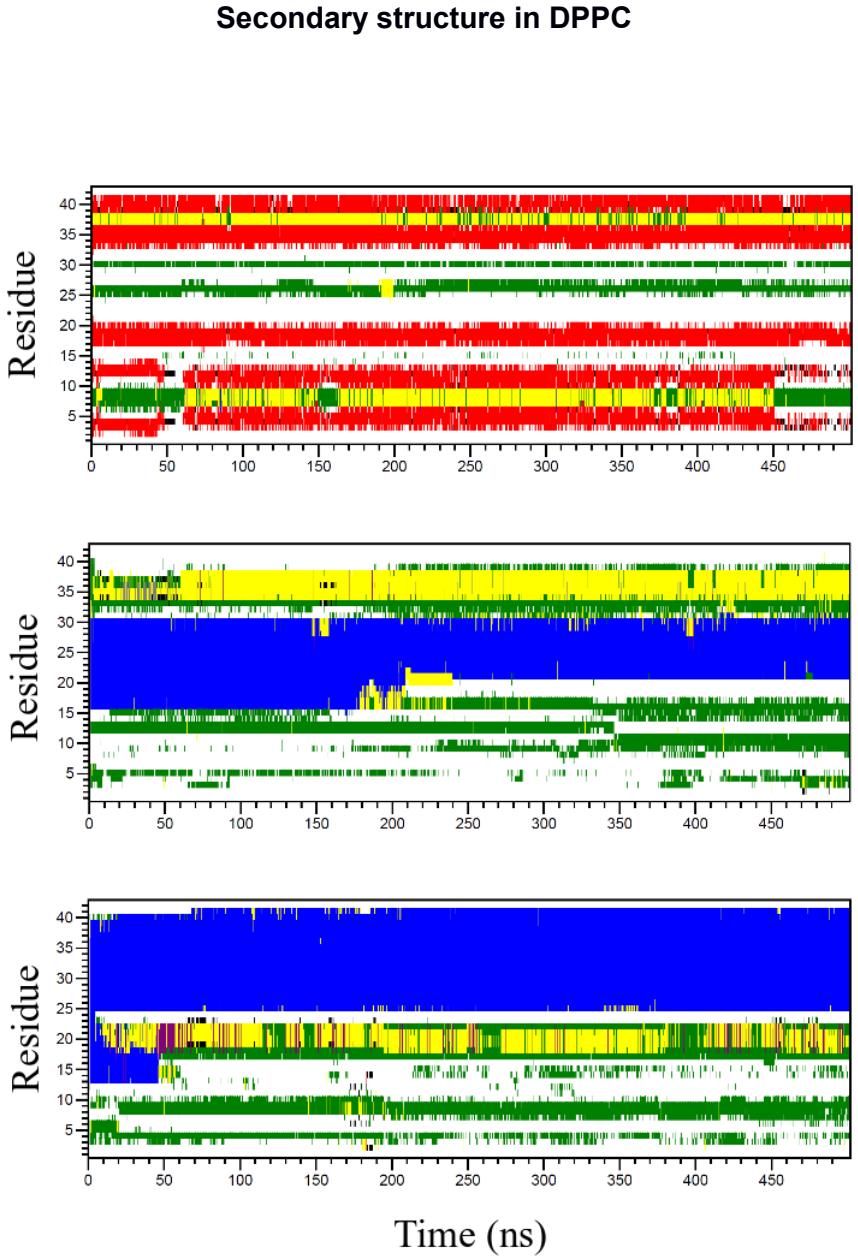


**FIGURE S2:** Secondary structure analysis using DSSP for 500 ns MD simulations of $A\beta_{42}$ monomer as (top) SHEET, (middle) HEL-16 and (bottom) HEL-23 in a DPPC bilayer. Legend: white, coil; red, β-sheet; black, β-bridge; green, bend; yellow, turn; blue, α-helix; purple, π-helix; grey, $3_{10}$-helix.

Poojari, Kukol and Strodel
How the amyloid-β peptide and membranes affect each other: an extensive simulation study

**Secondary structure in POPG**

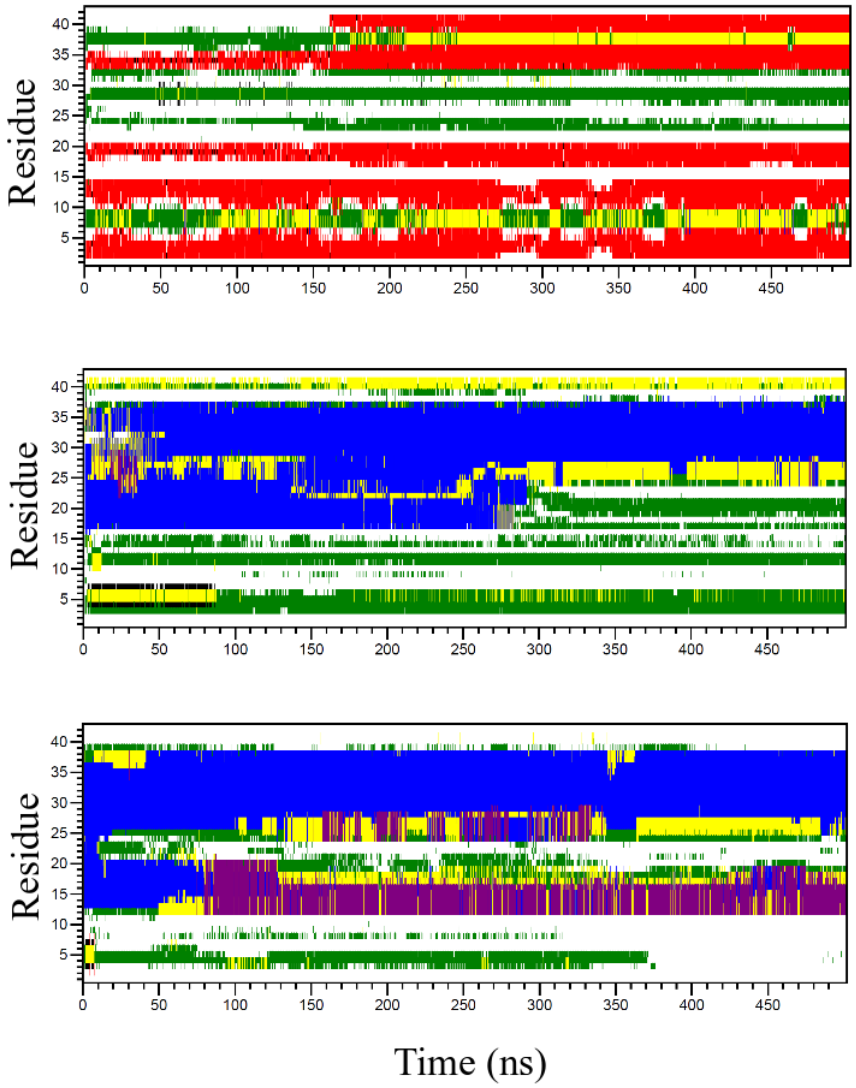


**FIGURE S3:** Secondary structure analysis using DSSP for 500 ns MD simulations of $A\beta_{42}$ monomer as (top) SHEET, (middle) HEL-16 and (bottom) HEL-23 in a POPG bilayer. Legend: white, coil; red, β-sheet; black, β-bridge; green, bend; yellow, turn; blue, α-helix; purple, π-helix; grey, $3_{10}$-helix.

**Secondary structure of the β-sheet tetramer in POPC**

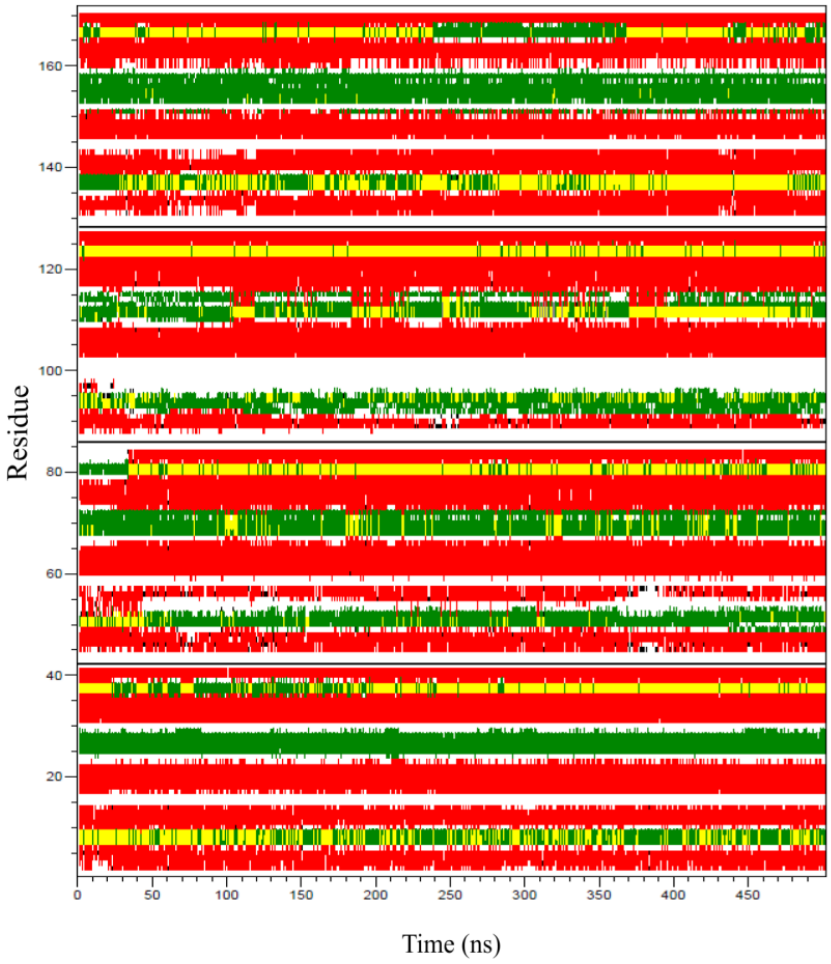


**FIGURE S4:** Secondary structure analysis using DSSP for the 500 ns MD simulation of $A\beta_{42}$ as β-sheet tetramer in a POPC bilayer. The four peptides are separated by black lines. Legend: white, coil; red, β-sheet; black, β-bridge; green, bend; yellow, turn; blue, α-helix; purple, π-helix; grey, $3_{10}$-helix.

**Simulations of SHEET in POPC**

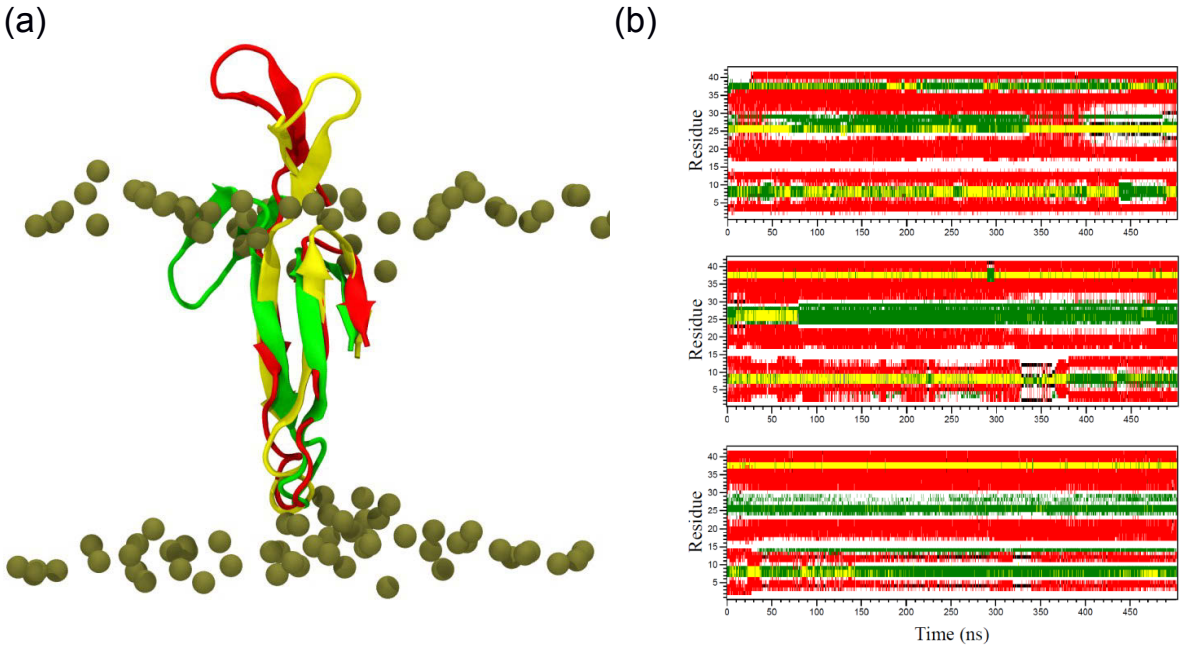


**FIGURE S5:** Comparison of the results obtained from three 500 ns MD simulations of SHEET in POPC, which were initiated from the same starting structure yet with different intitial velocity distributions. **(a)** Overlay of the final structures after 500 ns MD simulations. The peptide structures are shown in cartoon and colored in red, green and yellow, respectively. The bilayer phosphorus atoms are shown as van der Waals spheres in tan color. Lipid tails and water molecules are not shown for clarity. **(b)** Secondary structure analysis using DSSP for the 500 ns MD simulations of $A\beta_{42}$ as β-sheet in a POPC bilayer. The results of the three simulations are separated by black lines. Legend: white, coil; red, β-sheet; black, β-bridge; green, bend; yellow, turn; blue, α-helix; purple, π-helix; grey, $3_{10}$-helix.

**Analysis of bilayer thickness**

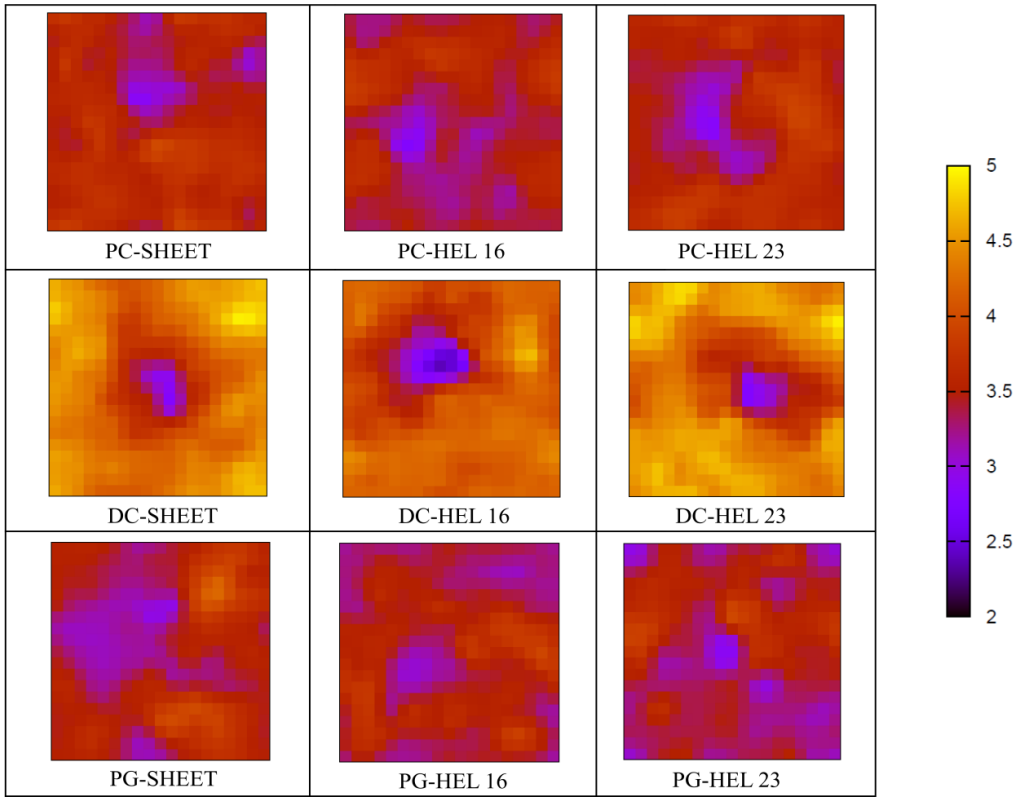


**FIGURE S6:** Bilayer phosphate-to-phosphate thickness for the final state of each 500 ns MD simulation. The axes of each plot correspond to the *x*- and *y*-direction of the lipid bilayer (both about 6.5 nm). The bilayer thickness was calculated with GRIDMAT-MD using 20 grid points in both directions. In each case, the peptide (not shown) is located near the center of each square where the thickness is smallest. The legend shows bilayer thickness (nm), mapped to the corresponding colors.

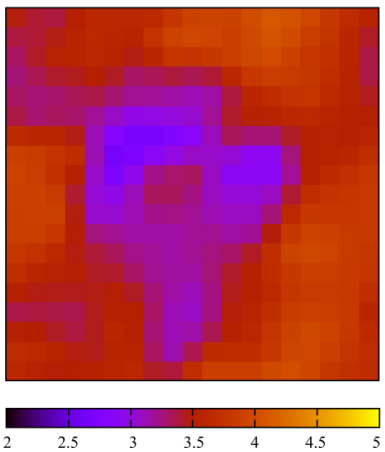


**FIGURE S7:** Bilayer phosphate-to-phosphate thickness for the final state of the 500 ns MD simulation of the $A\beta_{42}$ tetramer. For explanations see Figure S6.

Poojari, Kukol and Strodel
How the amyloid-β peptide and membranes affect each other: an extensive simulation study

**D23-K28 salt bridge in the SHEET structure**

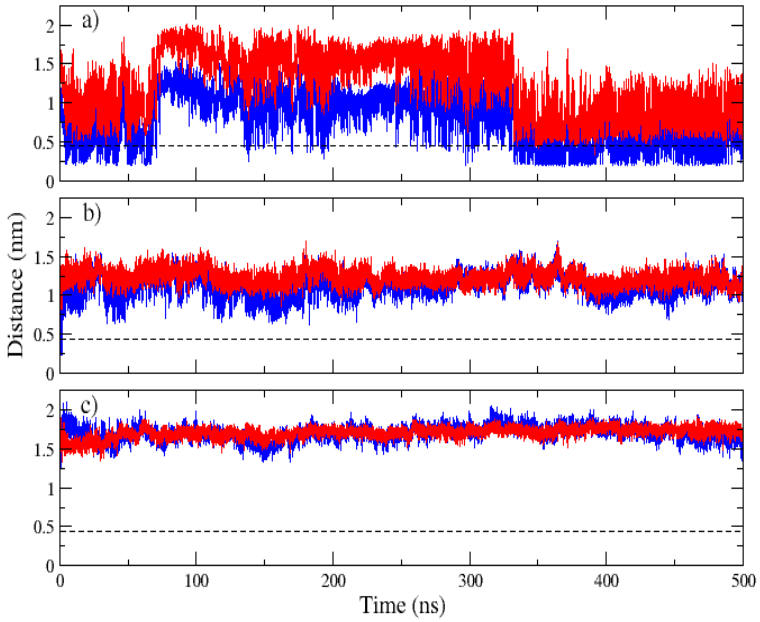


**FIGURE S8:** Minimum distance between the anionic carboxylate of either E22 (red) or D23 (blue) and the cationic ammonium from K28 in the SHEET structure in (a) POPC, (b) DPPC and (c) POPG. The black dashed line at 0.45 nm corresponds to cutoff distance to define a salt bridge in a protein. Amino acids greater than this distance do not qualify as forming a salt bridge.

Poojari, Kukol and Strodel
How the amyloid-β peptide and membranes affect each other: an extensive simulation study

**Peptide-ligand interaction energies**

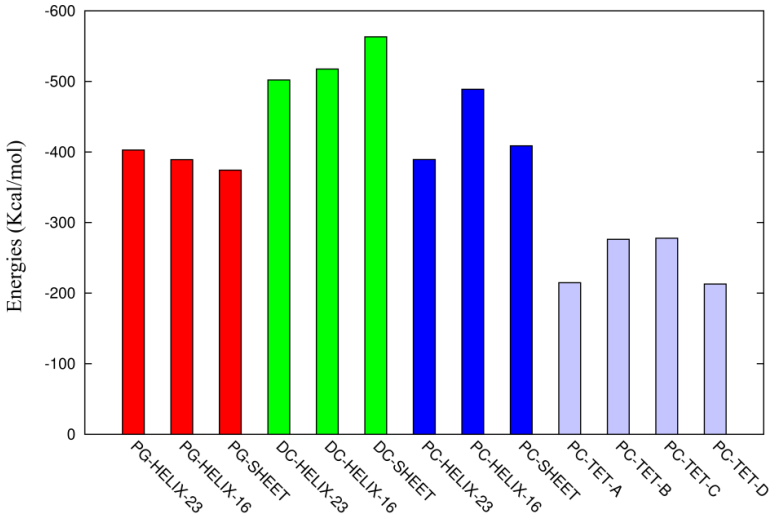


**FIGURE S9:** Peptide-lipid interaction energies between all residues of $A\beta_{42}$ and (red) POPG, (green) DPPC, and (blue) POPC lipids. The interaction energies, composed of electrostatic and van der Waals interactions, were averaged over the last 400 ns of the MD simulations. Results are shown for the SHEET, HEL-16, HEL-23 and β-sheet tetramer (light blue). For the tetramer the interaction energies are presented individually for the four peptides. This allows a comparison to the monomeric SHEET in POPC, which shows that the tetramer is stabilized by peptide-peptide interactions, leading to reduced peptide-lipid interactions.

**Water permeation: translocation times**

The water translocation in our simulations with $A\beta_{42}$ embedded in lipid bilayers is in most cases slowed down compared to the permeation in peptide-free bilyers as the translocation times in Table S1 show. The increased permeation times result from interactions of the water molecules entering the lipid bilayers with the inserted $A\beta_{42}$ peptide. To illustrate this process, representative trajectories of permeating water molecules in the vicinity of SHEET, HEL-16, HEL-23 and the β-sheet tetramer in POPC are depicted in Fig. S10. These trajectories are projected along the membrane normal.

Poojari, Kukol and Strodel
How the amyloid-β peptide and membranes affect each other: an extensive simulation study

| $A\beta_{42}$ structure | Bilayer | Mean time [ns] | Min time [ns] | Max time [ns] |
|---|---|---|---|---|
| Peptide-free | POPC | 1.1 | n/a | n/a |
| SHEET | | 12.2 | n/a | n/a |
| HEL-16 | | 7.8 | n/a | n/a |
| HEL-23 | | 2.3 | 1.3 | 3.7 |
| Tetramer | | 10.3 | 1.6 | 22.6 |
| Peptide-free | DPPC | 2.9 | 0.9 | 6.3 |
| SHEET | | 11.0 | 2.9 | 23.0 |
| HEL-16 | | 6.1 | 1.1 | 19.0 |
| HEL-23 | | 7.2 | 0.9 | 25.1 |
| Peptide-free | POPG | 1.3 | n/a | n/a |
| SHEET | | 2.7 | 0.4 | 5.0 |
| HEL-16 | | 2.9 | n/a | n/a |
| HEL-23 | | 2.1 | n/a | n/a |

**Table S1:** Water translocation times for peptide-free bilayers and bilayers containing $A\beta_{42}$. In the latter case, only water molecules permeating the bilayer in the vicinity of $A\beta_{42}$ were considered. Given are average times and, if applicable (i.e., if more than one water molecule permeated the bilayer) minimum and maximum translocation times.

The trajectory for SHEET is about 12 ns long with the water molecule spending the last ≈5 ns in the vicinity of the headgroup region once it translocated the hydrophobic core, before it diffuses into the bulk water. In case of the tetramer the water molecule needs 22 ns for crossing POPC as it resides most of the time close to the same $A\beta_{42}$ residues as in case of SHEET. For HEL-16 the water molecule needs ≈8 ns for the translocation process, while in case of HEL-23 the water molecule penetrates the membrane without considerably interacting with any of the $A\beta_{42}$ residues, leading to a fast translocation process of ≈1 ns.

These penetration events are representative as the average, minimum and maximum translocation times in Table S1 show. However, it should be noted that in some cases there was only one penetration event observed within the whole period of 500 ns of the simulation runs. Though in all cases water permeation is relatively fast (within nanoseconds), we observe system specific differences:

(i) For a given lipid type, i.e., POPC, DPPC and POPG, water penetration is generally fastest for HEL-23 and slowest for SHEET. This can be explained with the number of possible interaction sites for $H_2O$ along $A\beta_{42}$. Since SHEET has fewest and HEL-23 most intrapeptide H-bonds, more and fewer H-bonds can be formed with penetrating $H_2O$ molecules, respectively.

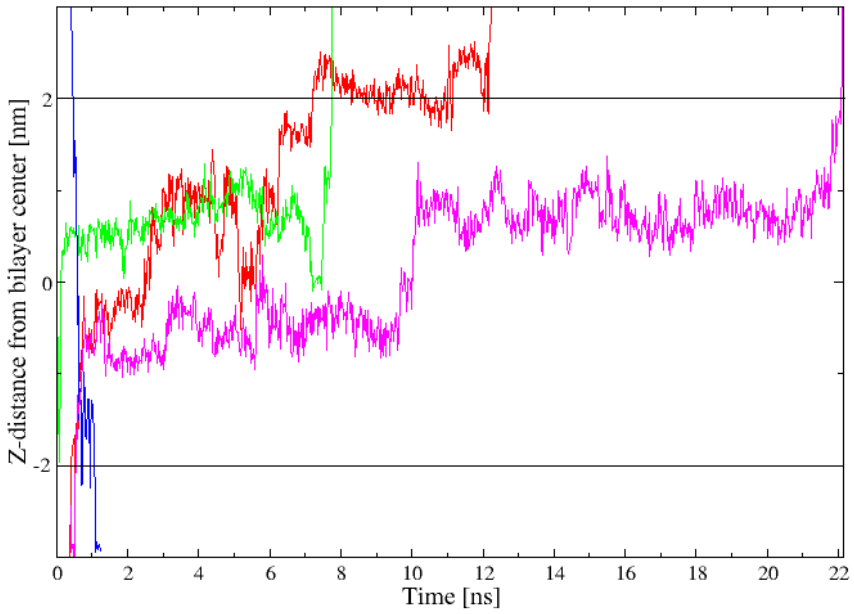


**Figure 10:** Representative trajectories of water molecules penetrating through a POPC bilayer with $A\beta_{42}$ as SHEET (red), HEL-16 (green), HEL-23 (blue) and β-sheet tetramer (magenta) inserted. Only the coordinate along the bilayer normal (*z*-coordinate) is plotted, and time is synchronized to the moment when the water molecule enters the membrane for each trajectory. The black horizontal lines indicate the headgroup region.

(ii) While DPPC allows more water molecules to cross the bilayer, the penetration is often slower than for POPC and POPG, which we can attribute to the smaller area per lipid and larger membrane thickness of DPPC. In addition, SHEET and HEL-16 are least stable in DPPC allowing them to form more H-bonds with the penetrating water molecules, slowing them down.

(iii) The fastest penetration processes are observed for POPG. As the membrane thickness for POPC and POPG are similar, this must be due to the reduced lipid density of POPG, resulting from the repulsion of the negative headgroup charges. This is in agreement with recent experiments, where it was shown that water permeation is strongly dependent on the area per lipid rather than on the membrane thickness.

(iv) For the β-sheet tetramer in POPC we observed the slowest penetration process while, at the same time, it allows the largest number of $H_2O$ molecules to pass the membrane compared to the other POPC simulations at 298 K and involving $A\beta_{42}$.

## 4.2 Stability of transmembrane amyloid $\beta$-peptide and membrane integrity tested by molecular modeling of site-specific A$\beta_{42}$ mutations

1

# Stability of transmembrane amyloid $\beta$-peptide and membrane integrity tested by molecular modeling of site-specific A$\beta_{42}$ mutations

Chetan Poojari[1], Birgit Strodel[1,2,*]

**1 Forschungszentrum Jülich GmbH, Institute of Complex Systems: Structural Biochemistry (ICS-6), 52425 Jülich, Germany**

**2 Institute of Theoretical and Computational Chemistry, Heinrich Heine University Düsseldorf, Universitätsstr. 1, 40225 Düsseldorf, Germany**

∗ **E-mail: b.strodel@fz-juelich.de**

## Abstract

Interactions of the amyloid $\beta$-protein (A$\beta$) with neuronal cell membranes, leading to the disruption of membrane integrity, are considered to play a key role in the development of Alzheimer's disease. Natural mutations in A$\beta_{42}$, such as the Arctic mutation (E22G) have been shown to increase A$\beta_{42}$ aggregation and neurotoxicity, leading to the early-onset of Alzheimer's disease. A correlation between the propensity of A$\beta_{42}$ to form protofibrils and its effect on neuronal dysfunction and degeneration has been established. Using rational mutagenesis of the A$\beta_{42}$ peptide it was further revealed that the aggregation of different A$\beta_{42}$ mutants in lipid membranes results in a variety of polymorphic aggregates in a mutation dependent manner. The mutant peptides also have a variable ability to disrupt bilayer integrity. To further test the connection between A$\beta_{42}$ mutation and peptide–membrane interactions, we performed molecular dynamics simulations of membrane-inserted A$\beta_{42}$ variants (wild-type and E22G, D23G, E22G/D23G, K16M/K28M and K16M/E22G/D23G/K28M mutants) as $\beta$-sheet monomers and tetramers. The effects of charged residues on transmembrane A$\beta_{42}$ stability and membrane integrity is analyzed at atomistic level. We observed an increased stability for the E22G A$\beta_{42}$ peptide and a decreased stability for D23G compared to wild-type A$\beta_{42}$, while D23G has the largest membrane-disruptive effect. These results suggest that the altered neurotoxicity arising from mutations in A$\beta$ is not only a result of the altered aggregation propensity, but also originates from modified A$\beta$ interactions with neuronal membranes.

## Author Summary

A wide range of diseases, including type 2 diabetes and Alzheimer's disease, are characterized by the formation of protein aggregates in the affected tissues. Alzheimer's disease, the most common neurodegenerative disorder, is caused by the aggregation and deposition of a peptide called A$\beta$ in the brain. Using variant forms of A$\beta$, so-called mutants, it was shown that the speed of peptide aggregation and A$\beta$ cell toxicity are correlated with each other. Furthermore, aggregation of different A$\beta$ mutants in lipid membranes results in a variety of polymorphic aggregates with variable abilities to disrupt membrane integrity in a mutation dependent manner. Our goal was to elucidate the different behavior of the various membrane-bound A$\beta$ peptides at the atomistic level. To this end we performed computational simulations of six variant forms of A$\beta$ to determine their stability and effects on membrane integrity. Our results reveal that the more toxic A$\beta$ mutants are either more stable in lipid membranes or have a larger membrane-disruptive effect or both.

## Introduction

Alzheimer's disease (AD) is the most common form of late-onset dementia resulting in the progressive impairment of memory and executive function [1]. It is associated with synaptic loss, abnormalities in neuronal function, an increase in neuronal cell death, and the extracellular accumulation of senile plaques composed of the amyloid $\beta$-peptide (A$\beta$) [2,3]. In general, A$\beta$ is a normal product of cellular metabolism throughout life and circulates as a soluble peptide in biological fluids. It is produced through posttranslational processing of the amyloid precursor protein (APP), a type-1 membrane integral glycoprotein via sequential cleavage by $\beta$- and $\gamma$-secretases [4]. Of the proteolytic cleavage products, which typically contain 39 to 43 residues, A$\beta_{42}$ is recognized as the most important alloform based on its ability to elicit neurotoxicity. It is the most prevalent alloform found in amyloid plaques, and has the highest propensity to aggregate into fibrils and plaques [5, 6]. The 'amyloid cascade hypothesis' proposes that assemblies of A$\beta$ initiate a process leading to neuronal dysfunction and cell death [7]. The most potent neurotoxic assemblies appear to be oligomeric, rather than fibrillar, in nature [8, 9]. There is acceptable evidence suggesting that A$\beta$ exerts its cytotoxic effect by interacting with membranes of neurons and other cerebral cells, such as astrocytes, microglial and cerebral endothelial cells [10, 11]. A potential pathway for A$\beta$ toxicity lies in its ability to alter biophysical membrane properties [12–14], causing membrane disruption

and permeability [15–17] and thereby allowing the leakage of ions, particularly calcium ions [17–20].

Familial forms of AD increase A$\beta$ production or the propensity of A$\beta$ to aggregate [7]. Until now four genes affecting APP, presenilin-1 (PS-1), presenilin-2 (PS-2) and apolipoprotein E have been identified to be linked to AD. So far 19 pathogenic missense mutations have been discovered in APP, of which seven are located in the region encoding A$\beta$. English (H6R) [21] and Tottori (D7N) [22] mutants show increased fibril elongation than wild-type (WT) A$\beta$ [23]. The Dutch mutant (E22Q) [24,25] favors A$\beta_{40}$ production and leads to a $\beta$-sheet structure [26–29]. The Flemish mutant (A21G) [30] forms stable oligomers with decreased fibril formation [31], while the Arctic mutation (E22G) [32] increases neurotoxic protofibril production [33, 34]. The Italian mutant (E22K) promotes faster aggregation of A$\beta_{40}$ and A$\beta_{42}$ [29] and the Iowa mutant (D23N) [35] forms fibrils faster than WT A$\beta$.

In a recent study, intact lipid bilayers were exposed to predominantly monomeric preparations of WT or different mutant forms of A$\beta_{40}$, and atomic force microscopy (AFM) was used to monitor aggregate formation and morphology as well as bilayer integrity over a 12 hour period [36]. The goal of this study was to determine how point mutations in A$\beta$, which alter peptide charge and hydrophobic character, influence interactions between A$\beta$ and the lipid surface. The Arctic, Italian, Iowa and Flemish mutations were considered. While fibril morphology did not appear to be significantly altered when mutants were prepared similarly and incubated under free solution conditions, aggregation in the lipid membranes resulted in a variety of polymorphic aggregates in a mutation dependent manner. It was further found that the ability of A$\beta$ to disrupt the structural integrity of bilayers is notably modulated by these mutations. An enhanced bilayer disruption was reported for the Arctic mutation. It was speculated that, in comparison to WT A$\beta$, the increased hydrophobic nature of E22G A$\beta$ increases its bilayer insertion. The membrane-bound oligomers of the Iowa mutation were extremely stable and the bilayer developed small, discrete areas of disrupted lipid morphology. Based on overall electrostatic and hydrophobic properties of D23N A$\beta$ this finding could not be explained [36].

One of the aims of the current molecular simulation study is to provide a better understanding of the experimental findings provided in [36]. In general, theoretical approaches are a complement to experimental studies probing the connection between A$\beta_{42}$ mutations, aggregation [37, 38] and A$\beta$–membrane interactions [39, 40]. So far various computational studies of A$\beta$ interacting with lipids have been performed to gain structural information at an atomistic level [41–61]. Structural models and experimental evidence support to the claim that transmembrane A$\beta$ is an assembly of loosely associated mobile $\beta$-

sheet subunits [41–43, 48]. In a recent study, Nussinov and co-workers used molecular simulations to demonstrate that amino acid substitutions help to infer which residues are essential for A$\beta$ channel structures [46]. The current study builds on our previous work, where we reported on the effects of lipid type and peptide oligomerization on membrane-bound WT A$\beta_{42}$ using molecular dynamics (MD) simulations on the sub-microsecond timescale [49]. We considered helical and $\beta$-sheet conformations embedded in zwitterionic palmitoyl-oleoyl phosphatidylcholine (POPC) and dipalmitoyl phosphatidylcholine (DPPC), and anionic palmitoyl-oleoyl phosphatidylglycerol (POPG) lipid bilayers. We observed that POPC increases the stability of transmembrane A$\beta_{42}$. Hydrophobic mismatch and lipid order of DPPC, and anionic surface charges of POPG bilayers are responsible for structural instabilities of A$\beta_{42}$ in these bilayers. From the considered structures the $\beta$-sheet tetramer was found to be most stable as a result of interpeptide interactions [48]. We performed a quantitative analysis of the translocation of water in the A$\beta_{42}$-bilayer systems. We observed that this process is generally fast (within a few nanoseconds) yet generally slower than in the absence of A$\beta_{42}$ in the bilayers. The rate limiting step is the permeation across the hydrophobic core, where interactions between A$\beta_{42}$ and permeating $H_2O$ molecules slow the translocation process. Finally, we showed that the $\beta$-sheet tetramer allows more water molecules to pass through the bilayer compared to monomeric A$\beta_{42}$ [49].

The goal of the present study is to investigate the effects of the charged residues K16, E22, D23 and K28 on the stability of transmembrane A$\beta_{42}$ in a POPC bilayer and their role on membrane integrity. To this end, we performed mutational studies for monomeric and tetrameric $\beta$-sheet structures of A$\beta_{42}$. We chose A$\beta_{42}$ to be in the $\beta$ state because there is sufficient evidence that amyloid oligomers adopt a $\beta$ conformation in the membrane [16, 62–65]. Since an experimental atomistic model of membrane-bound A$\beta$ is still lacking we chose a structure which we obtained from global optimization of transmembrane A$\beta_{42}$ [48], which was subsequently tested using MD simulations [49]. We considered the Arctic mutant E22G. To have a direct comparison with E22G, we studied the 'Arctic-type' D23G A$\beta_{42}$ mutant [66], and also tested the double mutant E22G/D23G. For the investigation of the effects of the positive charges of K16 and K28 we mutated these residues to methionine leading to the double mutant K16M/K28M A$\beta_{42}$. We chose methionine since, compared to all other amino acids, it has the smallest free energy barrier for translocation across the membrane headgroup region in either direction [67, 68]. Finally, we studied the quadruple mutant K16M/E22G/D23G/K28M where all peptide charges in the transmembrane region are removed. Our simulation results for WT, E22G and D23G A$\beta_{42}$ allow a better explanation of the

experimental findings testing the connection between A$\beta$ point mutations and A$\beta$-induced membrane disruption [36].

## Results and Discussion

In a recent study we investigated membrane-bound WT A$\beta_{42}$ as a $\beta$-sheet monomer and tetramer and as a helix [49]. The results obtained for the $\beta$-sheet structures will serve as comparison for the A$\beta_{42}$ mutants considered in the current study. The monomeric and tetrameric transmembrane A$\beta_{42}$ structures, from which our MD simulations were initiated, are shown in Fig. 1 [48].

### A$\beta_{42}$ monomer: Effects of charge removal on transmembrane stability

WT and A$\beta_{42}$ mutants were studied as monomer in the transmembrane $\beta$-sheet conformation in 500 ns MD simulations. The A$\beta_{42}$ monomer structures collected at the end of the MD simulations are shown in Fig. 2.

**Transmembrane A$\beta_{42}$ forms stable $\beta$-sheets.** Like WT A$\beta_{42}$ [49], all of the mutants remain in the lipid bilayer during the MD simulations. In general, the root mean square deviations (RMSD) and root mean square fluctuations (RMSF) for the peptide backbone atoms, which are presented in Fig. 3A and B, reveal a similar stability and fluctuation pattern for the A$\beta_{42}$ variants. D23G has the largest RMSD with values between 0.6 and 0.7 nm from the starting structure, while the RMSD of the other A$\beta_{42}$ variants fluctuates around 0.4 nm. To quantify the peptide motion along the membrane normal (i.e., the $z$-direction) inside the bilayer, we computed the center of mass motion of residues 25–30 in the lower A$\beta_{42}$ loop. The results of this analysis in Fig. 3C indicate that, after the initial 100 ns, the position of A$\beta_{42}$ inside the membrane is stable. Only for E22G and D23G a more pronounced motion along $z$ is observed leading to average positions of $2.9 \pm 0.18$ nm and $3.3 \pm 0.18$ nm, respectively. For the other four A$\beta_{42}$ variants the average position inside the membrane is 2.5–2.6 nm with standard deviations between 0.12 and 0.14 nm. The origin of the motion of E22G and D23G will be discussed below. Despite the removal of charged residues at the lipid–water interfaces, which in principle might act as electrostatic anchors in the transmembrane $\beta$-sheet structure of WT A$\beta_{42}$, the transmembrane $\beta$-sheet has a high propensity to stay inside the membrane. This is attributable to the many hydrophobic amino acids between residues

V24–A42, irrespective of the backbone carbonyl and amide groups which are not H-bonded in the $\beta$-sheet structure [49]. Between 14 and 17 out of the 26 residues between L17 and A42 are in $\beta$-conformation (Table 1 and Fig. 3D). Therefore, these transmembrane $\beta$-sheets are stable as also demonstrated by the final MD states and secondary structure analysis (Figs. S1–S3 in Supporting Information).

**A$\beta_{42}$ mutants display different transmembrane structures.** The A$\beta_{42}$ mutants exhibit somewhat higher mean RMSD values than WT A$\beta_{42}$. While the RMSD analysis is a measure for the overall motion of the peptide residues, the RMSF highlights the flexibility of individual A$\beta_{42}$ residues. The RMSF results in Fig. 3B indicate that the transmembrane A$\beta_{42}$ peptide (WT and mutants) is most flexible in the three turn regions, where the first one (residues 5–11) is outside the lipid bilayer and the other two (residues D23–G29 and G37–G38, respectively) are located within the hydrophobic core. The degree of fluctuation is different for each A$\beta_{42}$ variant and will be discussed below for each mutant. WT and E22G/D23G A$\beta_{42}$ are most flexible between residues 22 and 30. This WT result is at first sight surprising, as it is the only monomeric $\beta$-sheet where this turn region is occasionally stabilized by the intramolecular D23G–K28 salt bridge (Fig. S6). However, the breakage and formation of this salt bridge induces structural flexibility in this region. Furthermore, the existence of the D23G–K28 salt bridge does not help to stabilize the $\beta$-hairpin, which converts to coil-turn-coil after 400 ns of this simulation (Fig. S1). The instability of the WT A$\beta_{42}$ transmembrane $\beta$-sheet also results from residues E22 and D23 being located in the hydrophobic membrane core, where they can interact with the lower headgroups thereby destabilizing the $\beta$-sheet structure in this region.

**E22G.** The most stable transmembrane $\beta$-sheet is observed for the Arctic mutant as judged by the final MD structure (Fig. 2) and the DSSP plot (Fig. S2). The $\beta$-sheet stability of E22G with $15.4 \pm 0.8$ residues in $\beta$ conformation originates from the removal of the negatively charged E22 residue within the membrane hydrophobic core, leading to overall charge neutrality inside the membrane. The mutation increases the hydropathy index from 8.6 for WT A$\beta_{42}$ to 11.7 for E22G using the hydropathy scale of Kyte and Doolittle [69] (Table 1). The stability of E22G A$\beta_{42}$ is further supported by the RMSF result. The larger RMSD value and motion along $z$ compared to WT and most other A$\beta_{42}$ variants result from the tilt of E22G A$\beta_{42}$ inside the POPC bilayer. The reorientation occurs after 200 ns of the MD simulation and is only observed for this mutant. It is mainly driven by electrostatic interactions between E22G A$\beta_{42}$ and both headgroup regions (Fig. S7). Such a tilt is in agreement with the experimental

observation that the human islet amyloid polypeptide adopts an orientation of about 48° relative to the membrane surface when interacting with a dipalmitoylphosphoglycerol (DPPG) monolayer, which might have a strong damage to the lipid membrane [65].

**D23G.** In the Arctic-type mutant [66] the salt bridge between residues D23 and K28 cannot be formed, which destabilizes the bend region between residues G25 and K28 as shown in Fig. 2 and Fig. S2. Instead, residues D23–A30 adopt mainly coil conformations, resulting in a larger loop region, which allows E22 to interact with the upper headgroups. This interaction is accompanied by an upward movement and bending of the peptide (Fig. 3C), while the lipids surrounding the peptide in the upper leaflet move downwards. This can be seen from the positions of the lipid headgroups in Fig. 2 and will be discussed in detail in the next section. The D23G mutant shows the largest deviation from the starting structure, with an average RMSD value of 0.65 nm. D23G is nonetheless stable as $\beta$-sheet, as confirmed by the secondary structure analysis yielding, on average, $14.8 \pm 0.3$ residues in $\beta$ conformation inside the membrane. The interactions between K28 with the headgroups in the lower leaflet prevent the $\beta$-sheet from completely moving to the upper membrane–water interface. The balance between the interactions of E22–upper headgroups and K28–lower headgroups gives rise to a stable conformation, as demonstrated by the small fluctuations according to the RMSF analysis. However, on longer time scales the D23G mutant may migrate to the upper membrane-water surface, adopting a membrane-adsorbed rather than a transmembrane conformation.

**E22G/D23G.** A stable transmembrane $\beta$-sheet is regained for the double mutant E22G/D23G due to the removal of both negative charges from residues 22 and 23 within the membrane hydrophobic core, increasing the hydropathy index to 14.8. The elimination of the salt bridge between residues 23 and 28 leads to an extended loop region between residues 22 and 30 in E22G/D23G A$\beta_{42}$, which induces fluctuations in both transmembrane turns and reduces the $\beta$ count to $14.4 \pm 1.2$ residues. The deletion of charged groups removes any electrostatic interactions involving residues 22 and 23 with the lower headgroup region, while the interactions between the positive charge of K28 and the lower headgroup anchors the transmembrane position of the double mutant E22G/D23G, which stabilizes this configuration.

**K16M/K28M.** From all considered mutations the K16M/K28M double mutation has the highest transmembrane $\beta$ content with on average $16.5 \pm 0.6$ residues in $\beta$ conformation. The mutation K16M

allows the peptide to move more easily along the membrane normal [67, 68], enabling the peptide to move downwards (Fig. 3C) so that the turn residues G25–N27 are exposed to the water phase and the charged residues E22 and D23 can better interact with the membrane–water interface (see final structure in Fig. 2). These interactions reduce the conformational dynamics of K16M/K28M as demonstrated by the RMSF analysis, enabling it to form a stable transmembrane structure. Furthermore, the substitution of both lysine residues with methionine raises the hydropathy index of this A$\beta_{42}$ mutant to 20.2, causing it to be stable in a hydrophobic environment.

**K16M/E22G/D23G/K28M.** The quadruple mutant is also stable as transmembrane $\beta$-sheet. However, compared to the other A$\beta_{42}$ variants it is more flexible inside the membrane and has a lower $\beta$ count. The complete removal of charged residues inside the membrane induces peptide flexibility in the upper leaflet, involving residues 15–19 and 37–38 (see RMSF analysis in Fig. 3B). Because of the missing stabilization from the salt bridge between residues D23 and K28 an extended loop is formed involving residues G22–A30. The stability of this mutant as transmembrane $\beta$-sheet can thus be attributed to i) the inherent stability of this sheet structure, and ii) hydrophobic interactions between the peptide (its hydropathy index is 26.4) and the membrane core. Furthermore, the structure of the peptide is not perturbed by charged peptide residues positioned in the membrane core.

## A$\beta_{42}$ monomer: Effects of charge removal on lipid bilayer

**Area per lipid.** Table 1 summarizes the effects of the A$\beta_{42}$ mutants on lipid bilayer properties. It shows that the insertion of A$\beta_{42}$ into a POPC bilayer leads to a decrease in the area per lipid compared to the peptide-free bilayer. This area reduction is largest for WT A$\beta_{42}$ with area values of 6–7 Å$^2$ below the value for the pure POPC bilayer. It results from electrostatic attraction and H-bonds between A$\beta_{42}$ residues and lipid headgroups. Removal of charged A$\beta_{42}$ residues results in smaller reductions of the area per lipid with most values being only 2–4 Å$^2$ below the area of the peptide-free POPC bilayer. Interestingly, for E22G, where peptide charges were removed in the lower leaflet, not only the area per lipid in the lower but also in the upper leaflet are larger compared to WT A$\beta_{42}$. This result shows that the lipid packing in both leaflets is coupled to each other. For D23G, on the other hand, the area per lipid is reduced by about 5 Å$^2$ in the upper leaflet and slightly increased in the lower leaflet compared to the peptide-free POPC bilayer. This behavior can be explained by the conformational instability of the

D23G mutant inside the bilayer, which causes the whole peptide to move upward and bend to allow E22 to interact with the upper headgroups.

**Bilayer thickness.** This D23G–POPC interaction also leads to a marked reduction of the bilayer thickness around the peptide, which is for D23G most pronounced compared to the other mutants (Figs. S8 and S9). For the average bilayer thicknesses we find that they are hardly affected by embedded A$\beta_{42}$ with thickness changes within $\pm\,0.05$ nm compared to the peptide-free POPC bilayer (Table 1). However, Fig. S9 reveals that the POPC bilayer thickness around A$\beta_{42}$ is decreased in order to improve the hydrophobic matching between bilayer and A$\beta_{42}$, whose hydrophobic width is smaller than those of the lipids (i.e., negative hydrophobic mismatch). The POPC bilayers have a thickness of about 2.5–3.0 nm in the neighborhood of the A$\beta_{42}$ peptides, which corresponds to the hydrophobic width of the latter for $\beta$-sheet structures. However, for the quadruple mutant we observe only minor changes to the bilayer thickness around the peptide, because the four mutations increase the hydrophobic width of the $\beta$-sheet. In general, the thinner bilayer region close to A$\beta_{42}$ is compensated by a slight increase in thickness of the bilayer as the distance from A$\beta_{42}$ increases [49, 51, 70]. Therefore, the average bilayer thickness is almost not affected by the membrane-inserted A$\beta_{42}$ peptide.

**Lipid order.** An increased bilayer thickness results from increased lipid chain order. We therefore calculated the order parameter $S_{\mathrm{CD}}$ of acyl chain 1 (sn-1) separately for lipids within 0.5 nm of A$\beta_{42}$, and for the lipids, which are more than 0.5 nm away from A$\beta_{42}$. The results of this analysis are shown in Figs. S10 and S11. In these figures we also present $S_{\mathrm{CD}}$ of the POPC-only bilayer obtained from a 100 ns MD run of the peptide-free POPC bilayer [49] for comparison. The lipid order is generally decreased around the peptide as the corresponding $S_{\mathrm{CD}}$ value is smaller than the one for the peptide-free bilayer, while the lipid order is marginally increased for the lipids further away from the peptide. The lipid order reduction around A$\beta_{42}$ is strongest for E22G, D23G and K16M/K28M, while removal of all charged residues inside the membrane leads to such a good integration of the quadruple A$\beta_{42}$ mutant into the hydrophobic membrane core that the lipid order is almost unaffected by the peptide. Especially carbon atoms 6–15 of the sn-1 chains are not disturbed by the presence of this A$\beta_{42}$ variant. This finding is in agreement with our observation that this particular mutant does not decrease the bilayer thickness around the peptide.

**Water permeation.** The lipid disorder around A$\beta_{42}$ allows water molecules to enter the membrane hydrophobic core in the vicinity of the peptide. The water density profiles in Fig. 2 give an estimate for the water penetration into the membrane. The density profiles show that the headgroup regions of both bilayer leaflets are fully solvated. In all systems we see water penetration into the hydrophobic core, which is more prevalent in the top leaflet than in the bottom leaflet. This cannot be explained by the area per lipid as this quantity is generally smaller in the top than in the bottom leaflet. Yet one would expect that a large area per lipid allows water molecules to enter more easily. Instead, the interaction of the N-terminal residues 1–16 with the membrane surface, which disturbs headgroup packing (Fig. 2), facilitates the entry of water molecules into the membrane.

Lipid disorder is another factor, which could increase water penetration. The highest degree of water penetration is observed for D23G, which also shows the largest lipid disorder in the upper leaflet. Here, the water density has vanished only at $z \approx -1.0$ nm, while for WT A$\beta_{42}$ and the other mutants the water densities are zero between $-1$ nm $\lesssim z \lesssim +0.5$ nm. Water permeation is nonetheless small for D23G: only 5 water molecules passed through the membrane within 500 ns (Table 1). In case of the quadruple mutant we also observed 5 water translocation events, while for the other A$\beta_{42}$ peptides this number was even smaller with values between 1 (WT A$\beta_{42}$) and 4. For the peptide-free bilayer we did not observe any permeation event within 100 ns. We thus conclude that membrane-insertion of A$\beta_{42}$ monomer leads to a slight increase of membrane permeability [49], which gets amplified by lipid disorder resulting from peptide–lipid interactions. However, the example of K16M/E22G/D23G/K28M shows that other factors, such as the peptide charge distribution on both sides of the membrane, also affect water permeation through the membrane, since the lipid order is least impaired by this peptide.

## A$\beta_{42}$ tetramer: Effect of charge removal on transmembrane stability.

Our motivation for studying transmembrane $\beta$-sheet tetramers was to test whether they are more stable than the monomeric $\beta$-sheets and may constitute likely membrane-bound A$\beta$ structures, which are able to induce membrane damage. We performed the simulations for the tetramer only for WT, E22G and D23G A$\beta_{42}$ as these are the biologically relevant A$\beta_{42}$ variants. The final structures of these 500 ns MD simulation are shown in Fig. 4. The results for the WT A$\beta_{42}$ tetramer in POPC were discussed in detail in our previous study [49].

**Oligomerization increases transmembrane stability.** In all three cases we observe that, unlike in the monomeric $\beta$-sheets, the N-terminal $\beta$-hairpins are stable in the tetramer (see final snapshots and DSSP plots in Figs. S1, S4 and S5). The $\beta$-hairpins interact with each other rather than with the bilayer surface, causing the N-terminal regions to stick out into the water instead of being adsorbed to the bilayer surface, as we observed for the $\beta$-sheet monomers. In larger A$\beta$ assemblies composed of mobile $\beta$-sheets [43, 48] the water-exposed $\beta$-hairpins structure might act as a funnel for cations to be inserted into the membrane [49, 71]. The transmembrane tetramers are more stable than the $\beta$-sheet monomers, when the RMSD analysis in Figs. 3A and 5A are compared. The final RMSD values for the tetramers are between 0.2 and 0.3 nm, while they increased to average values of 0.35–0.65 nm for the monomers. The increased stability of the tetramers can be explained by interpeptide interactions [48, 49]. The different stabilities of E22G and D23G in relation to WT A$\beta_{42}$ tetramers will be now discussed in detail.

**E22G.** The Arctic mutant E22G is more stable than both WT and D23G A$\beta_{42}$ tetramers as the RMSD analysis (Fig. 5A) and secondary structure plot (Fig. S4) reveal. The $\beta$-sheet structure in the hydrophobic core is well conserved throughout the simulation (Fig. 5D), though the number of residues in $\beta$ conformation per peptide is very similar to the E22G monomer result. Only the secondary structure fluctuations are smaller in the tetramer than in the monomer. The average $\beta$ content of WT A$\beta_{42}$ tetramer is of similar size as for the E22G tetramer. However, for WT it fluctuates more (for both monomer and tetramer) as a result of the smaller stability of transmembrane WT A$\beta_{42}$ compared to E22G. Interestingly, the $\beta$ content for the E22G tetramer is lowest between 100 and 200 ns when the salt bridge D23–K28 in one of the four peptides is formed (Fig. S6). In general, the lower turn region involving residues 23–29 is the most flexible part in the peptides composing the E22G tetramer. The RMSF plot (Fig. 5B) shows that these residues fluctuate more than in both WT and D23G tetramer. This can be explained with the deep insertion of the turn region into the lower headgroup region, where the peptide structure becomes disturbed by interactions with the headgroups and water molecules. The downward motion between 100 and 200 ns is revealed by the analysis of the peptides center of mass motion along $z$ (Fig. 5C). Because of interpeptide interactions the $\beta$-sheets inside the membrane do not tilt as was observed for the E22G monomer.

**D23G.** The D23G tetramer remains stable until around 350 ns. At that time, the RMSD (Fig. 5A) increases because the peptides start bending towards the upper membrane surface. However, this bending

is not as strong as in the D23G monomer as interactions between the peptides counteract the attractive forces between residue E22 and the upper headgroups. Two of the peptides of the D23G tetramer move upwards inside the bilayer, causing the surrounding lipids to move with them. This movement leads to a marked reduction of the bilayer thickness around the tetramer. The lipid headgroups of the lower leaflet are pulled upwards by interactions with with E22 and K28 in the turn region, leading to membrane disruption (discussed below). As for the D23G monomer, the absence of the salt bridge between residues 23 and 28 destabilizes the turn region thereby inducing conformational flexibility. The $\beta$ content for the D23G tetramer belongs to the lowest values among the studied systems. While the average number of residues in $\beta$ conformation was 14.8 for the D23G monomer, it has dropped to 14.3 for the tetramer. Furthermore, the amount of $\beta$ fluctuation has increased for the tetramer. The structural flexibility is also evident in the RMSF (Fig. 5B), which is for most residues larger for D23 compared to both WT and E22G. Surprisingly, only the turn region involving residues V24–K28 fluctuates less than in the E22G tetramer despite the extended loop region in D23G A$\beta_{42}$. This is attributable to the interaction of D23 in E22G A$\beta_{42}$ with the lower headgroups exposing the turn regions to the water phase, which increases its flexibility.

## A$\beta_{42}$ tetramer: Effects on lipid bilayer

**Area per lipid, bilayer thickness and lipid order.** The effects on the properties of the POPC bilayer upon insertion of WT, E22G and D23G A$\beta_{42}$ tetramers are very similar to those observed for the corresponding monomers (Table 1). The WT tetramer has the largest effect on the area per lipid in both upper and lower leaflet. E22G leads to area reductions of about 4 Å$^2$ per lipid in both leaflets, while D23G leaves the area per lipid in the lower leaflet unaffected but reduces it by about 6 Å$^2$ in the upper leaflet. The average bilayer thickness is 0.02–0.05 nm smaller compared to the peptide-free bilayer. This reduction results from the hydrophobic mismatch between A$\beta_{42}$ and the membrane core, which compresses the bilayer near the peptides (Fig. S9). This in turn is accompanied by a reduction in lipid tail order, which can be seen from the analysis of $S_{\mathrm{CD}}$ of the lipids within 0.5 nm of the peptides (Fig. S12). WT and D23G tetramers have a larger disordering effect on nearby lipids than the E22G tetramer. The latter observation differs from the finding that E22G monomer disorders neighboring lipids. None of the tetramers increased (or only marginally in the case of WT) the lipid order in the sn-1 chains $>$ 0.5 nm away from the peptides, which explains why the average bilayer thickness is slightly

reduced, and not increased as for the A$\beta_{42}$ monomers.

**Water permeation.** The water density profiles for the A$\beta_{42}$ tetramers (Fig. 4) reveal an almost continuous water channel in case of D23G. Only at $z \approx 0$ the water density has almost declined to zero. The increased membrane permeability for D23G tetramer is also demonstrated by the translocation of 22 water molecules during the simulation. This number is substantially larger than the corresponding numbers for WT and E22G tetramer (5 and 8, respectively) and for the monomers ($\leq 5$ water translocations). The increased water flow induced by the D23G tetramer is due to the greater disruption of membrane integrity especially in the lower leaflet. The water density profiles for WT and E22G tetramers also reveal an increase in the average probability of finding water inside the membrane compared to that of the monomers. Only for $-0.5$ nm $\lesssim z \lesssim +0.5$ nm this probability is zero. Noteworthy, while the WT tetramer enables more water molecules to reside inside the membrane compared to the E22G tetramer, it supports fewer water permeation events. This again shows that membrane permeability in the vicinity of membrane-inserted amyloid peptide is a complex process, which is governed by a multitude of factors, such as lipid type, A$\beta_{42}$ conformation (as it influences the number and strength of interactions between A$\beta_{42}$ and permeating water molecules), and A$\beta_{42}$ oligomerization [49]. As in our previous study [49], we observe that A$\beta_{42}$ oligomerization is an important event, which causes an increase in membrane permeability. Here, we have shown that the removal of peptide charges inside the membrane further increases the amount of water inside the membrane and the number of permeation events.

## Conclusion

Based on the evidence that the cytotoxicity in AD originates from interactions of A$\beta$ with neuronal cell membranes disturbing the integrity of the membrane [15–17], we performed mutational studies to investigate the transmembrane stability of various A$\beta_{42}$ mutants in a $\beta$-sheet conformation [48]. Our 500 ns MD simulations of A$\beta_{1-42}$ mutants in a POPC bilayer reveal a similar or increased stability compared to WT A$\beta_{42}$ for all mutants except D23G. For the monomeric $\beta$-sheet we observed the highest stability for the Arctic mutant E22G and the double mutant K16M/K28M. The removal of positive charges by mutating K16 and K28 to methionine increases the hydropathy index of this mutant A$\beta_{42}$ by a factor of 2.34, which gives rise to a stable transmembrane $\beta$-sheet. The stability of the Arctic mutant E22G can be attributed to the removal of the negative E22 charge in combination with D23 and K28

interacting with the headgroups of the lower leaflet, leading to charge neutrality of the peptide inside the membrane. While the 'Arctic-type' D23G mutant has the same hydropathy index as E22G A$\beta_{42}$, it is not stable as transmembrane $\beta$-sheet, since the position of E22 inside the membrane causes the peptide to bend towards the upper membrane surface. The less toxic WT A$\beta_{42}$, on the other hand, looses some of its $\beta$ structure during the MD simulation due to its overall negative charge inside the membrane. Our results are supported by experimental findings for Arctic APP, whose transmembrane localization is altered compared to WT APP, with reduced levels at the cell surface making Arctic APP less available for non-amyloidogenic cleavage. As a result, the extent and subcellular location of A$\beta$ formation is changed, as revealed by increased A$\beta$ levels, especially at intracellular locations [72].

In our previous study [49] we demonstrated that a single transmembrane A$\beta_{42}$ peptide is not sufficient to explain the experimentally observed membrane damage resulting from membrane-bound A$\beta$, which causes cellular ionic imbalance [18–20]. This finding allowed us to conclude that membrane permeabilization by membrane-bound A$\beta$ as commonly observed experimentally [15–17] must be due to transmembrane A$\beta$ oligomers and not monomers as some studies conjectured [73, 74]. This conclusion is supported by the results of the current study. Based on size and biochemical considerations it is also evident that more than single A$\beta$ peptides enter the membranes [20, 36, 75]. Therefore, the water translocation arising from a monomeric transmembrane A$\beta$ $\beta$-sheet must not be overemphasized, yet its structural stability is a determinant for the stability of the corresponding transmembrane oligomer. For instance, the E22G A$\beta_{42}$ mutant is very stable both as monomeric and tetrameric transmembrane $\beta$-sheet, while D23G is least stable in either case. On the other hand, transmembrane D23G generates the largest amount of membrane permeation compared to the other monomers and tetramers.

This finding is in agreement with experimental observations. In situ AFM experiments with Arctic A$\beta_{40}$ exposed to total brain lipid extract (TBLE) bilayers showed small membrane-bound oligomeric aggregates with large areas of bilayer disruption [36]. These areas were seen to be populated with stable oligomers composed of 10–15 peptides per oligomer, rather than with fibrillar aggregates as observed for WT A$\beta_{40}$. The same kind of experiments with Iowa mutant (D23N) A$\beta_{40}$ revealed the formation of stable oligomeric aggregates on the TBLE surface within 2–3 hours [36]. However, after longer exposure (10–12 hours), the bilayer structural integrity was highly disrupted in small areas arising from D23N A$\beta_{40}$ oligomers inside the bilayer [36]. A possible explanation for the different behaviors of E22G and D23N can be provided based on our molecular simulations: E22G A$\beta$ has a higher tendency to insert

into a membrane compared to D23N, while D23N prefers binding to the surface. However, when D23N A$\beta$ manages to enter the membrane, it has a great capacity to disrupt membrane integrity. Here, we assumed that D23N behaves similarly to D23G A$\beta$. To our knowledge, no experiment on D23G A$\beta$ in the presence of a lipid membrane has been carried out yet. NMR studies have revealed a large destabilizing effect of the D23G mutation on the turn region involving residues 21–30 [66]. The D23G variant of A$\beta$ is also more prone to proteolytic degradation than WT A$\beta$ [66].

Our results on the interactions between A$\beta_{42}$ and a POPC bilayer, and the effect of A$\beta_{42}$ mutations on bilayer properties provides insight into the likely toxicity mechanism caused by membrane-inserted A$\beta_{42}$ oligomers. We conclude that the higher transmembrane stability of E22G and the increased membrane disturbing effect of D23G are possible reasons for the increased cytotoxicity of the E22G and D23N variants compared to WT A$\beta$ [36]. While our current simulations are still rather short investigating only small oligomers—simulations of larger than tetrameric oligomers on the millisecond time scale would be needed, which are yet prohibitively long with respect to computing time—we are able to state that A$\beta_{42}$ mutations have an effect on transmembrane stability and membrane integrity. This should be motivation enough for experimentalists and simulation scientists to perform further studies on these systems.

# Methods

## Starting structures

The initial A$\beta_{42}$ structure is a $\beta$-sheet, which was obtained from a study of the A$\beta_{42}$ monomer and small oligomers using a global optimization approach and an implicit membrane model [48]. In this structure, the more hydrophobic C-terminal region starting from residue 17 is fully inserted into the hydrophobic membrane core, forming an antiparallel $\beta$-sheet with two turn regions. The first turn ranges from residue 23 to 29, and the second one involves residues 37 and 38. In solution, the G37–G38 hinge structure has been identified as characteristic of A$\beta_{42}$ distinguishing it from its C-terminal truncated relative A$\beta_{40}$ [76]. The first turn is prominent in many A$\beta$ structures identified from experiment [77–80] and simulation [81–83]. While each of these models predict a distinct turn structure, they share the key structural features of a salt bridge between Asp23–Lys28 and the intramolecular hydrophobic cluster between Leu17/Phe19 and Ile32/Leu34. We decided to use our $\beta$-hairpin model as starting structure as it also provides a structural model for the more hydrophilic residues 1–16, which form a $\beta$-hairpin outside

the membrane [48]. The N- and C-terminals were capped to nullify the effect of terminal residues in peptide-lipid interactions.

## Molecular Dynamics Simulations

All MD simulations were performed with the GROMACS 4.0 package [84]. The A$\beta_{42}$ peptide was described using the GROMOS96 53A6 force field [85], and the POPC lipids were modeled with modified Berger force field parameters for use with the GROMOS96 53A6 force field [86]. Recently, we demonstrated that the GROMOS96 53A6 force field is able to correctly model the structural propensities of A$\beta_{40}$ and A$\beta_{42}$ [87] and already combined it with the lipid force field to study A$\beta_{42}$–membrane interactions [49]. Initial coordinates of 128 lipids for POPC bilayer equilibrated with water for 40 ns were obtained from Kukol's work on lipid models [86]. The A$\beta_{42}$ peptide was inserted into the pre-equilibrated lipid membrane using the INFLATEGRO script [88]. Once A$\beta_{42}$ was inserted into the lipid membrane, the structures were solvated with SPC water molecules, $Na^+$ counterions were added to balance the peptide charge, and 0.1 M NaCl salt added to bring the system to the a physiological salt concentration. The simulations were carried out in a $6.5 \times 6.5 \times 9.5$ nm$^3$ box. An initial equilibration under isothermal-isochoric conditions was performed for 100 ps during which the protein heavy atoms and phosphorous atoms of the lipid headgroups were restrained with a force constant of 1000 kJ mol$^{-1}$ nm$^{-2}$. Here, the v-rescale thermostat with a coupling constant of 0.1 ps was used to regulate the temperature of the peptide, lipids, and solvent/ions separately at 298 K. The systems were then equilibrated under isothermal-isobaric (NPT) conditions for 30 ns. For the NPT ensemble the Nose-Hoover thermostat was used to regulate the temperature along with semiisotropic Parrinello-Rahman pressure coupling. The bilayer normal $z$-direction and $xy$-plane were coupled separately with a time constant of 5.0 ps maintaining a constant pressure of 1 bar independently in all directions. An isothermal compressibility of $4.5 \times 10^5$ bar$^{-1}$ was applied in all box dimensions. Long-range electrostatics were calculated using the Particle Mesh-Ewald method in connection with periodic boundary conditions. Van der Waals and Coulombic interaction cutoffs were set to 1.2 nm and the LINCS algorithm was used to constrain all bond lengths. Following equilibration, production MD runs were performed for 500 ns for each system. Here the parameter settings were similar to the NPT equilibration step, except that all restraints were removed and the time constant for pressure coupling was set to 2.0 ps. The time step for integration was 2 fs with coordinates and velocities saved every 20 ps for analysis.

### Analysis

The structural stability (RMSD) and dynamic properties (RMSF) of A$\beta_{42}$ are analyzed for backbone atoms using GROMACS tools. To characterize the effects of the peptide on the orientational mobility of the lipid molecules we calculated the lipid tail order parameter $S_{\mathrm{CD}}$ defined as

$$S_{\mathrm{CD}} = \left\langle \frac{3\cos^2\theta - 1}{2} \right\rangle , \tag{1}$$

where $\theta$ is the angle between the C–H bond vector (in the simulation) or the C–D bond vector (in the experiment) and the bilayer normal. The angular brackets indicate averaging over lipids and over time. The center of mass motion (COM) is calculated for the turn region from residue 25 to 30 of A$\beta_{42}$ inside the membrane hydrophobic core. The secondary structure of A$\beta_{42}$ was analyzed using the DSSP method [89]. The salt bridge between D23 and K28 is considered to be formed when the distance between the anionic carboxylate of D23 and the cationic ammonium from K28 is $< 4.5$ Å. We used the grid-based membrane analysis tool GRIDMAT-MD to quantify the extent to which the peptide affects the lipid headgroup arrangement and bilayer thickness [90]. For the bilayer thickness we report phosphate-to-phosphate (P–P) distances. To measure the depth of water molecule penetration into the hydrophobic core, water density profiles projected onto the $z$-direction were calculated, while water permeation across the membrane was quantified using VMD [91].

## Acknowledgments

We gratefully acknowledge the Jülich Supercomputing Centre for providing and maintaining the computing resources used in this work (Computing time grant JICS62). We thank Dr. Michael Owen for fruitful discussions and proofreading the manuscript.

## References

1. Blennow K, de Leon M, Zetterberg H (2006) Alzheimers disease. Lancet 368: 387–403.

2. Selkoe DJ (2000) The origins of Alzheimer disease - A is for amyloid. J Am Med Assoc 283: 1615–1617.

3. Roberson ED, Mucke L (2006) 100 years and counting: Prospects for defeating Alzheimer's disease. Science 314: 781–784.

4. Thinakaran G, Koo EH (2008) Amyloid Precursor Protein Trafficking, Processing, and Function. J Biol Chem 283: 29615–29619.

5. Jarrett JT, Berger EP, Lansbury PT (1993) The carboxy terminus of the beta-amyloid protein is critical for the seeding of amyloid formation - implications for the pathogenesis of Alzheimers-disease. Biochemistry 32: 4693–4697.

6. Younkin SG (1998) The role of A beta 42 in Alzheimer's disease. J Physiol Paris 92: 289–292.

7. Haass C, Selkoe D (2007) Soluble protein oligomers in neurodegeneration: lessons from the alzheimers amyloid $\beta$-peptide. Nat Rev Mol Cell Biol 8: 101-112.

8. Kirkitadze M, Bitan G, Teplow D (2002) Paradigm shifts in alzheimers disease and other neurodegenerative disorders: the emerging role of oligomeric assemblies. J Neurosci Res 69: 567-577.

9. Walsh D, Selkoe D (2007) A$\beta$ oligomers: A decade of discovery. J Neurochem 101: 1172–1184.

10. Mohamed A, de Chaves EP (2011) A internalization by neurons and glia. Int J Alzheimers Dis 2011: 127984.

11. Williams TL, Serpell LC (2011) Membrane and surface interactions of alzheimers a$\beta$ peptide – insights into the mechanism of cytotoxicity. FEBS J 278: 17.

12. Terzi E, Hölzemann G, Seelig J (1997) Interaction of alzheimer -amyloid peptide(1-40) with lipid membranes. Biochemistry 36: 14845-14852.

13. Buchsteiner A, Hauss T, Dante S, Dencher NA (2010) Alzheimer's disease amyloid-beta peptide analogue alters the ps-dynamics of phospholipid membranes. Biochim Biophys Acta-Biomembr 1798: 1969–1976.

14. Eckert GP, Wood WG, Mueller WE (2010) Lipid Membranes and beta-Amyloid: A Harmful Connection. Curr Protein Pept Sci 11: 319–325.

15. Kayed R, Sokolov Y, Edmonds B, McIntire TM, Milton SC, et al. (2004) Permeabilization of lipid bilayers is a common conformation-dependent activity of soluble amyloid oligomers in protein misfolding diseases. J Biol Chem 279: 46363–46366.

16. Lau TL, Ambroggio EE, Tew DJ, Cappai R, Masters CL, et al. (2006) Amyloid-beta peptide disruption of lipid membranes and the effect of metal ions. J Mol Biol 356: 759–770.

17. Sepulveda FJ, Parodi J, Peoples RW, Opazo C, Aguayo LG (2010) Synaptotoxicity of Alzheimer beta amyloid can be explained by its membrane perforating property. PLoS ONE 5: e11820.

18. Arispe N, Pollard H, Rojas E (1994) $\beta$-amyloid $Ca^{2+}$-channel hypothesis for neuronal death in Alzheimer disease. Mol Cell Biochem 140: 119-125.

19. Lin H, Zhu Y, Lal R (1999) Amyloid $\beta$ protein (140) forms calcium-permeable, $Zn^{2+}$-sensitive channel in reconstituted lipid vesicles. Biochemistry 38: 11189–11196.

20. Quist A, Doudevski I, Lin H, Azimova R, Ng D, et al. (2005) Amyloid ion channels: A common structural link for protein misfolding disease. Proc Natl Acad Sci USA 102: 10427-10432.

21. Janssen J, Beck J, Campbell T, Dickinson A, Fox N, et al. (2003) Early onset familial alzheimer's disease - mutation frequency in 31 families. Neurology 60: 235–239.

22. Wakutani Y, Watanabe K, Adachi Y, Wada-Isoe K, Urakami K, et al. (2004) Novel amyloid precursor protein gene missense mutation (d678n) in probable familial alzheimer's disease. J Neurol Neurosurg Psychiatry 75: 1039–1042.

23. Hashimoto M, Hori Y, Yamada K, Wakutani Y, Condron MC, et al. (2004) App (h6r and d7n) mutations linked to familial alzheimers disease alter a amyloid assembly but not app processing. Soc Neurosci Abstr : 218.–214.

24. Levy E, Carman M, Fernandezmadrid I, Power M, Lieberburg I, et al. (1990) Mutation of the alzheimers-disease amyloid gene in hereditary cerebral-hemorrhage, dutch type. Science 248: 1124–1126.

25. Broeckhoven V, Haan J, Bakker E, Hardy J, Hul WV, et al. (1990) Amyloid beta protein precursor gene and hereditary cerebral hemorrhage with amyloidosis (dutch). Science 248.

26. Walsh D, Lomakin A, Benedek G, Condron M, Teplow D (1997) Amyloid beta-protein fibrillogenesis - detection of a protofibrillar intermediate. J Biol Chem 272: 22364–22372.

27. Clements A, Allsop D, Walsh D, Williams C (1996) Aggregation and metal-binding properties of mutant forms of the amyloid a beta peptide of alzheimer's disease. J Neurochem 66: 740–747.

28. Miravalle L, Tokuda T, Chiarle R, Giaccone G, Bugiani O, et al. (2000) Substitutions at codon 22 of alzheimer's a beta peptide induce diverse conformational changes and apoptotic effects in human cerebral endothelial cells. J Biol Chem 275: 27110–27116.

29. Murakami K, Irie K, Morimoto A, Ohigashi H, Shindo M, et al. (2003) Neurotoxicity and physicochemical properties of a beta mutant peptides from cerebral amyloid angiopathy - implication for the pathogenesis of cerebral amyloid angiopathy and alzheimer's disease. J Biol Chem 278: 46179–46187.

30. Hendriks L, Vanduijn C, Cras P, Cruts M, Vanhul W, et al. (1992) Presenile-dementia and cerebral-hemorrhage linked to a mutation at codon-692 of the beta-amyloid precursor protein gene. Nature Genet 1: 218–221.

31. Walsh D, Hartley D, Condron M, Selkoe D, Teplow D (2001) In vitro studies of amyloid beta-protein fibril assembly and toxicity provide clues to the aetiology of flemish variant (ala(692) -¿ gly) alzheimer's disease. Biochem J 355: 869–877.

32. Nilsberth C, Westlind-Danielsson A, Eckman C, Condron M, Axelman K, et al. (2001) The 'arctic' app mutation (e693g) causes alzheimer's disease by enhanced a beta protofibril formation. Nat Neurosci 4: 887–893.

33. Walsh D, Hartley D, Kusumoto Y, Fezoui Y, Condron M, et al. (1999) Amyloid beta-protein fibrillogenesis - structure and biological activity of protofibrillar intermediates. J Biol Chem 274: 25945–25952.

34. Hartley D, Walsh D, Ye C, Diehl T, Vasquez S, et al. (1999) Protofibrillar intermediates of amyloid beta-protein induce acute electrophysiological changes and progressive neurotoxicity in cortical neurons. J Neurosci 19: 8876–8884.

35. Grabowski T, Cho H, Vonsattel J, Rebeck G, Greenberg S (2001) Novel amyloid precursor protein mutation in an iowa family with dementia and severe cerebral amyloid angiopathy. Ann Neurol 49: 697–705.

36. Pifer PM, Yates EA, Legleiter J (2011) Point mutations in a$\beta$ result in the formation of distinct polymorphic aggregates in the presence of lipid bilayers. PLoS ONE 6: e16248.

37. Krone MG, Baumketner A, Bernstein SL, Wyttenbach T, Lazo ND, et al. (2008) Effects of familial alzheimers disease mutations on the folding nucleation of the amyloid -protein. J Mol Biol 381: 221 - 228.

38. Tarus B, Straub JE, Thirumalai D (2008) Structures and free-energy landscapes of the wild type and mutants of the a2130 peptide are determined by an interplay between intrapeptide electrostatic and hydrophobic interactions. J Mol Biol 379: 815 - 829.

39. Friedman R (2011) Aggregation of amyloids in a cellular context: modelling and experiment. Biochem J 438: 415-426.

40. Straub JE, Thirumalai D (2011) Toward a Molecular Theory of Early and Late Events in Monomer to Amyloid Fibril Formation. Annu Rev Phys Chem 62: 437-463.

41. Jang H, Zheng J, Lal R, Nussinov R (2008) New structures help the modeling of toxic amyloid beta ion channels. Trends BiochemSci 33: 91–100.

42. Jang H, Zheng J, Nussinov R (2007) Models of beta-amyloid ion channels in the membrane suggest that channel formation in the bilayer is a dynamic process. Biophys J 93: 1938–1949.

43. Jang H, Arce FT, Capone R, Ramachandran S, Lal R, et al. (2009) Misfolded Amyloid Ion Channels Present Mobile beta-Sheet Subunits in Contrast to Conventional Ion Channels. Biophys J 97: 3029–3037.

44. Jang H, Arce F, Mustata M, Ramachandran S, Capone R, et al. (2011) Antimicrobial protegrin-1 forms amyloid-like fibrils with rapid kinetics suggesting a functional link. Biophys J 100: 1775–1783.

45. Capone R, Mustata M, Jang H, Arce FT, Nussinov R, et al. (2010) Antimicrobial protegrin-1 forms ion channels: Molecular dynamic simulation, atomic force microscopy, and electrical conductance studies. Biophys J 98: 2644–2652.

46. Capone R, Jang H, Kotler SA, Kagan BL, Nussinov R, et al. (2012) Probing structural features of alzheimer's amyloid-beta pores in bilayers using site-specific amino acid substitutions. Biochemistry 51: 776-785.

47. Arce FT, Jang H, Ramachandran S, Landon PB, Nussinov R, et al. (2011) Polymorphism of amyloid beta peptide in different environments: implications for membrane insertion and pore formation. Soft Matter 7: 5267-5273.

48. Strodel B, Lee J, Whittleston C, Wales D (2010) Transmembrane structures for Alzheimer's A$\beta_{1-42}$ oligomers. J Am Chem Soc 132: 13300–13312.

49. Poojari C, Kukol A, Strodel B (2013) How the amyloid-$\beta$ peptide and membranes affect each other: an extensive simulation study. Biochim Biophys Acta (Biomembr)) 1828: 327–339.

50. Lemkul JA, Bevan DR (2008) A comparative molecular dynamics analysis of the amyloid beta-peptide in a lipid bilayer. Arch Biochem Biophys 470: 54–63.

51. Lemkul JA, Bevan DR (2009) Perturbation of membranes by the amyloid beta-peptide - a molecular dynamics study. FEBS J 276: 3060–3075.

52. Lemkul JA, Bevan DR (2011) Lipid composition influences the release of Alzheimer's amyloid beta-peptide from membranes. Protein Sci 20: 1530-1545.

53. Davis CH, Berkowitz ML (2009) Interaction between amyloid-beta peptide and phospholipid bilayers: A molecular dynamics study. Biophysical J 96: 785-797.

54. Davis CH, Berkowitz ML (2009) Structure of the Amyloid-beta (1-42) Monomer Absorbed To Model Phospholipid Bilayers: A Molecular Dynamics Study. J Phys Chem B 113: 14480–14486.

55. Davis CH, Berkowitz ML (2010) A molecular dynamics study of the early stages of amyloid-beta(1-42) oligomerization: The role of lipid membranes. Proteins 78: 2533–2545.

56. Xu YC, Shen JJ, Luo XM, Zhu WL, Chen KX, et al. (2005) Conformational transition of amyloid beta-peptide. Proc Natl Acad Sci U S A 102: 5403–5407.

57. Miyashita N, Straub JE, Thirumalai D (2009) Structures of $\beta$-amyloid peptide 1–40, 1–42, and 1–55—the 672–726 fragment of app—in a membrane environment with implications for interactions with $\gamma$-secretase. J Am Chem Soc 131: 17843-17852.

58. Friedman R, Pellarin R, Caflisch A (2009) Amyloid aggregation on lipid bilayers and its impact on membrane permeability. J Mol Biol 387: 407-415.

59. Friedman R, Pellarin R, Caflisch A (2010) Soluble protofibrils as metastable intermediates in simulations of amyloid fibril degradation induced by lipid vesicles. J Phys Chem Lett 1: 471-474.

60. Zhao J, Wang Q, Liang G, Zheng J (2011) Molecular Dynamics Simulations of Low-Ordered Alzheimer beta-Amyloid Oligomers from Dimer to Hexamer on Self-Assembled Monolayers. Langmuir 27: 14876-14887.

61. Zhao LN, Chiu SW, Benoit J, Chew LY, Mu Y (2011) Amyloid beta Peptides Aggregation in a Mixed Membrane Bilayer: A Molecular Dynamics Study. J Phys Chem B 115: 12247-12256.

62. de Planque MRR, Raussens V, Contera SA, Rijkers DTS, Liskamp RMJ, et al. (2007) beta-sheet structured beta-amyloid(1-40) perturbs phosphatidylcholine model membranes. J Mol Biol 368: 982–997.

63. Marchesi V (2005) An alternative interpretation of the amyloid A beta hypothesis with regard to the pathogenesis of Alzheimer's disease. Proc Natl Acad Sci USA 102: 9093–9098.

64. Arispe N (2004) Architecture of the Alzheimer's A$\beta$P ion channel pore. J Membrane Biol 197: 33-48.

65. Xiao D, Fu L, Liu J, Batista VS, Yan EC (2012) Amphiphilic Adsorption of Human Islet Amyloid Polypeptide Aggregates to Lipid/Aqueous Interfaces. J Mol Biol 421: 537 - 547.

66. Grant MA, Lazo ND, Lomakin A, Condron MM, Arai H, et al. (2007) Familial Alzheimer's disease mutations alter the stability of the amyloid beta-protein monomer folding nucleus. Proc Natl Acad Sci USA 104: 16522-16527.

67. MacCallum JL, Bennetta WFD, Tieleman DP (2008) Distribution of amino acids in a lipid bilayer from computer simulations. Biophys J 94: 3393-3404.

68. Monticelli L, Kandasamy S, Periole X, Larson R, Tieleman D, et al. (2008) The martini coarse grained forcefield: extension to proteins. J Chem Theor Comput 4: 819-834.

69. Kyte J, Doolittle RF (1982) A simple method for displaying the hydropathic character of a protein. J Mol Biol 157: 105 - 132.

70. Cordomí A, Perez JJ (2007) Molecular dynamics simulations of rhodopsin in different one-component lipid bilayers. J Phys Chem B 111: 7052–7063.

71. Shafrir Y, Durell S, Arispe N, Guy HR (2010) Models of membrane-bound alzheimer's abeta peptide assemblies. Proteins: Struct, Func and Bioinf 78: 3473-3487.

72. Sahlin C, Lord A, Magnusson K, Englund H, Almeida CG, et al. (2007) The Arctic Alzheimer mutation favors intracellular amyloid-$\beta$ production by making amyloid precursor protein less available to $\alpha$-secretase. J Neurochem 101: 854–862.

73. Mason RP, Jacob RF, Walter MF, Mason PE, Avdulov NA, et al. (1999) Distribution and fluidizing action of soluble and aggregated amyloid beta-peptide in rat synaptic plasma membranes. J Biol Chem 274: 18801–18807.

74. Ambroggio EE, Kim DH, Separovic F, Barrow CJ, Barnham KJ, et al. (2005) Surface behavior and lipid interaction of Alzheimer beta-amyloid peptide 1-42: A membrane-disrupting peptide. Biophys J 88: 2706–2713.

75. Lin H, Bhatia R, Lal R (2001) Amyloid $\beta$ protein forms ion channels: implications for alzheimers disease pathophysiology. FASEB J 15: 2433-2444.

76. Urbanc B, Cruz L, Yun S, Buldyrev SV, Bitan G, et al. (2004) In silico study of amyloid $\beta$-protein folding and oligomerization. Proc Natl Acad Sci USA 101: 17345-17350.

77. Barrow CJ, Yasuda A, Kenny PT, Zagorski MG (1992) Solution conformations and aggregational properties of synthetic amyloid $\beta$-peptides of alzheimer's disease: Analysis of circular dichroism spectra. J Mol Biol 225: 1075–1093.

78. Lee JP, Stimson ER, Ghilardi JR, Mantyh PW, Lu YA, et al. (1995) $^1$h nmr of a$\beta$ amyloid peptide congeners in water solution. conformational changes correlate with plaque competence. Biochemistry 34: 5191-5200.

79. Lührs T, Ritter C, Adrian M, Riek-Loher D, Bohrmann B, et al. (2005) 3d structure of alzheimer's amyloid-$\beta$(142) fibrils. Proc Natl Acad Sci USA 102: 17342–17347.

80. Petkova AT, Yau WM, Tycko R (2006) Experimental constraints on quaternary structure in alzheimer's $\beta$-amyloid fibrils. Biochemistry 45: 498-512.

81. Massi F, Peng JW, Lee JP, Straub JE (2001) Simulation study of the structure and dynamics of the alzheimer's amyloid peptide congener in solution. Biophys J 80: 31–44.

82. Straub JE, Guevara J, Huo S, Lee JP (2002) Long time dynamic simulations: Exploring the folding pathways of an alzheimer's amyloid a$\beta$-peptide. Acc Chem Res 35: 473481.

83. Ma B, Nussinov R (2002) Stabilities and conformations of alzheimer's $\beta$-amyloid peptide oligomers (A$\beta$(16-22), A$\beta$(16-35) and A$\beta$(10-35)): Sequence effects. Proc Natl Acad Sci USA 99: 14126-14131.

84. Hess B, Kutzner C, van der Spoel D, Lindahl E (2008) GROMACS 4: Algorithms for highly efficient, load-balanced, and scalable molecular simulation. J Chem Theor Comput 4: 435-447.

85. Oostenbrink C, Villa A, Mark AE, Gunsteren WFV (2004) A biomolecular force field based on the free enthalpy of hydration and solvation: The GROMOS force-field parameter sets 53A5 and 53A6. J Comput Chem 25: 1656–1676.

86. Kukol A (2009) Lipid Models for United-Atom Molecular Dynamics Simulations of Proteins. J Chem Theory Comput 5: 615–626.

87. Olubiyi OO, Strodel B (2012) Structures of the amyloid $\beta$-peptides A$\beta_{1-40}$ and A$\beta_{1-42}$ as influenced by pH and a D-peptide. J Phys Chem B 116: 3280–3291.

88. Kandt C, Ash WL, Tieleman DP (2007) Setting up and running molecular dynamics simulations of membrane proteins. Methods 41: 475–488.

89. Kabsch W, Sander C (1983) Dictionary of protein secondary structure: Pattern recognition of hydrogen-bonded and geometrical features. Biopolymers 22: 2577-2637.

90. Allen WJ, Lemkul JA, Bevan DR (2009) GridMAT-MD: A Grid-Based Membrane Analysis Tool for Use With Molecular Dynamics. J Comput Chem 30: 1952–1958.

91. Humphrey W, Dalke A, Schulten K (1996) VMD – visual molecular dynamics. J Molec Graphics 14: 33-38.

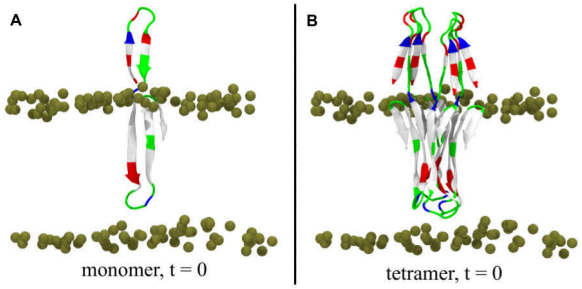


**Figure 1.** Initial structures for the MD runs: (A) $\beta$-sheet monomer, (B) $\beta$-sheet tetramer. The peptide is shown in cartoon and colored based on the physicochemical properties of the residues: blue, basic; red, acidic; white, hydrophobic; green, polar. The bilayer phosphorus atoms are shown as van der Waals spheres in tan color. Lipid tails and water molecules are not shown for clarity.

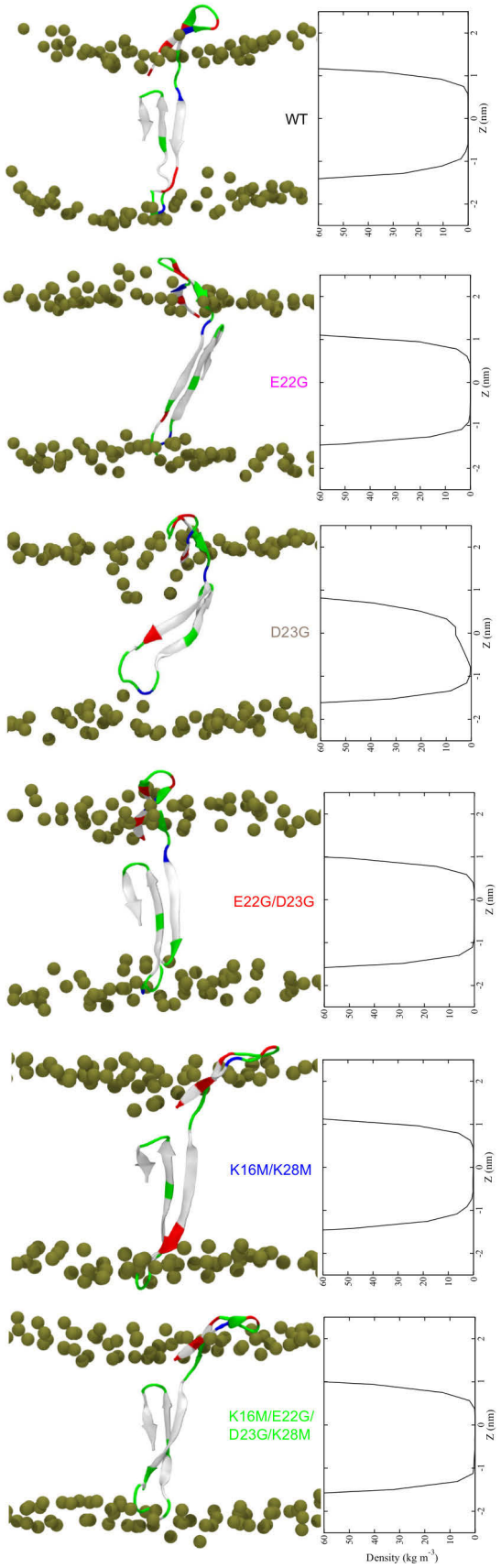


**Figure 2.** (Left) Final structures of the $\beta$-sheet monomer at $t = 500$ ns. The coloring explanation for the peptides and lipids is given in Fig. 1. (Right) Time averaged water density within the bilayer with inserted A$\beta_{42}$ monomer.

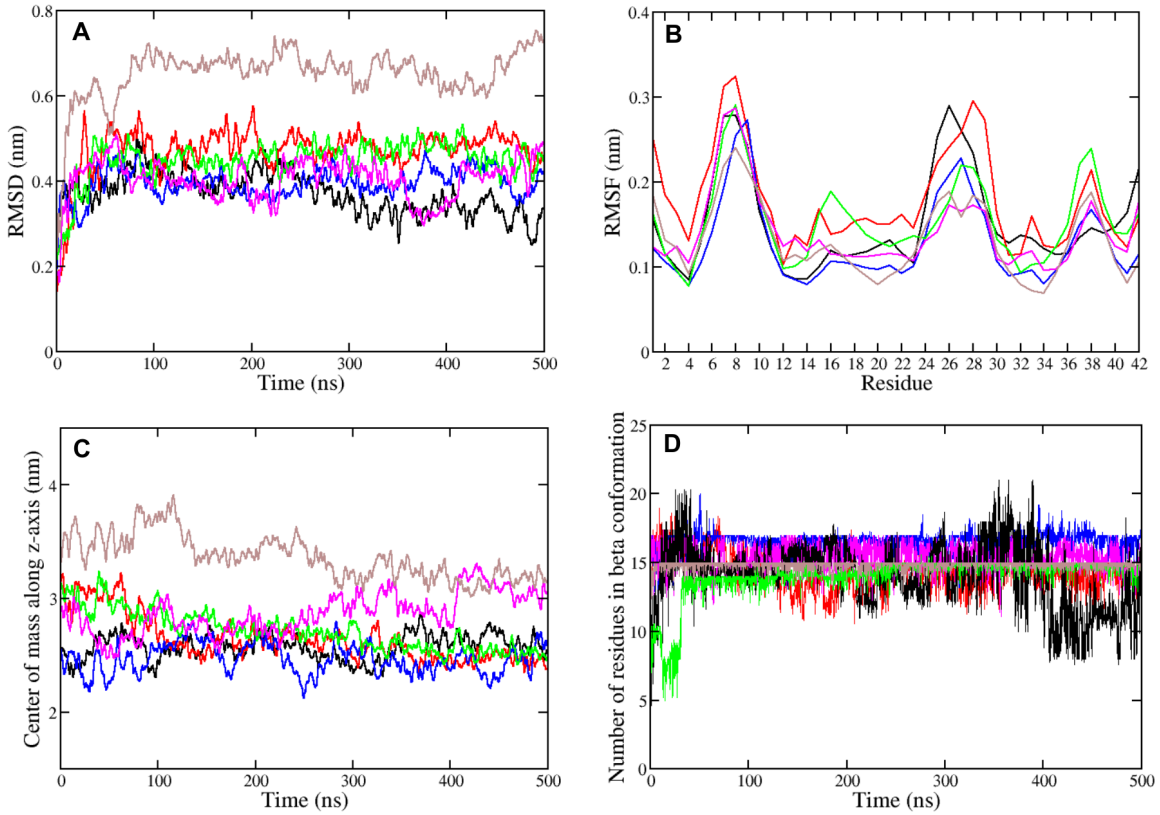


**Figure 3.** (A) Backbone root mean square deviation, (B) backbone root mean square fluctuation, (C) center of mass motion of residues 25 to 30, (D) number of transmembrane residues in $\beta$ conformation for the $\beta$-sheet monomer of wild type and mutant A$\beta_{42}$: black, WT; magenta, E22G; ochre, D23G; red, E22G/D23G; blue, K16M/K28M; green, K16M/E22G/D23G/K28M.

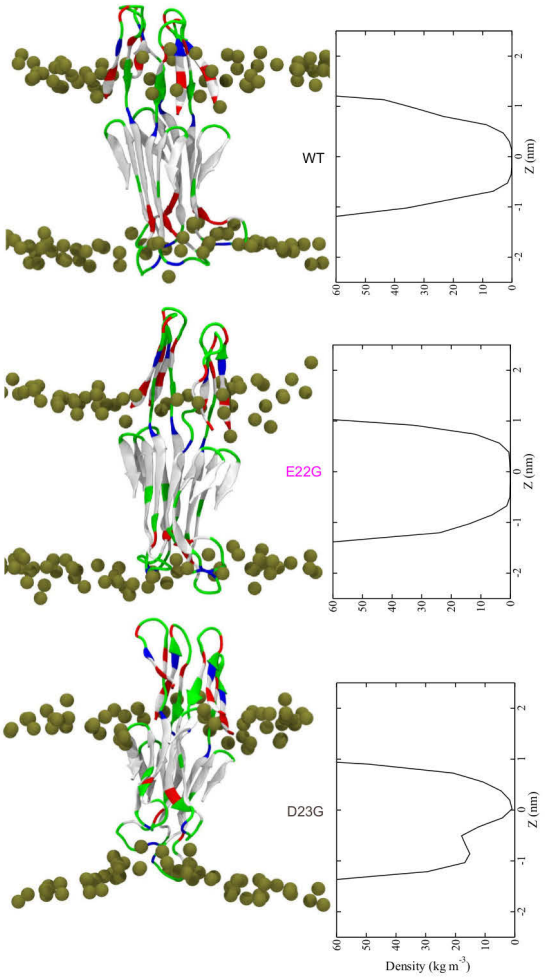


**Figure 4.** (Left) Final structures of the $\beta$-sheet tetramer at $t = 500$ ns. The coloring explanation for the peptides and lipids is given in Fig. 1. (Right) Time averaged water density within the bilayer with inserted A$\beta_{42}$ tetramer.

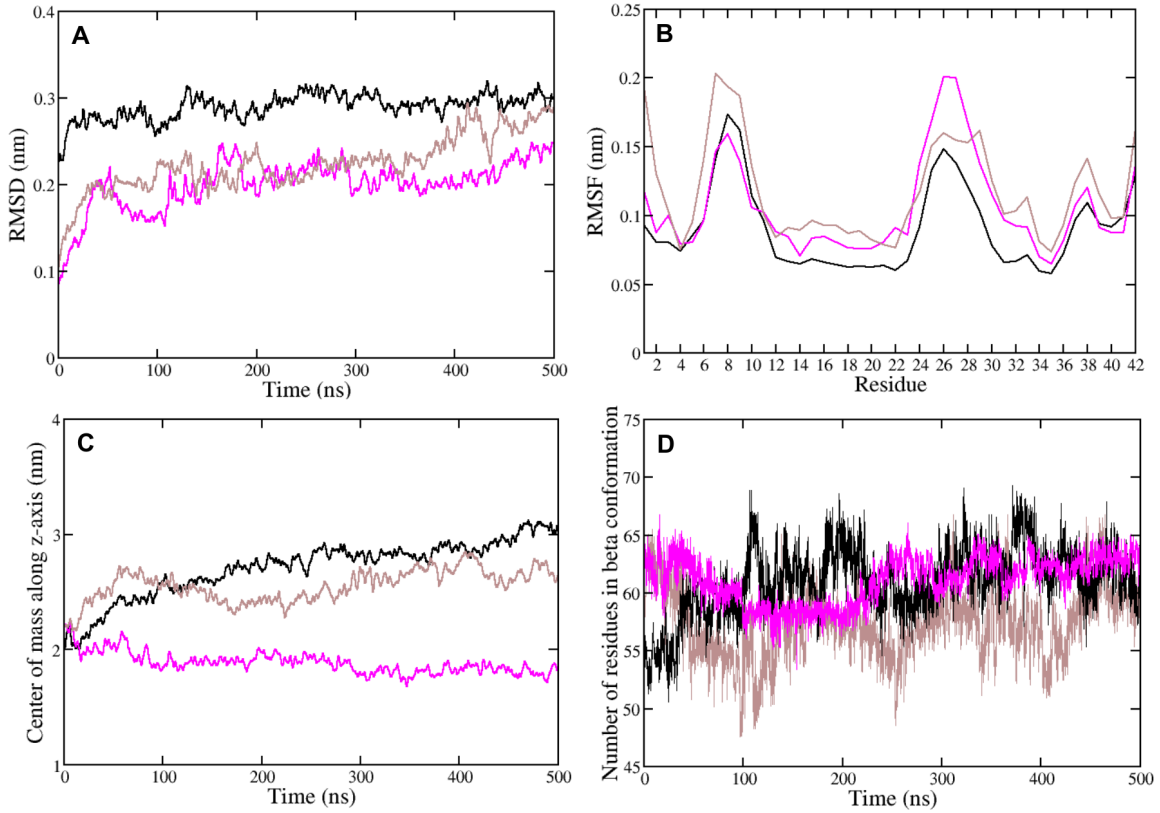


**Figure 5.** (A) Backbone root mean square deviation, (B) backbone root mean square fluctuation, (C) center of mass motion of residues 25 to 30, (D) number of transmembrane residues in $\beta$ conformation for the $\beta$-sheet tetramer of wild type and mutant A$\beta_{42}$: black, WT; magenta, E22G; ochre, D23G.

# Tables

**Table 1. Peptide and POPC bilayer properties resulting from membrane-inserted WT and mutant A$\beta_{42}$.**

| | A$\beta_{42}$ mutant | hyropathy index | $\beta$ count per peptide | Area per lipid [Å$^2$] top | Area per lipid [Å$^2$] bottom | bilayer thickness [nm] | # $H_2O$ passage |
|---|---|---|---|---|---|---|---|
| | peptide-free$^\dagger$ | n/a | n/a | 69.3 | 69.3 | 3.51 | 0 |
| monomer | WT | 8.6 | $14.1 \pm 2.3$ | 62.6 | 63.4 | 3.55 | 1 |
| monomer | E22G | 11.7 | $15.4 \pm 0.8$ | 66.1 | 66.3 | 3.54 | 3 |
| monomer | D23G | 11.7 | $14.8 \pm 0.3$ | 64.1 | 69.9 | 3.51 | 5 |
| monomer | E22G/D23G | 14.8 | $14.4 \pm 1.2$ | 66.7 | 66.8 | 3.54 | 2 |
| monomer | K16M/K28M | 20.2 | $16.5 \pm 0.6$ | 67.3 | 66.7 | 3.51 | 4 |
| monomer | K16M/E22G/ D23G/K28M | 26.4 | $14.0 \pm 1.6$ | 64.8 | 67.2 | 3.55 | 5 |
| tetramer | WT | 8.6 | $15.3 \pm 0.8$ | 62.6 | 65.3 | 3.49 | 5 |
| tetramer | E22G | 11.7 | $15.3 \pm 0.5$ | 65.4 | 65.2 | 3.46 | 8 |
| tetramer | D23G | 11.7 | $14.3 \pm 0.7$ | 63.2 | 69.1 | 3.48 | 22 |

Provided are the hydropathy index of WT and mutant A$\beta_{42}$ using the hydropathy scale of Kyte and Doolittle [69], time-averaged values for the number of transmembrane residues in $\beta$ conformation per peptide (with standard deviation), the area per lipid headgroup in the top and bottom leaflet, the P–P bilayer thickness, and the number of water molecules passing through the POPC bilayer.
$^\dagger$ The bilayer values for the peptide-free bilayer are taken from a 100 ns MD simulation of a POPC-only bilayer [49].

Supporting Information

# Stability of transmembrane amyloid β-peptide and membrane integrity tested by site-specific $A\beta_{42}$ mutations

Chetan Poojari[1] , Birgit Strodel[1,2,*]

[1] Forschungszentrum Jülich GmbH, Institute of Complex Systems: Structural Biochemistry (ICS-6), 52425 Jülich, Germany

[2] Institute of Theoretical and Computational Chemistry, Heinrich Heine University Düsseldorf, Universitätsstr. 1, 40225 Düsseldorf, Germany

* E-mail: b.strodel@fz-juelich.de

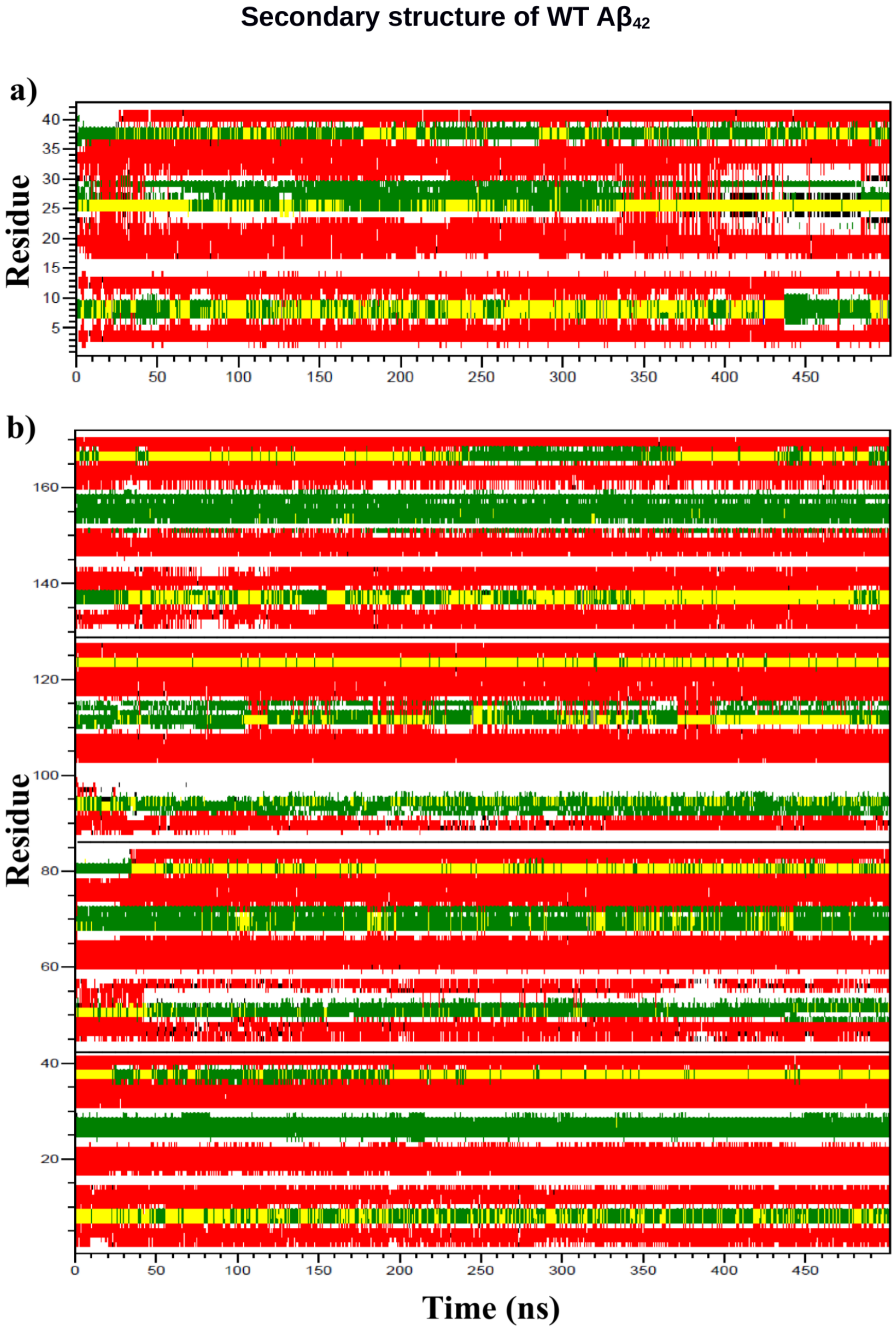


**Figure S1:** Secondary structure analysis for the 500 ns MD simulations of WT $A\beta_{42}$ as (a) β-sheet monomer and (b) β-sheet tetramer in a POPC bilayer. For the β-sheet tetramer, the four peptides are separated by black lines. Legend: white, coil; red, β-sheet; black, β-bridge; green, bend; yellow, turn.

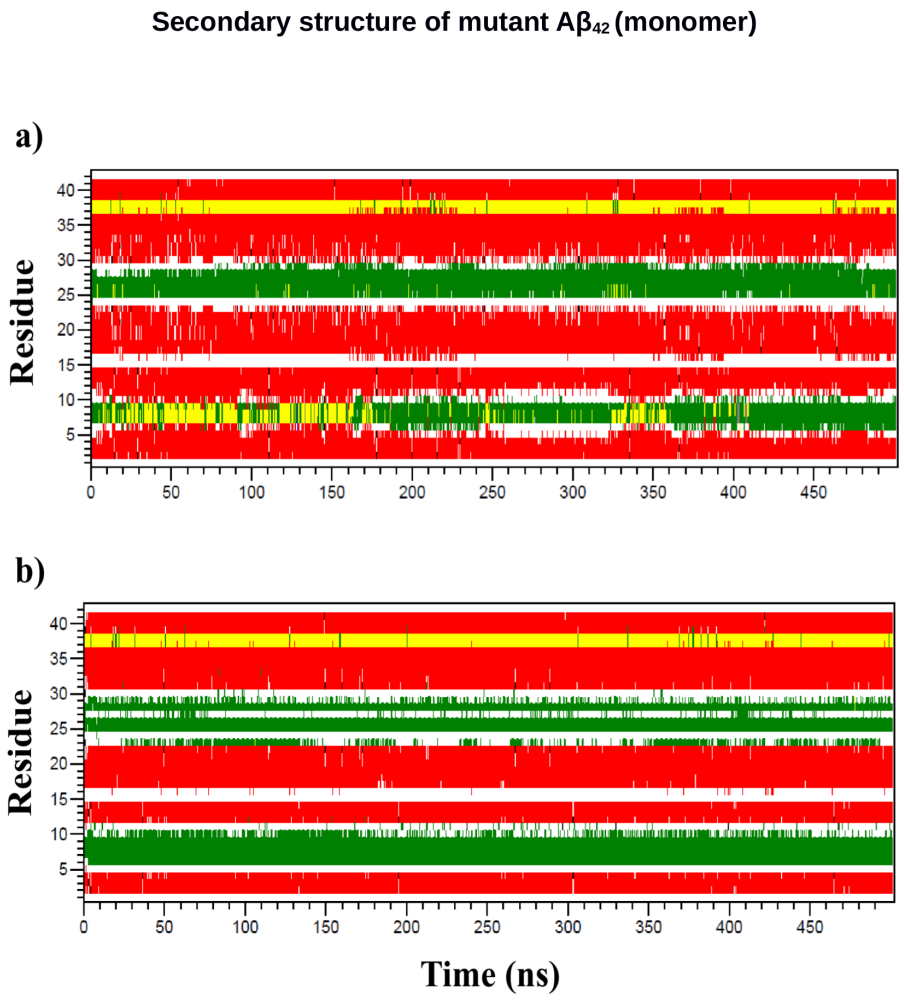


**Figure S2:** Secondary structure analysis for the 500 ns MD simulations of mutant $A\beta_{42}$ monomer as (a) E22G, (b) D23G in a POPC bilayer. Legend: white, coil; red, β-sheet; black, β-bridge; green, bend; yellow, turn.

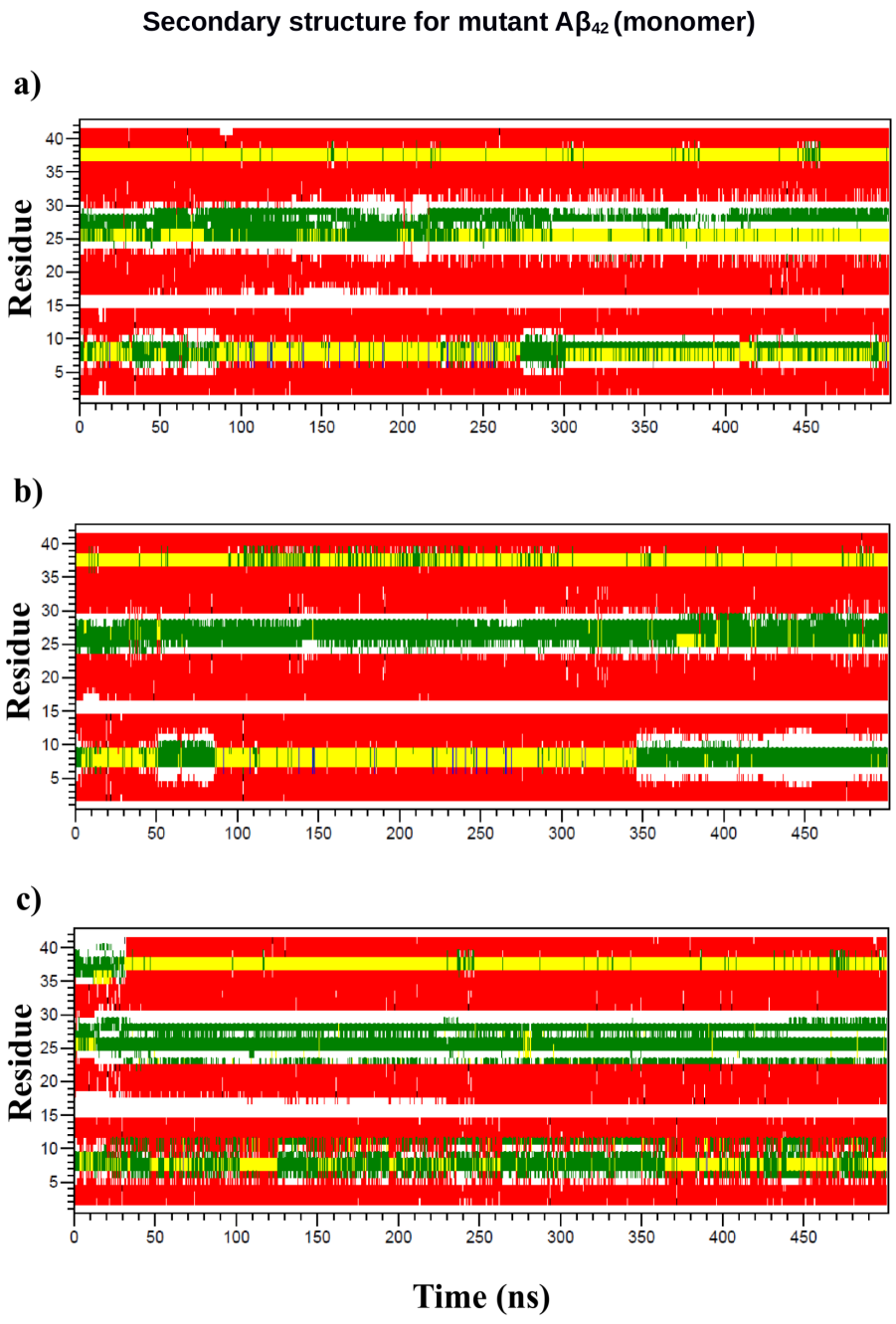


**Figure S3:** Secondary structure analysis for the 500 ns MD simulations of mutant $A\beta_{42}$ monomer as (a) E22G/D23G, (b) K16M/K28M, (c) K16M/E22G/D23G/K28M in a POPC bilayer. Legend: white, coil; red, β-sheet; black, β-bridge; green, bend; yellow, turn.

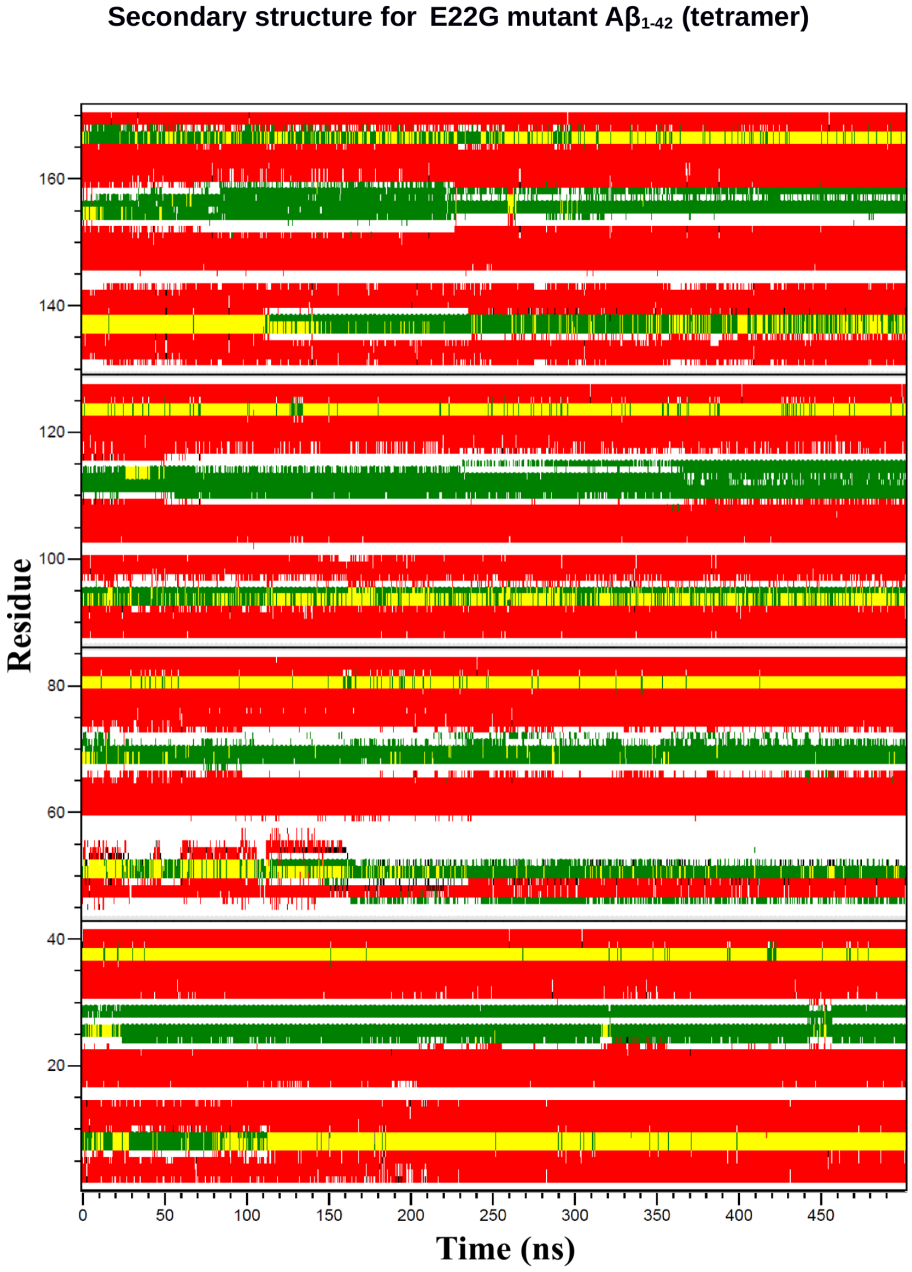


**Figure S4:** Secondary structure analysis for the 500 ns MD simulation of E22G $A\beta_{1-42}$ tetramer in a POPC bilayer. The four peptides are separated by black lines. Legend: white, coil; red, β-sheet; black, β-bridge; green, bend; yellow, turn.

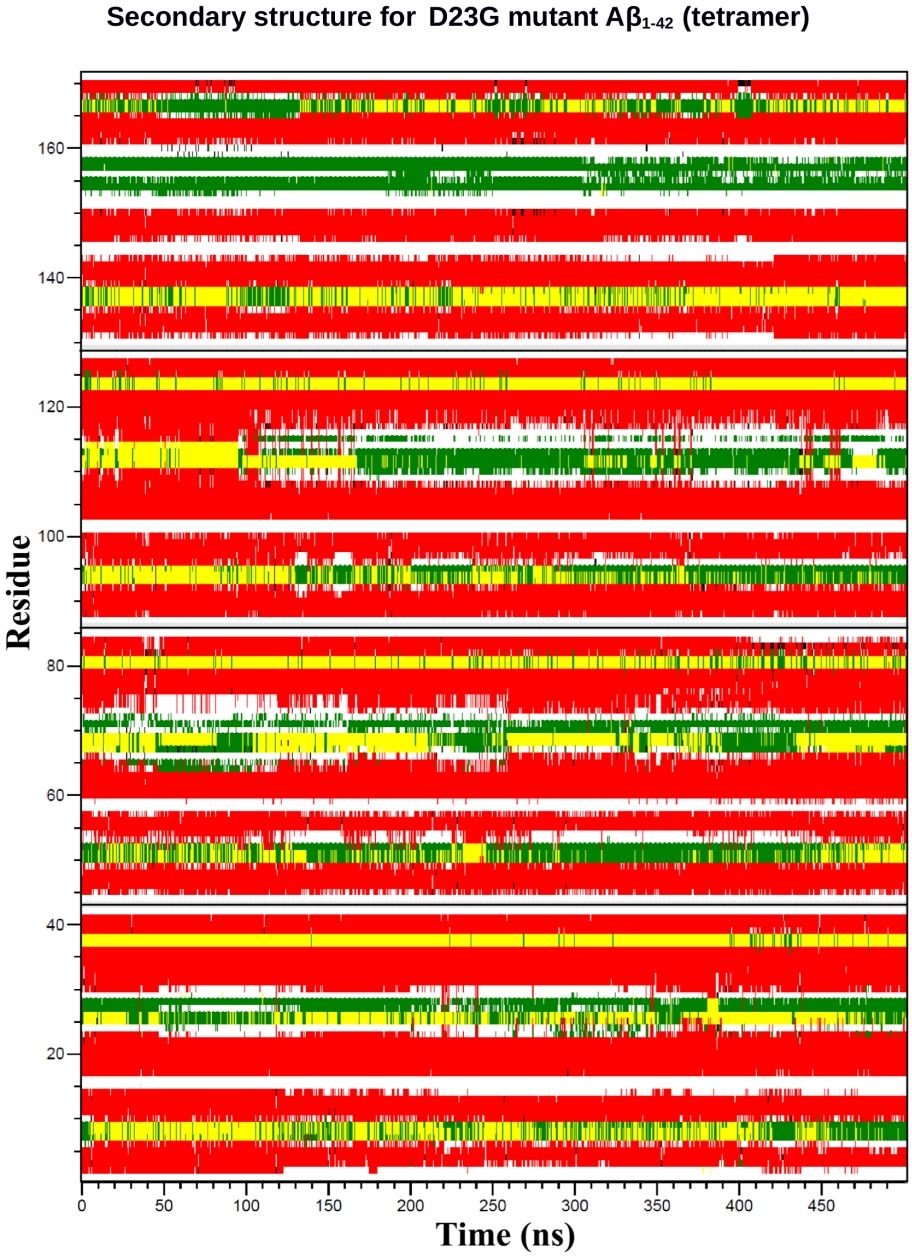


**Figure S5:** Secondary structure analysis for the 500 ns MD simulation of E22G $A\beta_{1-42}$ tetramer in a POPC bilayer. The four peptides are separated by black lines. Legend: white, coil; red, β-sheet; black, β-bridge; green, bend; yellow, turn.

**D23-K28 salt bridge in the sheet structure**

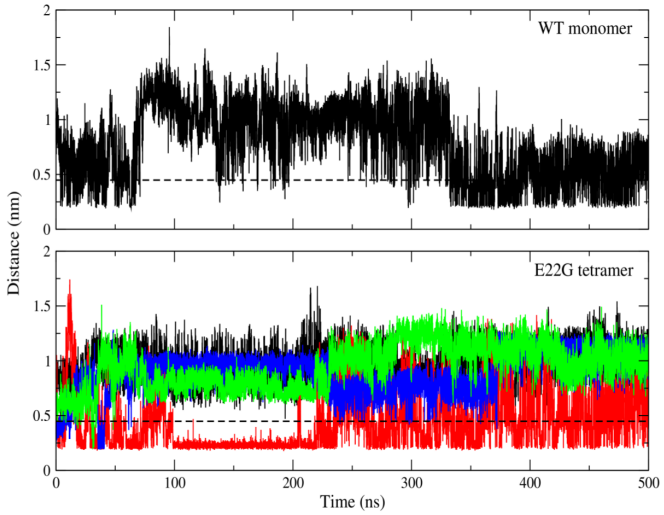


**Figure S6:** Minimum distance between the anionic carboxylate of D23 and the cationic ammonium from K28 in the WT monomer and the E22G tetramer. For E22G tetramer, this distance is analysed for all four peptides. The black dashed line at 0.45 nm corresponds to the cutoff distance to define a salt bridge in a protein. This analysis was performed for all systems studied. Only for the two systems, where salt bridge formation was observed, results are shown here.

**Peptide-lipid interactions for E22G monomer**

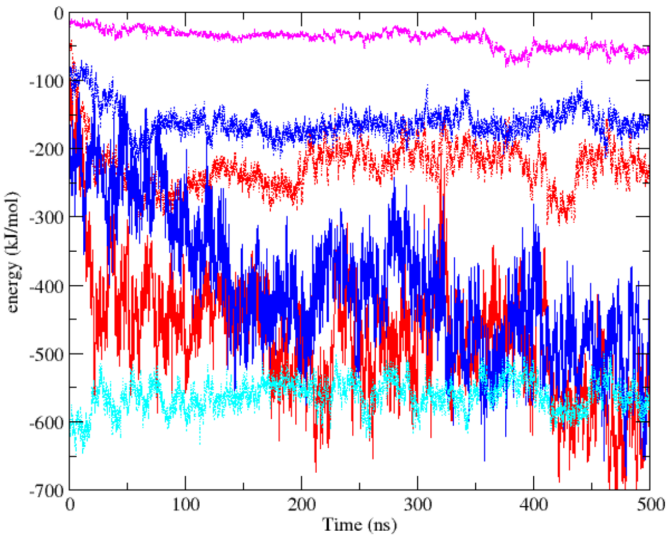


**Figure S7:** Peptide-lipid interactions for the E22G monomer decomposed into Coulomb (solid) and Lennard-Jones (LJ) interactions (dashed). Shown are the interactions of residues 1–16 with the lipid headgroups (red, Coulomb and LJ) and lipid tails (magenta, LJ), and of residues 17–42 with the lipid headgroups (blue, Coulomb and LJ) and lipd tails (cyan, LJ).

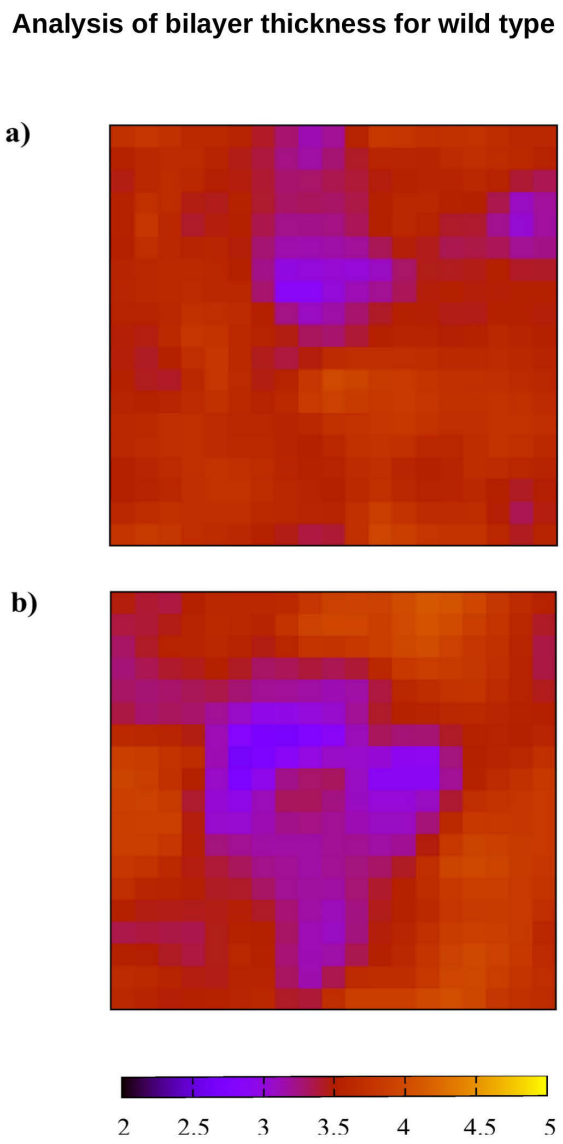


**Figure S8:** Bilayer phosphate-to-phosphate thickness, averaged over the last 400 ns of the 500 ns MD simulations of WT $A\beta_{1-42}$ as (a) β-sheet monomer and (b) β-sheet tetramer in a POPC bilayer. The axes of each plot corresponds to the *x*- and *y*- direction of the lipid bilayer (both about 6.5 nm). The bilayer thickness was calculated with GRIDMAT-MD using 20 grid points in both directions. In each case, the peptide (not shown) is located near the center of each square where the thickness is smallest. The legend shows bilayer thickness (nm), mapped to the corresponding colors.

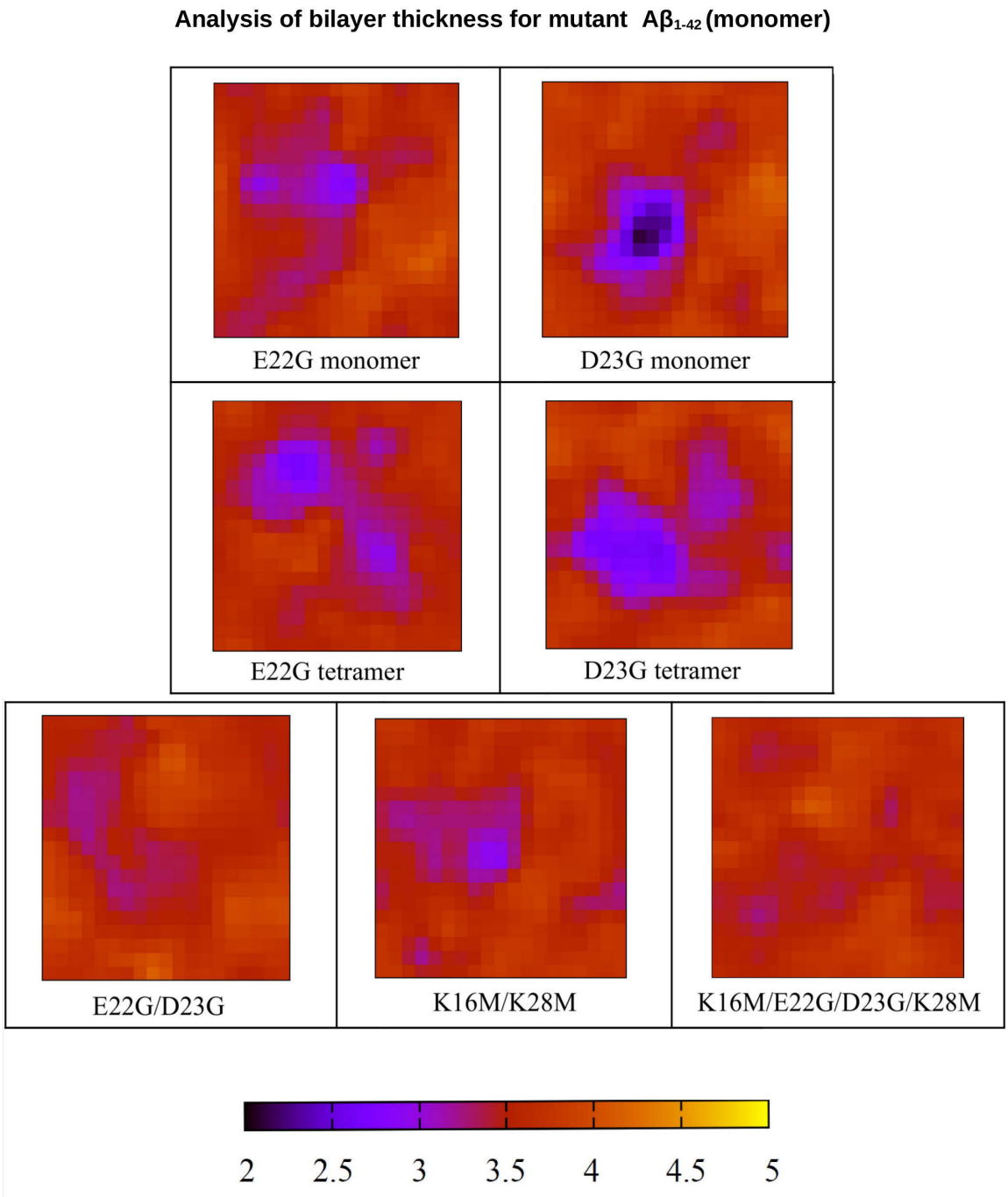


**Figure S9:** Bilayer phosphate-to-phosphate thickness, averaged over last 400 ns of the 500 ns MD simulations of $A\beta_{1\text{-}42}$ mutants (monomers and tetramers). For the coloring explanation, see Fig. S11.

**Deuterium order parameters for Aβ$_{1-42}$ (monomer)–POPC bilayer systems**

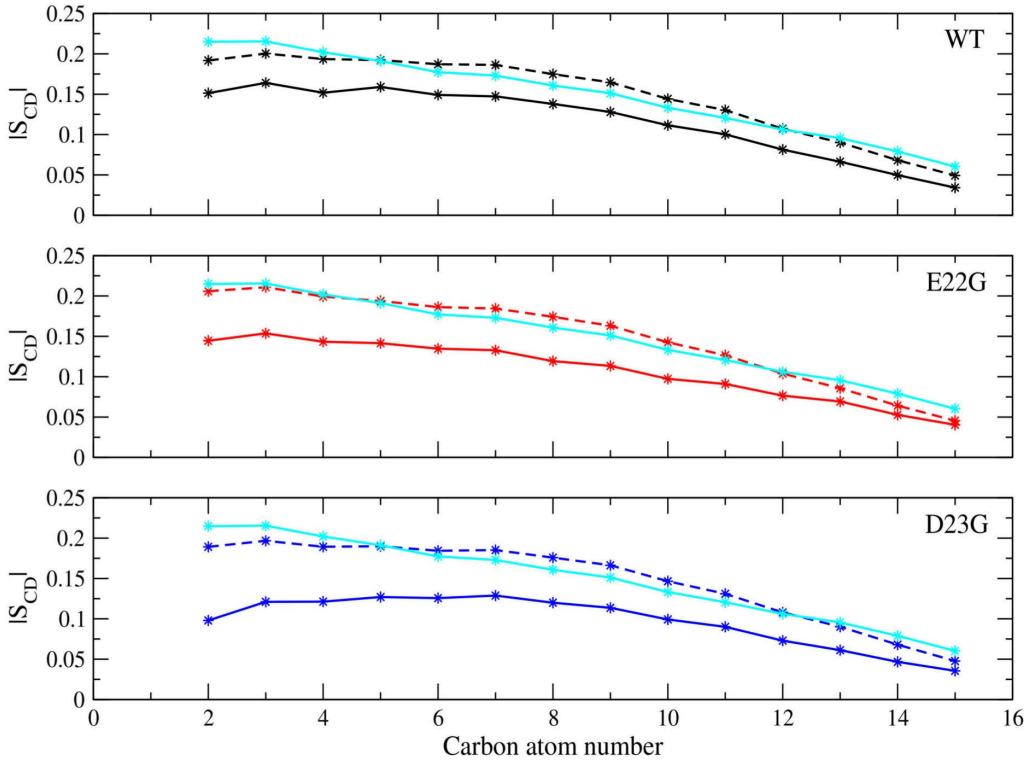


**Figure S10:** Time-averaged (over the last 400 ns of the MD simulations) order parameter $S_{CD}$ of the sn-1 chain of the POPC lipids. Results are shown for wild type and mutant Aβ$_{1-42}$ and are distinguished for the lipids within 5 Å of Aβ$_{1-42}$ (solid) and for the lipids >5 Å away from Aβ$_{1-42}$ (dashed). For comparison, $S_{CD}$ of the sn-1 chain obtained from a 100 ns MD run of peptide-free POPC bilayer is also presented (cyan).

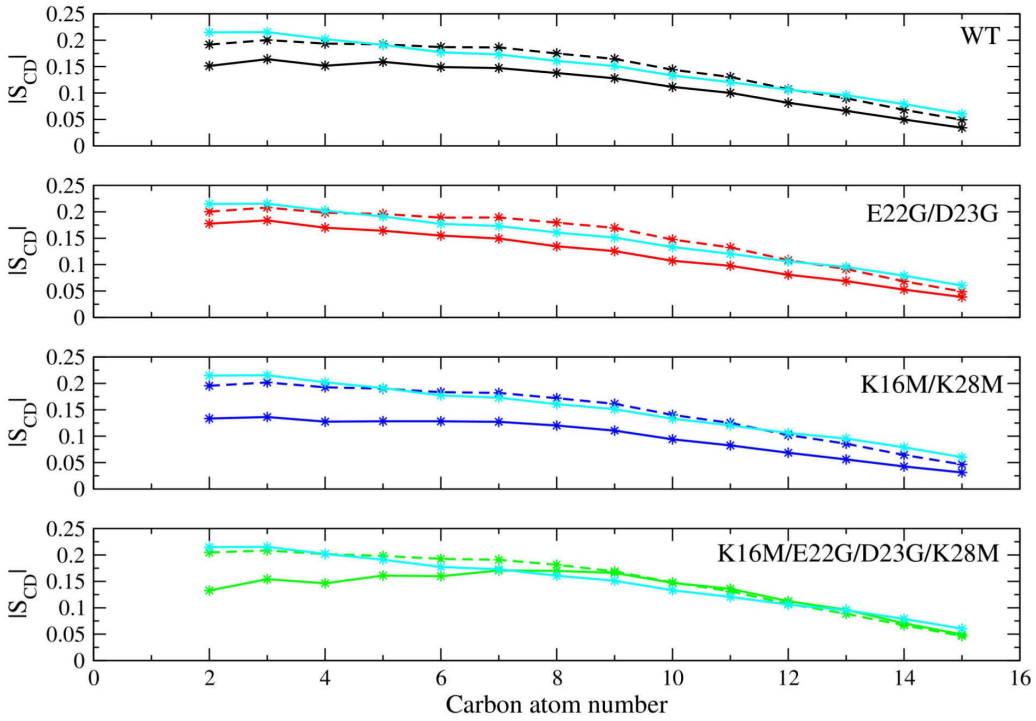


**Figure S11:** Time-averaged (over the last 400 ns of the MD simulations) order parameter $S_{CD}$ of the sn-1 chain of the POPC lipids. Results are shown for wild type and mutant $A\beta_{1-42}$ and are distinguished for the lipids within 5 Å of $A\beta_{1-42}$ (solid) and for the lipids >5 Å away from $A\beta_{1-42}$ (dashed). For comparison, $S_{CD}$ of the sn-1 chain obtained from a 100 ns MD run of peptide-free POPC bilayer is also presented (cyan).

**Deuterium order parameters for Aβ$_{1-42}$ (tetramer)–POPC bilayer systems**

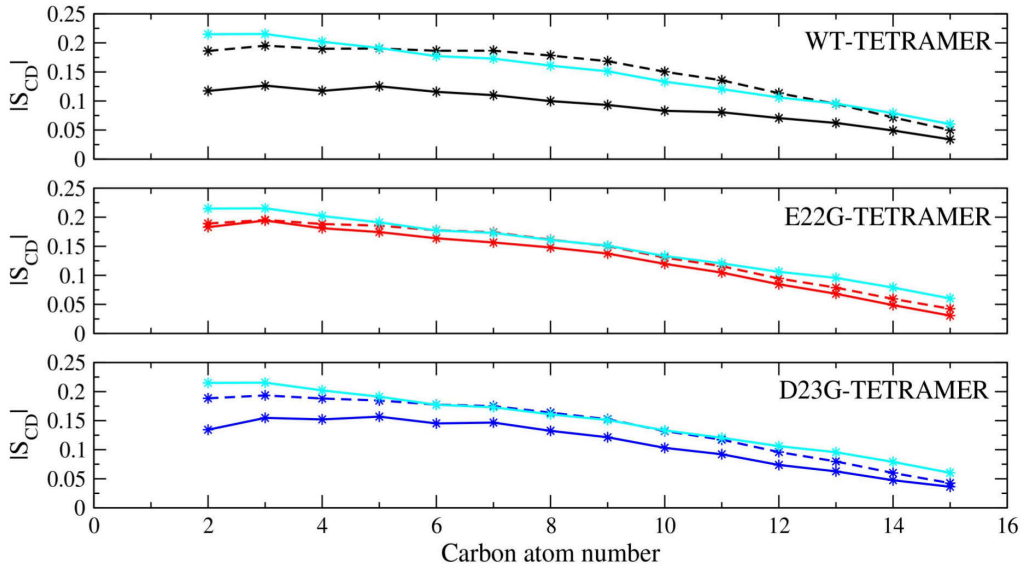


**Figure S12:** Time-averaged (over the last 400 ns of the MD simulations) order parameter $S_{CD}$ of the sn-1 chain of the POPC lipids. Results are shown for wild type and mutant Aβ$_{1-42}$ and are distinguished for the lipids within 5 Å of Aβ$_{1-42}$ (solid) and for the lipids >5 Å away from Aβ$_{1-42}$ (dashed). For comparison, $S_{CD}$ of the sn-1 chain obtained from a 100 ns MD run of peptide-free POPC bilayer is also presented (cyan).

## 4.3 Membrane permeation induced by aggregates of human islet amyloid polypeptides

# Membrane permeation induced by aggregates of human islet amyloid polypeptides

Chetan Poojari
Forschungszentrum Jülich GmbH,
Institute of Complex Systems: Structural Biochemistry (ICS-6)
52425 Jülich, Germany

Dequan Xiao
Department of Chemistry
Yale University, New Haven, CT 06520, USA

Victor S. Batista*
Department of Chemistry
Yale University, New Haven, CT 06520, USA

Birgit Strodel*
Forschungszentrum Jülich GmbH,
Institute of Complex Systems: Structural Biochemistry (ICS-6)
52425 Jülich, Germany
Institute of Theoretical and Computational Chemistry,
Heinrich Heine University Düsseldorf, 40225 Düsseldorf, Germany

*Corresponding Authors: victor.batista@yale.edu; b.strodel@fz-juelich.de

May 3, 2013

**Abstract**

Several neurodegenerative diseases such as Alzheimer's and Parkinson's diseases as well as non-neuropathic diseases such as type II diabetes and atrial amyloidosis are associated with aggregation of amyloid polypeptides into fibrillar structures, or plaques. Here, we focus on aggregates of the human islet amyloid polypeptide (hIAPP) implicated in type II diabetes. We find that hIAPP trimers and tetramers preserve their $\beta$-sheet secondary structures when inserted into lipid bilayers and lead to water permeation and $Na^+$ intrusion, consistent with ion-toxicity in islet $\beta$-cells. In particular, hIAPP trimers insert into bilayers of dipalmitoyl-phosphatidylglycerol (DPPG) at 60° relative to the membrane/water interface and form barrel-like structures that induce water permeability comparable to channel-forming proteins, like aquaporins and gramicidin-A. The predicted disruptive orientation is consistent with the amphiphilic properties of the hIAPP aggregates and could be probed by chiral sum frequency generation (SFG) spectroscopy, as predicted by the simulated SFG spectra.

*Keywords:* hIAPP aggregates; phospholipid membranes; protein-membrane interactions; permeability; water channel; type II diabetes

*Membrane permeation induced by hIAPP oligomers* 2

# Introduction

Fibrillar structures formed by protein aggregation are commonly associated with neurodegenerative diseases such as Alzheimer's, Parkinson's and Huntington's diseases as well as non-neuropathic diseases such as type II diabetes and atrial amyloidosis (1). Fibrils readily form *in vitro* and are typically composed of several twisted protofilaments that form cross $\beta$-sheets (2–5). These small oligomers are thought to affect the integrity of cellular membranes and induce ion toxicity (6–8). However, the molecular interactions responsible for the potential membrane disruptive effect of $\beta$-sheet aggregates remain unknown (9–14). Here, we explore these fundamental interactions through a fully atomistic study of hIAPP oligomers inserted in lipid bilayers, including molecular dynamics simulations of hIAPP trimers and tetramers at dipalmitoyl-phosphatidylglycerol (DPPG)/water interfaces.

Aggregates of human islet amyloid polypeptides (hIAPPs) are known to be associated with type II diabetes and are thought to be detrimental to $\beta$-cells (15–17). At physiological concentrations, hIAPP is a neuroendocrine hormone expressed by $\beta$-cells of the pancreatic islets of Langerhans (18, 19). hIAPP is cosecreted with insulin and regulates several metabolisms by reducing food intake (20), suppressing gastric emptying (21), and inhibiting glucagon release from pancreatic $\alpha$-cells (22, 23). In such a normal state, the 37-residue hIAPP adopts an unstructured conformation. At higher concentrations, however, hIAPP misfolds into $\beta$-sheet-rich amyloids, as shown by solid-state NMR studies (24), electron paramagnetic resonance spectroscopy, and infrared reflection absorption spectroscopy studies (25, 26), and acts as an insulin antagonist by inhibiting insulin secretion (27–29).

Several amino acid residues are known to be crucial for establishing the hIAPP secondary structure. In particular, it has been shown that residues from Ser20 to Ser29 are critical for fibril formation and toxicity (30), including Gly24–Ser28 in the mid-region. In fact, rodent IAPP (rIAPP) which differs from hIAPP in this amyloidogenic region by three proline amino acid substitutions at positions 25, 28 and 29 does not form fibrils (31). In addition, a single hIAPP missense mutation at position 20 (S20G) is associated with early onset of type II diabetes and has been shown to be more fibrillogenic and cytotoxic than wild type (WT) hIAPP (32).

Apart from amino acid substitutions inducing or inhibiting hIAPP fibrillization, it is known that interactions with membranes can enhance nucleation and catalyze fibril formation (33–36). Atomic force microscopy (AFM) has also revealed pore-like structures in membranes, indicating channel formation by hIAPP (37). However, it remains unclear whether hIAPP inserts

into these pores by preserving its $\beta$-sheet conformation. Insight on the conformation adopted by membrane-bound hIAPP could provide understanding of the interactions leading to membrane disruption and guidelines for the development of inhibitors of hIAPP insertion into lipid bilayers, aggregation, or misfolding into $\beta$-sheets. In fact, it is known that hIAPP can adopt different secondary structures when exposed to different conditions. For example, in addition to the unstructured conformation in the normal physiological state, hIAPP adopts an $\alpha$-helical structure in the presence of large unilamellar vesicles (LUVs) (36). The $\alpha$-helix conformation was also seen in the membrane-mimicking solvent trifluoroethanol (38). After longer incubation with LUVs, however, hIAPP adopts a $\beta$-sheet conformation (36).

Over the last decade several mechanisms of amyloidogenic cytotoxicity have been reported (6–8), including ion channel formation by oligomers (37, 39) and alteration of membrane morphology by fibril growth at the membrane surface (9, 40–43). It was demonstrated that hIAPP monomers are also capable of inserting into lipid monolayers, followed by aggregation inside the membrane or with hIAPP species on the membrane surface (26, 44). Fibril growth by aggregation at the membrane surface can change the overall membrane morphology or fluidity. Another reported mechanism for cytotoxicity is extraction of lipid molecules by hIAPP aggregates, a process that might induce ion permeation (34, 45). However, the hIAPP-membrane interactions remain poorly understood (35).

The initial interaction between hIAPP and negatively charged membranes is thought to be mediated by the N-terminal residues Lys1, Arg11 and His18 (35). In particular, His18 is thought to be essential for hIAPP/membrane interactions. In fact, a fluorescence microscopy study showed rapid increase in the intracellular calcium level after addition of $\text{hIAPP}_{1-19}$ to large unilamellar vesicles, while $\text{rIAPP}_{1-19}$ (which differs only in Arg18) was ineffective (46). The protonation state of His18 (pKa=6.2) is also important as revealed by the membrane disruption ability of $\text{hIAPP}_{1-19}$ which is pH dependent. At pH 6.0, where His18 is protonated, $\text{hIAPP}_{1-19}$ behaves like $\text{rIAPP}_{1-19}$ while at pH 7.3 the membrane disruption ability of $\text{hIAPP}_{1-19}$ was regained (46). Such disruption is correlated with the peptide conformation. NMR experiments of $\text{IAPP}_{1-19}$ showed that the toxic hIAPP polypeptide adopts a transmembrane orientation at pH 7.3, while the nontoxic rat polypeptide remains bound to the membrane surface (47). At pH 6.0, however, $\text{hIAPP}_{1-19}$ orients at the micelle surface similarly to $\text{rIAPP}_{1-19}$ (47). This change in orientation correlates with the significantly reduced ability of $\text{hIAPP}_{1-19}$ to induce ion permeability.

Previous molecular simulations studies have explored $\alpha$-helical hIAPP

polypeptides (48–50). One of these studies has shown that hIAPP aggregation of monomers and dimers takes place via the C-terminal peptide segment, when the N-terminal segment is preinserted into an anionic lipid bilayer, while electrostatic interactions due to the lipid headgroups attract the N-terminal residues to the membrane surface (48). Another study explored the stability of helical structures of $hIAPP_{1-25}$ segments, including WT and the S20G mutant interacting with the membrane surface. While the WT $hIAPP_{1-25}$ preserved the helical structure throughout the simulation, the S20G $hIAPP_{1-25}$ mutant adopted an L-shaped 'fibril-like' structure in (49). Another study explored annular hIAPP structures inserted into a zwitterionic lipid bilayer. The channels were seen to break into small oligomeric subunits, resembling the pore-like structures observed in AFM experiments (50). More recently, hIAPP aggregates were analyzed at the water/lipid interface by combining experimental chiral SFG spectroscopy and ab initio SFG simulations. It was found that hIAPP $\beta$-sheets orient with a tilting angle of $48^\circ$ relative to the surface when interacting with dipalmitoylphosphoglycerol (DPPG) monolayers, an orientation that is expected to induce disruption of the lipid membrane integrity (51). However, explicit molecular dynamics simulations of hIAPP $\beta$-sheets have yet to be reported. Here, we complement earlier studies of hIAPP/membrane interactions by exploring the insertion of hIAPP $\beta$-sheet aggregates into lipid layers, and analyzing their orientation relative to the lipid/water interface as correlated to their disruptive effect on membrane integrity. We perform molecular dynamics (MD) simulations of hIAPP trimers and tetramers in lipid layers, including hIAPP oligomers interacting with both monolayers and bilayers of DPPG. The reported simulations provide insights on the potential pathogenic effect of hIAPP, at the molecular level, particularly relevant to studies of the early stages of type II diabetes and other amyloid diseases.

# Methods

## Molecular Dynamics Simulations

All MD simulations reported in this paper, including studies hIAPP $\beta$-sheet trimers and tetramers inserted into DPPG monolayers and bilayers, were performed by using GROMACS 4.0 (52). The hIAPP peptide was described according to the GROMOS96 53A6 force-field (53) and a model of DPPG was buit by adding two carbon atoms to each of the acyl chains of dimyristoylphosphoglycerol (DMPG) (54). The initial configuration of hIAPP was prepared according to the parallel $\beta$-sheet structure determined by

solid-state NMR (24), where the $\beta$-strands Ala8–Val17 and Ser28–Tyr37 are separated by a turn region from His18 to Leu27. The N-terminal residues Lys1–Cys7 are mainly unstructured.

Figure 1 defines the orientation of hIAPP, relative to the membrane surface. The initial configurations of the hIAPP models were typically defined inserted into the lipid layer at 90°, relative to the membrane surface, or at about 48° as defined by our previous study based on chiral SFG spectroscopy and ab initio quantum chemistry (51) (Fig. S1). The tilted orientation is consistent with the amphiphilic properties of hIAPP $\beta$-sheets as it allows the N-terminal residues to reside in the water environment and most hydrophobic residues 12–27 in the hydrophobic membrane core (55, 56). The larger insertion angle in the DPPG monolayer was used to check that the results were independent of the initial configuration.

**DPPG bilayer setup.** The PACKMOL package (57) was used to build a DPPG bilayer patch of 256 lipids with 128 lipids in each leaflet. The DPPG bilayer patch was solvated with 9888 SPC water molecules and 256 $Na^+$ ions were added to neutralize the negatively charged DPPG molecules with each ion taking the place of a randomly chosen water molecule. The resulting DPPG bilayer system contained 42,208 atoms in a simulation box with dimensions of $8.6 \times 8.6 \times 8.0$ nm$^3$. The system was simulated for 100 ns at 323 K using a Nose-Hoover thermostat to regulate the temperature along with semiisotropic Parrinello-Rahman pressure coupling. The bilayer normal $z$-direction and $xy$-plane were coupled separately with a time constant of 2 ps maintaining a constant pressure of 1 bar independently in all directions. An isothermal compressibility of $4.5 \times 10^5$ bar$^{-1}$ was applied in all box dimensions. The analysis of the equilibrated DPPG bilayer yielded a highly ordered arrangement of DPPG tails (Fig. S2), with an average area of 0.6 nm$^2$ per lipid (Fig. S3), in agreement with previous studies of DPPG bilayers (58–60).

**DPPG monolayer setup.** DPPG monolayers were built from the DPPG bilayer system by separating the two leaflets (61). The lower leaflet was moved in the positive $z$-direction while the upper leaflet was displaced in the negative $z$-direction until the separation between both membrane surfaces was 5.4 nm. Thus, the resulting system consisted of two monolayers with 128 DPPG lipids per layer separated by a central layer, which was filled with 11,389 SPC water molecules and 256 $Na^+$ ions. The complete DPPG monolayer system included 47,271 atoms within the simulation box

of dimensions $8.6 \times 8.6 \times 16.0$ nm$^3$. The large box length in the $z$-direction is necessary to create a vacuum region above and below the lipid tails of the upper and lower monolayer, respectively, to avoid any interactions between tail atoms of the two monolayers. A representative configuration of the DPPG monolayer system is shown in Fig. S4. This system was simulated for 100 ns at 323 K using a Nose-Hoover thermostat to regulate the temperature with a time constant of 1 ps. To control the pressure, a surface tension pressure coupling scheme with a time constant of 4 ps was employed. An isothermal compressibility of $4.5 \times 10^5$ bar$^{-1}$ was applied in the lateral $x$ and $y$-directions, while the compressibility was set to zero in the $z$-direction to prevent box contraction.

**Simulations of membrane-inserted hIAPP.** Aggregates of hIAPP were inserted into DPPG membranes (i.e., monolayer and bilayer) by first removing the water molecules and $Na^+$ ions from the equilibrated model systems. Next, we inserted the hIAPP oligomers into the membranes by using the INFLATEGRO script (62), and then we solvated the systems with SPC water molecules and $Na^+$ counterions. The box dimensions were the same as for the corresponding simulations of the membranes without hIAPP. In the case of the monolayer system, hIAPP was inserted in only one of the two monolayers in the model system. An initial equilibration under isothermal-isochoric (NVT) conditions was performed for 1 ns during which the protein heavy atoms and phosphorous atoms of the lipid headgroups were restrained with a force constant of 10,000 kJ mol$^{-1}$ nm$^{-2}$. The systems were then equilibrated under isothermal-isobaric (NPT) conditions for 10 ns. Long-range electrostatic interactions were calculated using the Particle Mesh-Ewald sum method with periodic boundary conditions. Van der Waals and Coulombic interaction cutoffs were set to 1.2 nm and the LINCS algorithm was used to constrain all bond-lengths. Following equilibration, all restraints were removed and production MD runs were performed for 150 ns for each system. The time step for integration was 2 fs with coordinates and velocities saved every 20 ps for analysis.

## Analysis of the MD simulations

The structural stability of hIAPP was tested by calculating the root mean square deviation (RMSD) of backbone atoms. The secondary structure of hIAPP was analyzed using the DSSP (dictionary of protein secondary structure) method (63). The probability of hydrogen bond (H-bond) formation was considered based on a cutoff distance of 0.36 nm between donor and

acceptor atoms and a cutoff angle off linearity of 30°. For the representation of the predominant transmembrane hIAPP oligomers, we clustered the sampled configurations in each trajectory using the method by Daura *et al.* with a 0.2 nm cutoff for the backbone atoms (64). Here, we have used the last 100 ns of the trajectories only. To quantify the orientation of the hIAPP $\beta$-sheets relative to the lipid membrane surface we computed the tilt angle of $\beta$-strands using the GROMACS analysis tools g_bundle. Here, each $\beta$-strand was considered separately, yielding 6 angles for the trimer and 8 for the tetramer. To define the strand orientation we used the $C_\alpha$–$C_\alpha$ vector between residues Arg11 and Phe15 for the first $\beta$-strand in each peptide, and residues Leu27–Asn31 for the second $\beta$-strand per peptide (Fig. 1). Subsequently, we calculated the mean angle averaged over time and $\beta$-strands.

Various quantities were computed to gain insight into the effect of hIAPP on the membrane integrity. Water and ion permeation across the membrane was quantified by using the g_flux and g_count utilities (65). We used the grid-based membrane analysis tool GRIDMAT-MD to calculate the area per lipid and the bilayer thickness (66). For the bilayer thickness we report phosphate-to-phosphate (P–P) distances. To characterize the effects of the peptide on the orientational mobility of the lipid molecules we calculated the lipid tail order parameter $S_{\mathrm{CD}}$ defined as

$$S_{\mathrm{CD}} = \left\langle \frac{3\cos^2\theta - 1}{2} \right\rangle , \tag{1}$$

where the angular brackets indicate average over lipids and over time and $\theta$ is the angle between the C–H bond vector (in the simulation), or C–D bond vector (in the experiment), relative to the bilayer normal.

## Computation of water permeability coefficients

The calculation of permeability coefficients and the comparison with measured values provide a very valuable test of the simulations (67). The best-studied permeability coefficient is the osmotic permeability $p_{\mathrm{f}}$, which can be defined from the net water flux $j_{\mathrm{w}}$ in response to the concentration gradient of some solute, $\Delta c_{\mathrm{s}}$ across the membrane (68):

$$j_{\mathrm{w}} = p_{\mathrm{f}} \Delta c_{\mathrm{s}} \tag{2}$$

Based on the fluctuation dissipation theorem it is possible to compute the nonequilibrium quantity $p_{\mathrm{f}}$ from spontaneous permeation events under equilibrium (69, 70). In this study, we derive the water permeability from equilibrium simulations. Accordingly, the bulk water concentration $c_{\mathrm{w}}$ in the two

water compartments (beneath and above the membrane) equaled, and the water crossed the membrane in both possible directions (positive and negative $z$ direction). Assuming that permeation events in opposite directions are independent, we can thus replace the concentration gradients $\Delta c(+)$ and $\Delta c(-)$ by $c_{\mathrm{w}}$ when computing $p_{\mathrm{f}}$ under equilibrium conditions. Hence, by counting permeation events from our equilibrium MD simulations we can calculate $p_{\mathrm{f}}$ (70):

$$p_{\mathrm{f}} = \frac{n_{\mathrm{w}}}{2tc_{\mathrm{w}}}, \tag{3}$$

where $n_{\mathrm{w}}$ denotes the number of permeation events and $t$ is the simulation time. The factor of $1/2$ corrects for the permeation events counted in both directions during the simulation, while $p_{\mathrm{f}}$ is defined from the flux in one direction in response to a concentration gradient.

### Sum frequency generation spectrum simulations

We computed hyperpolarizability elements of the parallel $\beta$-sheet structures as previously reported (24, 51). The models are built by dividing the $\beta$-sheets into two $\beta$-sheet regions, the upper one including amino acid residues 8–17 and the lower one including amino acid residues 28–37. These two regions were subsequently subdivided into 16 partially overlapping tripeptide pairs (TPPs). The covalency of the dangling bonds in the fragments was completed according to the link-H atom scheme, forming amine and amide groups in the N- and C-terminal ends, respectively. The geometry of each TPP was optimized, subject to the constraint of fixed backbone dihedral angles to preserve the $\beta$-sheet configuration. Energy minimization and normal mode analysis were then performed at the density functional theory level, using the B3LYP functional and the 6-31G* basis set. Dipole derivatives of each vibrational mode were obtained using the keyword 'iop(7/33 = 1)' during a frequency calculation, and polarizability derivatives were obtained by performing the Raman vibrational analysis with the 'polar' keyword. All ab initio calculations were performed by using Gaussian 09 (71).

## Results

### Stability and orientation of membrane-bound hIAPP $\beta$-sheets

**hIAPP in lipid monolayers.** Figure 3 shows the tilt angle of the $\beta$-strands relative to the membrane normal, quantifying the orientation of the hIAPP model trimer and tetramer inserted in a DPPG monolayer. We show

that both hIAPP trimers and tetramers remain inserted in the lipid layer during the whole simulation time (as shown in Figs. 2 and 3), with an average angle of about 40° reached after the initial relaxation time of about 50–75 ns. This orientation is similar to the 48° angle predicted by chiral SFG spectroscopy and quantum chemistry calculations of hIAPP inserted in DPPG monolayers (51). The analysis of thermal fluctuations shows that the angles adopted by different $\beta$-strands exhibit larger fluctuations in the more flexible trimer than in the tetramer. The trimeric $\beta$-sheet is more flexible since it has only one interior peptide and the two peptides at the edges are less stabilized by intrasheet interactions than the interior peptides.

The analysis of trajectories shows that the tilted orientation of the hIAPP $\beta$-sheets is induced by three main electrostatic interactions. First, the hIAPP aggregates tend to align Arg11 at the membrane–water interface. Second, electrostatic attractions between Lys1 and the anionic DPPG head-groups anchor the N-terminus at the membrane surface. Third, the hydrophobic mismatch between the $\beta$-sheets and the lipid tails of the monolayer force hIAPP to tilt so that the polar and charged residues remain in the aqueous environment while the more hydrophobic residues remain inside the membrane (Fig. 2(a) and (b)). Consistent with these observations, we observe that the RMSD of the hIAPP trimer inserted in a monolayer is about 0.7 nm while the corresponding RMSD for the tetramer is about 0.45 nm (Fig. S5). Also, the average interpeptide interaction is −3239 kJ/mol per peptide in the tetramer while it is only −3112 kJ/mol per peptide in the trimer.

The reduced interpeptide interactions in the trimer are typically compensated by peptide-lipid (−605 kJ/mol per peptide) and peptide-water (−1457 kJ/mol per peptide) interactions. These interactions are weaker in the tetramer (−523 kJ/mol and −1418 kJ/mol, respectively) and correlate with changes in orientation of the $\beta$-sheet, as shown in Fig. S7. For instance, the peptide–peptide interaction increases slightly with time in the trimer as a result of the $\beta$-sheet partial solvation. At the same time, the tilt angle decreases, as driven by the more favorable peptide–lipid interactions. For both trimer and tetramer, water molecules embedded in the monolayer usually remain in the vicinity of polar residues between Ser20 and Ser29. The number of water molecules in the monolayer is larger for the trimer than for the tetramer (Fig. 3). $Na^+$ ions hardly ever insert into the lipid monolayer and when they do, they remain close to the membrane surface. The overall effect of these interactions is to preserve the almost perfect U-shape of the strand-turn-strand conformation in the tetramer but disrupt it in the trimer.

**hIAPP in lipid bilayers.** The analysis of hIAPP $\beta$-sheets inserted into lipid bilayers shows that the hIAPP aggregates are stable, during the whole simulation time of 150 ns, and insert more deeply into the hydrophobic membrane than into lipid monolayers. As shown in Fig. 2, the U-shape of the hIAPP conformation is fully preserved for the tetramer with a RMSD of only 0.35 nm. The trimer shows more flexibility with an average RMSD of 0.65 nm. The deep insertion increases the peptide-lipid hydrophobic interactions as well as the favorable contact of hydrophilic side chains and polar head groups on both sides of the lipid bilayer. These interactions lead to an orientation of about 60° relative to the membrane surface, as shown in Fig. 4 for the time evolution of the angles adopted by each $\beta$-strand and average orientation. As before, the $\beta$-strands in the trimer are more flexible than in the tetramer and enable the formation of a channel-like structure. In that structure, the $\beta$-sheets are staggered [Fig. S9(b)] leading to the formation of a distorted yet water-filled $\beta$-barrel, which is discussed in detail below.

Electrostatic interactions between the negatively charged lipid headgroups and the positively charged amino acid residues Arg11 and Lys1 couple the N-terminal residues and the surface of the lipid bilayer. The resulting interactions between hIAPP and the lipid environment are stronger for the trimer than for the tetramer, while the tetramer exhibits stronger peptide–peptide interactions. Quantitatively, the average peptide–peptide, peptide–lipid and peptide–water interaction energies per peptide are −3026 kJ/mol, −1002 kJ/mol and −1491 kJ/mol for the trimer, and −3164 kJ/mol, −710 kJ/mol, and −1434 kJ/mol, respectively, for the tetramer. Peptide-lipid interactions are stronger than in the monolayer since hIAPP interacts with lipid headgroups in both sides of the bilayer.

Thermal fluctuations of hIAPP oligomers inserted into lipid bilayers disturb the arrangement of lipids due to the tilted orientation of hIAPP aggregate relative to the membrane surface. These fluctuations induce displacements of the head groups (Fig. 2) that enable water and $Na^+$ ions to diffuse into the lipid bilayer. At equilibrium, we typically find 20–40 water molecules and as much as 5 $Na^+$ ions inside the DPPG bilayer, preferentially hydrating residues Ser20 to Ser29 (Fig. 4), which are known to be critical for fibril formation and toxicity (30). In particular, the trimer forms a channel-like structure across the lipid membrane and induces more water permeability than the tetramer, as quantified by the number of water molecules that translocate across the bilayer per unit time. We find that as much as 27 water molecules typically permeate the bilayer in 150 ns of dynamics when inserted by the hIAPP trimer while only 16 water molecules translocate in the same amount of time when inserted by the hIAPP tetramer.

## Membrane disruption by hIAPP oligomers

**Effect of hIAPP on membrane ordering.** hIAPP oligomers are known to disrupt the membrane integrity (6–8). However, little is known at the molecular level. Therefore, we have characterized the lipid properties as influenced by the perturbation of hIAPP aggregates. We compared the deuterium order parameter, $S_{\mathrm{CD}}$, of both acyl chains 1 and 2 (sn-1 and sn-2) for lipids within 0.5 nm of hIAPP to the corresponding values for lipids that are farther away from the peptide (72). Figs. S10–S13 show the results of the analysis along with $S_{\mathrm{CD}}$ for the peptide-free DPPG membranes. The comparison reveals a disordered, fluid phase, peptides next to hIAPP. The intrinsic disorder is caused by protein-lipid interactions that tilt the lipid chains (Fig. S14), as previously observed for other amyloid $\beta$-peptides implicated in Alzheimer's disease (72). Figs. S10–S13 also show that lipids that are $> 0.5$ nm away from the hIAPP aggregates are largely unaffected by hIAPP-lipid interactions. We note that the lipid disorder is less pronounced in the monolayer than in the bilayer since the hIAPP orientation enables the acyl chains in the monolayer to adjust better to the inserted peptides. In particular, note that the disorder due to the bulky side chains of Arg11, Phe15 and Phe23 is less extended in the monolayer than in the bilayer [Fig. S14(a) vs. (b)].

Another structural effect due to lipid disorder is the reduced thickness of the lipid bilayer next to the hIAPP aggregate. Fig. S15 shows that the bilayer is thinned by 1–2 nm in the vicinity of the peptides, while the lipids farther away from the peptide maintain the bilayer thickness of $\sim 4.2$ nm as in the absence of the hIAPP aggregate. We note that the reduced thickness results from favorable interactions between the protein and the lipid headgroups causing the lipids to be drawn into the membrane core (Fig. 2). These interactions also affect the Area-Per-Lipid (APL), as shown in Figs. S16–S17. Note that the average APL in the top leaflet of the trimer is reduced by more than 0.06 $\mathrm{nm}^2$ when compared to the peptide-free bilayer. In contrast, the lower leaflet remains almost unaffected. For the tetramer, however, the APL is reduced by about 0.04 $\mathrm{nm}^2$ for both leaflets. These differences between the trimer and tetramer effects result from the subtle interplay between hIAPP conformation, orientation, insertion-depth. The influence on APL also depends on the lipid layer morphology. For example, in DPPG monolayers both hIAPP trimers and tetramers increase the APL when compared to the monolayers without hIAPP. The APL increase is more significant around the hIAPP, as seen in Fig. 2.

**Membrane permeation resulting from hIAPP channel formation.** Figure 5(a) shows that the trimer loses its initial motif (i.e., the U-shaped strand-turn-strand conformation) by tilting the $\beta$-strands to form a channel-like structure in the lipid bilayer. The analysis of the trimer RMSD (Fig. S6) shows that the resulting conformation remains stable after the initial 70 ns relaxation in the lipid bilayer. The formation of this barrel-like structure is driven by formation of intra- and inter-peptide H-bonds in the hIAPP trimer [Fig. S9(a)]. Some of these H-bonds are formed between the two strands of one of the outer peptides (peptide 3 in Fig. S9), closing this side of the trimer. On the other side, however, the structure partially opens by breaking H-bonds in peptide 1. When adopting this partially open conformation, the trimer establishes a continuous transmembrane water-channel consistent with the calculated water density plot [Fig. 5(b)]. Water molecules typically enter through the open side of the distorted barrel and follow the channel-like structure of the hIAPP trimer on their path through the membrane [Fig. 5(a)]. The resulting water density correlates with the distribution of $Na^+$ ions [Fig. 5(b)]. $Na^+$ ions diffuse deep into the membrane and displace the lipid headgroups with them, inducing structural disorder. During the 150 ns simulation time, however, none of the $Na^+$ ions was able to translocate across the bilayer or exchange with $Na^+$ ions in the bulk. Therefore, it remains to be explored by longer time simulations whether ions translocate across the channels established by the hIAPP aggregates. The flow of ions would be consistent with the hypothesis that hIAPP induce ion permeability leading to the observed imbalance in ion homeostasis and toxicity (37, 73) that might be the cause for islet $\beta$-cell toxicity (26, 34, 44, 45).

Water molecules flow through the channel formed by the hIAPP trimer from one side of the lipid bilayer to the other (Fig. S18). While translocation can occur in 1 or 2 ns, in most cases the flux is slowed down as water molecules find stable positions inside the hIAPP/membrane complex. Therefore, the overall translocation can take as much as 20 ns before a water molecule permeates through the membrane. Most of the water molecules which stay longer inside the bilayer are preferentially found in the middle of the bilayer where the two leaflets meet. This is attributed to a free energy minimum in this region of the bilayer, for water molecules percolating through the hIAPP/bilayer (74), due to the of increase free volume in the middle of the bilayer even when there are no favorable interactions between water and hIAPP since the hIAPP residues in this region are all hydrophobic. According to Eq. (3) we can approximate the osmotic permeability $p_\mathrm{f}$. With $n_\mathrm{w} = 27$, $t = 150$ ns, and the molar concentration of water $c_\mathrm{w} = 1$ mol/18 cm$^3$ we obtain $p_\mathrm{f} = 2.7 \times 10^{-15}$ cm$^{-3}$/s. This value

is about one order of magnitude smaller than permeabilities reported (from simulation and experiment) for channel forming proteins such as aquaporins and gramicidin-A (69). However, we note that depending on the method used for determining $p_f$, these values can vary by almost an order of magnitude. Furthermore, the permeability we obtained here for hIAPP has to be considered as a rough estimate since it is based on only limited statistical data.

## Validating the orientation of hIAPP by chiral SFG spectra

Figure 6 compares the chiral SFG spectra of hIAPP aggregates (trimers and tetramers) embedded in DPPG monolayers and bilayers. The calculated traces correspond to angle-dependent PSP (p-polarized SFG, s-polarized visible, and p-polarized infrared) chiral SFG spectra, averaged over 75–100 ns spectra. These calculations could allow for the validation of the predicted arrangement, orientation and fluctuation of hIAPP at lipid/aqueous interfaces through direct comparisons with experimental data. Recent experiments have suggested that hIAPP $\beta$-sheet aggregates orient with an average tilt angle ($\psi$) of about 48° when interacting with a monolayer of DPPG lipids (panel a, Ref. (51)). Analogous experiments for DPPG bilayers, however, have yet to be reported.

Figure 6 (panel a) shows that the spectrum of a 1:1 mixture of hIAPP trimers and tetramers inserted into DPPG lipid monolayers with an average tilt angle of about 39° and 36°, respectively, is quite similar to the experimental spectrum obtained under typical experimental conditions. The small differences seen in panel (a), between the calculated and experimental spectra, might suggest that monomers, dimers and perhaps also larger aggregates (not included in the calculations) are part of the mixture probed by experiments.

Figure 6) (panels b and c) show that thermal fluctuations give rise to standard deviations in the calculated SFG spectra. Nevertheless, the spectrum obtained with a single average orientation (dash traces in Fig. 6) is very similar to the spectrum obtained by averaging all of the spectra computed along the MD trajectory (solid traces in Fig. 6). This indicates that the distributions of configurations of $\psi$ generated by thermal fluctuations must be quite symmetric around the average value. Another interesting observation is than the amide bands (I B, centered at 1620 $cm^{-1}$ and I A centered at 1660 $cm^{-1}$), are affected differently by thermal fluctuations. In fact, the standard deviation for the I B band are significantly larger that those of the I A band (error bars in Fig. 6), suggesting that the I A band is

more insensitive to fluctuations in the aggregate orientation.

The chiral SFG spectra obtained for hIAPP aggregates embedded in DPPG bilayers (close mimics of cellular membranes) are quite different from the corresponding spectra obtained for hIAPP in monolayers. Note that the ratio of intensities $I(B)/I(A)$ between the B and A bands is significantly larger for the bilayer than for the monolayer. In fact, the clear shoulder observed for the A band in monolayers transforms into a very diffuse feature in the bilayer spectra. This is due to the change in orientation of the hIAPP aggregates, with an increase in the average angle $\psi$ from $36 - 39^\circ$ in the monolayer to $59 - 60^\circ$ in the bilayer. These results also predict smaller standard deviations for both the amide I A-mode and B-mode regions in the lipid bilayer since the span of tilting angle around the average value of $\sim 60^\circ$ is relatively narrow. This is also observed in the comparison of the average SFG spectrum (solid lines) to the spectrum of the aggregate in the average orientation, indicating that the distribution of $\psi$ angles does not dramatically influence the SFG spectra in this case. Hence, we anticipate that the predicted orientation of hIAPP aggregates in lipid bilayers could be confirmed by future chiral SFG spectroscopy since the spectra of hIAPP interacting with lipid bilayers or cellular membranes are quite distinct from the spectra of hIAPP interacting with lipid monolayers.

# Discussion and Conclusions

## Transmembrane hIAPP $\beta$-sheets

We have performed MD simulations to investigate the position and orientation of $\beta$-sheet hIAPP oligomers at DPPG/water interfaces. We found that hIAPP aggregates maintain their $\beta$-sheet secondary structure and insert into the lipid layers in a tilted, membrane disruptive, configuration that exposes hydrophobic groups to the membrane and hydrophilic residues to the aqueous phase. In lipid monolayers, the average orientation of hIAPP trimers and trimers is rather flat, with a tilt angle relative to the membrane surface of close to $40^\circ$ (Fig. 2), in agreement with the overall orientation predicted by a single average configuration consistent with chiral SFG spectroscopy (51). In the lipid bilayer, hIAPP adopts a more upright orientation with a tilt angle close to $60^\circ$, due to interactions of the $\beta$-sheet with lipid headgroups and counterions on both sides of the membrane (Fig. 2). Differences in the orientation of hIAPP aggregates embedded in the monolayers versus bilayers are due to the balance of interactions at the peptide-membrane/water interface.

Several aspects of the hIAPP structural models, including the hydrophilic or hydrophobic environment of several sections of the hIAPP, are consistent with experimental observations. For example, MD simulations predict that the disulfide bond between residues 2 and 7 is in the aqueous phase, consistent with experiments showing that the disulphide bond is mildly perturbed upon membrane insertion (75). In addition, residues 1–10 remain in the water compartment, enabling Lys1 to interact with the membrane surface. Furthermore, the positively charged amino-acid residue Arg11 is stabilized by the negatively charged DPPG head groups, anchoring hIAPP to the lipid/water interface in both monolayers and bilayers. Residues 20–27 remain in the lipid phase, consistent with previously work suggesting that this segment of residues must be exposed to a hydrophobic environment (55, 56). In addition, His18 remains in the lipid phase during the MD simulations, consistent with the observation that in its deprotonated form (at pH 7.5) His18 induces more membrane disruption than when it is protonated at pH 6.0 (46).

Simulations of SFG spectra, averaged over orientations of the hIAPP aggregates sampled by MD simulations provide predictions that could be directly compared to experimental data. We find that a 1:1 mixture of hIAPP tetramers and timers gives a chiral SFG spectrum for hIAPP in DPPG monolayers in good agreement with experimental data. Thermal fluctuations broaden the distribution of orientations, relative to an average configuration, but do not dramatically change the resulting SFG spectra when compared to the spectrum obtained for that single average configuration. For example, for the hIAPP tetramer inserted in DPPG monolayers, spreading the tilt angle $\psi$ from a $\delta$-distribution at 36° to a thermal distribution in the $30 - 44°$ range produces at most a change of about 5% in the SFG spectra. Analogously, for the hIAPP tetramer in DPPG bilayers, spreading $\psi$ from a $\delta$-distribution at 59° to a distribution with a $55 - 61°$ range does not produce any significant effect on the resulting SFG spectrum. These findings imply that deducing the average orientation of the aggregate from comparisons of calculated and experimental chiral SFG spectra is a valid and useful approach, even when there is a distribution of orientations generated by thermal fluctuations under typical experimental conditions. At the same time, these results suggest that SFG spectroscopy could be directly applied and compared to the predicted orientations of hIAPP in DPPG bilayer, based on MD simulations.

## Biomedical Implications: Membrane Permeability

MD simulations of hIAPP aggregates inserted into DPPG bilayers predict intrusion of both water and monovalent ions (*e.g.*, $Na^+$) into the membrane/hIAPP complex. Water molecules form a continuous channel and permeate through the membrane, allowing $Na^+$ ions to diffuse into the otherwise hydrophobic membrane bilayer core. The comparative analysis of hIAPP trimers and tetramers in both DPPG monolayers and bilayers shows that changing the size of the aggregate from trimer to tetramer significantly affects the membrane permeability. In fact, only the trimer inserted in the DPPG bilayer generates a water channel due to the barrel-like conformation of the hIAPP aggregate. In contrast, the tetrameric $\beta$-sheet seems to be too stiff to enable formation of a (distorted) barrel. These results are particularly valuable since to the best of our knowledge this is the first study that shows channel formation by membrane-bound hIAPP oligomers, although a previous study has probed the channel activity of preformed hIAPP pores (50). It is therefore natural to expect that other amyloidogenic proteins might also be able to form channels and permeabilize the lipid bilayer.

Our estimate for the osmotic permeability $p_\mathrm{f}$ in Eq. (3) based on the permeation events observed for the hIAPP trimer in a DPPG bilayer during 150 ns of MD simulations predict that the calculated permeability coefficient is only about one order of magnitude smaller than the permeabilities reported for channel forming proteins (69). We thus conclude that membrane permeation by small hIAPP oligomers is indeed a likely mechanism for hIAPP cytotoxicity (26, 34, 44, 45). We observe that $Na^+$ ions diffuse into the membrane but do not permeate from one side of the membrane to the other in 150 ns. Therefore, longer MD trajectories are required to address whether the barrel-like hIAPP structure allows for ion permeation in the longer time scale. Factors influencing such process, such as membrane composition, ion type and hIAPP oligomer size would have to be considered. Furthermore, nonequilibrium simulations would be required to validate the values of osmotic permeability estimated in this study, $p_\mathrm{f} = 2.7 \times 10^{-15}$ $\mathrm{cm}^{-3}/\mathrm{s}$. Such simulations would allow to obtain the free energy barrier for water translocation through the hIAPP channel, which could be correlated to the permeation rate (69) and enable determination of the translocation pathway as well as the various factors that might influence ion permeation.

## Acknowledgments

The authors thank Professor Elsa C. Y. Yan for providing the experimental SFG spectrum measured for hIAPP in DPPG monolayers. C.P. and B.S. gratefully acknowledge the Jülich Supercomputing Centre for providing and maintaining the computing resources used in this work (Computing time grant JICS62). V.S.B acknowledges financial support by the National Science Foundation (Grant CHE 0911520) and supercomputer time from NERSC and from the High Performance Computing facilities at Yale University.

## References

1. Chiti, F., and C. M. Dobson, 2006. Protein misfolding, functional amyloid, and human disease. *Annu. Rev. Biochem.* 75:333–366.

2. Walsh, D. M., I. Klyubin, J. V. Fadeeva, W. K. Cullen, R. Anwyl, M. S. Wolfe, M. J. Rowan, and D. J. Selkoe, 2002. Naturally secreted oligomers of amyloid $\beta$ protein potently inhibit hippocampal long-term potentiation *in vivo*. *Nature* 416:535–539.

3. Kirkitadze, M., G. Bitan, and D. Teplow, 2002. Paradigm shifts in Alzheimer's disease and other neurodegenerative disorders: the emerging role of oligomeric assemblies. *J. Neurosci. Res.* 69:567–577.

4. Bucciantini, M., E. Giannoni, F. Chiti, F. Baroni, L. Formigli, J. Zurdo, N. Taddei, G. Ramponi, C. M. Dobson, and M. Stefani, 2002. Inherent toxicity of aggregates implies a common mechanism for protein misfolding diseases. *Nature* 416:507–511.

5. Klein, W. L., W. B. Stine, and D. B. Teplow, 2004. Small assemblies of unmodified amyloid $\beta$-protein are the proximate neurotoxin in Alzheimer's disease. *Neurobiol Aging* 25:569–580.

6. Butterfield, S. M., and H. A. Lashuel, 2010. Amyloidogenic Protein–Membrane Interactions: Mechanistic Insight from Model Systems. *Angew. Chem. Int. Ed. Engl.* 49:5628–5654.

7. Stefani, M., 2010. Biochemical and biophysical features of both oligomer/fibril and cell membrane in amyloid cytotoxicity. *FEBS Journal* 277:4602–4613.

8. Williams, T. L., and L. C. Serpell, 2011. Membrane and surface interactions of Alzheimer's A$\beta$ peptide – insights into the mechanism of cytotoxicity. *FEBS J.* 278:17.

9. Janson, J., R. H. Ashley, D. Harrison, S. McIntyre, and P. C. Butler, 1999. The mechanism of islet amyloid polypeptide toxicity is membrane disruption by intermediate-sized toxic amyloid particles. *Diabetes* 48:491–498.

10. Anguiano, M., R. J. Nowak, and J. Lansbury, Peter T, 2002. Protofibrillar islet amyloid polypeptide permeabilizes synthetic vesicles by a pore-like mechanism that may be relevant to type II diabetes. *Biochemistry* 41:11338–11343.

11. Porat, Y., S. Kolusheva, R. Jelinek, and E. Gazit, 2003. The human islet amyloid polypeptide forms transient membrane-active prefibrillar assemblies. *Biochemistry* 42:10971–10977.

12. Kayed, R., Y. Sokolov, B. Edmonds, T. M. McIntire, S. C. Milton, J. E. Hall, and C. G. Glabe, 2004. Permeabilization of lipid bilayers is a common conformation-dependent activity of soluble amyloid oligomers in protein misfolding diseases. *J. Biol. Chem.* 279:46363–46366.

13. Demuro, A., E. Mina, R. Kayed, S. C. Milton, I. Parker, and C. G. Glabe, 2005. Calcium dysregulation and membrane disruption as a ubiquitous neurotoxic mechanism of soluble amyloid oligomers. *J. Biol Chem* 280:17294–17300.

14. Ritzel, R. A., J. J. Meier, C.-Y. Lin, J. D. Veldhuis, and P. C. Butler, 2007. Human islet amyloid polypeptide oligomers disrupt cell coupling, induce apoptosis, and impair insulin secretion in isolated human islets. *Diabetes* 56:65–71.

15. Clark, A., C. A. Wells, I. D. Buley, J. K. Cruickshank, R. I. Vanhegan, D. R. Matthews, G. J. Cooper, R. R. Holman, and R. C. Turner, 1988. Islet amyloid, increased A-cells, reduced B-cells and exocrine fibrosis: quantitative changes in the pancreas in type 2 diabetes. *Diabetes Res.* 9:151–159.

16. Hull, R. L., G. T. Westermark, P. Westermark, and S. E. Kahn, 2004. Islet Amyloid: A Critical Entity in the Pathogenesis of Type 2 Diabetes. *J Clin Endocr Metab* 89:3629–3643.

17. Kahn, S. E., S. Andrikopoulos, and C. B. Verchere, 1999. Islet amyloid: a long-recognized but underappreciated pathological feature of type 2 diabetes. *Diabetes* 48:241–253.

18. Höppener, J. W., C. Oosterwijk, K. L. van Hulst, J. S. Verbeek, P. J. Capel, E. J. de Koning, A. Clark, H. S. Jansz, and C. J. Lips, 1994. Molecular physiology of the islet amyloid polypeptide (IAPP)/amylin gene in man, rat, and transgenic mice. *J Cell Biochem* 55 Suppl:39–53.

19. Kahn, S. E., D. A. D'Alessio, M. W. Schwartz, W. Y. Fujimoto, J. W. Ensinck, J. Taborsky, G J, and J. Porte, D, 1990. Evidence of cosecretion of islet amyloid polypeptide and insulin by beta-cells. *Diabetes* 39:634–638.

20. Morley, J. E., J. F. Flood, M. Horowitz, P. M. Morley, and M. J. Walter, 1994. Modulation of food intake by peripherally administered amylin. *Am J Physiol.* 267:R178–184.

21. Young, A. A., B. Gedulin, W. Vine, A. Percy, and T. J. Rink, 1995. Gastric emptying is accelerated in diabetic BB rats and is slowed by subcutaneous injections of amylin. *Diabetologia* 38:642–648.

22. Åkesson, B., G. Panagiotidis, P. Westermark, and I. Lundquist, 2003. Islet amyloid polypeptide inhibits glucagon release and exerts a dual action on insulin release from isolated islets. *Regul Peptides* 111:55–60.

23. Gedulin, B. R., T. J. Rink, and A. A. Young, 1997. Dose-response for glucagonostatic effect of amylin in rats. *Metabolism* 46:67–70.

24. Luca, S., W. Yau, R. Leapman, and R. Tycko, 2007. Peptide conformation and supramolecular organization in amylin fibrils: constraints from solid-state NMR. *Biochemistry* 46:13505–13522.

25. Jayasinghe, S., and R. Langen, 2004. Identifying structural features of fibrillar islet amyloid polypeptide using site-directed spin labeling. *J. Biol. Chem.* 279:48420–48425.

26. Lopes, D. H. J., A. Meister, A. Gohlke, A. Hauser, A. Blume, and R. Winter, 2007. Mechanism of islet amyloid polypeptide fibrillation at lipid interfaces studied by infrared reflection absorption spectroscopy. *Biophys J* 93:3132–3141.

27. Dégano, P., R. A. Silvestre, M. Salas, E. Peiró, and J. Marco, 1993. Amylin inhibits glucose-induced insulin secretion in a dose-dependent manner. Study in the perfused rat pancreas. *Regul Peptides* 43:91–96.

28. Ahrén, B., C. Oosterwijk, C. J. Lips, and J. W. Höppener, 1998. Transgenic overexpression of human islet amyloid polypeptide inhibits insulin secretion and glucose elimination after gastric glucose gavage in mice. *Diabetologia* 41:1374–1380.

29. Gebre-Medhin, S., H. Mulder, M. Pekny, G. Westermark, J. Törnell, P. Westermark, F. Sundler, B. Ahrén, and C. Betsholtz, 1998. Increased insulin secretion and glucose tolerance in mice lacking islet amyloid polypeptide (amylin). *Biochem Bioph Res Co* 250:271–277.

30. Westermark, P., U. Engström, K. H. Johnson, G. T. Westermark, and C. Betsholtz, 1990. Islet amyloid polypeptide: pinpointing amino acid residues linked to amyloid fibril formation. *Proc. Natl. Acad. Sci. USA.* 87:5036–5040.

31. Jaikaran, E. T., C. E. Higham, L. C. Serpell, J. Zurdo, M. Gross, A. Clark, and P. E. Fraser, 2001. Identification of a novel human islet amyloid polypeptide beta-sheet domain and factors influencing fibrillogenesis. *J Mol Biol* 308:515–525.

32. Seino, S., 2001. S20G mutation of the amylin gene is associated with Type II diabetes in Japanese. Study Group of Comprehensive Analysis of Genetic Factors in Diabetes Mellitus. *Diabetologia* 44:906–909.

33. Jayasinghe, S. A., and R. Langen, 2005. Lipid membranes modulate the structure of islet amyloid polypeptide. *Biochemistry* 44:12113–12119.

34. Knight, J. D., and A. D. Miranker, 2004. Phospholipid catalysis of diabetic amyloid assembly. *J Mol Biol* 341:1175–1187.

35. Knight, J. D., J. A. Hebda, and A. D. Miranker, 2006. Conserved and cooperative assembly of membrane-bound alpha-helical states of islet amyloid polypeptide. *Biochemistry* 45:9496–9508.

36. Sparr, E., M. F. M. Engel, D. V. Sakharov, M. Sprong, J. Jacobs, B. de Kruijff, J. W. M. Höppener, and J. A. Killian, 2004. Islet amyloid polypeptide-induced membrane leakage involves uptake of lipids by forming amyloid fibers. *FEBS Lett* 577:117–120.

37. Quist, A., I. Doudevski, H. Lin, R. Azimova, D. Ng, B. Frangione, B. Kagan, J. Ghiso, and R. Lal, 2005. Amyloid ion channels: A common structural link for protein misfolding disease. *Proc. Natl. Acad. Sci. USA* 102:10427–10432.

38. McLean, L. R., and A. Balasubramaniam, 1992. Promotion of beta-structure by interaction of diabetes associated polypeptide (amylin) with phosphatidylcholine. *Biochim Biophys Acta* 1122:317–320.

39. Mirzabekov, T. A., M.-c. Lin, and B. L. Kagan, 1996. Pore Formation by the Cytotoxic Islet Amyloid Peptide Amylin. *J Biol Chem* 271:1988–1992.

40. Lorenzo, A., B. Razzaboni, G. C. Weir, and B. A. Yankner, 1994. Pancreatic islet cell toxicity of amylin associated with type-2 diabetes mellitus. *Nature* 368:756–760.

41. O'Brien, T. D., P. C. Butler, D. K. Kreutter, L. A. Kane, and N. L. Eberhardt, 1995. Human islet amyloid polypeptide expression in COS-1 cells. A model of intracellular amyloidogenesis. *Am J Pathol* 147:609–616.

42. Hiddinga, H. J., and N. L. Eberhardt, 1999. Intracellular amyloidogenesis by human islet amyloid polypeptide induces apoptosis in COS-1 cells. *Am J Pathol* 154:1077–1088.

43. Kayed, R., Y. Sokolov, B. Edmonds, T. M. McIntire, S. C. Milton, J. E. Hall, and C. G. Glabe, 2004. Permeabilization of lipid bilayers is a common conformation-dependent activity of soluble amyloid oligomers in protein misfolding diseases. *J Biol Chem* 279:46363–46366.

44. Engel, M. F. M., H. Yigittop, R. C. Elgersma, D. T. S. Rijkers, R. M. J. Liskamp, B. de Kruijff, J. W. M. Höppener, and J. Antoinette Killian, 2006. Islet amyloid polypeptide inserts into phospholipid monolayers as monomer. *J Mol Biol* 356:783–789.

45. Lee, C.-C., Y. Sun, and H. W. Huang, 2012. How type II diabetes-related islet amyloid polypeptide damages lipid bilayers. *Biophys J* 102:1059–1068.

46. Brender, J. R., K. Hartman, K. R. Reid, R. T. Kennedy, and A. Ramamoorthy, 2008. A single mutation in the nonamyloidogenic region of islet amyloid polypeptide greatly reduces toxicity. *Biochemistry* 47:12680–12688.

47. Nanga, R. P. R., J. R. Brender, J. Xu, G. Veglia, and A. Ramamoorthy, 2008. Structures of Rat and Human Islet Amyloid Polypeptide IAPP(1–19) in Micelles by NMR Spectroscopy. *Biochemistry* 47:12689–12697.

48. Zhang, Y., Y. Luo, Y. Deng, Y. Mu, and G. Wei, 2012. Lipid interaction and membrane perturbation of human islet amyloid polypeptide monomer and dimer by molecular dynamics simulations. *PloS ONE* 7:e38191.

49. Duan, M., J. Fan, and S. Huo, 2012. Conformations of Islet Amyloid Polypeptide Monomers in a Membrane Environment: Implications for Fibril Formation. *PloS ONE* 7:e47150.

50. Zhao, J., Y. Luo, H. Jang, X. Yu, G. Wei, R. Nussinov, and J. Zheng, 2012. Probing ion channel activity of human islet amyloid polypeptide (amylin). *Biochim Biophys Acta* 1818:3121–3130.

51. Xiao, D., L. Fu, J. Liu, V. S. Batista, and E. C. Yan, 2012. Amphiphilic Adsorption of Human Islet Amyloid Polypeptide Aggregates to Lipid/Aqueous Interfaces. *J. Mol. Biol.* 421:537 – 547.

52. Hess, B., C. Kutzner, D. van der Spoel, and E. Lindahl, 2008. GROMACS 4: Algorithms for Highly Efficient, Load-Balanced, and Scalable Molecular Simulation. *J. Chem. Theor. Comput.* 4:435–447.

53. Oostenbrink, C., A. Villa, A. Mark, and W. van Gunsteren, 2004. A biomolecular force field based on the free enthalpy of hydration and solvation: the GROMOS force-field parameter sets 53a5 and 53a6. *J. Comput. Chem.* 25:1656–1676.

54. Piggot, T. J., D. A. Holdbrook, and S. Khalid, 2011. Electroporation of the E. coli and S. Aureus Membranes: Molecular Dynamics Simulations of Complex Bacterial Membranes. *J. Phys. Chem. B* 115:13381–13388.

55. Goldsbury, C., K. Goldie, J. Pellaud, J. Seelig, P. Frey, S. Müller, J. Kistler, G. Cooper, and U. Aebi, 2000. Amyloid Fibril Formation from Full-Length and Fragments of Amylin. *J Struct Biol* 130:352–362.

56. Madine, J., E. Jack, P. Stockley, S. Radford, L. Serpell, and D. Middleton, 2008. Structural insights into the polymorphism of amyloid-like fibrils formed by region 20–29 of amylin revealed by solid-state NMR and X-ray fiber diffraction. *J. Am. Chem. Soc.* 130:14990–15001.

57. Martinez, L., R. Andrade, E. G. Birgin, and J. M. Martinez, 2009. PACKMOL: A Package for Building Initial Configurations for Molecular Dynamics Simulations. *J. Comput. Chem.* 30:2157–2164.

58. Kaznessis, Y., S. Kim, and R. Larson, 2002. Simulations of zwitterionic and anionic phospholipid monolayers. *Biophys. J.* 82:1731–1742.

59. Zaraiskaya, T., and K. Jeffrey, 2005. Molecular dynamics simulations and H-2 NMR study of the GalCer/DPPG lipid bilayer. *Biophys. J.* 88:4017–4031.

60. Pabst, G., S. L. Grage, S. Danner-Pongratz, W. Jing, A. S. Ullrich, A. Watts, K. Lohner, and A. Hickel, 2008. Membrane Thickening by the Antimicrobial Peptide PGLa. *Biophys. J.* 95:5779–5788.

61. Feller, S. E., Y. Zhang, and R. W. Pastor, 1995. Computer simulation of liquid/liquid interfaces. II. Surface tension–area dependence of a bilayer and monolayer. *J Chem Phys* 103:10267–10276.

62. Kandt, C., W. L. Asha, and D. P. Tieleman, 2007. Setting up and running molecular dyanmics simulations of membrane proteins. *Methods* 41:475–488.

63. Kabsch, W., and C. Sander, 1983. Dictionary of protein secondary structure: Pattern recognition of hydrogen-bonded and geometrical features. *Biopolymers* 22:2577–2637.

64. Daura, X., K. Gademann, B. Jaun, D. Seebach, W. van Gunsteren, and A. Mark, 1999. Peptide Folding: When Simulation Meets Experiment. *Angew. Chem., Int. Ed.* 38:236–240.

65. Beckstein, O., and M. S. P. Sansom, 2004. The influence of geometry, surface character, and flexibility on the permeation of ions and water through biological pores. *Phys Biol* 1:42–52.

66. Allen, W. J., J. A. Lemkul, and D. R. Bevan, 2009. GridMAT-MD: A grid-based membrane analysis tool for use with molecular dynamics. *J Comput Chem* 30:1952–1958.

67. Engel, A., and H. Stahlberg, 2002. Aquaglyceroporins: channel proteins with a conserved core, multiple functions and variable surfaces. *Int. Rev. Cytol.* 215:75–104.

68. Finkelstein, A., 1987. Water Movement Through Lipid Bilayers, Pores, and Plasma Membranes. Theory and Reality. John Wiley & Sons, New York.

69. Hub, J. S., H. Grubmüller, and B. L. de Groot, 2009. Dynamics and Energetics of Permeation Through Aquaporins. What Do We Learn from Molecular Dynamics Simulations? *In* E. Beitz, editor, Aquaporins, Springer Berlin Heidelberg, volume 190 of *Handbook of Experimental Pharmacology*, 57–76.

70. Hub, J. S., F. K. Winkler, M. Merrick, and B. L. de Groot, 2010. Potentials of Mean Force and Permeabilities for Carbon Dioxide, Ammonia, and Water Flux across a Rhesus Protein Channel and Lipid Membranes. *J Am Chem Soc* 132:13251–13263.

71. Frisch, M., G. Trucks, H. Schlegel, G. Scuseria, M. Robb, J. Cheeseman, G. Scalmani, V. Barone, B. Mennucci, G. Petersson, H. Nakatsuji, M. Caricato, X. Li, H. Hratchian, A. Izmaylov, J. Bloino, G. Zheng, J. Sonnenberg, M. Hada, M. Ehara, K. Toyota, R. Fukuda, J. Hasegawa, M. Ishida, T. Nakajima, Y. Honda, O. Kitao, H. Nakai, T. Vreven, J. Montgomery Jr., J. Peralta, F. Ogliaro, M. Bearpark, J. Heyd, E. Brothers, K. Kudin, V. Staroverov, R. Kobayashi, J. Normand, K. Raghavachari, A. Rendell, J. Burant, S. Iyengar, J. Tomasi, M. Cossi, N. Rega, J. Millam, M. Klene, J. Knox, J. Cross, V. Bakken, C. Adamo, J. Jaramillo, R. Gomperts, R. Stratmann, O. Yazyev, A. Austin, R. Cammi, C. Pomelli, J. Ochterski, R. Martin, K. Morokuma, V. Zakrzewski, G. Voth, P. Salvador, J. Dannenberg, S. Dapprich, A. Daniels, . Farkas, J. Foresman, J. Ortiz, J. Cioslowski, and D. Fox. Gaussian 09 Revision A.1. Gaussian Inc. Wallingford CT 2009.

72. Poojari, C., A. Kukol, and B. Strodel, 2013. How the amyloid-$\beta$ peptide and membranes affect each other: an extensive simulation study. *Biochim. Biophys. Acta (Biomembr.))* 1828:327–339.

73. Mirzabekov, T., M. Lin, and B. Kagan, 1996. Pore formation by the cytotoxic islet amyloid peptide amylin. *J. Biol. Chem.* 271:1988–1992.

74. Saito, H., and W. Shinoda, 2011. Cholesterol Effect on Water Permeability through DPPC and PSM Lipid Bilayers: A Molecular Dynamics Study. *J Phys Chem B* 115:15241–15250.

75. Khemtémourian, L., M. F. Engel, J. A. Kruijtzer, J. W. Höppener, R. M. Liskamp, and J. A. Killian, 2010. The role of the disulfide bond in the

interaction of islet amyloid polypeptide with membranes. *Eur. Biophys. J.* 39:1359–1364.

# Figure Legends

**Figure 1.**

Definition of tilt angles relative to the membrane surface. To define the strand orientation we used the $C_\alpha$–$C_\alpha$ vector between residues Arg11 and Phe15 for the first $\beta$-strand in each peptide, and residues Leu27–Asn31 for the second $\beta$-strand per peptide. These residues are marked by spheres in each strand. This procedure results in six different angles for the trimer and eight for the tetramer, for which the corresponding sphere colors are used in Figs. 3 and 4. The peptides are shown in New Cartoon and colored based on the physicochemical properties of the residues: blue, basic; white, hydrophobic; and green, polar. The bilayer phosphorus atoms are shown as vdW spheres in voilet color. Lipid tails are shown as lines in gray color, water molecules are not shown for clarity.

**Figure 2.**

The most stable structures obtained from cluster analysis applied to the last 100 ns of the MD trajectories. The coloring explanation for the peptides and lipids is given in Fig. 1.

**Figure 3.**

hIAPP in monolayer: (a) trimer and (b) tetramer. Top: Average (black) and individual (color definition given in Fig. 1) tilt angles of $\beta$-strands relative to the membrane surface. Bottom: Number of water molecules (red) and $Na^+$ ions (blue) inside the hydrophobic core.

**Figure 4.**

hIAPP in bilayer: (a) trimer and (b) tetramer. Top: Average (black) and individual (color definition given in Fig. 1) tilt angles of $\beta$-strands relative to the membrane surface. Bottom: Number of water molecules (red) and $Na^+$ ions (blue) inside the hydrophobic core, as well as the cumulative number of water permeation events (black).

**Figure 5.**

(a) Water channel formed by the hIAPP trimer in the DPPG bilayer. The coloring explanation for the peptides and lipids is given in Fig. 1. Water

molecules (red and white vdW spheres for oxygen and hydrogen, respectively) and $Na^+$ (cyan vdW spheres) inside the bilayer are shown. (b) Averaged particle density of water and $Na^+$ within the the bilayer.

**Figure 6.**

(a): Experimental chiral SFG spectrum for hIAPP aggregates in a DPPG monolayer (circles), compared to the calculated spectrum obtained for a 1:1 mixture of hIAPP tetramer and trimer (red line). (b) and (c): Comparisons of the calculated chiral SFG spectra for the hIAPP trimer (b) and tetramer (c) in the DPPG monolayer (blue) and bilayer (black). The error bars denote the standard deviations of the calculated spectra that are averaged for 10 orientation angles evenly distributed in the period of 50-150 ns in the molecular dynamics simulation trajectories. The average overall tilt angels are labelled for the averaged spectra. The SFG spectra with a $\delta$-distribution at the average tilt angles are shown in the dash lines.

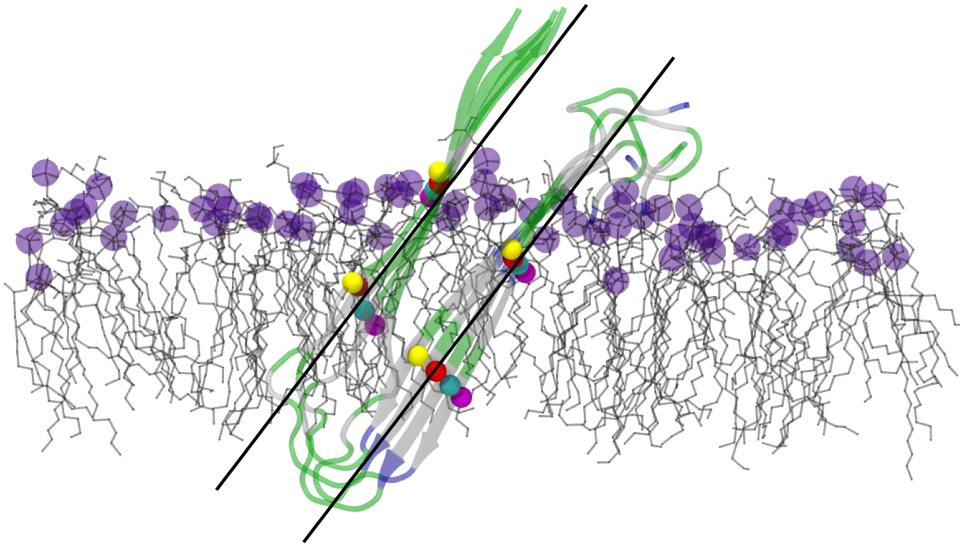

Figure 1:

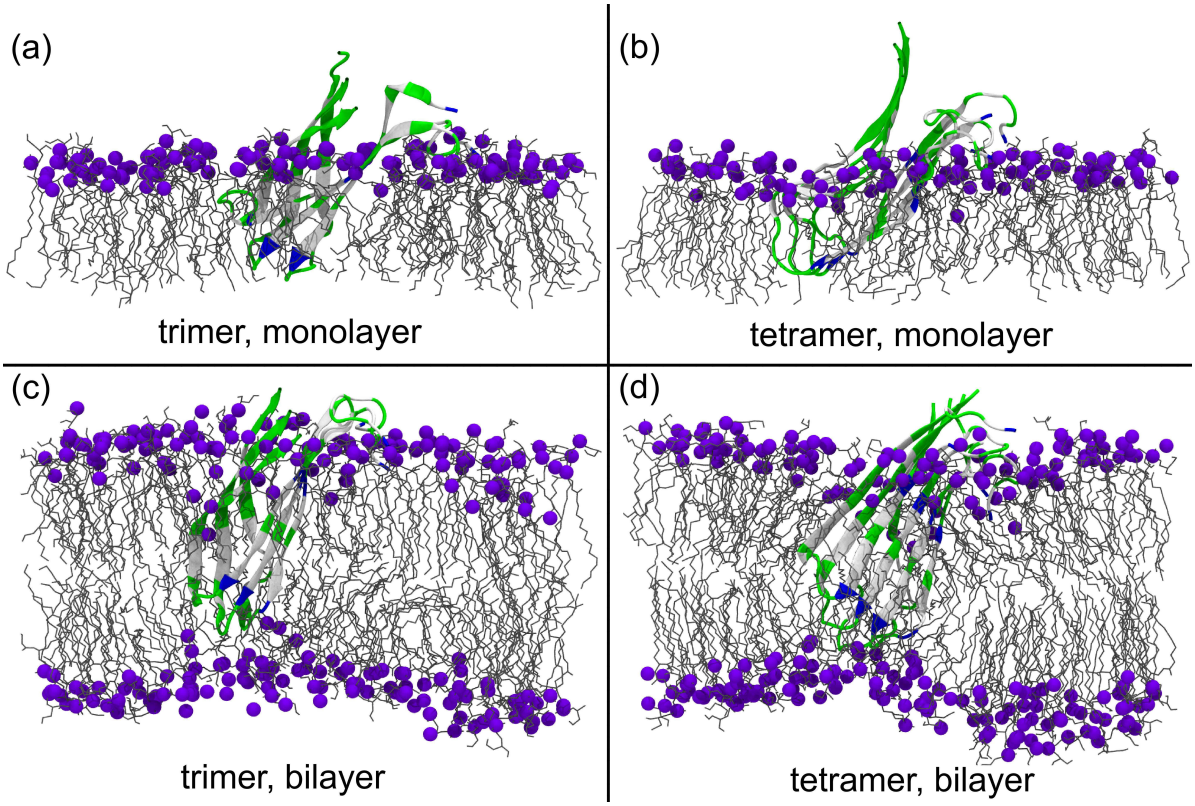
(a)
trimer, monolayer
(b)
tetramer, monolayer
(c)
trimer, bilayer
(d)
tetramer, bilayer

Figure 2:

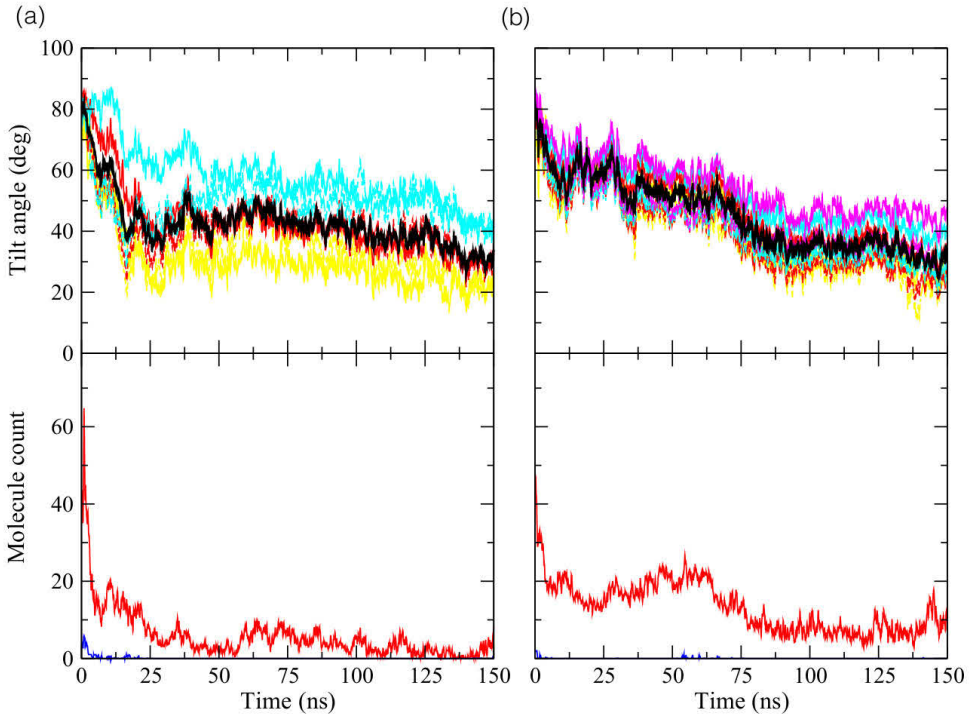
(a)
(b)
Tilt angle (deg)
Molecule count
Time (ns)
Time (ns)
0
20
40
60
80
100
0
25
50
75
100
125
150

Figure 3:

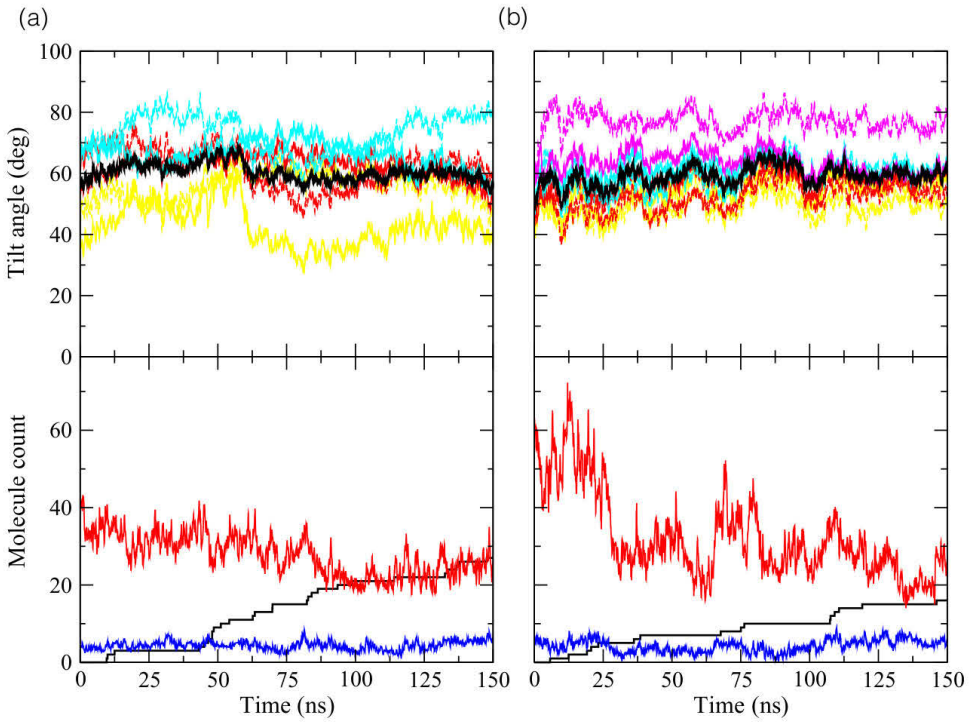
(a)
(b)
Tilt angle (deg)
Molecule count
Time (ns)
Time (ns)
0
20
40
60
80
100
0
25
50
75
100
125
150

Figure 4:

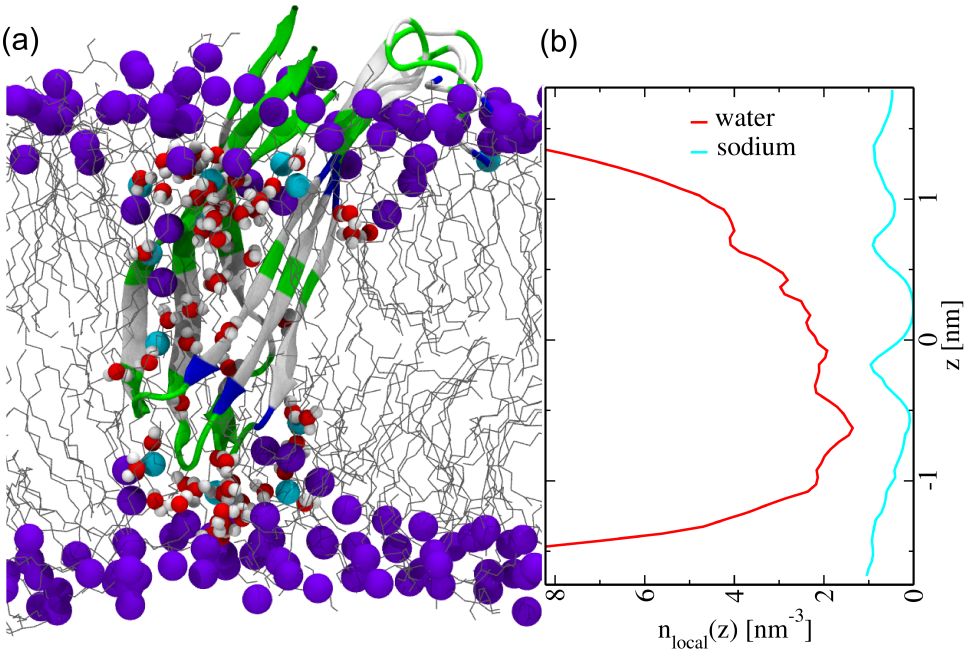


Figure 5:

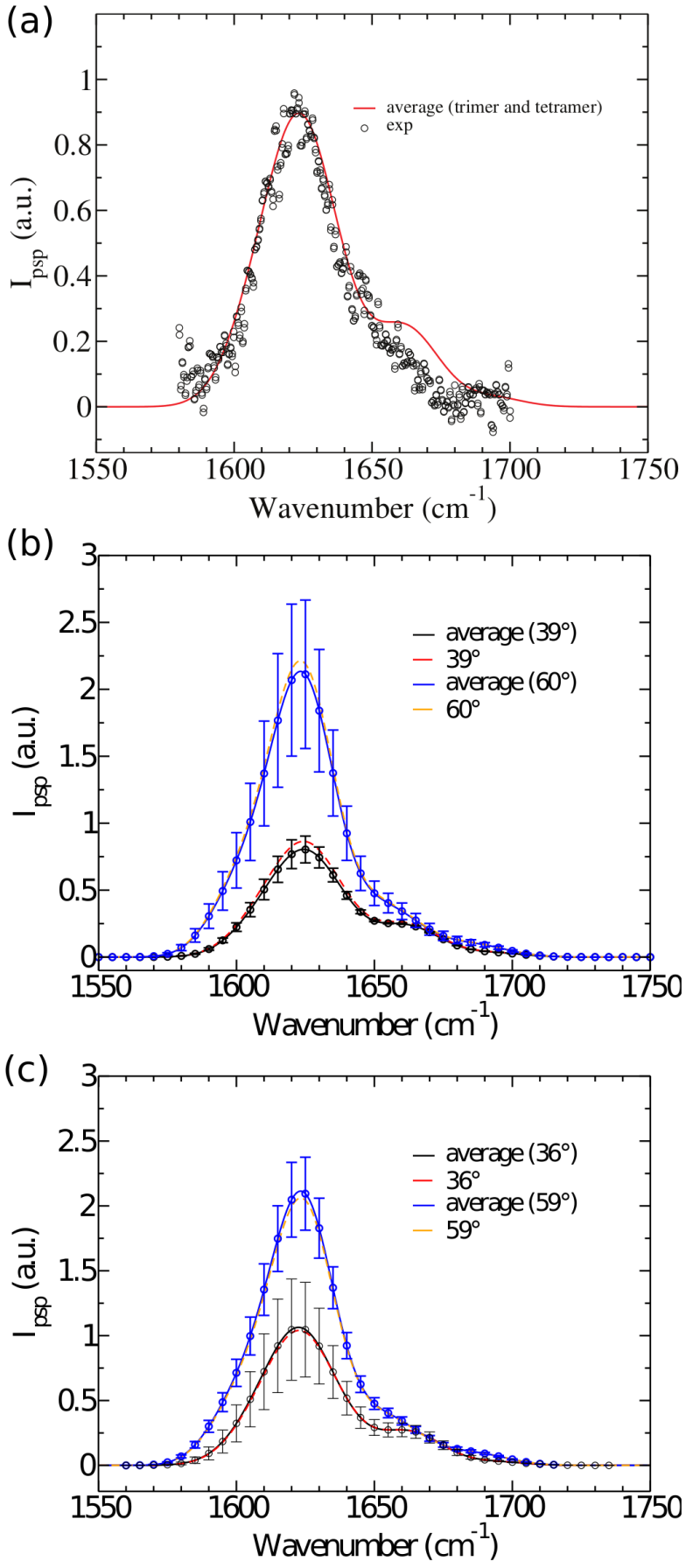
(a)
average (trimer and tetramer)
exp
$I_{psp}$ (a.u.)
Wavenumber ($cm^{-1}$)
(b)
average (39°)
39°
average (60°)
60°
$I_{psp}$ (a.u.)
Wavenumber ($cm^{-1}$)
(c)
average (36°)
36°
average (59°)
59°
$I_{psp}$ (a.u.)
Wavenumber ($cm^{-1}$)

144
Figure 6:

Supporting material

# Membrane permeation induced by aggregates of human islet amyloid polypeptides

Chetan Poojari
Forschungszentrum Jülich GmbH,
Institute of Complex Systems: Structural Biochemistry (ICS-6),
52425 Jülich, Germany

Dequan Xiao
Department of Chemistry,
Yale University
New Haven, CT 06520, USA

Victor S. Batista*
Department of Chemistry,
Yale University
New Haven, CT 06520, USA

Birgit Strodel*
Forschungszentrum Jülich GmbH,
Institute of Complex Systems: Structural Biochemistry (ICS-6),
52425 Jülich, Germany

Institute of Theoretical and Computational Chemistry,
Heinrich Heine University Düsseldorf, 40225 Düsseldorf, Germany

*Corresponding Authors: victor.batista@yale.edu; b.strodel@fz-juelich.de

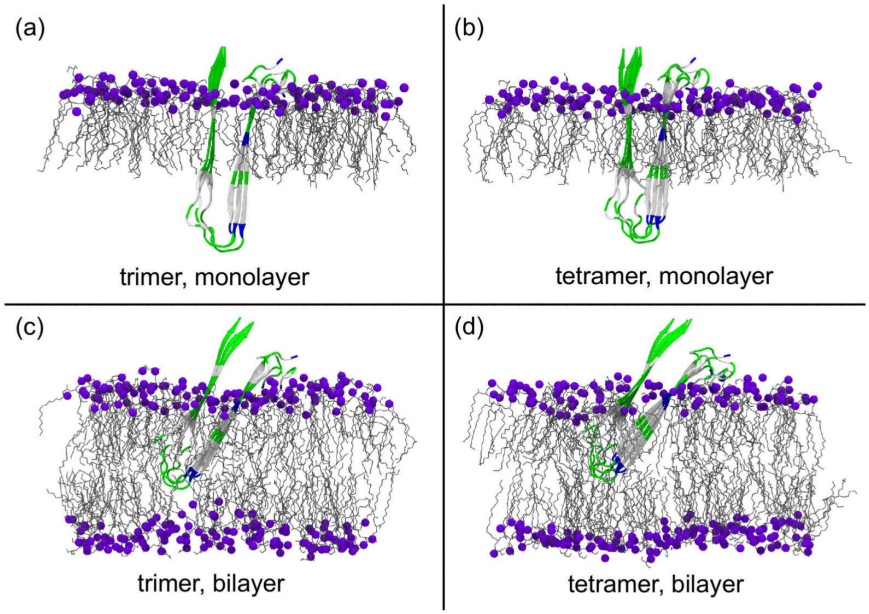


**Figure S1:** Starting structures showing the initial positions of hIAPP trimer and tetramer in both DPPG monolayer and bilayer.

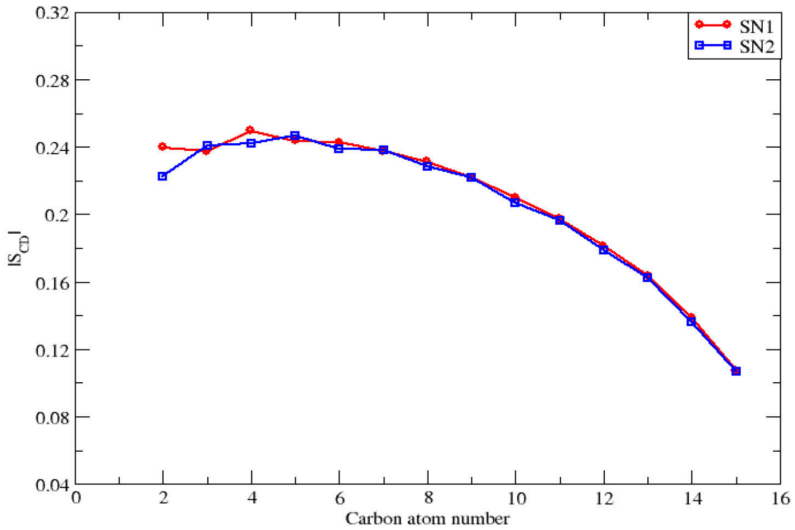


**Figure S2:** Time-averaged order parameter $|S_{CD}|$ of the sn-1 and sn-2 lipid chains obtained from a 100 ns MD simulation of a peptide-free DPPG bilayer.

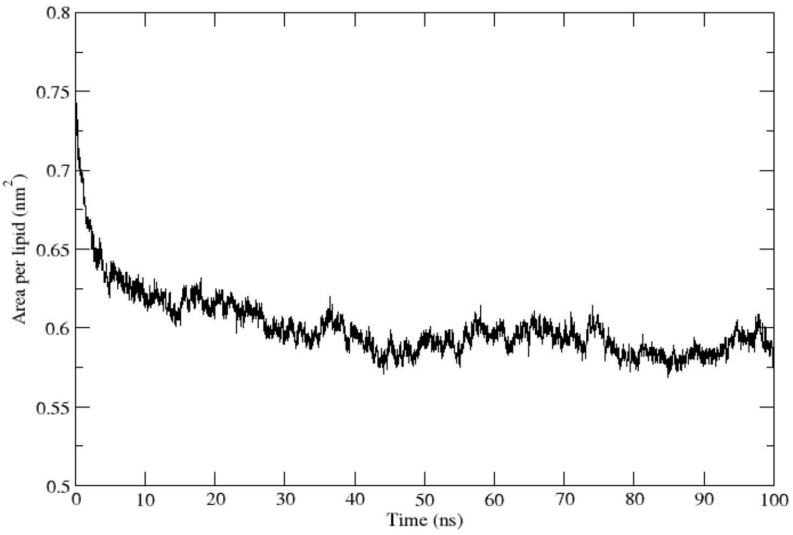


**Figure S3:** Area per lipid as a function of time as obtained during a 100 ns MD simulation of a peptide-free DPPG lipid bilayer.

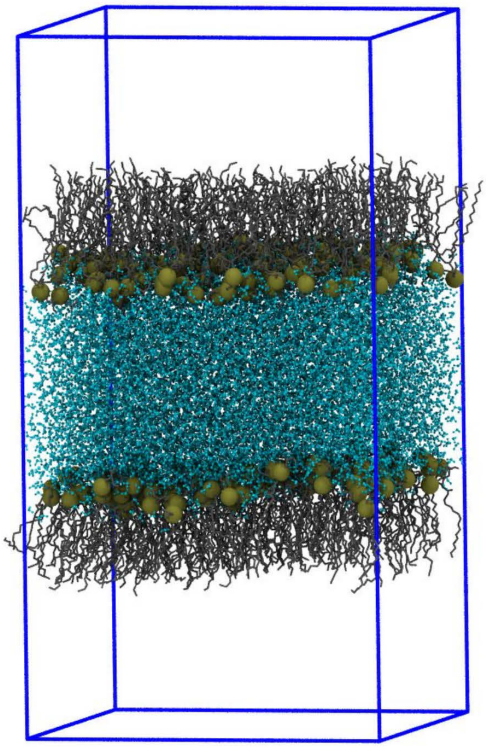

**Figure S4:** Snapshot showing the DPPG monolayer-water system. The monolayer phosphorus atoms (tan) are shown as van der Waals spheres, lipid tails (gray) as licorice and water molecules (blue) are shown as CPK. The simulation box is drawn to emphasize the empty space representing the air above and below the lipid tails in the upper and lower monolayer, respectively.

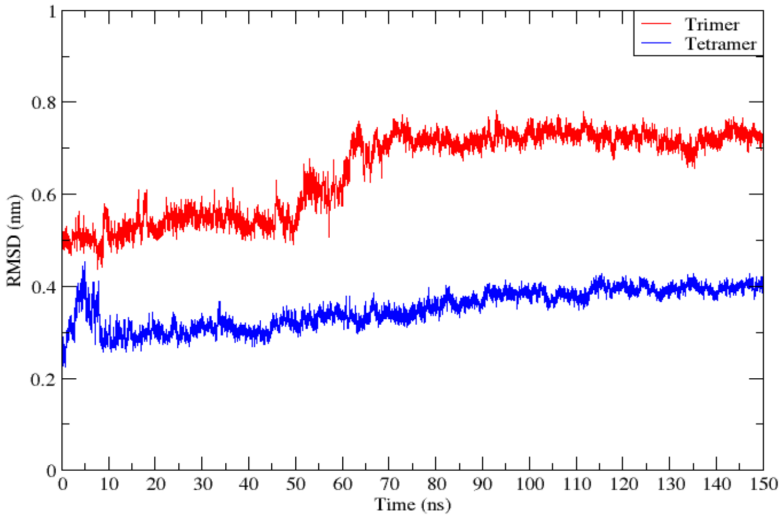


**Figure S5:** Backbone RMSD of hIAPP in DPPG monolayer.

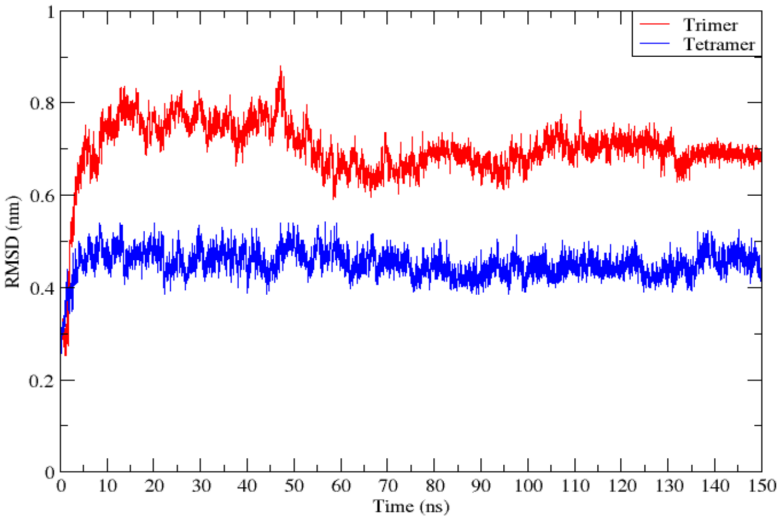


**Figure S6:** Backbone RMSD of hIAPP in DPPG bilayer.

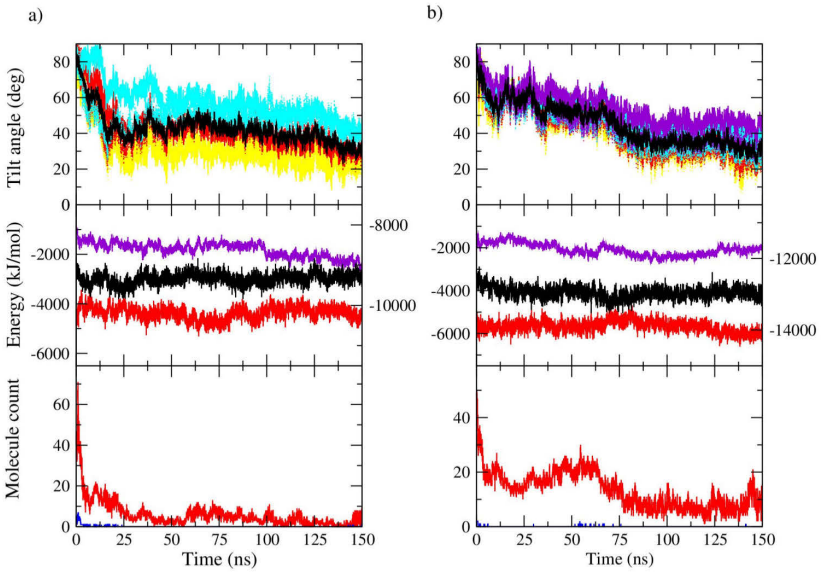


**Figure S7:** hIAPP in monolayer; (a) hIAPP trimer and (b) hIAPP tetramer. Top: Average (black) and individual tilt angles of β-strands relative to the membrane surface. Middle: Total interaction energies for hIAPP–lipid headgroups (purple), hIAPP–hIAPP (black, right *y*-axis), hIAPP–water/ions (red) interactions. Bottom: Number of water molecules (red) and $Na^+$ ions (blue) inside the hydrophobic core.

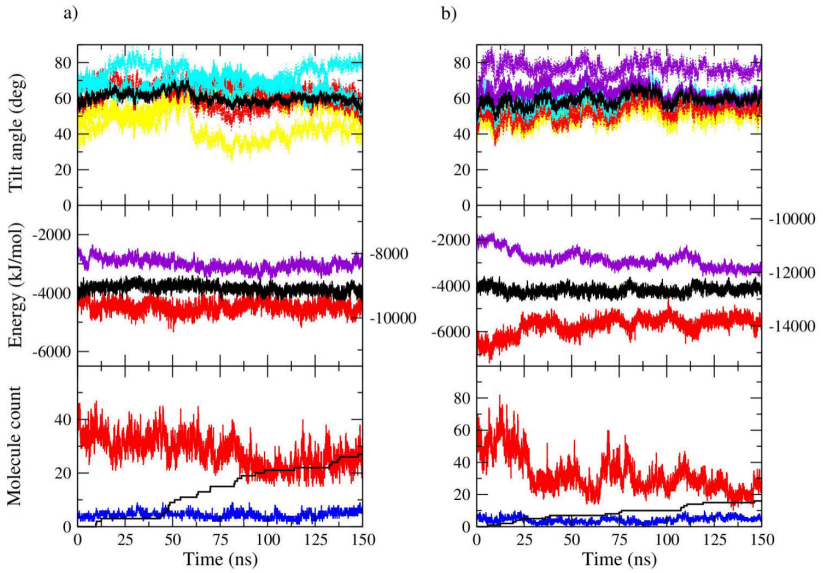


**Figure S8:** hIAPP in bilayer; (a) hIAPP trimer and (b) hIAPP tetramer. Top: Average (black) and individual tilt angles of β-strands relative to the membrane surface. Middle: Total interaction energies for hIAPP–lipid headgroups (purple), hIAPP–hIAPP (black, right *y*-axis), hIAPP–water/ions (red) interactions. Bottom: Number of water molecules (red) and $Na^+$ ions (blue) inside the hydrophobic core, as well as the cumulative number of water permeation events (black).

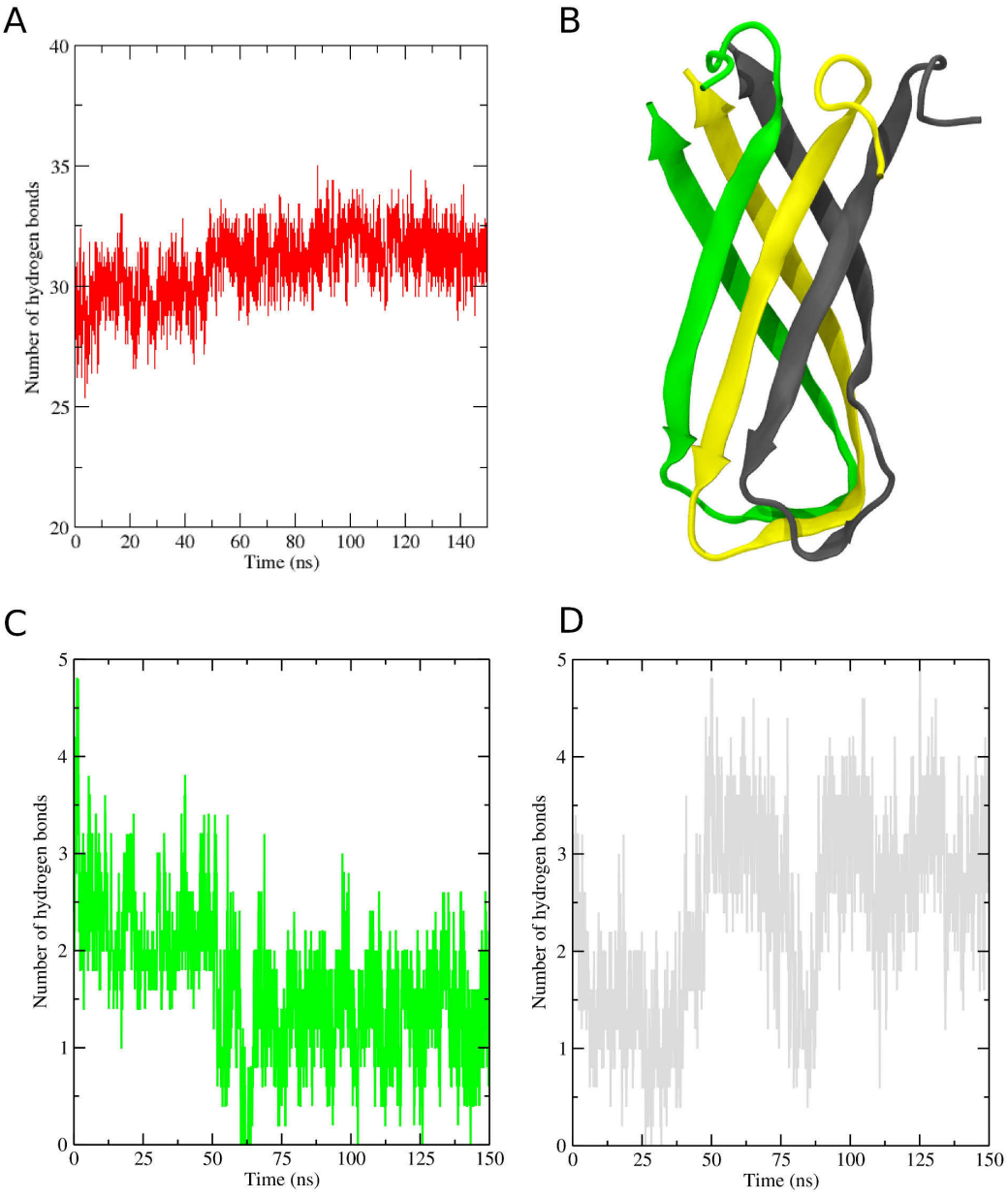


**Figure S9:** (a) Number of intra- and interpeptide hydrogen bonds in the hIAPP trimer in DPPG bilayer. (b) Most stable trimer structure colored by peptide numer (peptide 1, 2 and 3 in green, yellow and grey, respectively). (c) and (d) Number of H-bonds formed between the two β-sheets of peptide 1 (green) and peptide 3 (grey).

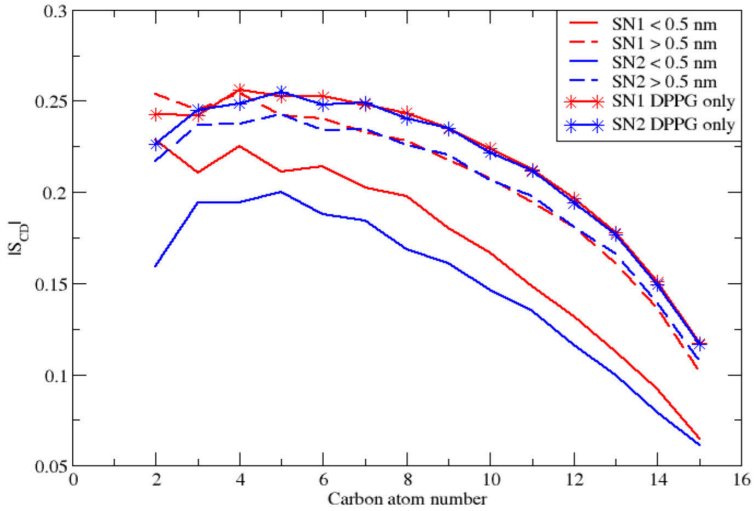


**Figure S10:** Time-averaged order parameter $|S_{CD}|$ of the sn-1 and sn-2 lipid chains resulting from the MD simulation of the hIAPP trimer in DPPG monolayer. $S_{CD}$ is analyzed for lipids within 0.5 nm of protein and for lipids more than 0.5 nm away from protein. For comparison, $|S_{CD}|$ for lipids from the DPPG-only simulation is shown.

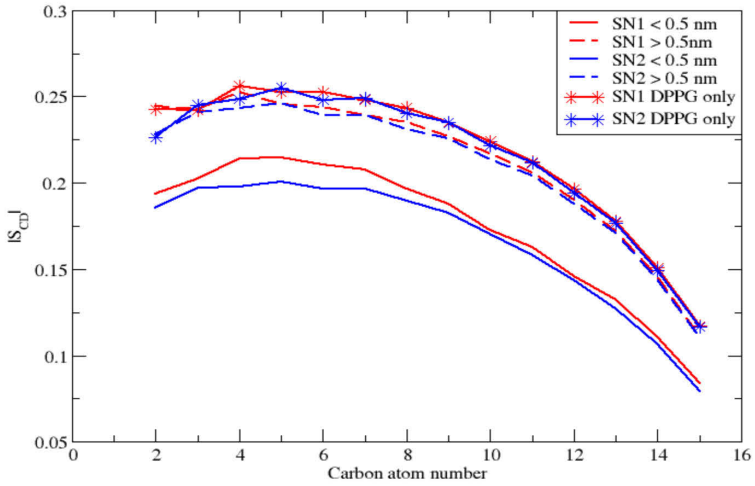


**Figure S11:** Time-averaged order parameter $|S_{CD}|$ of the sn-1 and sn-2 lipid chains resulting from the MD simulation of the hIAPP tetramer in DPPG monolayer. $S_{CD}$ is analyzed for lipids within 0.5 nm of protein and for lipids more than 0.5 nm away from protein. For comparison, $|S_{CD}|$ for lipids from the DPPG-only simulation is shown.

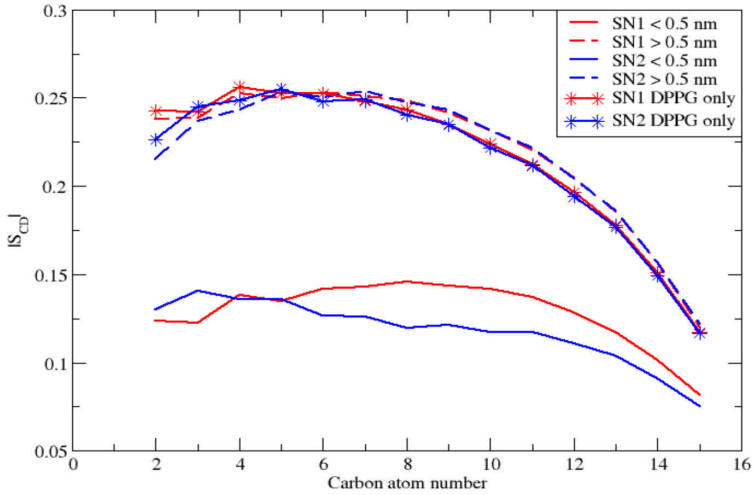


**Figure S12:** Time-averaged order parameter $|S_{CD}|$ of the sn-1 and sn-2 lipid chains resulting from the MD simulation of the hIAPP trimer in DPPG bilayer. $S_{CD}$ is analyzed for lipids within 0.5 nm of protein and for lipids more than 0.5 nm away from protein. For comparison, $|S_{CD}|$ for lipids from the DPPG-only simulation is shown.

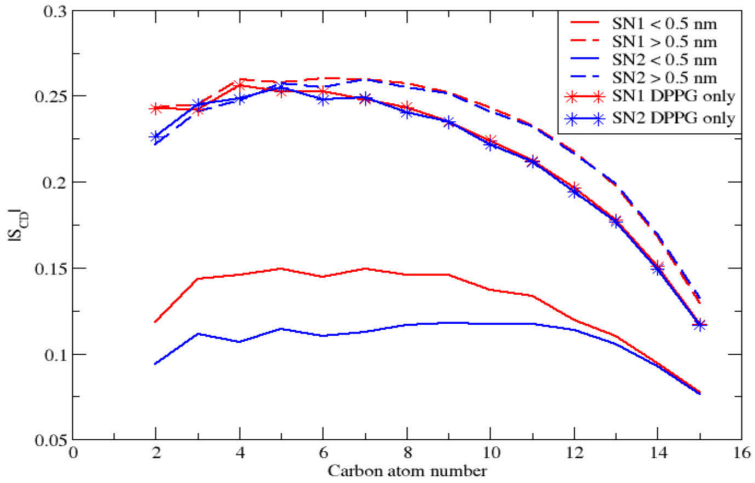


**Figure S13:** Time-averaged order parameter $|S_{CD}|$ of the sn-1 and sn-2 lipid chains resulting from the MD simulation of the hIAPP tetramer in DPPG bilayer. $S_{CD}$ is analyzed for lipids within 0.5 nm of protein and for lipids more than 0.5 nm away from protein. For comparison, $|S_{CD}|$ for lipids from the DPPG-only simulation is shown.

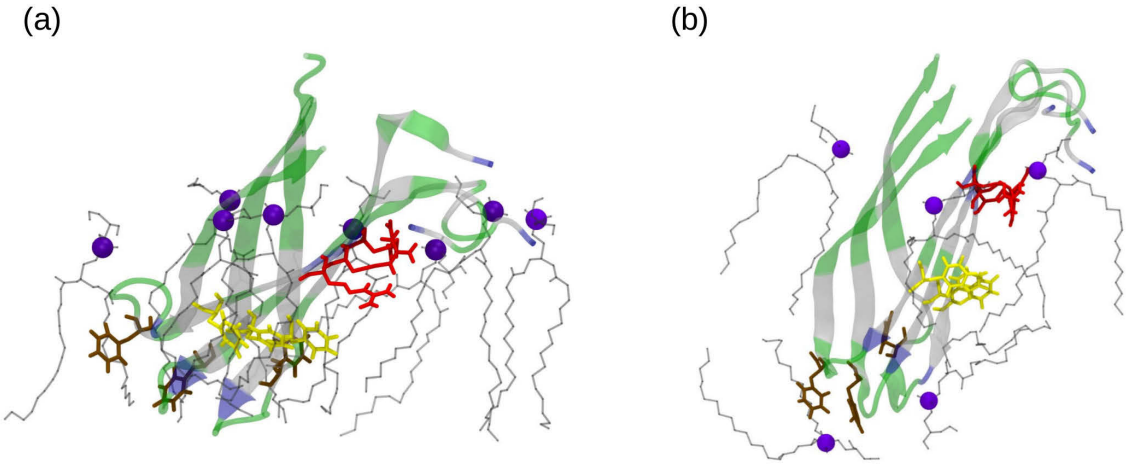


**Figure S14:** hIAPP trimer causing lipids in the (a) monolayer and (b) bilayer to tilt in the near vicinity of the peptides. The side chains with the strongest effect on acyl chain order are shown: Arg11 (red), Phe15 (yellow) and Phe23 (ochre).

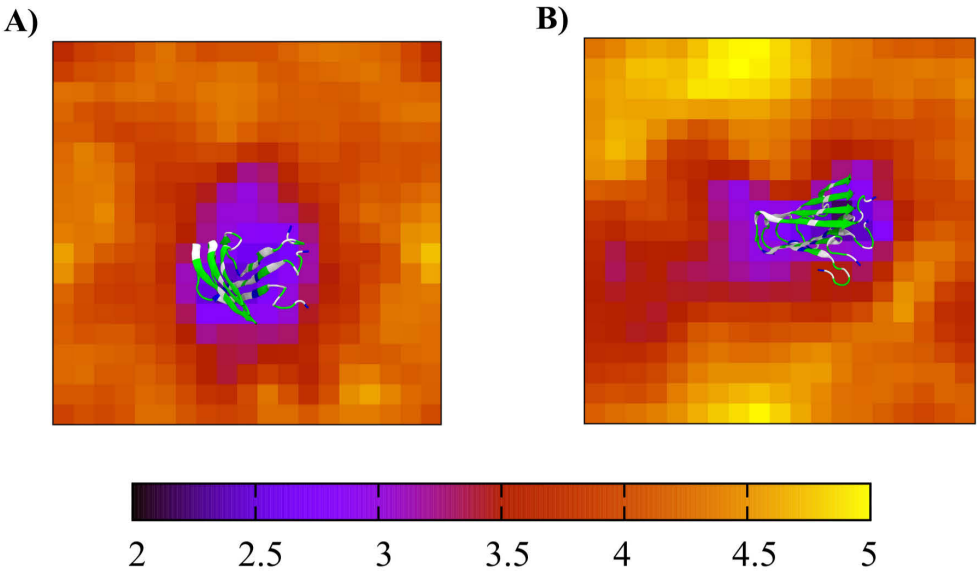


**Figure S15:** Bilayer thickness around embedded hIAPP for (a) trimer and (b) tetramer calculated for the final MD frame. For clarity, hIAPP was placed on the plots to indicate its position in the bilayer. The legend shows the bilayer thickness (nm) mapped to the corresponding colors.

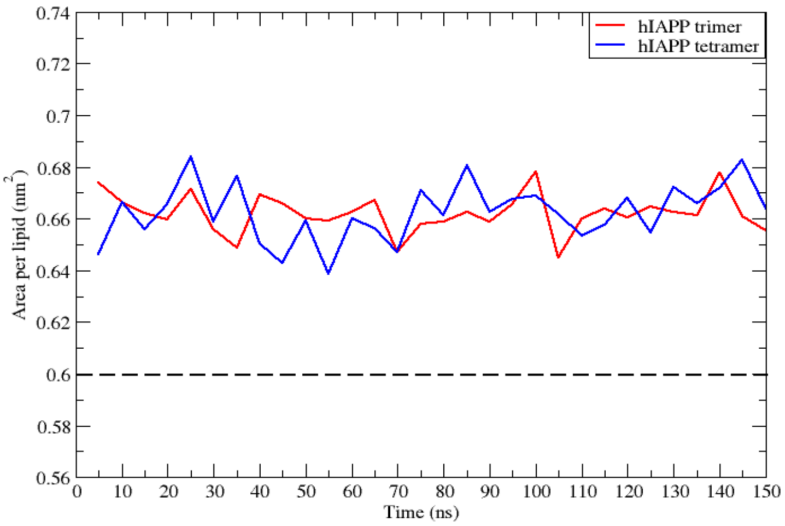


**Figure S16:** Area per lipid as a function of time for the DPPG monolayer simulations with hIAPP trimer (red) and tetramer (blue). For comparison, the average area per lipid obtained from a peptide-free DPPG bilayer is shown as black dashed line.

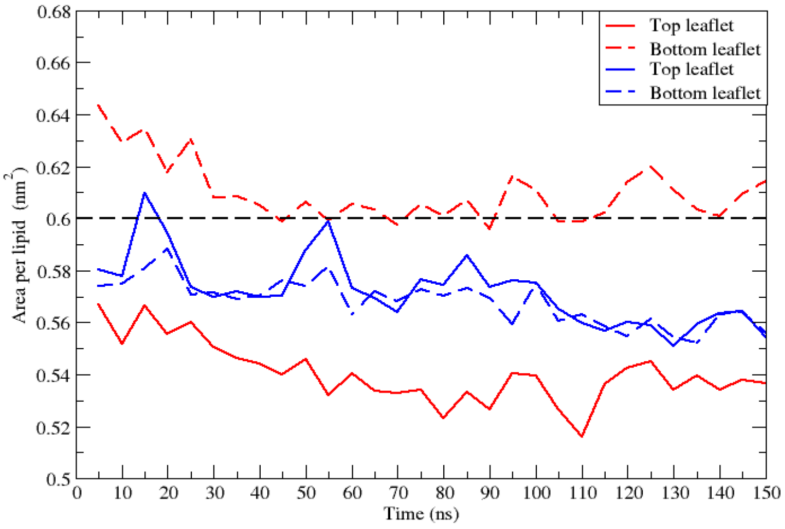


**Figure S17:** Area per lipid as a function of time for the DPPG bilayer simulations with hIAPP trimer (red) and tetramer (blue). For comparison, the average area per lipid obtained from a peptide-free DPPG bilayer is shown as black dashed line.

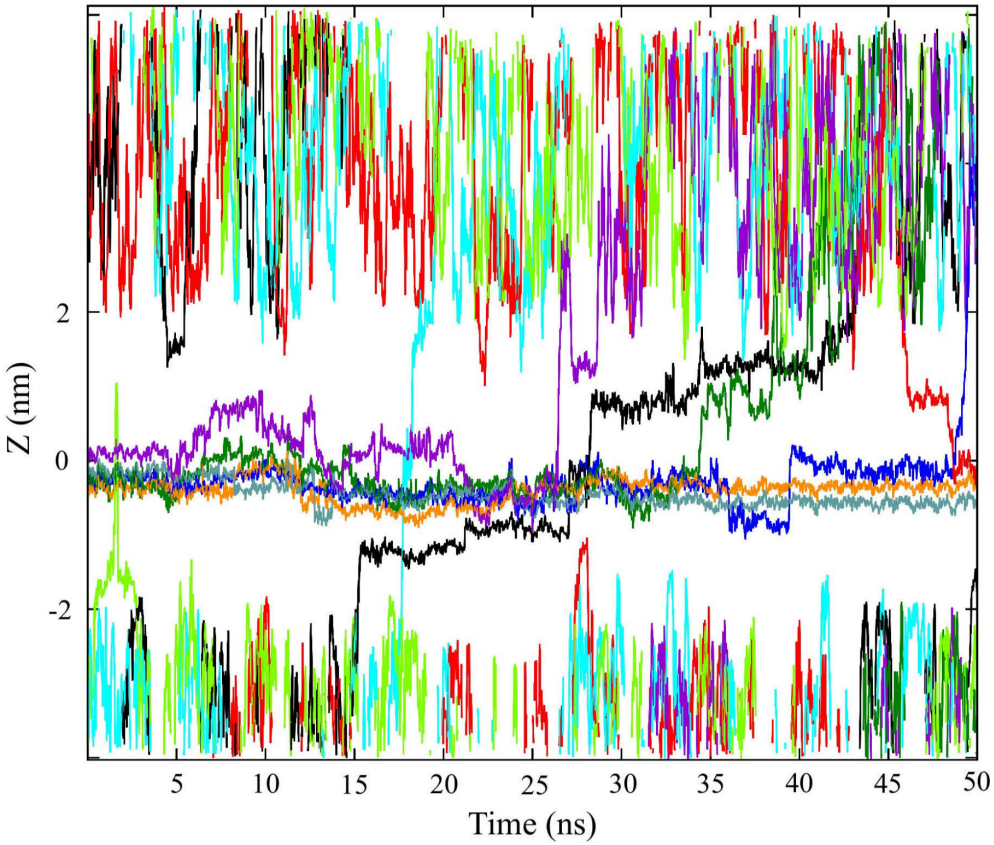


**Figure S18:** Representative trajectories of water molecules permeating the DPPG bilayer with hIAPP trimer inserted. Only the coordinate along the bilayer normal (*z*-axis) is plotted, and only permeation events occurring during the last 50 ns of the 150 ns MD simulation are shown.

## 4.4 Trapping the events of amyloid-$\beta$ insertion into membranes

# Trapping the events of amyloid-$\beta$ insertion into membranes

Chetan Poojari
Forschungszentrum Jülich GmbH,
Institute of Complex Systems: Structural Biochemistry (ICS-6)
52425 Jülich, Germany

Birgit Strodel*
Forschungszentrum Jülich GmbH,
Institute of Complex Systems: Structural Biochemistry (ICS-6)
52425 Jülich, Germany
Institute of Theoretical and Computational Chemistry,
Heinrich Heine University Düsseldorf, 40225 Düsseldorf, Germany

*Corresponding Author: b.strodel@fz-juelich.de

May 23, 2013

# Introduction

The aggregation of amyloid peptides into neurotoxic oligomers is a hallmark of neurodegenerative diseases. In particular, Alzheimer's disease (AD) is associated with synaptic loss, abnormalities in functioning of neurons, neuronal cell death and extracellular accumulation of senile plaques composed of the neurotoxic amyloid-$\beta$ peptide (A$\beta$) [1, 2]. Association and insertion of A$\beta$ into neuronal membranes is linked to the pathology of AD [3]. Experimental studies have shown that both A$\beta$ monomer and oligomers are able to penetrate into the hydrophobic core of membranes [4]. The insertion of A$\beta$ into membranes is known to alter biophysical membrane properties by increasing their permeability and causing an imbalance in calcium homeostasis[3], which promotes neuronal excitotoxicity [3, 5]. Atomic force microscopy (AFM) experiments with the A$\beta$ isoforms A$\beta_{40}$ A$\beta_{42}$ [6, 7] revealed ion-channel-like structures in membranes, which are able to cause cellular ionic imbalance [7–11]. Using molecular simulations, various A$\beta$ pore models composed of mobile $\beta$-sheet subunits ranging in size from tetramer to hexamers were proposed [12–14].

In the current study we investigate the membrane insertion of the 10-residue fragment A$\beta_{21-30}$. Using proteolysis experiments, Lazo et al.[15] revealed that A$\beta_{21-30}$ is protease-resistance in both A$\beta_{40}$ and A$\beta_{42}$. This decapeptide, exhibits a similar protease resistance as full length A$\beta$, suggesting its role in folding and aggregation of A$\beta$ into toxic oligomers. Lazo et al [15] also postulated that partial unfolding of the A$\beta_{21-30}$ segment would be necessary for fibrillization of A$\beta$ to occur. Several experimental and computational studies investigated the structure and aggregation of A$\beta_{21-30}$ and discussed the importance of both hydrophobic and electrostatic interactions in the A$\beta_{21-30}$ folding processes and aggregation [16–22].

In our previous work we studied both wild type and mutant A$\beta_{42}$ peptide (monomers and tetramers) preinserted into lipid bilayers at various insertion depths [23]. In all our simulations A$\beta_{42}$ remained well embedded in the

membrane hydrophobic core, causing membrane disruption and increased membrane permeability. However, it is still unclear how A$\beta$ inserts into membranes. A molecular understanding of this process is very important for unravelling events in the development of the AD. Davis et al.[24, 25] carried out umbrella sampling (US) simulations to study the distribution of A$\beta$ on the bilayer surface and reported electrostatic interactions at the bilayer surface to be important for peptide distribution. In this work, we investigate the pathways and kinetics for A$\beta$ insertion into a 1-palmitoyl 2-oleoyl phosphatidylcholine (POPC) lipid bilayer. To this end we use US molecular dynamics (MD) simulations. Here, we calculate the potential of mean force (PMF) for the insertion of A$\beta_{21-32}$ into a POPC membrane along a single reaction coordinate. The turn segment of A$\beta$, A$\beta_{21-30}$ is experimentally known to nucleate the folding process and promote aggregation of A$\beta$ into toxic oligomers, a key pathological event in AD [15]. Here we perform atomistic US simulations for short segment of wild type A$\beta$, A$\beta_{21-32}$ (WT) which has a total net charge of $-1$. In addition, we also examine the effect of amino acid substitution which is linked to cerebral amyloid angiopathy (CAA) [26] -Arctic type [Glu-22]A$\beta_{21-32}$ (E22G), which has total charge of 0. Here A$\beta_{21-32}$ (WT) and Arctic type [Glu-22]A$\beta_{21-32}$ (E22G) is studied to investigate the effect of charges, as E22G mutant [27] is known to increase neurotoxic protofibril production [28, 29] and is more toxic than the WT.

# Methods

## Peptide model

As starting structure of A$\beta_{21-32}$ for the US simulations, we used the turn segment of A$\beta_{42}$, which was observed experimentally and in simulation studies. A distance restraint is applied between residues Ala-21 and Ile-32, in order to stabilize the turn conformation in the A$\beta_{21-32}$ fragment. The terminals of A$\beta_{21-32}$ were capped to nullify the effect of terminal residues in peptide-lipid

interactions.

## Umbrella sampling MD simulations

All MD simulations were performed with the GROMACS 4.0 package [30]. The A$\beta_{21-32}$ fragment was described using the GROMOS96 53A6 force field [31], and the lipids were modeled with modified Berger force field parameters for use with the GROMOS96 53A6 force field [32]. Initial coordinates of 128 lipids composing a POPC bilayer equilibrated with water for 40 ns were obtained from Kukol's work on lipid models [32]. The A$\beta_{21-32}$ fragment was placed 1.5 nm above the lipid membrane to avoid any initial interactions with the lipid headgroup atoms. The system was solvated subsequently with SPC water molecules, 0.1 M NaCl salt was added to bring the system to a near physiological salt concentration and in case of WT A$\beta_{21-32}$ an extra $Na^+$ ion was added to balance the peptide charge. The simulations were carried out in a $6.7 \times 6.7 \times 16.5$ nm$^3$ box at 298 K and 1 bar. Here, the same simulation parameters were used as in our previous studies [23].

For the US simulations, the A$\beta_{21-32}$ fragment was pulled into the POPC lipid bilayer along the $z$-axis, using a spring constant of 500 kJ mol$^{-1}$ nm$^{-2}$ and a pull rate of 0.005 nm ps$^{-1}$. The peptide was pulled from the solvent-environment above the bilayer into the membrane reaching the headgroups of the lower leaflet. From this initial pulling simulations, snapshots were taken to generate the starting configurations for the umbrella sampling windows. Each window was spaced at a distance of 0.2 nm in the bulk water phase, and 0.1 nm in the barrier-crossing region in the membrane, resulting in 42 windows for both WT and E22G A$\beta_{21-32}$. The system of each window was equilibrated for 100 ps in an NPT ensemble followed by 40 ns of MD simulation per window. Thus, the aggregated simulation time per A$\beta_{21-32}$ fragment is 1.6 $\mu$s. Weighted histogram analysis method (WHAM) [33] is used to calculate the free energy from the US simulations.

# Results and Discussion

## Pulling simulations

Spontaneous insertion of A$\beta$ into membrane does not occur on the feasible $\mu$s time scale of MD simulations. COM pulling simulations offer the possibility to study events which are otherwise not observable using equilibrium MD simulations. Here, we use a harmonic restraining potential to pull the A$\beta_{21-32}$ fragment across the POPC membrane. Figures 1 and 2 show the insertion pathway for the WT and E22G fragments, respectively.

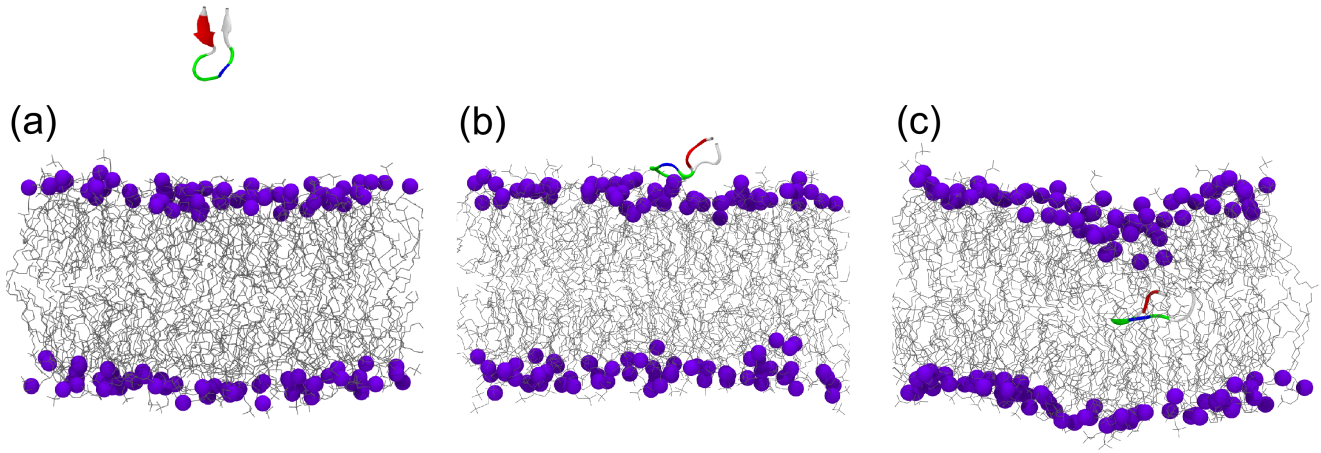


Figure 1: Insertion pathway for WT A$\beta_{21-32}$ peptide. Key stages are shown (a) free state, (b) adsorbed state and (c) inserted state.

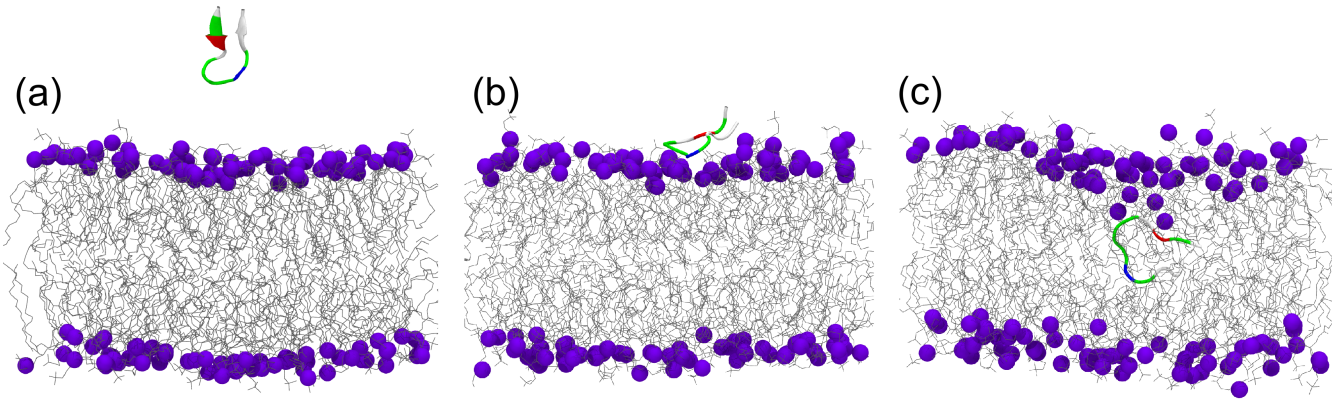


Figure 2: Insertion pathway for E22G A$\beta_{21-32}$ peptide. Key stages are shown (a) free state, (b) adsorbed state and (c) inserted state.

The peptide was initially placed perpendicular to the membrane surface at a distance of 1.5 nm above the lipid membrane. On interacting with lipid headgroups, the peptide orients towards the membrane surface, and then enters the hydrophobic core of the membrane in a tilted conformation. The entry of A$\beta_{21-32}$ into the membrane causes a disruption of lipid headgroup packing and allows diffusion of water molecules into the membrane. During this process the lipids of the lowerleaflet are not perturbed. Pulling the peptide beyond the center of the bilayer into the towards the lower leaflet disrupts the lipid organization in the lower leaflet similar to the disruption of the upper leaflet.

## Umbrella sampling simulations

The COM pulling simulation described above generates a series of configurations, which are used as starting points for the subsequent umbrella sampling simulations. The potential of mean force (PMF) curve obtained for the WT and E22G fragments are shown for successive 10 ns windows in Figures 3 and 4.

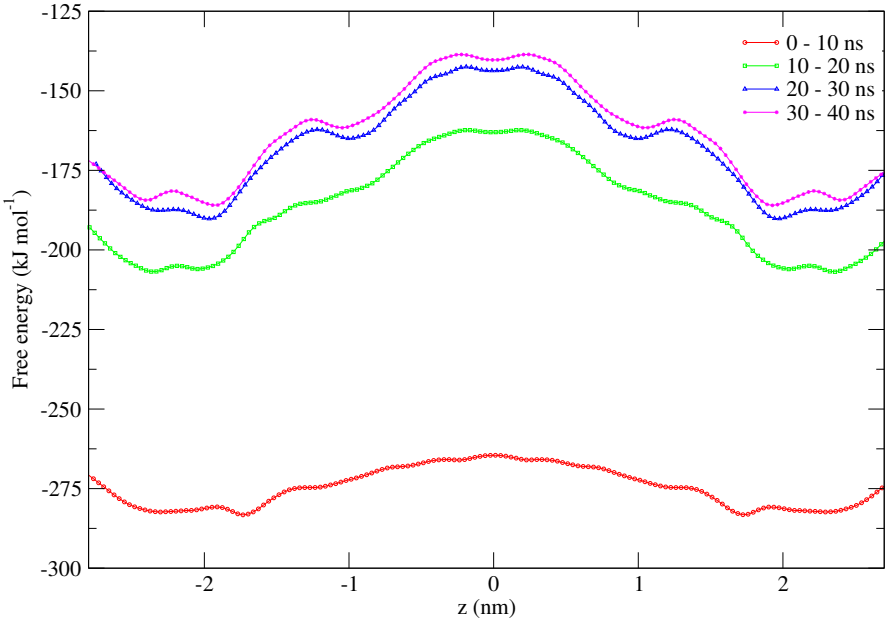


Figure 3: The free energy profile for tranfer of WT A$\beta_{21-32}$ peptide across POPC membrane. The $z = 0$ corresponds to membrane center.

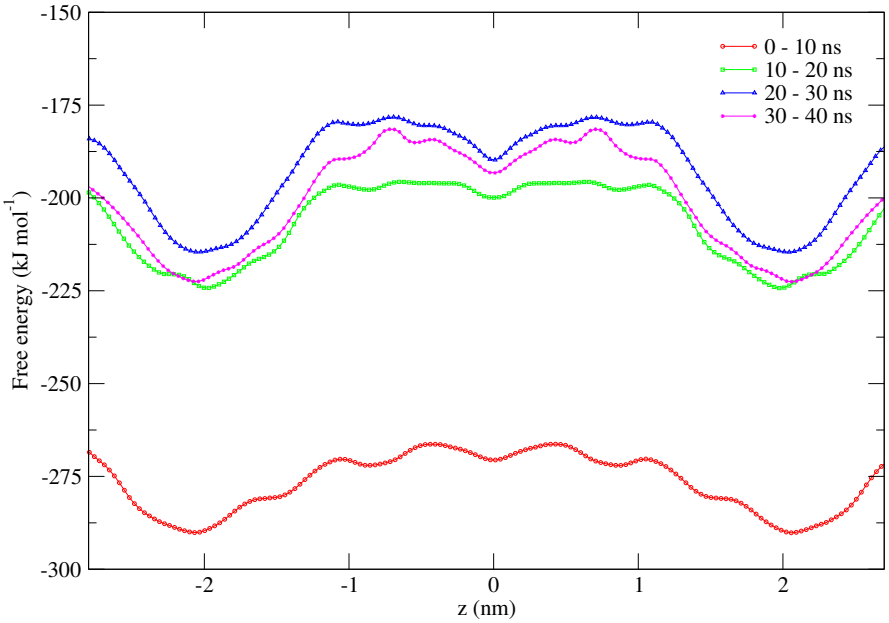


Figure 4: The free energy profile for tranfer of E22G A$\beta_{21-32}$ peptide across POPC membrane. The $z = 0$ corresponds to membrane center.

The symmetrized PMF plots for WT and E22G indicate differences with respect to the free energy values and profile of the curves. For WT, the PMF shows shallow wider minima in the region from $z = 2-2.3$ nm, corresponding to the state where the peptide initially interacts with the membrane surface. Here, the electrostatic interactions between the peptide and lipid headgroups is reduced due to the presence of water molecules and ions at the interface region, which is also for E22G. The PMF reaches a maximum close to the membrane center at $z = 0$ nm, the state where the peptide is deeply inserted into the hydrophobic core of the membrane and no longer interacts with the headgroup region. This state is governed by hydrophobic interactions between the peptide and lipid tails. In the case of E22G, the PMF shows a much deeper minimum in the region from $z = 2 - 2.3$ nm, where the peptide makes initial contact with the membrane, and a maximum inside the membrane center at $z = 0.8$ nm. For WT, an energy dip is observed in the region $z = 1$ nm, corresponding to the state where the peptide starts to leave the headgroup region to enter the hydrophobic membrane center. The dip in the region $z = 1$ nm is not prominent for E22G due to the absence of the charged E22 residue. The barrier-crossing region from $z = 1-2$ nm is dominated by strong electrostatic interactions and van der Waals forces between the peptide and lipid headgroups. The PMF profiles for the different simulation times in Figures 3 and 4 reveal that the US simulations are not fully converged yet. Nevertheless, the PMF profiles reveal three essential details. Firstly, a deeper minimum at the headgroup region due to the removal of one negative charge assists in stronger membrane adsorption of E22G. Secondly, the overall free-energy barrier for translocation of E22G is smaller than for WT A$\beta_{21-32}$. For E22G, the free energy in the middle of the membrane is $\Delta G = -193$ KJ/mol and for WT $\Delta G = -139$ KJ/mol (Figures 3 and 4). Thirdly, E22G has a free energy minimum at $z = 0$ nm.

## Insertion mechanism of A$\beta_{21-32}$

The sequential pathway leading to insertion of the peptide can be viewed from Figures 1 and 2. During the insertion both WT and E22G A$\beta_{21-32}$ alter their initial orientation on interacting with the membrane surface. Here, we analyse the insertion angles adopted by the peptide with respect to membrane normal and diffusion coefficients (D) to study the possible events in insertion of the peptides into the hydrophobic core of the membrane. Tilt angle and diffusion coefficients calculated are averaged at three different regions, at the adsorption region ($z = 2 - 2.3$ nm), where the peptide obliquely orients and adsorbs onto the membrane surface at an angle of 49.2° for WT and at 48.8° for E22G. In the initial stages of adsorption, both WT and E22G orient with the positively charged residue Lys28 facing the membrane surface whereas the negatively charged residues face the bulk water phase. Lys28 interacting with the lipid headgroups disrupts the membrane integrity and drives the initial insertion into the membrane. The process of binding and insertion is similar to those previously reported for protegrin-1 (PG-1) [34–36]. The diffusion coefficients are similar for both peptides at the adsorption region D $= 3.72 \times 10^{-7}$ cm$^2$ s$^{-1}$ for WT and D $= 4.72 \times 10^{-7}$ cm$^2$ s$^{-1}$) for E22G. At the barrier-crossing region ($z = 1 - 2$ nm), the peptide gets completely immersed into the lipid headgroup area and starts to enter the hydrophobic core of the membrane. The orientation of the peptides represents the state during the insertion process. WT orients to an angle of 39.5°, whereas E22G orients to an angle of 32.7°, allowing to move faster through the lipid headgroup region. E22G possesses a larger diffusion coefficient of $10.61 \times 10^{-7}$ cm$^2$ s$^{-1}$ than WT with D $= 3.06 \times 10^{-7}$ cm$^2$ s$^{-1}$. Faster diffusion of E22G in the barrier-crossing region allows easier translocation into the membrane. At the inserted region ($z = 0$), both peptides orient almost parallel to the membrane surface at an angle of 2.5° and 4.3° for WT and E22G, respectively.The diffusion coefficient decreases for E22G to $2.13 \times 10^{-7}$ cm$^2$ s$^{-1}$ at the membrane center. This corresponds to the PMF minimum at $z = 0$

indicating a metastable state for this peptide inside the membrane. For WT, the diffusion coefficient is $4.85 \times 10^{-7}$ $cm^2$ $s^{-1}$, which is similar to diffusion coefficient at the adsorption and barrier-crossing regions.

# Conclusions

Experimentally, it is known that both A$\beta$ monomers and oligomers intercalate the membrane [4] but the mechanism of insertion is not clear. Spontaneous membrane insertion of A$\beta$ peptide as reported from experiments, cannot be observed on the timescale of MD simulations. To overcome the limitation of timescale, we used a harmonic restraining potential to force the A$\beta_{21-32}$ peptide into the membrane. The PMF generated from the pulling simulation followed by umbrella sampling MD gives a thermodynamic aspect on the translocation of A$\beta_{21-32}$ across the membrane. The peptide binds obliquely to the membrane surface, with relatively similar tilt angles and diffusion coefficients observed for both WT and E22G A$\beta_{21-32}$. Lys28 mediates the initial interaction of the peptide with the membrane and subsequently drives the insertion process. At the barrier-crossing region, the peptide – membrane interactions are dominated by electrostatic interactions and van der Waals forces. The E22G A$\beta_{21-32}$ fragment undergoes faster reorientation and more rapid diffusion than the WT peptide, allowing E22G to more easily move into the hydrophobic core of the membrane. Also, the PMF barrier associated with translocation of WT is consistently higher compared to E22G, suggesting E22G A$\beta_{21-32}$ fragment to readily translocate across the membrane.

# References

[1] Selkoe DJ. The origins of alzheimer disease: A is for amyloid. *JAMA*, 283(12):1615–1617, 2000.

[2] Erik D. Roberson and Lennart Mucke. 100 years and counting: Prospects for defeating alzheimer's disease. *Science*, 314(5800):781–784, 2006.

[3] Fernando J. Sepulveda, Jorge Parodi, Robert W. Peoples, Carlos Opazo, and Luis G. Aguayo. Synaptotoxicity of alzheimer beta amyloid can be explained by its membrane perforating property. *PLoS ONE*, 5(7):e11820, 2010.

[4] R P Mason, R F Jacob, M F Walter, P E Mason, N A Avdulov, S V Chochina, U Igbavboa, and W G Wood. Distribution and fluidizing action of soluble and aggregated amyloid beta-peptide in rat synaptic plasma membranes. *J. Biol. Chem.*, 274(26):18801–18807, 1999.

[5] M. P. Mattson, B. Cheng, D. Davis, K. Bryant, I. Lieberburg, and R. Rydel. beta-amyloid peptides destabilize calcium homeostasis and render human cortical neurons vulnerable to excitotoxicity. *J. Neurosci.*, 12:376–389, 1992.

[6] Hai Lin, Rajinder Bhatia, and Ratneshwar Lal. Amyloid protein forms ion channels: implications for alzheimers disease pathophysiology. *The FASEB Journal*, 15(13):2433–2444, 2001.

[7] H. Lin, Y.J. Zhu, and R. Lal. Amyloid $\beta$ protein (140) forms calcium-permeable, $Zn^{2+}$-sensitive channel in reconstituted lipid vesicles. *Biochemistry*, 38:11189–11196, 1999.

[8] Arjan Quist, Ivo Doudevski, Hai Lin, Rushana Azimova, Douglas Ng, Blas Frangione, Bruce Kagan, Jorge Ghiso, and Ratnesh Lal. Amyloid

ion channels: a common structural link for protein-misfolding disease. *PNAS*, 102(30):10427–10432, 2005.

[9] N. Arispe, H.B. Pollard, and E. Rojas. $\beta$-amyloid $Ca^{2+}$-channel hypothesis for neuronal death in Alzheimer disease. *Mol. Cell. Biochem.*, 140:119–125, 1994.

[10] S. K. Rhee, A. P. Quist, and R. Lal. Amyloid $\beta$ protein (142) forms calcium-permeable, $Zn^{2+}$-sensitive channel. *J. Biol. Chem.*, 273:13379–13382, 1998.

[11] Yutaka Hirakura, Meng-Chin Lin, and Bruce L. Kagan. Alzheimer amyloid abeta142 channels: Effects of solvent, pH, and congo red. *J. Neurosci.*, 57(4):458466, 1999.

[12] H. Jang, J. Zheng, and R. Nussinov. Models of beta-amyloid ion channels in the membrane suggest that channel formation in the bilayer is a dynamic process. *Biophys. J.*, 93:1938–1949, 2007.

[13] H. Jang, J. Zheng, R. Lal, and R. Nussinov. New structures help the modeling of toxic amyloidbeta ion channels. *Trends in Biochem. Sci.*, 33:91–100, 2008.

[14] B. Strodel, J.W.L. Lee, C.S. Whittleston, and D.J. Wales. Transmembrane structures for Alzheimer's $A\beta_{1-42}$ oligomers. *J. Am. Chem. Soc.*, 132:13300–13312, 2010.

[15] Noel D. Lazo, Marianne A. Grant, Margaret C. Condron, Alan C. Rigby, and David B. Teplow. On the nucleation of amyloid $\beta$-protein monomer folding. *Protein Science : A Publication of the Protein Society*, 14(6):1581–1596, 2005.

[16] Wei Chen, Normand Mousseau, and Philippe Derreumaux. The conformations of the amyloid-beta (21-30) fragment can be described by three families in solution. *J. Chem. Phys.*, 125(8):084911, 2006.

[17] Nicolas L Fawzi, Aaron H Phillips, Jory Z Ruscio, Michaeleen Doucleff, David E Wemmer, and Teresa Head-Gordon. Structure and dynamics of the abeta(21-30) peptide from the interplay of NMR experiments and molecular simulations. *J. Am. Chem. Soc.*, 130(19):6145–6158, 2008.

[18] Andrij Baumketner, Summer L. Bernstein, Thomas Wyttenbach, Noel D. Lazo, David B. Teplow, Michael T. Bowers, and Joan-Emma Shea. Structure of the 21-30 fragment of amyloid beta-protein. *Protein Science : A Publication of the Protein Society*, 15(6):1239–1247, 2006.

[19] Jose M Borreguero, Brigita Urbanc, Noel D Lazo, Sergey V Buldyrev, David B Teplow, and H Eugene Stanley. Folding events in the 21-30 region of amyloid beta-protein (abeta) studied in silico. *PNAS*, 102(17):6015–6020, 2005.

[20] Mary Griffin Krone, Andrij Baumketner, Summer L Bernstein, Thomas Wyttenbach, Noel D Lazo, David B Teplow, Michael T Bowers, and Joan-Emma Shea. Effects of familial alzheimer's disease mutations on the folding nucleation of the amyloid beta-protein. *J. Mol. Biol.*, 381(1):221–228, 2008.

[21] Luis Cruz, Brigita Urbanc, Jose M Borreguero, Noel D Lazo, David B Teplow, and H Eugene Stanley. Solvent and mutation effects on the nucleation of amyloid beta-protein folding. *PNAS*, 102(51):18258–18263, 2005.

[22] Marianne A Grant, Noel D Lazo, Aleksey Lomakin, Margaret M Condron, Hiromi Arai, Ghiam Yamin, Alan C Rigby, and David B Teplow. Familial alzheimer's disease mutations alter the stability of the amyloid beta-protein monomer folding nucleus. *PNAS*, 104(42):16522–16527, 2007.

[23] Chetan Poojari, Andreas Kukol, and Birgit Strodel. How the amyloid-peptide and membranes affect each other: An extensive simula-

tion study. *Biochimica et Biophysica Acta (BBA) - Biomembranes*, 1828(2):327–339, 2013.

[24] C. H. Davis and M. L. Berkowitz. Structure of the amyloid- beta (1-42) monomer absorbed to model phospholipid bilayers: A molecular dynamics study. *J. Phys. Chem. B*, 113:14480–14486, 2009.

[25] C. H. Davis and M. L. Berkowitz. Interaction between amyloid-beta peptide and phospholipid bilayers: A molecular dynamics study. *Biophysical J.*, 96:785–797, 2009.

[26] Dennis J Selkoe and Marcia B Podlisny. Deciphering the genetic basis of alzheimer's disease. *Annual review of genomics and human genetics*, 3:67–99, 2002.

[27] C Nilsberth, A Westlind-Danielsson, CB Eckman, MM Condron, K Axelman, C Forsell, C Stenh, J Luthman, DB Teplow, SG Younkin, J Naslund, and L Lannfelt. The 'arctic' app mutation (e693g) causes alzheimer's disease by enhanced a beta protofibril formation. *Nat. Neurosci.*, 4(9):887–893, SEP 2001.

[28] DM Walsh, DM Hartley, Y Kusumoto, Y Fezoui, MM Condron, A Lomakin, GB Benedek, DJ Selkoe, and DB Teplow. Amyloid beta-protein fibrillogenesis - structure and biological activity of protofibrillar intermediates. *J. Biol. Chem.*, 274(36):25945–25952, SEP 3 1999.

[29] DM Hartley, DM Walsh, CPP Ye, T Diehl, S Vasquez, PM Vassilev, DB Teplow, and DJ Selkoe. Protofibrillar intermediates of amyloid beta-protein induce acute electrophysiological changes and progressive neurotoxicity in cortical neurons. *J. Neurosci.*, 19(20):8876–8884, OCT 15 1999.

[30] Berk Hess, Carsten Kutzner, David van der Spoel, and Erik Lindahl.

GROMACS 4: Algorithms for highly efficient, load-balanced, and scalable molecular simulation. *JCTC*, 4(3):435–447, March 2008.

[31] C. Oostenbrink, A. Villa, A.E. Mark, and W.F. van Gunsteren. A biomolecular force field based on the free enthalpy of hydration and solvation: the gromos force-field parameter sets 53a5 and 53a6. *J. Comput. Chem.*, 25:1656–1676, 2004.

[32] A. Kukol. Lipid models for united-atom molecular dynamics simulations of proteins. *J. Chem. Theor. Comput.*, 5:615–626, 2009.

[33] Shankar Kumar, John M. Rosenberg, Djamal Bouzida, Robert H. Swendsen, and Peter A. Kollman. THE weighted histogram analysis method for free-energy calculations on biomolecules. i. the method. *J. Comput. Chem.*, 13(8):1011–1021, 1992.

[34] Victor Vivcharuk and Yiannis N Kaznessis. Thermodynamic analysis of protegrin-1 insertion and permeation through a lipid bilayer. *J. Phys. Chem. B*, 115(49):14704–14712, 2011.

[35] Hyunbum Jang, Buyong Ma, Thomas B. Woolf, and Ruth Nussinov. Interaction of protegrin-1 with lipid bilayers: Membrane thinning effect. *Biophys. J.*, 91(8):2848–2859, 2006.

[36] Hyunbum Jang, Buyong Ma, and Ruth Nussinov. Conformational study of the protegrin-1 (PG-1) dimer interaction with lipid bilayers and its effect. *BMC Structural Biology*, 7(1):21, 2007.

# 5 Conclusions

Several mechanisms have been proposed to explain amyloid toxicity. Association of amyloids with cell membranes and resulting membrane damage is one of the well known hypotheses [75,76,230], with amyloids exerting their cytotoxic effect by increasing membrane fluidity [99]. Both A$\beta$ and hIAPP exhibit a similar mechanism of toxicity, through aggregation of monomers into toxic oligomers, accompanied by membrane association and insertion. Several experimental studies have demonstrated the insertion of amyloids into membranes and formation of ion-channels leading to dysregulation of ion homeostasis [85,95–97,184–186,231]. Inspite of several pioneering work, an experimental atomistic model of membrane-bound amyloid is still lacking. Molecular simulations offer the potential of predicting such structures [112,232,233], and, in addition, provide information about conformational transitions of amyloids and their interactions with lipid bilayers.

In our first study, we performed MD simulations of transmembrane A$\beta_{42}$ considering both helical and $\beta$-sheet conformations preinserted in POPC, DPPC and POPG bilayers. The MD simulations on the sub-microsecond timescale revealed the highest stability in POPC for both helical and $\beta$-sheet A$\beta_{42}$. Hydrophobic mismatch and lipid order of DPPC, and anionic surface charges of POPG bilayers are responsible for structural instabilities of A$\beta_{42}$ in these bilayers. However, A$\beta_{42}$ remained embedded in the bilayers in all of our MD simulations. The stability of the transmembrane $\beta$-sheet structure can be increased via oligomerization, where favorable interpeptide interactions, especially the formation of interpeptide H-bonds add to the stability of this structure [112]. We observed the translocation of one or more water molecules in the vicinity of the membrane-inserted A$\beta_{42}$. Water translocation is governed by a number of factors, such as the lipid type, simulation temperature and the A$\beta_{42}$ structure. Compared to the monomeric A$\beta_{42}$ structures in POPC, the $\beta$-sheet tetramer increases the translocation of water through the POPC bilayers. This finding allows us to conclude that membrane permeabilization by membrane-bound A$\beta$ must be due to A$\beta$ oligomers, which is in agreement with experimental findings [101].

Our second study focused on mutational studies, to investigate the transmembrane stability of various A$\beta_{42}$ mutants in a $\beta$-sheet conformation [112]. Our 500 ns MD simulations of A$\beta_{1-42}$ mutants in a POPC bilayer reveal a similar or increased stability compared to wild type A$\beta_{42}$ for all mutants except D23G. For the monomeric $\beta$-sheet we observed

the highest stability for the Arctic mutant E22G and the double mutant K16M/K28M. The removal of positive charges by mutating K16 and K28 to methionine increases the hydropathy index of this mutant A$\beta_{42}$ by a factor of 2.34, which gives rise to a stable transmembrane $\beta$-sheet. The stability of the Arctic mutant E22G can be attributed to the removal of the negative E22 charge in combination with D23 and K28 interacting with the headgroups of the lower leaflet, leading to charge neutrality of the peptide inside the membrane. While the 'Arctic-type' D23G mutant has the same hydropathy index as E22G A$\beta_{42}$, it is not stable as transmembrane $\beta$-sheet, since the position of E22 inside the membrane causes the peptide to bend towards the upper membrane surface. The less toxic wild type A$\beta_{42}$, on the other hand, looses some of its $\beta$ structure during the MD simulation due to its overall negative charge inside the membrane. Furthermore, our studies on tetrameric mutants revealed an increased membrane disruption ability compared to wild type A$\beta_{1-42}$, with the D23G tetramer showing the larger membrane disruption and water permeation compared to the other monomers and tetramers. In the case of the Arctic A$\beta$ tetramer it was found that the $\beta$-sheet secondary structure is crucial for membrane damage. Our findings are consistent with experimental studies where it was shown that a high $\beta$-sheet content is necessary for fast aggregation and neurotoxicity for A$\beta_{1-42}$ [234]. Furthermore, our studies revealed the D23G mutant to have the largest membrane-disruptive effect. A similar finding was reported using AFM studies [235], were they showed the D23N mutant to have a larger membrane disruptive effect (but only in discrete areas) than E22G A$\beta_{1-40}$. Together, these results suggest that the altered neurotoxicity arising from mutations in A$\beta$ is not only a result of the altered aggregation propensity, but also originates from modified A$\beta$ interactions with neuronal membranes.

With A$\beta$ and hIAPP sharing similar mechanism of membrane disruption, our third study focused on investigating the position and orientation of $\beta$-sheet hIAPP oligomers at DPPG/water interfaces. In lipid monolayers, the average orientation of hIAPP trimers and tetramers is rather flat, with a tilt angle relative to the membrane surface of close to 40°, in agreement with the overall orientation predicted by a single average configuration consistent with chiral SFG spectroscopy [199]. In the lipid bilayer, hIAPP adopts a more upright orientation with a tilt angle close to 60°, due to interactions of the $\beta$-sheet with lipid headgroups and counterions on both sides of the membrane. Differences in the orientation of hIAPP aggregates embedded in the monolayers versus bilayers are due to the balance of interactions at the peptide-membrane/water interface. MD simulations of hIAPP aggregates inserted into DPPG bilayers predict intrusion of both water and monovalent ions (*e.g.*, $Na^+$) into the membrane/hIAPP complex. Water molecules form a continuous channel and permeate through the membrane, allowing $Na^+$ ions to diffuse into the otherwise hydrophobic membrane bilayer core. Only the trimer inserted in the DPPG bilayer generates a water channel due to the barrel-like conformation of the hIAPP

aggregate. In contrast, the tetrameric $\beta$-sheet seems to be too stiff to enable formation of a (distorted) barrel. These results are particularly valuable since to the best of our knowledge this is the first study that shows channel formation by membrane-bound hIAPP oligomers, although a previous study has probed the channel activity of preformed hIAPP pores [198]. We thus conclude that membrane permeation by small hIAPP oligomers is indeed a likely mechanism for hIAPP cytotoxicity [175,180,192,193].

Experimentally, it is known that both A$\beta$ monomers and oligomers intercalate the membrane [236] but the mechanism of insertion is not clear. Spontaneous translocation of A$\beta$ peptide reported in experiments cannot be observed on the timescale of molecular simulations. To overcome the limitations of timescale, we used a harmonic restraining potential to force the A$\beta_{21-32}$ peptide into the membrane. The free-energy profile generated from a series of pulling simulations gives a thermodynamic aspect on translocation of A$\beta_{21-32}$ across the membrane. The peptide binds obliquely to the membrane surface with relatively similar tilt angles and diffusion coefficients observed for both wild-type and E22G A$\beta_{21-32}$. Residue K28 mediates the interaction of the peptide with the membrane and subsequently drives the insertion process. In the barrier-crossing region, peptide and membrane interactions are dominated by electrostatic interactions and van der Waals forces. E22G A$\beta_{21-32}$ fragment undergoes faster orientation and more rapid diffusion than the wild-type peptide, allowing E22G to more easily insert into the hydrophobic core of the membrane. The overall barrier associated with the translocation of wild-type A$\beta_{21-32}$ is consistently higher when compared to E22G, suggesting E22G A$\beta_{21-32}$ fragment to more readily translocate across the membrane. In the Arctic mutant, the negatively charged glutamate is replaced by a glycine residue, which has a neutral charge. This replacement increases the hydrophobicity of the A$\beta_{21-32}$ peptide, enabling it to insert more easily into the membrane. Thus, increased toxicity and membrane disruption ability of E22G A$\beta_{1-42}$ can be attributed to its hydrophobic property.

Our results on the interactions between A$\beta_{42}$ and lipid membranes, and the effect of A$\beta_{42}$ mutations on lipid membranes properties provides insight into the likely toxicity mechanism caused by membrane-inserted A$\beta_{42}$ oligomers. Experimental work focused on resolving the structure of A$\beta$ in and on lipid membranes would assist in modeling the molecular events leading to AD. Our studies on hIAPP highlight the formation of barrel-like conformations by membrane-bound hIAPP oligomers. Such channel formation gives rise to a continuous water channel within the membrane, also allowing $Na^+$ ions to diffuse into the hydrophobic core of the membrane bilayer. It is natural to expect that other amyloidogenic proteins might also be able to form channels and permeabilize the lipid bilayer.

# Bibliography


[1] S J Singer and G L Nicolson. The fluid mosaic model of the structure of cell membranes. *Science (New York, N.Y.)*, 175(4023):720–731, 1972.

[2] A G Lee, N J M Birdsall, J C Metcalfe, Penelope A Toon, and G B Warren. Clusters in lipid bilayers and the interpretation of thermal effects in biological membranes. *Biochemistry*, 13(18):3699–3705, 1974.

[3] F Wunderlich, A Ronai, V Speth, J Seelig, and A Blume. Thermotropic lipid clustering in tetrahymena membranes. *Biochemistry*, 14(17):3730–3735, 1975.

[4] Frank Wunderlich, Werner Kreutz, Peter Mahler, Adam Ronai, and Gerlinde Heppeler. Thermotropic fluid ordered "discontinuous" phase separation in microsomal lipids of tetrahymena. an x-ray diffraction study. *Biochemistry*, 17(10):2005–2010, 1978.

[5] The concept of lipid domains in membranes. *J. Cell Biol.*, 94(1):1–6, 1982.

[6] F Goodsaid-Zalduondo, D A Rintoul, J C Carlson, and W Hansel. Luteolysis-induced changes in phase composition and fluidity of bovine luteal cell membranes. *PNAS*, 79(14):4332–4336, 1982.

[7] Kai Simons and Gerrit Van Meer. Lipid sorting in epithelial cells. *Biochemistry*, 27(17):6197–6202, 1988.

[8] Kai Simons and Elina Ikonen. Functional rafts in cell membranes. *Nature*, 387(6633):569–572, 1997.

[9] Linda J. Pike. Rafts defined: a report on the keystone symposium on lipid rafts and cell function. *J. Lipid Res.*, 47(7):1597–1598, 2006.

[10] David L Daleke. Phospholipid flippases. *J. Biol. Chem.*, 282(2):821–825, 2007.

[11] Philippe F Devaux and Roger Morris. Transmembrane asymmetry and lateral domains in biological membranes. *Traffic*, 5(4):241–246, 2004.

[12] Ehud Gazit, Anita Boman, Hans G. Boman, and Yechiel Shai. Interaction of the mammalian antibacterial peptide cecropin p1 with phospholipid vesicles. *Biochemistry*, 34(36):11479–11488, 1995.

[13] H D Zucht, M Raida, K Adermann, H J Mgert, and W G Forssmann. Casocidin-i: a casein-alpha s2 derived peptide exhibits antibacterial activity. *FEBS Lett.*, 372(2-3):185–188, 1995.

[14] Miguel A Campos, Miguel A Vargas, Vernica Regueiro, Catalina M Llompart, Sebastin Albert, and Jos A Bengoechea. Capsule polysaccharide mediates bacterial resistance to antimicrobial peptides. *Infect. Immun.*, 72(12):7107–7114, 2004.

[15] M Amiche, A A Seon, T N Pierre, and P Nicolas. The dermaseptin precursors: a protein family with a common preproregion and a variable c-terminal antimicrobial domain. *FEBS Lett.*, 456(3):352–356, 1999.

[16] Michael E Greenberg, Mingjiang Sun, Renliang Zhang, Maria Febbraio, Roy Silverstein, and Stanley L Hazen. Oxidized phosphatidylserine-CD36 interactions play an essential role in macrophage-dependent phagocytosis of apoptotic cells. *J. Exp. Med.*, 203(12):2613–2625, 2006.

[17] J Pereira, I Palomo, M Ocqueteau, M Soto, E Aranda, and D Mezzano. Platelet aging in vivo is associated with loss of membrane phospholipid asymmetry. *J. Thromb. Haemost.*, 82(4):1318–1321, 1999.

[18] F A Kuypers and K de Jong. The role of phosphatidylserine in recognition and removal of erythrocytes. *Mol. Cell. Biol*, 50(2):147–158, 2004.

[19] Sophia Ran, Amber Downes, and Philip E Thorpe. Increased exposure of anionic phospholipids on the surface of tumor blood vessels. *Cancer Res.*, 62(21):6132–6140, 2002.

[20] M J Osborn, P D Rick, V Lehmann, E Rupprecht, and M Singh. Structure and biogenesis of the cell envelope of gram-negative bacteria. *Ann N Y Acad Sci.*, 235(0):52–65, 1974.

[21] C R Raetz. Enzymology, genetics, and regulation of membrane phospholipid synthesis in escherichia coli. *Annu. Rev. Microbiol.*, 42(3):614–659, 1978.

[22] M J Osborn. Structure and biosynthesis of the bacterial cell wall. *Annu. Rev. Biochem.*, 38:501–538, 1969.

[23] W Dowhan. Molecular basis for membrane phospholipid diversity:why are there so many lipids? *Annu. Rev. Biochem.*, 66(1):199–232, 1997.

[24] Eoin Fahy, Manish Sud, Dawn Cotter, and Shankar Subramaniam. LIPID MAPS online tools for lipid research. *Nucleic Acids Res.*, 35(Web Server issue):W606–W612, 2007.

[25] D Chapman. Phase transitions and fluidity characteristics of lipids and cell membranes. *Quart. Rev. Biophys.*, 8(2):185–235, 1975.

[26] Gerrit van Meer, Dennis R Voelker, and Gerald W Feigenson. Membrane lipids: where they are and how they behave. *Nat. Rev. Mol. Cell Biol.*, 9(2):112–124, 2008.

[27] D J Recktenwald and H M McConnell. Phase equilibria in binary mixtures of phosphatidylcholine and cholesterol. *Biochemistry*, 20(15):4505–4510, 1981.

[28] Alex H. de Vries, Serge Yefimov, Alan E. Mark, and Siewert J. Marrink. Molecular structure of the lecithin ripple phase. *PNAS*, 102(15):5392–5396, 2005.

[29] P A Janmey and P K J Kinnunen. Biophysical properties of lipids and dynamic membranes. *Trends Cell Biol.*, 16(10):538–546, 2006.

[30] Kai Simons and Julio L. Sampaio. Membrane organization and lipid rafts. *Cold Spring Harb. Perspect. Biol.*, 2011.

[31] P R Cullis and B de Kruijff. Lipid polymorphism and the functional roles of lipids in biological membranes. *Biochim. Biophys. Acta*, 559(4):399–420, 1979.

[32] Ehud M. Landau and Jrg P. Rosenbusch. Lipidic cubic phases: A novel concept for the crystallization of membrane proteins. *PNAS*, 93(25):14532–14535, 1996.

[33] Ben de Kruijff. Lipid polymorphism and biomembrane function. *Curr Opin Chem Biol*, 1(4):564–569, 1997.

[34] Vadim A Frolov, Anna V Shnyrova, and Joshua Zimmerberg. Lipid polymorphisms and membrane shape. *Cold Spring Harb. Perspect. Biol.*, 3(11):a004747, 2011.

[35] S M Gruner. Intrinsic curvature hypothesis for biomembrane lipid composition: a role for nonbilayer lipids. *PNAS*, 82(11):3665–3669, 1985.

[36] Anthony G. Lee. How lipids affect the activities of integral membrane proteins. *Biochimica et Biophysica Acta (BBA) - Biomembranes*, 1666(12):62–87, 2004.

[37] W. Rawicz, K.C. Olbrich, T. McIntosh, D. Needham, and E. Evans. Effect of chain length and unsaturation on elasticity of lipid bilayers. *Biophys. J.*, 79(1):328–339, 2000.

[38] Sarah L. Veatch and Sarah L. Keller. Seeing spots: Complex phase behavior in simple membranes. *Biochim. Biophys. Acta*, 1746(3):172–185, 2005.

[39] Stephanie Tristram-Nagle and John F. Nagle. Lipid bilayers: thermodynamics, structure, fluctuations, and interactions. *Chem. Phys. Lipids*, 127(1):3–14, 2004.

[40] Gerald W. Feigenson. Phase boundaries and biological membranes. *Annu. Rev. Biophys. Biomol. Struct.*, 36(1):63–77, 2007.

[41] Frederick A. Heberle and Gerald W. Feigenson. Phase separation in lipid membranes. *Cold Spring Harb. Perspect. Biol.*, 2011.

[42] Sagar A. Pandit, S. Vasudevan, S. W. Chiu, R. Jay Mashl, Eric Jakobsson, and H. L. Scott. Sphingomyelin-cholesterol domains in phospholipid membranes: Atomistic simulation. *Biophys. J.*, 87(2):1092–1100, 2004.

[43] Sagar A. Pandit, Eric Jakobsson, and H. L. Scott. Simulation of the early stages of nano-domain formation in mixed bilayers of sphingomyelin, cholesterol, and dioleylphosphatidylcholine. *Biophys. J.*, 87(5):3312–3322, 2004.

[44] Lawrence Rajendran and Kai Simons. Lipid rafts and membrane dynamics. *J. Cell Sci.*, 118(6):1099–1102, 2005.

[45] John F. Hancock. Lipid rafts: contentious only from simplistic standpoints. *Nat. Rev. Mol. Cell Biol.*, 7(6):456–462, 2006.

[46] Elliot L. Elson, Eliot Fried, John E. Dolbow, and Guy M. Genin. Phase separation in biological membranes: Integration of theory and experiment. *Annu. Rev. Biophys.*, 39(1):207–226, 2010.

[47] Chunbo Yuan, Jennifer Furlong, Pierre Burgos, and Linda J. Johnston. The size of lipid rafts: An atomic force microscopy study of ganglioside GM1 domains in Sphingomyelin/DOPC/Cholesterol membranes. *Biophys. J.*, 82(5):2526–2535, 2002.

[48] Peter I. Kuzmin, Sergey A. Akimov, Yuri A. Chizmadzhev, Joshua Zimmerberg, and Fredric S. Cohen. Line tension and interaction energies of membrane rafts calculated from lipid splay and tilt. *Biophys. J.*, 88(2):1120–1133, 2005.

[49] Jared C. Lawrence, David E. Saslowsky, J. Michael Edwardson, and Robert M. Henderson. Real-time analysis of the effects of cholesterol on lipid raft behavior using atomic force microscopy. *Biophys. J.*, 84(3):1827–1832, 2003.

[50] A.G Lee. Lipidprotein interactions in biological membranes: a structural perspective. *Biochimica et Biophysica Acta (BBA) - Biomembranes*, 1612(1):1–40, 2003.

[51] Richard G. W. Anderson and Ken Jacobson. A role for lipid shells in targeting proteins to caveolae, rafts, and other lipid domains. *Science*, 296(5574):1821–1825, 2002.

[52] Francesc-Xabier Contreras, Andreas Max Ernst, Felix Wieland, and Britta Brgger. Specificity of intramembrane ProteinLipid interactions. *Cold Spring Harb. Perspect. Biol.*, 3(6), 2011.

[53] Robert S. Cantor. Lipid composition and the lateral pressure profile in bilayers. *Biophys. J.*, 76(5):2625–2639, 1999.

[54] Robert S. Cantor. The influence of membrane lateral pressures on simple geometric models of protein conformational equilibria. *Chem. Phys. Lipids*, 101(1):45–56, 1999.

[55] Andrew M. Powl, J. Malcolm East, and Anthony G. Lee. Anionic phospholipids affect the rate and extent of flux through the mechanosensitive channel of large conductance MscL. *Biochemistry*, 47(14):4317–4328, 2008.

[56] Andrew M. Powl, J. Malcolm East, and Anthony G. Lee. Importance of direct interactions with lipids for the function of the mechanosensitive channel MscL. *Biochemistry*, 47(46):12175–12184, 2008.

[57] J. Girshman, D.V. Greathouse, R.E. Koeppe 2nd, and O.S. Andersen. Gramicidin channels in phospholipid bilayers with unsaturated acyl chains. *Biophys. J.*, 73(3):1310–1319, 1997.

[58] Niloufar Mobashery, Claus Nielsen, and Olaf S Andersen. The conformational preference of gramicidin channels is a function of lipid bilayer thickness. *FEBS Letters*, 412(1):15–20, 1997.

[59] R E Koeppe and O S Anderson. Engineering the gramicidin channel. *Annu. Rev. Biophys. and Biomolecular Structure*, 25(1):231–258, 1996.

[60] Johann Deisenhofer and Hartmut Michel. The photosynthetic reaction center from the purple bacterium rhodopseudomonas viridis. *Science*, 245(4925):1463–1473, 1989.

[61] Anja N. J. A. Ridder, Sven Morein, Jeanette G. Stam, Andreas Kuhn, Ben de Kruijff, and J. Antoinette Killian. Analysis of the role of interfacial tryptophan residues in controlling the topology of membrane proteins. *Biochemistry*, 39(21):6521–6528, 2000.

[62] Hartmut Luecke, Brigitte Schobert, Hans-Thomas Richter, Jean-Philippe Cartailler, and Janos K. Lanyi. Structure of bacteriorhodopsin at 1.55 resolution. *J. Mol. Biol.*, 291(4):899–911, 1999.

[63] Christian Lange, Juergen H. Nett, Bernard L. Trumpower, and Carola Hunte. Specific roles of proteinphospholipid interactions in the yeast cytochrome bc1 complex structure. *The EMBO Journal*, 20(23):6591–6600, 2001.

[64] F. Chiti and C. M. Dobson. Protein misfolding, functional amyloid, and human disease. *Annu. Rev. Biochem.*, 75:333–366, 2006.

[65] D. M. Walsh, I. Klyubin, J. V. Fadeeva, W. K. Cullen, R. Anwyl, M. S. Wolfe, M. J. Rowan, and D. J. Selkoe. Naturally secreted oligomers of amyloid $\beta$ protein potently inhibit hippocampal long-term potentiation *in vivo*. *Nature*, 416:535–539, 2002.

[66] M.D. Kirkitadze, G. Bitan, and D.B. Teplow. Paradigm shifts in alzheimers disease and other neurodegenerative disorders: the emerging role of oligomeric assemblies. *J. Neurosci. Res.*, 69:567–577, 2002.

[67] M. Bucciantini, E. Giannoni, F. Chiti, F. Baroni, L. Formigli, J. Zurdo, N. Taddei, G. Ramponi, C. M. Dobson, and M. Stefani. Inherent toxicity of aggregates implies a common mechanism for protein misfolding diseases. *Nature*, 416:507–511, 2002.

[68] W. L. Klein, W. B. Stine, and D. B. Teplow. Small assemblies of unmodied amyloid $\beta$-protein are the proximate neurotoxin in alzheimers disease. *Neurobiol Aging*, 25:569–580, 2004.

[69] J. Janson, R. H. Ashley, D. Harrison, S. McIntyre, and P. C. Butler. The mechanism of islet amyloid polypeptide toxicity is membrane disruption by intermediate-sized toxic amyloid particles. *Diabetes*, 48:491–498, 1999.

[70] Magdalena Anguiano, Richard J Nowak, and Jr Lansbury, Peter T. Protofibrillar islet amyloid polypeptide permeabilizes synthetic vesicles by a pore-like mechanism that may be relevant to type II diabetes. *Biochemistry*, 41:11338–11343, 2002.

[71] Yair Porat, Sofiya Kolusheva, Raz Jelinek, and Ehud Gazit. The human islet amyloid polypeptide forms transient membrane-active prefibrillar assemblies. *Biochemistry*, 42:10971–10977, 2003.

[72] R. Kayed, Y. Sokolov, B. Edmonds, T. M. McIntire, S. C. Milton, J. E. Hall, and C. G. Glabe. Permeabilization of lipid bilayers is a common conformation-dependent activity of soluble amyloid oligomers in protein misfolding diseases. *J. Biol. Chem.*, 279:46363–46366, 2004.

[73] Angelo Demuro, Erene Mina, Rakez Kayed, Saskia C Milton, Ian Parker, and Charles G Glabe. Calcium dysregulation and membrane disruption as a ubiquitous neurotoxic mechanism of soluble amyloid oligomers. *J. Biol Chem*, 280:17294–17300, 2005.

[74] Robert A Ritzel, Juris J Meier, Chia-Yu Lin, Johannes D Veldhuis, and Peter C Butler. Human islet amyloid polypeptide oligomers disrupt cell coupling, induce apoptosis, and impair insulin secretion in isolated human islets. *Diabetes*, 56:65–71, 2007.

[75] Lucie Khemtmourian, J Antoinette Killian, Jo W M Hppener, and Maarten F M Engel. Recent insights in islet amyloid polypeptide-induced membrane disruption and its role in beta-cell death in type 2 diabetes mellitus. *Exp. diabetes res.*, 2008:421287, 2008.

[76] Per Westermark, Arne Andersson, and Gunilla T Westermark. Islet amyloid polypeptide, islet amyloid, and diabetes mellitus. *Physiol. Rev.*, 91(3):795–826, 2011.

[77] DJ Selkoe. The origins of Alzheimer disease - A is for amyloid. *JAMA*, 283(12):1615–1617, 2000.

[78] Erik D. Roberson and Lennart Mucke. 100 years and counting: Prospects for defeating Alzheimer's disease. *Science*, 314(5800):781–784, 2006.

[79] Gopal Thinakaran and Edward H. Koo. Amyloid Precursor Protein Trafficking, Processing, and Function. *J. Biol. Chem.*, 283(44):29615–29619, 2008.

[80] Joseph T. Jarrett, Elizabeth P. Berger, and Peter T. Lansbury Jr. The carboxy terminus of the $\beta$ amyloid protein is critical for the seeding of amyloid formation: Implications for the pathogenesis of alzheimer's disease. *Biochemistry*, 32:4693–4697, 1993.

[81] SG Younkin. The role of Abeta 42 in Alzheimer's disease. *J. Physiol.*, 92(3-4):289–292, 1998.

[82] C. Haass and D.J. Selkoe. Soluble protein oligomers in neurodegeneration: lessons from the alzheimers amyloid $\beta$-peptide. *Nat. Rev. Mol. Cell Biol.*, 8:101–112, 2007.

[83] D.M. Walsh and D.J. Selkoe. A$\beta$ oligomers: A decade of discovery. *J. Neurochem.*, 101:1172–1184, 2007.

[84] A. Mohamed and E. P. de Chaves. A internalization by neurons and glia. *Int. J. Alzheimers Dis.*, 2011:127984, 2011.

[85] Thomas L. Williams and Louise C. Serpell. Membrane and surface interactions of alzheimers a$\beta$ peptide – insights into the mechanism of cytotoxicity. *FEBS J.*, 278:17, 2011.

[86] Ran Friedman, Riccardo Pellarin, and Amedeo Caflisch. Amyloid Aggregation on Lipid Bilayers and Its Impact on Membrane Permeability. *J. Mol. Biol.*, 387(2):407–415, 2009.

[87] E Terzi, G Holzemann, and J Seelig. Interaction of Alzheimer beta-amyloid peptide(1-40) with lipid membranes. *Biochemistry*, 36(48):14845–14852, 1997.

[88] Alexandra Buchsteiner, Thomas Hauss, Silvia Dante, and Norbert A. Dencher. Alzheimer's disease amyloid-beta peptide analogue alters the ps-dynamics of phospholipid membranes. *Biochim. Biophys. Acta-Biomembr.*, 1798(10):1969–1976, 2010.

[89] G. P. Eckert, W. G. Wood, and W. E. Mueller. Lipid Membranes and beta-Amyloid: A Harmful Connection. *Curr. Protein Pept. Sci.*, 11(5):319–325, 2010.

[90] Fernando J. Sepulveda, Jorge Parodi, Robert W. Peoples, Carlos Opazo, and Luis G. Aguayo. Synaptotoxicity of Alzheimer Beta Amyloid Can Be Explained by Its Membrane Perforating Property. *PLos One*, 5(7), 2010.

[91] M. P. Mattson, B. Cheng, D. Davis, K. Bryant, I. Lieberburg, and R. Rydel. beta-amyloid peptides destabilize calcium homeostasis and render human cortical neurons vulnerable to excitotoxicity. *J. Neurosci.*, 12:376–389, 1992.

[92] Imke Peters, Urule Igbavboa, Tanja Schuett, Schamim Haidari, Ulrike Hartig, Ximena Rosello, Steffi Boettner, Ekaterini Copanaki, Thomas Deller, Donat Koegel, W. Gibson Wood, Walter E. Mueller, and Gunter P. Eckert. The interaction of beta-amyloid protein with cellular membranes stimulates its own production. *Biochim. Biophys. Acta-Biomembr.*, 1788(5):964–972, 2009.

[93] Arjan Quist, Ivo Doudevski, Hai Lin, Rushana Azimova, Douglas Ng, Blas Frangione, Bruce Kagan, Jorge Ghiso, and Ratnesh Lal. Amyloid ion channels: a common structural link for protein-misfolding disease. *PNAS*, 102(30):10427–10432, 2005.

[94] Hai Lin, Rajinder Bhatia, and Ratneshwar Lal. Amyloid protein forms ion channels: implications for alzheimers disease pathophysiology. *The FASEB Journal*, 15(13):2433–2444, 2001.

[95] N. Arispe, H.B. Pollard, and E. Rojas. $\beta$-amyloid $Ca^{2+}$-channel hypothesis for neuronal death in Alzheimer disease. *Mol. Cell. Biochem.*, 140:119–125, 1994.

[96] H. Lin, Y.J. Zhu, and R. Lal. Amyloid $\beta$ protein (140) forms calcium-permeable, $Zn^{2+}$-sensitive channel in reconstituted lipid vesicles. *Biochemistry*, 38:11189–11196, 1999.

[97] S. K. Rhee, A. P. Quist, and R. Lal. Amyloid $\beta$ protein-(142) forms calcium-permeable, $Zn^{2+}$-sensitive channel. *J. Biol. Chem.*, 273:13379–13382, 1998.

[98] Yutaka Hirakura, Meng-Chin Lin, and Bruce L. Kagan. Alzheimer amyloid a142 channels: Effects of solvent, pH, and congo red. *J. Neurosci. Res.*, 57(4):458466, 1999.

[99] RP Mason, RF Jacob, MF Walter, PE Mason, NA Avdulov, SV Chochina, U Igbavboa, and WG Wood. Distribution and fluidizing action of soluble and aggregated amyloid beta-peptide in rat synaptic plasma membranes. *J. Biol. Chem.*, 274(26):18801–18807, 1999.

[100] EE Ambroggio, DH Kim, F Separovic, CJ Barrow, CJ Barrow, KJ Barnham, LA Bagatolli, and GD Fidelio. Surface behavior and lipid interaction of Alzheimer beta-amyloid peptide 1-42: A membrane-disrupting peptide. *Biophys. J.*, 88(4):2706–2713, 2005.

[101] R Kayed, Y Sokolov, B Edmonds, TM McIntire, SC Milton, JE Hall, and CG Glabe. Permeabilization of lipid bilayers is a common conformation-dependent activity of soluble amyloid oligomers in protein misfolding diseases. *J. Biol. Chem.*, 279(45):46363–46366, 2004.

[102] Maurits R. R. de Planque, Vincent Raussens, Sonia Antoranz Contera, Dirk T. S. Rijkers, Rob M. J. Liskamp, Jean-Marie Ruysschaert, John F. Ryan, Frances Separovic, and Anthony Watts. beta-sheet structured beta-amyloid(1-40) perturbs phosphatidylcholine model membranes. *J. Mol. Biol.*, 368(4):982–997, 2007.

[103] M Coles, W Bicknell, AA Watson, DP Fairlie, and DJ Craik. Solution structure of amyloid beta-peptide(1-40) in a water-micelle environment. Is the membrane-spanning domain where we think it is? *Biochemistry*, 37(31):11064–11077, 1998.

[104] E Tischer and B Cordell. beta-amyloid precursor protein - Location of transmembrane domain and specificity of gamma-secretase cleavage. *J. Biol. Chem.*, 271(36):21914–21919, 1996.

[105] Hyunbum Jang, Jie Zheng, Ratnesh Lal, and Ruth Nussinov. New structures help the modeling of toxic amyloid beta ion channels. *Trends Biochem.Sci.*, 33(2):91–100, 2008.

[106] Hyunbum Jang, Jie Zheng, and Ruth Nussinov. Models of beta-amyloid ion channels in the membrane suggest that channel formation in the bilayer is a dynamic process. *Biophys. J.*, 93(6):1938–1949, 2007.

[107] Hyunbum Jang, Fernando Teran Arce, Ricardo Capone, Srinivasan Ramachandran, Ratnesh Lal, and Ruth Nussinov. Misfolded Amyloid Ion Channels Present Mobile beta-Sheet Subunits in Contrast to Conventional Ion Channels. *Biophys. J.*, 97(11):3029–3037, 2009.

[108] Hyunbum Jang, FernandoTeran Arce, Mirela Mustata, Srinivasan Ramachandran, Ricardo Capone, Ruth Nussinov, and Ratnesh Lal. Antimicrobial protegrin-1 forms amyloid-like fibrils with rapid kinetics suggesting a functional link. *Biophys. J.*, 100:1775–1783, 2011.

[109] Ricardo Capone, Mirela Mustata, Hyunbum Jang, Fernando Teran Arce, Ruth Nussinov, and Ratnesh Lal. Antimicrobial protegrin-1 forms ion channels: Molecular dynamic simulation, atomic force microscopy, and electrical conductance studies. *Biophys. J.*, 98:2644–2652, 2010.

[110] Ricardo Capone, Hyunbum Jang, Samuel A. Kotler, Bruce L. Kagan, Ruth Nussinov, and Ratnesh Lal. Probing structural features of alzheimer's amyloid-beta pores in bilayers using site-specific amino acid substitutions. *Biochemistry*, 51:776–785, 2012.

[111] Fernando Teran Arce, Hyunbum Jang, Srinivasan Ramachandran, Preston B. Landon, Ruth Nussinov, and Ratnesh Lal. Polymorphism of amyloid beta peptide in different environments: implications for membrane insertion and pore formation. *Soft Matter*, 7:5267–5273, 2011.

[112] B. Strodel, J.W.L. Lee, C.S. Whittleston, and D.J. Wales. Transmembrane structures for Alzheimer's A$\beta_{1-42}$ oligomers. *J. Am. Chem. Soc.*, 132:13300–13312, 2010.

[113] Z. Chang, Y. Luo, Y. Zhang, and G. Wei. Interactions of A$\beta$25-35 $\beta$-barrel-like oligomers with anionic lipid bilayers and resulting membrane leakage: An all-atom molecular dynamics study. *J. Phys. Chem. B*, 115:1165–1174, 2011.

[114] Justin A. Lemkul and David R. Bevan. A comparative molecular dynamics analysis of the amyloid beta-peptide in a lipid bilayer. *Arch. Biochem. Biophys.*, 470(1):54–63, 2008.

[115] Justin A. Lemkul and David R. Bevan. Perturbation of membranes by the amyloid beta-peptide - a molecular dynamics study. *FEBS J.*, 276(11):3060–3075, 2009.

[116] Justin A. Lemkul and David R. Bevan. Lipid composition influences the release of Alzheimer's amyloid beta-peptide from membranes. *Protein Sci.*, 20:1530–1545, 2011.

[117] C. H. Davis and M. L. Berkowitz. Interaction between amyloid-beta peptide and phospholipid bilayers: A molecular dynamics study. *Biophysical J.*, 96:785–797, 2009.

[118] Charles H. Davis and Max L. Berkowitz. Structure of the Amyloid-beta (1-42) Monomer Absorbed To Model Phospholipid Bilayers: A Molecular Dynamics Study. *J. Phys. Chem. B*, 113:14480–14486, 2009.

[119] Charles H. Davis and Max L. Berkowitz. A molecular dynamics study of the early stages of amyloid-beta(1-42) oligomerization: The role of lipid membranes. *Proteins*, 78:2533–2545, 2010.

[120] YC Xu, JJ Shen, XM Luo, WL Zhu, KX Chen, JP Ma, and HL Jiang. Conformational transition of amyloid beta-peptide. *PNAS*, 102(15):5403–5407, 2005.

[121] Naoyuki Miyashita, John E. Straub, and D. Thirumalai. Structures of $\beta$-amyloid peptide 1–40, 1–42, and 1–55—the 672–726 fragment of app—in a membrane environment with implications for interactions with $\gamma$-secretase. *J. Am. Chem. Soc.*, 131:17843–17852, 2009.

[122] R. Friedman, R. Pellarin, and A. Caflisch. Amyloid aggregation on lipid bilayers and its impact on membrane permeability. *J. Mol. Biol.*, 387:407–415, 2009.

[123] R. Friedman, R. Pellarin, and A. Caflisch. Soluble protofibrils as metastable intermediates in simulations of amyloid fibril degradation induced by lipid vesicles. *J. Phys. Chem. Lett.*, 1:471–474, 2010.

[124] Jun Zhao, Qiuming Wang, Guizhao Liang, and Jie Zheng. Molecular Dynamics Simulations of Low-Ordered Alzheimer beta-Amyloid Oligomers from Dimer to Hexamer on Self-Assembled Monolayers. *Langmuir*, 27:14876–14887, 2011.

[125] Li Na Zhao, See-Wing Chiu, Jerome Benoit, Lock Yue Chew, and Yuguang Mu. Amyloid beta Peptides Aggregation in a Mixed Membrane Bilayer: A Molecular Dynamics Study. *J. Phys. Chem. B*, 115(42):12247–12256, 2011.

[126] JC Janssen, JA Beck, TA Campbell, A Dickinson, NC Fox, RJ Harvey, H Houlden, MN Rossor, and J Collinge. Early onset familial alzheimer's disease - mutation frequency in 31 families. *Neurology*, 60(2):235–239, 2003.

[127] Y Wakutani, K Watanabe, Y Adachi, K Wada-Isoe, K Urakami, H Ninomiya, TC Saido, T Hashimoto, T Iwatsubo, and K Nakashima. Novel amyloid precursor protein gene missense mutation (d678n) in probable familial alzheimer's disease. *J. Neurol. Neurosurg. Psychiatry*, 75(7):1039–1042, 2004.

[128] M Hashimoto, Y Hori, K Yamada, Y Wakutani, M C Condron, S Tsubuki, T C Saido, and D B Teplow. App (h6r and d7n) mutations linked to familial alzheimers disease alter a amyloid assembly but not app processing. *Soc Neurosci Abstr*, pages 218.–214., 2004.

[129] E Levy, MD Carman, IJ Fernandezmadrid, MD Power, I Lieberburg, SG Vanduinen, Gtam Bots, W Luyendijk, and B Frangione. Mutation of the alzheimers-disease amyloid gene in hereditary cerebral-hemorrhage, dutch type. *Science*, 248(4959):1124–1126, 1990.

[130] Van Broeckhoven, J Haan, E Bakker, JA Hardy, W Van Hul, A Wehnert, M Vegter-Van der Vlis, and RA Roos. Amyloid beta protein precursor gene and hereditary cerebral hemorrhage with amyloidosis (dutch). *Science*, 248, 1990.

[131] DM Walsh, A Lomakin, GB Benedek, MM Condron, and DB Teplow. Amyloid beta-protein fibrillogenesis - detection of a protofibrillar intermediate. *J. Biol. Chem.*, 272(35):22364–22372, 1997.

[132] A Clements, D Allsop, DM Walsh, and CH Williams. Aggregation and metal-binding properties of mutant forms of the amyloid a beta peptide of alzheimer's disease. *J. Neurochem.*, 66(2):740–747, 1996.

[133] L Miravalle, T Tokuda, R Chiarle, G Giaccone, O Bugiani, F Tagliavini, B Frangione, and J Ghiso. Substitutions at codon 22 of alzheimer's a beta peptide induce diverse conformational changes and apoptotic effects in human cerebral endothelial cells. *J. Biol. Chem.*, 275(35):27110–27116, 2000.

[134] K Murakami, K Irie, A Morimoto, H Ohigashi, M Shindo, M Nagao, T Shimizu, and T Shirasawa. Neurotoxicity and physicochemical properties of a beta mutant peptides from cerebral amyloid angiopathy - implication for the pathogenesis of cerebral amyloid angiopathy and alzheimer's disease. *J. Biol. Chem.*, 278(46):46179–46187, 2003.

[135] L Hendriks, CM Vanduijn, P Cras, M Cruts, W Vanhul, F Vanharskamp, A Warren, MG Mcinnis, SE Antonarakis, JJ Martin, A Hofman, and C Vanbroeckhoven. Presenile-dementia and cerebral-hemorrhage linked to a mutation at codon-692 of the beta-amyloid precursor protein gene. *Nature Genet.*, 1(3):218–221, 1992.

[136] DM Walsh, DM Hartley, MM Condron, DJ Selkoe, and DB Teplow. In vitro studies of amyloid beta-protein fibril assembly and toxicity provide clues to the aetiology of flemish variant (ala(692) - gly) alzheimer's disease. *Biochem. J.*, 355(Part 3):869–877, 2001.

[137] C Nilsberth, A Westlind-Danielsson, CB Eckman, MM Condron, K Axelman, C Forsell, C Stenh, J Luthman, DB Teplow, SG Younkin, J Naslund, and L Lannfelt. The 'arctic' app mutation (e693g) causes alzheimer's disease by enhanced a beta protofibril formation. *Nat. Neurosci.*, 4(9):887–893, 2001.

[138] DM Walsh, DM Hartley, Y Kusumoto, Y Fezoui, MM Condron, A Lomakin, GB Benedek, DJ Selkoe, and DB Teplow. Amyloid beta-protein fibrillogenesis - structure and biological activity of protofibrillar intermediates. *J. Biol. Chem.*, 274(36):25945–25952, 1999.

[139] DM Hartley, DM Walsh, CPP Ye, T Diehl, S Vasquez, PM Vassilev, DB Teplow, and DJ Selkoe. Protofibrillar intermediates of amyloid beta-protein induce acute electrophysiological changes and progressive neurotoxicity in cortical neurons. *J. Neurosci.*, 19(20):8876–8884, 1999.

[140] TJ Grabowski, HS Cho, JPG Vonsattel, GW Rebeck, and SM Greenberg. Novel amyloid precursor protein mutation in an iowa family with dementia and severe cerebral amyloid angiopathy. *Ann. Neurol.*, 49(6):697–705, 2001.

[141] Noel D. Lazo, Marianne A. Grant, Margaret C. Condron, Alan C. Rigby, and David B. Teplow. On the nucleation of amyloid beta-protein monomer folding. *Protein Science : A Publication of the Protein Society*, 14(6):1581–1596, 2005.

[142] Wei Chen, Normand Mousseau, and Philippe Derreumaux. The conformations of the amyloid-beta (21-30) fragment can be described by three families in solution. *J. Chem. Phys.*, 125(8):084911, 2006.

[143] Nicolas L Fawzi, Aaron H Phillips, Jory Z Ruscio, Michaeleen Doucleff, David E Wemmer, and Teresa Head-Gordon. Structure and dynamics of the abeta(21-30) peptide from the interplay of NMR experiments and molecular simulations. *JACS*, 130(19):6145–6158, 2008.

[144] Andrij Baumketner, Summer L. Bernstein, Thomas Wyttenbach, Noel D. Lazo, David B. Teplow, Michael T. Bowers, and Joan-Emma Shea. Structure of the 21-30 fragment of amyloid beta-protein. *Protein Science : A Publication of the Protein Society*, 15(6):1239–1247, 2006.

[145] Jose M Borreguero, Brigita Urbanc, Noel D Lazo, Sergey V Buldyrev, David B Teplow, and H Eugene Stanley. Folding events in the 21-30 region of amyloid beta-protein (abeta) studied in silico. *PNAS*, 102(17):6015–6020, 2005.

[146] Mary Griffin Krone, Andrij Baumketner, Summer L Bernstein, Thomas Wyttenbach, Noel D Lazo, David B Teplow, Michael T Bowers, and Joan-Emma Shea. Effects of familial alzheimer's disease mutations on the folding nucleation of the amyloid beta-protein. *J. Mol. Biol.*, 381(1):221–228, 2008.

[147] Luis Cruz, Brigita Urbanc, Jose M Borreguero, Noel D Lazo, David B Teplow, and H Eugene Stanley. Solvent and mutation effects on the nucleation of amyloid beta-protein folding. *PNAS*, 102(51):18258–18263, 2005.

[148] Marianne A Grant, Noel D Lazo, Aleksey Lomakin, Margaret M Condron, Hiromi Arai, Ghiam Yamin, Alan C Rigby, and David B Teplow. Familial alzheimer's disease mutations alter the stability of the amyloid beta-protein monomer folding nucleus. *PNAS*, 104(42):16522–16527, 2007.

[149] J W Höppener, C Oosterwijk, K L van Hulst, J S Verbeek, P J Capel, E J de Koning, A Clark, H S Jansz, and C J Lips. Molecular physiology of the islet amyloid polypeptide (IAPP)/amylin gene in man, rat, and transgenic mice. *J Cell Biochem*, 55 Suppl:39–53, 1994.

[150] S E Kahn, D A D'Alessio, M W Schwartz, W Y Fujimoto, J W Ensinck, Jr Taborsky, G J, and Jr Porte, D. Evidence of cosecretion of islet amyloid polypeptide and insulin by beta-cells. *Diabetes*, 39:634–638, 1990.

[151] A Clark, C A Wells, I D Buley, J K Cruickshank, R I Vanhegan, D R Matthews, G J Cooper, R R Holman, and R C Turner. Islet amyloid, increased a-cells, reduced b-cells and exocrine fibrosis: quantitative changes in the pancreas in type 2 diabetes. *Diabetes Res.*, 9:151–159, 1988.

[152] Rebecca L. Hull, Gunilla T. Westermark, Per Westermark, and Steven E. Kahn. Islet amyloid: A critical entity in the pathogenesis of type 2 diabetes. *J Clin Endocr Metab*, 89:3629–3643, 2004.

[153] S E Kahn, S Andrikopoulos, and C B Verchere. Islet amyloid: a long-recognized but underappreciated pathological feature of type 2 diabetes. *Diabetes*, 48:241–253, 1999.

[154] J E Morley, J F Flood, M Horowitz, P M Morley, and M J Walter. Modulation of food intake by peripherally administered amylin. *Am J Physiol.*, 267:R178–184, 1994.

[155] A A Young, B Gedulin, W Vine, A Percy, and T J Rink. Gastric emptying is accelerated in diabetic BB rats and is slowed by subcutaneous injections of amylin. *Diabetologia*, 38:642–648, 1995.

[156] Bjrn kesson, Georgios Panagiotidis, Per Westermark, and Ingmar Lundquist. Islet amyloid polypeptide inhibits glucagon release and exerts a dual action on insulin release from isolated islets. *Regul Peptides*, 111:55–60, 2003.

[157] B R Gedulin, T J Rink, and A A Young. Dose-response for glucagonostatic effect of amylin in rats. *Metabolism*, 46:67–70, 1997.

[158] P Dgano, R A Silvestre, M Salas, E Peir, and J Marco. Amylin inhibits glucose-induced insulin secretion in a dose-dependent manner. study in the perfused rat pancreas. *Regul Peptides*, 43:91–96, 1993.

[159] B Ahrn, C Oosterwijk, C J Lips, and J W Hppener. Transgenic overexpression of human islet amyloid polypeptide inhibits insulin secretion and glucose elimination after gastric glucose gavage in mice. *Diabetologia*, 41:1374–1380, 1998.

[160] S Gebre-Medhin, H Mulder, M Pekny, G Westermark, J Trnell, P Westermark, F Sundler, B Ahrn, and C Betsholtz. Increased insulin secretion and glucose tolerance in mice lacking islet amyloid polypeptide (amylin). *Biochem Bioph Res Co*, 250:271–277, 1998.

[161] P Westermark, E Wilander, G T Westermark, and K H Johnson. Islet amyloid polypeptide-like immunoreactivity in the islet b cells of type 2 (non-insulin-dependent) diabetic and non-diabetic individuals. *Diabetologia*, 30(11):887–892, 1987.

[162] K H Johnson, T D O'Brien, D W Hayden, K Jordan, H K Ghobrial, W C Mahoney, and P Westermark. Immunolocalization of islet amyloid polypeptide (IAPP) in pancreatic beta cells by means of peroxidase-antiperoxidase (PAP) and protein a-gold techniques. *Am. J. Pathol.*, 130(1):1–8, 1988.

[163] A Clark, C A Edwards, L R Ostle, R Sutton, J B Rothbard, J F Morris, and R C Turner. Localisation of islet amyloid peptide in lipofuscin bodies and secretory granules of human b-cells and in islets of type-2 diabetic subjects. *Cell Tissue Res.*, 257(1):179–185, 1989.

[164] A Lukinius, E Wilander, G T Westermark, U Engstrm, and P Westermark. Co-localization of islet amyloid polypeptide and insulin in the b cell secretory granules of the human pancreatic islets. *Diabetologia*, 32(4):240–244, 1989.

[165] T Sanke, G I Bell, C Sample, A H Rubenstein, and D F Steiner. An islet amyloid peptide is derived from an 89-amino acid precursor by proteolytic processing. *J. Biol. Chem.*, 263(33):17243–17246, 1988.

[166] M Nishi, T Sanke, S Seino, R L Eddy, Y S Fan, M G Byers, T B Shows, G I Bell, and D F Steiner. Human islet amyloid polypeptide gene: complete nucleotide sequence, chromosomal localization, and evolutionary history. *J. Mol. Endocrinol.*, 3(11):1775–1781, 1989.

[167] C Betsholtz, V Svensson, F Rorsman, U Engstrm, G T Westermark, E Wilander, K Johnson, and P Westermark. Islet amyloid polypeptide (IAPP):cDNA cloning and identification of an amyloidogenic region associated with the species-specific occurrence of age-related diabetes mellitus. *Exp. Cell Res.*, 183(2):484–493, 1989.

[168] Michael K. Badman, Kathleen I.J. Shennan, Joanne L. Jermany, Kevin Docherty, and Anne Clark. Processing of pro-islet amyloid polypeptide (proIAPP) by the prohormone convertase PC2. *FEBS Letters*, 378(3):227–231, 1996.

[169] C E Higham, R L Hull, L Lawrie, K I Shennan, J F Morris, N P Birch, K Docherty, and A Clark. Processing of synthetic pro-islet amyloid polypeptide (proIAPP) 'amylin' by recombinant prohormone convertase enzymes, PC2 and PC3, in vitro. *Eur. J. Biochem. / FEBS*, 267(16):4998–5004, 2000.

[170] J Wang, J Xu, J Finnerty, M Furuta, D F Steiner, and C B Verchere. The prohormone convertase enzyme 2 (PC2) is essential for processing pro-islet amyloid polypeptide at the NH2-terminal cleavage site. *Diabetes*, 50(3):534–539, 2001.

[171] Lucy Marzban, Genny Trigo-Gonzalez, Xiaorong Zhu, Christopher J Rhodes, Philippe A Halban, Donald F Steiner, and C Bruce Verchere. Role of beta-cell prohormone convertase (PC)1/3 in processing of pro-islet amyloid polypeptide. *Diabetes*, 53(1):141–148, 2004.

[172] A N Roberts, B Leighton, J A Todd, D Cockburn, P N Schofield, R Sutton, S Holt, Y Boyd, A J Day, and E A Foot. Molecular and functional characterization of

amylin, a peptide associated with type 2 diabetes mellitus. *PNAS*, 86(24):9662–9666, 1989.

[173] S. Luca, W.M. Yau, R. Leapman, and R. Tycko. Peptide conformation and supramolecular organization in amylin fibrils: constraints from solid-state nmr. *Biochemistry*, 46:13505–13522, 2007.

[174] S.A. Jayasinghe and R. Langen. Identifying structural features of fibrillar islet amyloid polypeptide using site-directed spin labeling. *J. Biol. Chem.*, 279:48420–48425, 2004.

[175] D H J Lopes, A Meister, A Gohlke, A Hauser, A Blume, and R Winter. Mechanism of islet amyloid polypeptide fibrillation at lipid interfaces studied by infrared reflection absorption spectroscopy. *Biophys J*, 93:3132–3141, 2007.

[176] P Westermark, U Engstrm, K H Johnson, G T Westermark, and C Betsholtz. Islet amyloid polypeptide: pinpointing amino acid residues linked to amyloid fibril formation. *Proc. Natl. Acad. Sci. USA*, 87:5036–5040, 1990.

[177] E T Jaikaran, C E Higham, L C Serpell, J Zurdo, M Gross, A Clark, and P E Fraser. Identification of a novel human islet amyloid polypeptide beta-sheet domain and factors influencing fibrillogenesis. *J Mol Biol*, 308:515–525, 2001.

[178] S Seino. S20G mutation of the amylin gene is associated with type II diabetes in japanese. study group of comprehensive analysis of genetic factors in diabetes mellitus. *Diabetologia*, 44:906–909, 2001.

[179] Sajith A Jayasinghe and Ralf Langen. Lipid membranes modulate the structure of islet amyloid polypeptide. *Biochemistry*, 44:12113–12119, 2005.

[180] Jefferson D Knight and Andrew D Miranker. Phospholipid catalysis of diabetic amyloid assembly. *J Mol Biol*, 341:1175–1187, 2004.

[181] Jefferson D Knight, James A Hebda, and Andrew D Miranker. Conserved and cooperative assembly of membrane-bound alpha-helical states of islet amyloid polypeptide. *Biochemistry*, 45:9496–9508, 2006.

[182] Emma Sparr, Maarten F M Engel, Dmitri V Sakharov, Mariette Sprong, Jet Jacobs, Ben de Kruijff, Jo W M Höppener, and J Antoinette Killian. Islet amyloid polypeptide-induced membrane leakage involves uptake of lipids by forming amyloid fibers. *FEBS Lett*, 577:117–120, 2004.

[183] L R McLean and A Balasubramaniam. Promotion of beta-structure by interaction of diabetes associated polypeptide (amylin) with phosphatidylcholine. *Biochim Biophys Acta*, 1122:317–320, 1992.

[184] A. Quist, I. Doudevski, H. Lin, R. Azimova, D. Ng, B. Frangione, B. Kagan, J. Ghiso, and R. Lal. Amyloid ion channels: A common structural link for protein misfolding disease. *Proc. Natl. Acad. Sci. USA*, 102:10427–10432, 2005.

[185] Sara M. Butterfield and Hilal A. Lashuel. Amyloidogenic ProteinMembrane interactions: Mechanistic insight from model systems. *Angew. Chem. Int. Ed. Engl.*, 49(33):56285654, 2010.

[186] Massimo Stefani. Biochemical and biophysical features of both oligomer/fibril and cell membrane in amyloid cytotoxicity. *FEBS Journal*, 277:46024613, 2010.

[187] Tajib A. Mirzabekov, Meng-chin Lin, and Bruce L. Kagan. Pore formation by the cytotoxic islet amyloid peptide amylin. *J Biol Chem*, 271:1988–1992, 1996.

[188] Alfredo Lorenzo, Bronwyn Razzaboni, Gordon C. Weir, and Bruce A. Yankner. Pancreatic islet cell toxicity of amylin associated with type-2 diabetes mellitus. *Nature*, 368:756–760, 1994.

[189] T. D. O'Brien, P. C. Butler, D. K. Kreutter, L. A. Kane, and N. L. Eberhardt. Human islet amyloid polypeptide expression in COS-1 cells. a model of intracellular amyloidogenesis. *Am J Pathol*, 147:609–616, 1995.

[190] H J Hiddinga and N L Eberhardt. Intracellular amyloidogenesis by human islet amyloid polypeptide induces apoptosis in COS-1 cells. *Am J Pathol*, 154:1077–1088, 1999.

[191] Rakez Kayed, Yuri Sokolov, Brian Edmonds, Theresa M McIntire, Saskia C Milton, James E Hall, and Charles G Glabe. Permeabilization of lipid bilayers is a common conformation-dependent activity of soluble amyloid oligomers in protein misfolding diseases. *J Biol Chem*, 279:46363–46366, 2004.

[192] Maarten F M Engel, HaciAli Yigittop, Ronald C Elgersma, Dirk T S Rijkers, Rob M J Liskamp, Ben de Kruijff, Jo W M Höppener, and J Antoinette Killian. Islet amyloid polypeptide inserts into phospholipid monolayers as monomer. *J Mol Biol*, 356:783–789, 2006.

[193] Chang-Chun Lee, Yen Sun, and Huey W Huang. How type II diabetes-related islet amyloid polypeptide damages lipid bilayers. *Biophys J*, 102:1059–1068, 2012.

[194] Jeffrey R Brender, Kevin Hartman, Kendra R Reid, Robert T Kennedy, and Ayyalusamy Ramamoorthy. A single mutation in the nonamyloidogenic region of islet amyloid polypeptide greatly reduces toxicity. *Biochemistry*, 47:12680–12688, 2008.

[195] Ravi Prakash Reddy Nanga, Jeffrey R. Brender, Jiadi Xu, Gianluigi Veglia, and Ayyalusamy Ramamoorthy. Structures of rat and human islet amyloid polypeptide IAPP119 in micelles by NMR spectroscopy. *Biochemistry*, 47:12689–12697, 2008.

[196] Yun Zhang, Yin Luo, Yonghua Deng, Yuguang Mu, and Guanghong Wei. Lipid interaction and membrane perturbation of human islet amyloid polypeptide monomer and dimer by molecular dynamics simulations. *PloS ONE*, 7:e38191, 2012.

[197] Mojie Duan, Jue Fan, and Shuanghong Huo. Conformations of islet amyloid polypeptide monomers in a membrane environment: Implications for fibril formation. *PloS ONE*, 7:e47150, 2012.

[198] Jun Zhao, Yin Luo, Hyunbum Jang, Xiang Yu, Guanghong Wei, Ruth Nussinov, and Jie Zheng. Probing ion channel activity of human islet amyloid polypeptide (amylin). *Biochim Biophys Acta*, 1818:3121–3130, 2012.

[199] Dequan Xiao, Li Fu, Jian Liu, Victor S. Batista, and Elsa C.Y. Yan. Amphiphilic Adsorption of Human Islet Amyloid Polypeptide Aggregates to Lipid/Aqueous Interfaces. *J. Mol. Biol.*, 421:537 – 547, 2012.

[200] Leach A.R. *Molecular modelling: principles and applications*. Pearson Prentice Hall, Harlow, GB, 2001.

[201] Roland Stote, Annick Dejaegere, Dmitry Kuznetsov, and Laurent Falquet. `http://www.ch.embnet.org/MD_tutorial/`.

[202] Loup Verlet. Computer "Experiments" on classical fluids. i. thermodynamical properties of lennard-jones molecules. *Phys. Rev.*, 159(1):98–103, 1967.

[203] R.W Hockney, S.P Goel, and J.W Eastwood. Quiet high-resolution computer models of a plasma. *J. Comput. Phys.*, 14(2):148–158, 1974.

[204] William C. Swope, Hans C. Andersen, Peter H. Berens, and Kent R. Wilson. A computer simulation method for the calculation of equilibrium constants for the formation of physical clusters of molecules: Application to small water clusters. *J. Chem. Phys.*, 76(1):637–649, 1982.

[205] Hong Qian Daniel A. Beard. *Chemical Biophysics: Quantitative Analysis of Cellular Systems*. Cambridge University Press, UK, 2008.

[206] Laurent Capolungo Mohammed Cherkaoui. *Atomistic and Continuum Modeling of Nanocrystalline Materials: Deformation Mechanisms and Scale Transition*. Springer, 2009.

[207] O Berger, O Edholm, and F Jahnig. Molecular dynamics simulations of a fluid bilayer of dipalmitoylphosphatidylcholine at full hydration, constant pressure, and constant temperature. *Biophys. J.*, 72(5):2002–2013, 1997.

[208] H. J. C. Berendsen, J. P. M. Postma, W. F. van Gunsteren, A. DiNola, and J. R. Haak. Molecular dynamics with coupling to an external bath. *J. Chem. Phys.*, 81(8):3684–3690, 1984.

[209] Giovanni Bussi, Davide Donadio, and Michele Parrinello. Canonical sampling through velocity rescaling. *J. Chem. Phys.*, 126(1):014101–014101–7, 2007.

[210] Shichi Nos. A molecular dynamics method for simulations in the canonical ensemble. *Mol. Phys.*, 52(2):255–268, 1984.

[211] William G. Hoover. Canonical dynamics: Equilibrium phase-space distributions. *Phys. Rev. A*, 31(3):1695–1697, 1985.

[212] M. Parrinello and A. Rahman. Polymorphic transitions in single crystals: A new molecular dynamics method. *J. Appl. Phys.*, 52(12):7182–7190, 1981.

[213] Shuichi Nos and M.L. Klein. Constant pressure molecular dynamics for molecular systems. *Mol. Phys.*, 50(5):1055–1076, 1983.

[214] Jensen F. *Introduction to Computational Chemistry*. John Wiley 'I&' Sons Ltd, UK, 2007.

[215] P. P. Ewald. Die berechnung optischer und elektrostatischer gitterpotentiale. *Annalen der Physik*, 369(3):253287, 1921.

[216] Tom Darden, Darrin York, and Lee Pedersen. Particle mesh ewald: An nlog(n) method for ewald sums in large systems. *J. Chem. Phys.*, 98(12):10089–10092, 1993.

[217] Ulrich Essmann, Lalith Perera, Max L. Berkowitz, Tom Darden, Hsing Lee, and Lee G. Pedersen. A smooth particle mesh ewald method. *J. Chem. Phys.*, 103(19):8577–8593, 1995.

[218] R. W. Hockney and J. W Eastwood. *Computer simulation using particles*. New York:McGraw-Hill, 1981.

[219] Brock A. Luty, Ilario G. Tironi, and Wilfred F. van Gunsteren. Latticesum methods for calculating electrostatic interactions in molecular simulations. *J. Chem. Phys.*, 103(8):3014–3021, 1995.

[220] T B Woolf and B Roux. Molecular dynamics simulation of the gramicidin channel in a phospholipid bilayer. *PNAS*, 91(24):11631–11635, 1994.

[221] Walter L Ash, Marian R Zlomislic, Eliud O Oloo, and D Peter Tieleman. Computer simulations of membrane proteins. *Biochimica et biophysica acta*, 1666(1-2):158–189, 2004.

[222] James Gumbart, Yi Wang, Alekseij Aksimentiev, Emad Tajkhorshid, and Klaus Schulten. Molecular dynamics simulations of proteins in lipid bilayers. *Curr. Opin. Struct. Biol.*, 15(4):423–431, 2005.

[223] Christian Kandt, Walter L. Asha, and D. Peter Tieleman. Setting up and running molecular dyanmics simulations of membrane proteins. *Methods*, 41:475–488, 2007.

[224] W. Humphrey, A. Dalke, and K. Schulten. VMD – visual molecular dynamics. *J. Molec. Graphics*, 14:33–38, 1996.

[225] B. Hess, C. Kutzner, D. van der Spoel, and E. Lindahl. GROMACS 4: Algorithms for highly efficient, load-balanced, and scalable molecular simulation. *J. Chem. Theory Comput.*, 4:435–447, 2008.

[226] A. Kukol. Lipid models for united-atom molecular dynamics simulations of proteins. *J. Chem. Theory Comput.*, 5:615–626, 2009.

[227] Berk Hess, Henk Bekker, Herman J. C. Berendsen, and Johannes G. E. M. Fraaije. LINCS: a linear constraint solver for molecular simulations. *J. Comput. Chem.*, 18(12):14631472, 1997.

[228] William J. Allen, Justin A. Lemkul, and David R. Bevan. GridMAT-MD: a grid-based membrane analysis tool for use with molecular dynamics. *J Comput Chem*, 30:1952–1958, 2009.

[229] Christian Tischer and Philippe I. H. Bastiaens. Lateral phosphorylation propagation: an aspect of feedback signalling? *Nat. Rev. Mol. Cell Biol.*, 4(12):971–975, 2003.

[230] O. Wirths, G. Multhaup, and T. A. Bayer. A modified beta-amyloid hypothesis: intraneuronal accumulation of the beta-amyloid peptide–the first step of a fatal cascade. *J Neurochem.*, 91:513–520, 2004.

[231] Yutaka Hirakura, Meng-Chin Lin, and Bruce L. Kagan. Alzheimer amyloid a$\beta$1-42 channels: Effects of solvent, ph, and congo red. *J. Neurosci. Res.*, 57:458–466, 1999.

[232] Y. Shafrir, S. Durell, N. Arispe, and H. R. Guy. Models of membrane-bound alzheimer's abeta peptide assemblies. *Proteins: Struct., Func. and Bioinf.*, 78:3473–3487, 2010.

[233] S.R. Durell, H.R. Guy, N. Arsipe, E. Rojas, and H.B. Pollard. Theoretical models of the ion channel structure of amyloid $\beta$-protein. *Biophys. J.*, 67:2137–2145, 1994.

[234] K Murakami, K Irie, A Morimoto, H Ohigashi, M Shindo, M Nagao, T Shimizu, and T Shirasawa. Synthesis, aggregation, neurotoxicity, and secondary structure of various A beta 1-42 mutants of familial Alzheimer's disease at positions 21-23. *Biochem. Biophys. Res. Commun.*, 294:5–10, 2002.

[235] Phillip M. Pifer, Elizabeth A. Yates, and Justin Legleiter. Point mutations in a$\beta$ result in the formation of distinct polymorphic aggregates in the presence of lipid bilayers. *PLoS ONE*, 6:e16248, 2011.

[236] R P Mason, R F Jacob, M F Walter, P E Mason, N A Avdulov, S V Chochina, U Igbavboa, and W G Wood. Distribution and fluidizing action of soluble and aggregated amyloid beta-peptide in rat synaptic plasma membranes. *J. Biol. Chem.*, 274(26):18801–18807, 1999.